

Biomechanical Analysis of Femoral Damage Mechanisms Related to Total Hip Arthroplasty

ノル アイマン ノル イズミン

<https://hdl.handle.net/2324/7157373>

出版情報 : Kyushu University, 2023, 博士 (工学), 課程博士
バージョン :
権利関係 :

**Biomechanical Analysis of Femoral Damage Mechanism Related to
Total Hip Arthroplasty**

PhD Thesis

Submitted as partial fulfillment of the requirements for the degree

Doctor of Engineering

by

Nor Aiman Nor Izmin

3ES20116G

Department of Molecular and Material Sciences

Interdisciplinary Graduate School of Engineering Sciences

Kyushu University

Japan

2023

ACKNOWLEDGEMENTS

First and foremost, all praises to Allah, the Almighty, for His showers and blessings for easing my passage in completing my Ph.D. degree, successfully. Peace and salutation are poured down upon beloved Prophet Muhammad SAW and his family and companions. My deep sincere gratitude goes first to my supervisor, Associate Professor Dr. Mitsugu Todo, for his exceptional guidance and invaluable expertise throughout the journey. Thank you for giving me the opportunity to become one of your students. Your dedication and patience have been instrumental in making this dissertation possible, and I am truly grateful to work under your mentorship.

To my dearest wife Dr. Fatin Hazwani, I am forever indebted to you. You, yourself, has been the fuel that has kept me going when the going got tough. I cannot thank you enough for your constant presence and your endless support. To my beloved parents, Mr. Nor Izmin Hasbullah and Ms. Nor Azwa Baharain, this is for both of you. Your endless prayers have made this possible. Thank you for raising me into the person I am today. Likewise, to both my family members and in-laws far away, who have reached out to me through phone calls, visits, and unwavering support, exceeding any expectations I may have had. Their constant encouragement has been a source of great strength throughout this journey.

To all my seniors and my laboratory colleagues; Dr. Wu Shun, Dr. Hiroko Kurita, Dr. Zaw Linn Htun, Dr. Hisyam Marwan, Mr. Matsufuji Ryota, Mr. Daisuke Miyahara, and all the others, thank you for your invaluable assistance and support; in both academic and life matters.

I would like to extend my deepest gratitude to Mrs. Yoshizu and Mr. Hayashi Daigo for their outstanding organizational abilities. Their remarkable skills have played a crucial role in ensuring the seamless execution of my academic endeavors. To all the staff members at the student support center of Kyushu University Chikushi campus, thank you for your invaluable assistance. My thanks also go to my friends, Mr. Ainuddin Azani, Mr. Yasin Zamri, Mr. Haikal Omar, and others for being such a kind and supportive friend.

I am sincerely grateful to Dr. Carol Ling Sze Yee from the University of Malaya for her invaluable guidance and unwavering support on the technical aspects of total hip surgery. Her expertise and assistance have been instrumental in my journey. Additionally, I would like to extend my heartfelt appreciation to Associate Professor Dr. Desmond Chong Yok Rue from the Singapore Institute of Technology, as well as Dr. Halim Abdullah, Dr. Shahrizan Adenan, and Dr. Fazli Manan from Universiti Teknologi MARA for their invaluable contributions in enhancing my understanding of research. Their dedication and support have been truly remarkable.

I am eternally grateful to Teijin Nakashima Medical and Shirouzu Susugu Foundation for their invaluable financial support throughout my Ph.D. journey. Their generous assistance has been instrumental in enabling me to successfully complete my Ph.D. thesis.

Last but not least, thank you to those who have kept me in your prayers.

AIMAN IZMIN

ABSTRACT

Total hip arthroplasty (THA) has become a common solution for addressing end-stage hip diseases in middle-aged and older patients. Risk factors that contribute to the complications following THA may related to bone variables (quality, strength, geometry), implant design and implant position. Numerous studies have focused on improving THA outcomes by utilizing computational techniques such as finite element analysis to enhance implant design. However, these studies have been limited to homogeneous bone models, which do not accurately reflect the reality of bone structure. Due to the unrealistic computational bone model, biomechanical analyses investigating the relationship between bone variables and outcomes after THA are rarely conducted. In Chapter 1, we discussed the different fixation methods employed in THA procedures, namely cemented and cementless methods, as well as the implant designs that are currently used for both fixation methods. We also identified the association between fixation methods and implant design, to the potential biomechanical complications such as implant loosening and periprosthetic femoral fractures. Additionally, this chapter reviewed existing biomechanical studies concerning implant design and computational bone models.

In Chapter 2, we investigate the mechanisms of micro-damage formation in femoral bones using the CT-image-based finite element method (CT-FEM) under two different boundary conditions: lateral bending and torsional conditions. Two inhomogeneous finite element bone models were developed based on CT images of 61-year-old and 87-year-old patients, and three types of stems were introduced to represent corresponding cementless THA models. A quantitative comparison of bone mineral density between the two bones

was conducted, followed by finite element analyses using non-linear damage analysis under both boundary conditions. The results revealed that implant geometries, such as shoulder size, stem length, and cross-section shape, influenced the damage behaviour of the models. Furthermore, it was observed that the elderly patient had a higher risk of implant loosening, even at lower loading magnitudes, compared to the younger patient. Additionally, several fracture locations were predicted on both femoral models upon complete failure. Notably, the fracture types were clearly classified according to the Vancouver classification and the AO Foundation/Orthopaedic Trauma Association.

In Chapter 3, we conducted further investigation to determine the mechanism of bone micro-damage formation under different falling configurations, specifically from the lateral to posterolateral side of the femur. Two inhomogeneous finite element bone models were developed based on the 61-year-old and 87-year-old patients, and three different stem designs (stem I, stem II, and stem III) were implanted into the femur. The study revealed a correlation between stem geometry and damage behaviour in the internal region of bone X under varying falling configurations. However, no correlation was observed in bone Y. Additionally, the internal damage distribution of the THA models in bone X exhibited a pattern of concentrated damage at zone 1 and zone 7 of the Gruen zone system, which remained consistent across all stem designs and falling configurations. In THA models of bone Y, the damaged distributions were scattered throughout the bone-stem interfaces, with damaged elements found in all zones of the Gruen zone system. Furthermore, the fracture location in all models was successfully predicted, and the observed fractures aligned with type A_G of the Vancouver fracture classification, which occurred in all THA models.

In Chapter 4, we examined the impact of bone variables, including density, geometry, angle of femoral torsion, and thickness of the femoral cortices, on the formation of bone micro-damage following THA. Using CT images of avascular necrosis patients, we developed 28 intact femoral bone models with ages ranging from 19 to 87 years to explore the relationship between age and bone density. Among these 28 femur models, 10 models were selected for implantation with the Zweymuller stem, divided into two groups based on the highest and lowest bone mineral density (BMD). After proper stem insertion into the femoral bone canal, finite element analyses with nonlinear damage analysis were performed on the THA models under three boundary conditions: stance, lateral bending, and torsion. The study revealed a strong correlation between bone density and fracture load in the 10 THA models, which remained consistent across all three boundary conditions: stance ($r = 0.74$), lateral bending ($r = 0.79$), and torsion ($r = 0.88$). However, a moderate correlation was observed between bone density and the number of solid element failures, which also remained consistent across all boundary conditions: stance ($r = -0.40$), lateral bending ($r = -0.51$), and torsion ($r = -0.48$). Furthermore, femoral models with a bent shape of the femoral shaft and thin cortices experienced greater bone damage compared to models with normal geometry. Additionally, THA models with retroversion stem placement resulted in higher bone damage compared to models with normal anteversion placement.

The primary objective of cementless total hip arthroplasty is to achieve biological fixation or osseointegration, where the implant's primary stability plays a crucial role in promoting this process. In Chapter 5, a collarless and collared version of a similar cementless THA stem was implanted into a finite element bone model developed from a CT image of a 61-year-old patient with avascular necrosis. Finite element analyses with nonlinear damage analysis were conducted under two different boundary conditions: axial compression and torsion, after the stem was properly inserted into the femoral canal. The applied hip loading was normalized to body weight (BW), ranging from 0.5 BW to 3 BW. The results revealed higher strain values in the bone model implanted with the collarless stem compared to the collared stem under both boundary conditions. However, the percentage difference in strain values between the two models was more significant under axial compression. Furthermore, greater internal bone damage was observed in the collarless model than in the collared model under both boundary conditions, as indicated by the distribution of solid element failures. Additionally, the presence of a collar was found to affect the strength of the bone, and the location of the bone fracture was similar in both models, as illustrated by the shell element failures. The collared stem version may improve implant stability following cementless total hip arthroplasty and promote better outcomes.

Finally, in Chapter 6, all results are summarized as a general conclusion.

TABLE OF CONTENTS

| | |
|--|-----------|
| ACKNOWLEDGEMENTS | 2 |
| ABSTRACT | 4 |
| LIST OF TABLES | 11 |
| LIST OF FIGURES | 12 |
| CHAPTER 1: INTRODUCTION | |
| 1.1 Background | 17 |
| 1.2 Total Hip Arthroplasty | 22 |
| 1.3 Implant design in Total Hip Arthroplasty | 25 |
| 1.3.1 Implant design in cemented total hip arthroplasty | 25 |
| 1.3.2 Implant design in cementless total hip arthroplasty | 28 |
| 1.4 Complications after Total Hip Arthroplasty | 36 |
| 1.4.1 Aseptic/ mechanical loosening | 36 |
| 1.4.2 Periprosthetic femoral fractures | 40 |
| 1.5 Biomechanical study of Total Hip Arthroplasty | 44 |
| 1.6 Problem statement | 48 |
| 1.7 Research objectives | 49 |
| 1.8 Scope and limitations | 49 |
| CHAPTER 2: DAMAGE MECHANISMS UNDER LATERAL BENDING AND TORSIONAL CONDITIONS | |
| 2.1 Overview | 50 |
| 2.2 Construction of intact femoral models | 51 |
| 2.3 Construction of THA models | 52 |
| 2.4 Loading and boundary conditions | 55 |
| 2.5 Mechanical theories and material properties | 56 |
| 2.6 Results and Discussion | 59 |

| | | |
|--|---|------------|
| 2.6.1 | Distribution of bone mineral density | 59 |
| 2.6.2 | Accumulation of element failures as bone micro-damage | 62 |
| 2.6.3 | Distribution of solid and shell element failures | 70 |
| 2.6.4 | Solid element failures within the bone-stem interface at the critical stage | 80 |
| 2.6.5 | Classification of femoral fractures following total hip arthroplasty | 82 |
| 2.7 | Conclusion | 83 |
| | | |
| CHAPTER 3: DAMAGE MECHANISMS UNDER FALLING CONDITIONS | | |
| 3.1 | Overview | 85 |
| 3.2 | Construction of intact femoral model | 86 |
| 3.3 | Construction of THA models | 87 |
| 3.4 | Loading and boundary conditions | 90 |
| 3.5 | Mechanical theories and material properties | 92 |
| 3.6 | Results and Discussion | 94 |
| 3.6.1 | Fracture load under different falling configuration | 94 |
| 3.6.2 | Accumulation of element failures as bone micro-damage | 96 |
| 3.6.3 | Distribution of solid and shell element failures | 105 |
| 3.7 | Conclusion | 124 |
| | | |
| CHAPTER 4: EFFECTS OF BONE VARIABLES AND IMPLANT POSITION | | |
| 4.1 | Overview | 126 |
| 4.2 | Construction of intact femoral models | 127 |
| 4.3 | Construction of THA models | 128 |
| 4.4 | Loading and boundary conditions | 130 |
| 4.5 | Mechanical theories and material properties | 131 |
| 4.6 | Results and Discussion | 133 |
| 4.6.1 | Relationship between age and bone density | 133 |
| 4.6.2 | Correlation of bone density and element failures in THA models | 135 |
| 4.6.3 | Effect of bone variables and implant position to bone damage formation | 138 |
| 4.7 | Conclusion | 158 |

| | |
|--|------------|
| CHAPTER 5: COMPARISON OF COLLARLESS AND COLLARED STEM DESIGNS | |
| 5.1 Overview | 159 |
| 5.2 Construction of intact femoral model | 160 |
| 5.3 Construction of THA model | 161 |
| 5.4 Loading and boundary conditions | 163 |
| 5.5 Mechanical theories and material properties | 164 |
| 5.6 Results and Discussion | 166 |
| 5.6.1 Distribution of bone strain | 166 |
| 5.6.2 Accumulation of bone element failures as bone micro-damage | 171 |
| 5.6.3 Distribution of solid and shell element failures | 173 |
| 5.7 Conclusion | 177 |
| CHAPTER 6: GENERAL CONCLUSIONS | 179 |
| REFERENCES | 184 |

LIST OF TABLES

| | |
|---|-----|
| Table 1. 1: Classification system of cementless implant design..... | 30 |
| Table 2. 1: Illustration of stem I, stem II, and stem III..... | 53 |
| Table 2. 2: Mechanical properties of THA implant..... | 54 |
| Table 2. 3: Relationship between BMD and the material properties..... | 57 |
| Table 2. 4: Failure criterions under tensile and compressive stress states..... | 58 |
| Table 2. 5: Data summarization of bone X and bone Y under LBC and TC..... | 69 |
| Table 3. 1: Illustration of stem I, stem II and stem III..... | 88 |
| Table 3. 2: Mechanical properties of THA implant..... | 89 |
| Table 3. 3 Relationship between BMD and the material properties..... | 93 |
| Table 3. 4: Failure criterions under tensile and compressive stress states..... | 94 |
| Table 3. 5: Data summarization of element failures under all FCs..... | 104 |
| Table 4. 1: Mechanical properties of THA implant..... | 129 |
| Table 4. 2: Selected intact femoral model for implantation..... | 134 |

LIST OF FIGURES

| | |
|--|----|
| Figure 1. 1: Illustration of healthy hip joint and hip joint with osteoarthritis..... | 18 |
| Figure 1. 2: Illustration of AVN of femoral head and the progressive stages of healthy hip joint (stage I) to the collapse of femoral head (stage II to IV)..... | 20 |
| Figure 1. 3: Prosthetic components of total hip arthroplasty | 23 |
| Figure 1. 4: Type of tapered femoral stems | 26 |
| Figure 1. 5: Illustration of implant model in the concept of loaded-taper and composite-beam cement fixation | 28 |
| Figure 1. 6: Progressed stress shielding from (a) 0 year after surgery to (b) 6 years after surgery..... | 39 |
| Figure 1. 7: Vancouver classification of periprosthetic femoral fractures | 43 |
| | |
| Figure 2. 1: THA model of (a) bone X and (b) bone Y implanted with stem I, stem II and stem III | 54 |
| Figure 2. 2: Loading and boundary conditions: (a) lateral bending (LBC) and (b) torsional (TC)..... | 56 |
| Figure 2. 3: Inhomogeneous distribution of BMD: (a) bone X and (b) bone Y | 60 |
| Figure 2. 4: Comparison of volumetric bone mineral density (vBMD) distribution of bone X and bone Y. Point A-B and F-G: Distal cortical bone area. Point B-C and G-H: Area of bone marrow. Point C-D and H-I: Cancellous bone area. Point D-E and I-J: Proximal cortical bone area of bone X and Y, respectively | 61 |

| | |
|--|----|
| Figure 2. 5: Anterior cross-sectional view of bone X and Y: (a) bone density and (b) young's modulus | 62 |
| Figure 2. 6: Number of solid element failures under LBC condition | 64 |
| Figure 2. 7: Number of solid element failures under TC condition..... | 65 |
| Figure 2. 8: Number of shell element failures under LBC condition | 66 |
| Figure 2. 9: Number of shell element failures under TC condition | 67 |
| Figure 2. 10: Distribution of element failures under LBC: (a) intact, (b) stem I, (c) stem II and (d) stem III..... | 72 |
| Figure 2. 11: Distribution of element failures under TC: (a) intact, (b) stem I, (c) stem II and (d) stem III..... | 76 |
| Figure 2. 12: Number of solid element failures in the bone-stem interface region at the critical stage | 81 |
| | |
| Figure 3. 1: THA model of (a) bone X and (b) bone Y implanted with stem I, stem II, and stem III | 89 |
| Figure 3. 2: Loading and boundary conditions (a) FC1, (b) FC2, (c) FC3 and (d) FC4... | 91 |
| Figure 3. 3: Fracture load of intact and THA models of bone X and Y in all falling configurations | 95 |
| Figure 3. 4: Number of solid element failures in tensile (left) and compressive (right) under (a) FC1 and (b) FC2..... | 97 |
| Figure 3. 5: Number of solid element failures in tensile (left) and compressive (right) under (a) FC3 and (b) FC4..... | 98 |

| | |
|---|-----|
| Figure 3. 6: Number of shell element failures in tensile (left) and compressive (right) under (a) FC1 and (b) FC2..... | 99 |
| Figure 3. 7: Number of shell element failures in tensile (left) and compressive (right) under (a) FC3 and (b) FC4..... | 100 |
| Figure 3. 8: Distribution of solid element failures in bone X based on Gruen zone under (a) FC1, (b) FC2, (c) FC3 and (d) FC4 | 106 |
| Figure 3. 9: Distribution of solid element failures in bone Y based on Gruen zone under (a) FC1, (b) FC2, (c) FC3 and (d) FC4 | 107 |
| Figure 3. 10: Distribution of solid and shell element failures under FC1: (a) intact, (b) stem I, (c) stem II and (d) stem III..... | 108 |
| Figure 3. 11: Distribution of solid and shell element failures under FC2: (a) intact, (b) stem I, (c) stem II and (d) stem III..... | 112 |
| Figure 3. 12: Distribution of solid and shell element failures under FC3: (a) intact, (b) stem I, (c) stem II and (d) stem III..... | 116 |
| Figure 3. 13: Distribution of solid and shell element failures under FC4: (a) intact, (b) stem I, (c) stem II and (d) stem III..... | 120 |
| | |
| Figure 4. 1: Zweymuller stem..... | 128 |
| Figure 4. 2: Comparison on the placement of THA implant and original femoral head from (a) anterior view (b) superior view and (c) lateral view | 129 |
| Figure 4. 3: Loading and boundary conditions: (a) stance condition (SC), (b) lateral bending condition (LBC) and (c) torsion condition (TC)..... | 131 |
| Figure 4. 4: Correlation coefficient between age and bone density in 28 femurs | 133 |

| | |
|--|-----|
| Figure 4. 5: Correlation coefficient between BMD and fracture load of THA models under (a) SC, (b) LBC and (c) TC | 136 |
| Figure 4. 6: Correlation coefficient between BMD and solid element failures of THA models under (a) SC, (b) LBC and (c) TC..... | 137 |
| Figure 4. 7: Solid element failures within the interfacial areas of bone and stem at final load under (a) SC, (b) LBC and (c) TC | 139 |
| Figure 4. 8: Comparison between (a) thick femoral cortices, L5 and (b) thin femoral cortices, L2..... | 140 |
| Figure 4. 9: Implant placement (a) normal anteversion and (b) retroversion | 141 |
| Figure 4. 10: Comparison of bone geometry and bone damage formation from external and internal region: (a) straight shaft, H2 and (b) bend shaft, L4 | 142 |
| Figure 4. 11: Distribution of element failures under SC..... | 143 |
| Figure 4. 12: Distribution of element failures under LBC..... | 148 |
| Figure 4. 13: Distribution of element failures under TC | 153 |
| | |
| Figure 5. 1: Version of (a) collarless and (b) collared stem..... | 162 |
| Figure 5. 2: THA model of (a) collarless and (b) collared stem | 162 |
| Figure 5. 3: Loading and boundary conditions: (a) axial compression condition (ACC), (b) anterior view of torsional condition (TC) and (c) superior view of torsion condition (TC) | 164 |
| Figure 5. 4: Distribution of bone strain in (a) tensile and (b) compressive under ACC. | 166 |
| Figure 5. 5: Distribution of bone strain in (a) tensile and (b) compressive under TC | 167 |
| Figure 5. 6: Average value of maximum and minimum principal strain under ACC | 169 |

Figure 5. 7: Average value of maximum and minimum principal strain under TC..... 170

Figure 5. 8: Number of solid element failures in tensile (left) and compressive (right) under
(a) ACC and (b) TC 172

Figure 5. 9: Number of shell element failures in tensile (left) and compressive (right) under
(a) ACC and (b) TC 173

Figure 5. 10: Distribution of solid element failures under ACC..... 174

Figure 5. 11: Distribution of solid element failures under TC..... 175

Figure 5. 12: Formation of shell element failures under (a) ACC and (b) TC 176

CHAPTER 1: INTRODUCTION

1.1 Background

Hip diseases have always been associated with a substantial health burden that adversely affects the quality of life. Hip diseases primarily affect the hip joint, which is the ball-and-socket joint between the head of the femoral bone and the acetabulum. The most common examples of hip disease are hip osteoarthritis and avascular necrosis of the femoral head.

Hip osteoarthritis (OA) is an age-related disease caused by the degeneration of cartilage, which is a strong and flexible tissue present at the ends of the bone. Additionally, cartilage functions as a bone protector and shock absorber, minimizing friction between bones during joint movement. The breakdown of cartilage tissue decreases joint protection, resulting in bones rubbing against each other and causing damage. Over time, the damaged bones will begin to grow outward and develop bone spurs, also known as osteophytes, leading to severe pain and disability.

It has been reported that the global incidence of hip OA increased from 0.74 million to 1.58 million between year 1990 to 2019, representing a percentage increment of 115 % [1]. While hip OA was traditionally associated with elderly patients, several studies have reported that risk factors such as female gender, higher body mass index, ethnicity, and genetic variables also contribute to the occurrence of the disease [2]–[4]. However, in recent years, the number of younger patients affected has shown an increasing trend [5], [6]. Risk factors such as sports injuries, hip deformities, sedentary lifestyle, and obesity

have been mentioned [7]. The high prevalence of hip OA in younger populations poses a new public health issue since they will live with hip OA for a longer time compared to previous generations, increasing their chances of disability. Therefore, hip OA is now considered not only a hip degeneration disease but also a form of total joint failure [8]. Figure 1.1 illustrates the comparison between a healthy hip joint and a hip joint with osteoarthritis.

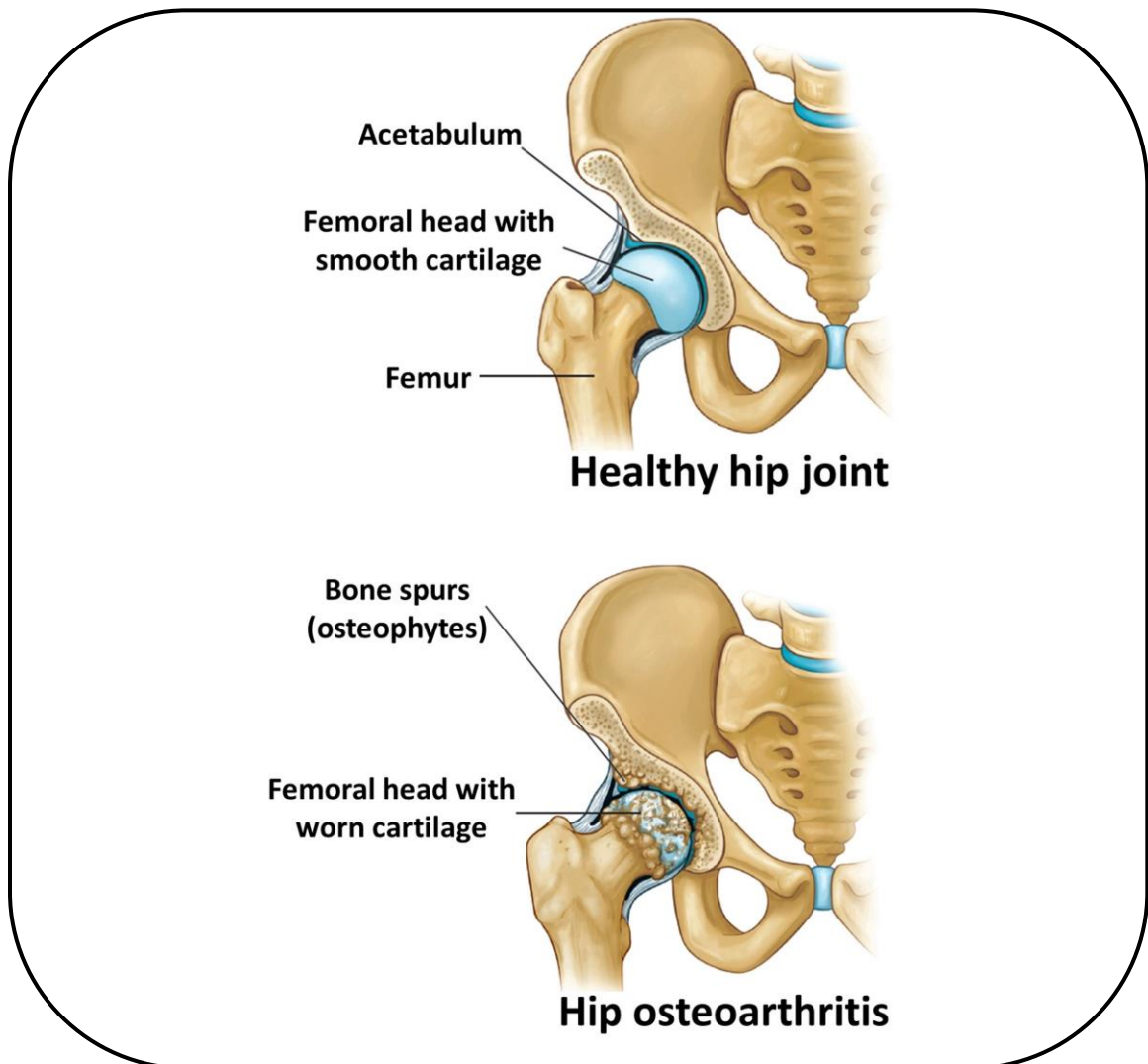


Figure 1. 1: Illustration of healthy hip joint and hip joint with osteoarthritis [9]

Avascular necrosis (AVN) of the femoral head, on the other hand, is a disease where the bone at the head of the femur collapses due to the death of bone tissue. This occurs as a result of disrupted blood supply to the bone. Blood serves as a medium for transporting oxygen and nutrients to the bones to regenerate and maintain their health. Therefore, a loss of blood supply leads to bone tissue death. In such cases, tiny breaks in the bone will appear before it eventually collapses.

According to a universal stratification system for the classification of femoral head AVN, the severity of the disease can be categorized into four stages, which explain the progression from a normal and healthy hip (stage I) to the collapse of the femoral head (stage IV) [10]. In the later stages, patients may experience severe pain and difficulties in movement, and without proper treatment, it could lead to disability.

The known causes of AVN are mostly related to the use of corticosteroids, excessive alcohol intake, smoking, and trauma such as hip fractures or dislocations, which can damage blood vessels and lead to the development of AVN [11], [12]. According to Mont et al., the total number of patients worldwide affected by AVN is projected to reach 20 million in the next decade [13]. Additionally, approximately 10,000 to 20,000 new patients are affected by AVN in the United States every year, while the annual prevalence in Japan and Korea exceeds 10,000 [14]–[16]. Based on an article published in a medical journal, this disease predominantly occurs in younger patients, with the average age at treatment ranging from 33 to 38 years, and a male-to-female ratio of 3:1 [17]. Figure 1.2 illustrates the stages of AVN of the femoral head, from I to IV.

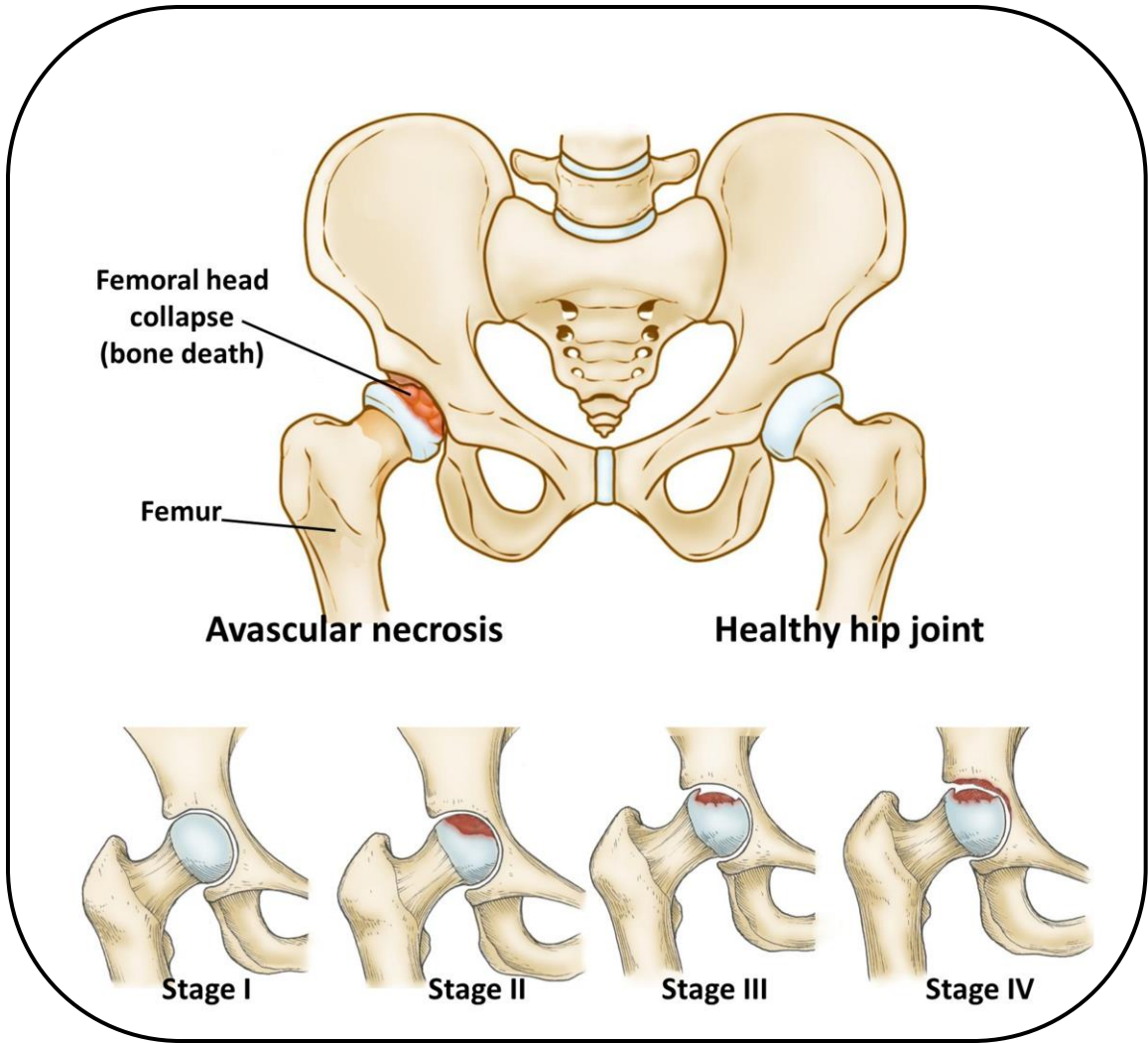


Figure 1. 2: Illustration of AVN of femoral head and the progressive stages of healthy hip joint (stage I) to the collapse of femoral head (stage II to IV) [18]

In general, there are several treatment options available to relieve joint pain caused by hip disease. These options consist of surgical and non-surgical treatments that depend on the severity of the pain. In the case of the early stage, where the pain does not significantly affect the patient's daily routine, non-surgical treatments such as lifestyle changes are often suggested by medical experts. Lifestyle changes may include weight loss, transitioning from high-impact to low-impact exercises, and engaging in physical therapy. These measures can help reduce stress on the hip joint, improve hip range of motion, and strengthen the muscles supporting the joint [19]–[21]. These methods may slow down the progression of the disease. However, if the pain has started to affect the patient's daily routine, non-surgical treatment with medication, such as anti-inflammatory drugs, may be recommended to relieve the pain [22]. In the later stages of hip disease, where the pain worsens and causes disability, surgical treatment options such as joint replacement surgery or total hip arthroplasty are considered to be suitable and successful in improving the patient's quality of life, where the diseased hip joint will be replaced with an artificial joint to restore the function of the hip.

1.2 Total Hip Arthroplasty

Over the years, total hip arthroplasty (THA) has become a common treatment for end-stage degenerative hip diseases, known to improve the patient's quality of life and provide long-term pain relief [23], [24]. It has been reported that over one million THA procedures are performed globally each year, and this number is projected to double within the next ten years [25], [26]. The process involves surgically removing the damaged femoral head and replacing the hip joint with prosthetic components. These components include the acetabular cup, artificial femoral head, and femoral stem, which transfer the load from body weight to the femur by inserting a metallic stem into the femoral canal.

Briefly, in the primary THA procedure, the orthopedic surgeon will remove the damaged femoral head and cartilage, preserving the remaining healthy bone. The femoral stem is then placed into the femoral canal using either a "press fit" fixation technique (cementless THA) or by pressing it into the femoral canal filled with cement (cemented THA). The artificial femoral head, or femoral ball, is attached to the upper end of the stem as a replacement for the damaged femoral bone head. In cases of severe arthritis, the damaged cartilage on the surface of the acetabulum is trimmed using a hemispheric reamer before placing the acetabular cup in the reshaped socket. Finally, a liner made of plastic or ceramic is attached to the acetabular cup to allow smooth and low-friction movement within the new artificial hip joint after the femoral ball is attached to the cup. Figure 1.3 illustrates the prosthetic components of THA.

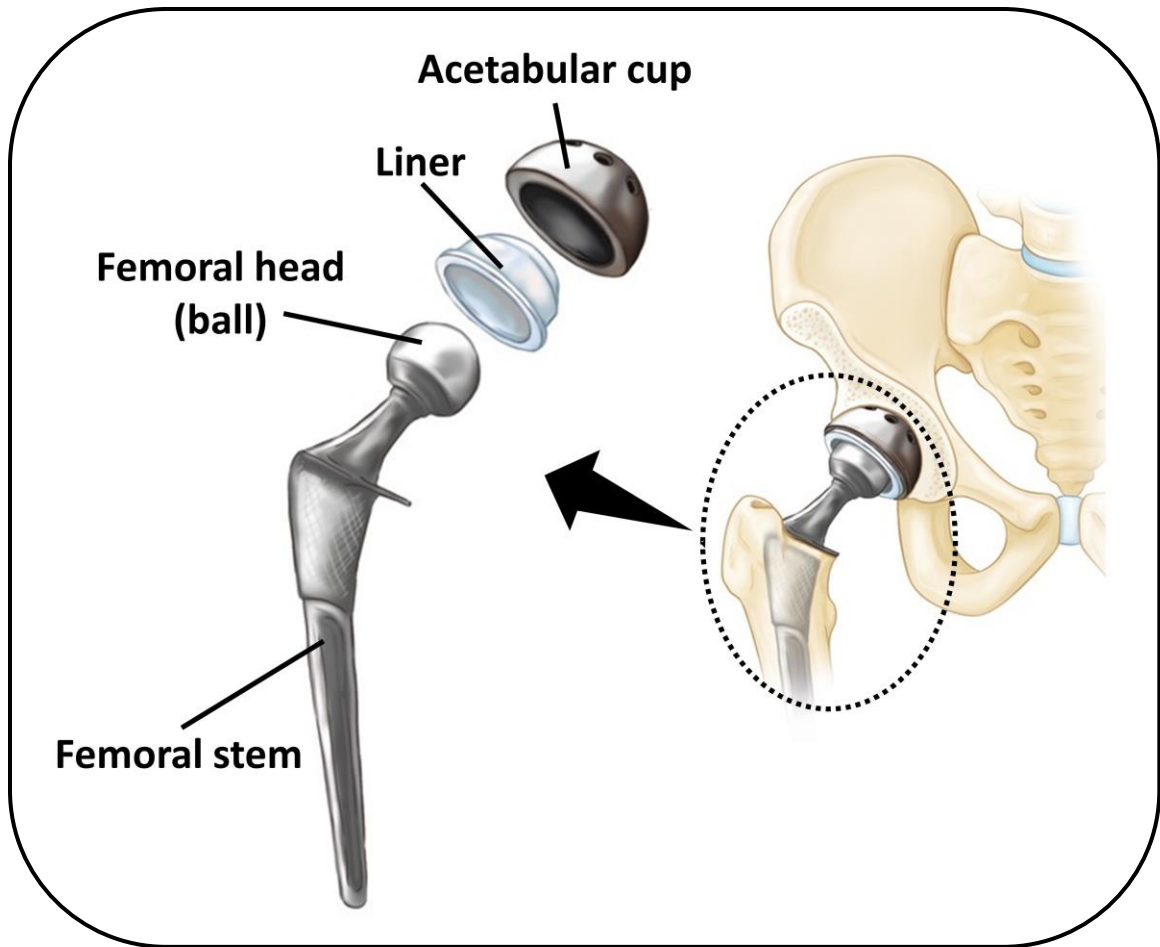


Figure 1. 3: Prosthetic components of total hip arthroplasty [27]

It is predicted that the total annual counts and utilization of THA will continue to grow globally in the following years, leading to a proportional increase in the number of complications associated with the procedure [28]–[30]. Despite the excellent clinical outcomes of THA in addressing hip-related problems, the burden of revision surgery has remained unchanged for many years. In the United States alone, the rate of revision surgery has increased to 60% since 2005, from 9.5 per 100,000 to 15.2 per 100,000. By 2030, the revision rate is projected to increase by up to 137% [31]. According to the Swedish Hip

Arthroplasty Register, the most common causes of revision surgery after THA are complications such as aseptic/mechanical loosening and osteolysis (75%), infections (8%), implant dislocations (6%), periprosthetic femoral fractures (5%), and implant fracture (1%) [30]. Similar findings were reported in another study conducted by Bozic et al., which mentioned that 22% of revision cases were due to instability, followed by aseptic/mechanical loosening (20%), infection (15%), implant failures (10%), osteolysis (7%), and periprosthetic femoral fractures (6%) [32].

Revision THA is a major surgery that carries greater risks and potential complications compared to the primary surgery [33], [34]. The surgical procedures are more challenging and require extensive surgical exposure and proper management of periprosthetic bone loss [35]. Risks and complications such as infections, dislocations, instability, loosening, blood clots in the veins, bone fracture and mortality are known to be associated with revision THA [34], [36]–[39]. Additionally, the patient's quality of life is reduced after revision THA compared to the primary surgery [40], [41]. Therefore, it is important to further understand the risk factors contributing to complications and failure following primary THA in order to minimize the rate of revision surgery.

1.3 Implant design in Total Hip Arthroplasty

In essence, there are two main types of fixations in the procedure of THA, namely cemented and cementless, and the designs of the THA implant have evolved according to these stem fixation methods. Briefly, cemented stem fixation is mainly used for patients who lack stability in their internal bone structure. Thus, bone cement is used to achieve a mechanical interlock between the surface of the bone and the stem. Meanwhile, cementless stem fixation is adopted for patients with good bone quality, characterized by high bone mineral content and density. In this case, the stem will be 'press-fitted' into the bone, relying on the biological fixation process known as osseointegration. Osseointegration refers to a direct connection between the bone-to-implant interface without any interposition of non-bone tissue. An implant is considered as osseointegrated upon the absence of ongoing relative motion between the implant and the bone it directly interfaces with [42].

1.3.1 Implant design in cemented total hip arthroplasty

In cemented THA, the ideal shape of a stem must be able to transmit axial and torsional loads to the cement and bone without generating damaging peak stresses and excessive micromovement. The stem should exhibit long-term mechanical stability, even when exposed to repetitive loading. To achieve these objectives, two principles of fixation have been adopted: "loaded-taper" cement fixation and "composite-beam" cement fixation.

Tapered femoral stems can be categorized based on their geometry, including single taper, double taper, and triple taper. A single-taper stem exhibits taper (reduction in dimension) in the frontal plane, while the dimension in the sagittal plane remains constant. A double-taper stem features taper in both the sagittal and frontal planes, while a triple-

taper stem exhibits taper in all three planes. The reduction in dimension occurs in the sagittal and frontal planes, similar to the double-taper stem, and the third taper reduces the anteroposterior dimension in the transverse plane. This reduction occurs through the cross-section of the stem from lateral to medial. Figure 1.4 illustrates the different types of tapered femoral stems.

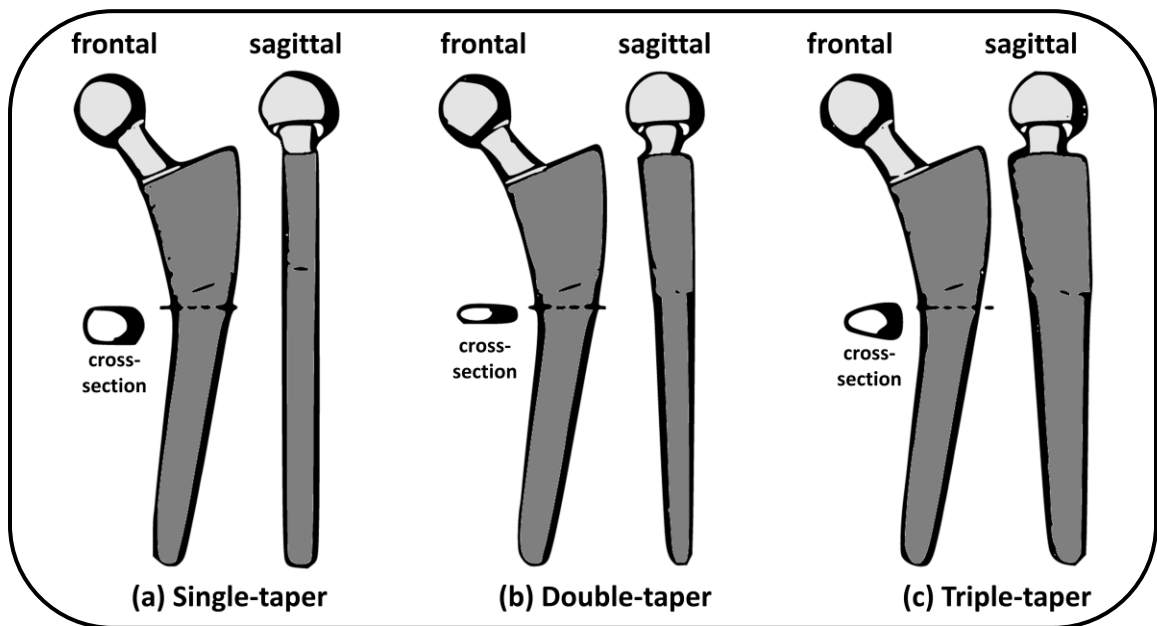


Figure 1. 4: Type of tapered femoral stems

In loaded-taper cement fixation, the Exeter hip stem serves as a prominent example. The Exeter hip stem was developed around 50 years ago, and its main design features are a double-taper and collarless stem. The purpose of these features is to allow the stem to slightly subside into the acrylic cement during axial loading, creating hoop stresses [43]–[45], thereby reducing the peak stresses in the proximal and distal cement mantle [46]. The tapered stem achieves self-locking with load and continues to self-tighten with the cement

over time. Since subsidence of the stem is required in this type of fixation method, a highly polished surface finish of the stem is preferred to minimize metal and cement abrasion resulting from natural micromotion [47]. Generally, the stem design used in loaded-taper cemented fixation is referred to as CPT stems, which stands for collarless, polished, and tapered stems [48].

Unlike the concept in loaded-taper fixation, the stem in composite-beam fixation must be rigidly bound to the cement. Any subsidence of the stem will damage the cement. When the stem subsides, the collision between the surfaces will generate debris from the polymethyl methacrylate (PMMA) cement and the metal. Toxic reactions from the debris can lead to the ultimate failure of the implant [49]. Therefore, most stems adhering to this principle are often designed with geometry and surface finishes that can prevent motion at the cement-bone interface, such as a collared stem and rough surface finish. These features can prevent subsidence due to the presence of the stem collar, and the rough surface will increase bonding between the cement and the stem. The illustration in Figure 1.5 shows the concept of the 'loaded-taper' and 'composite-beam' fixation methods.

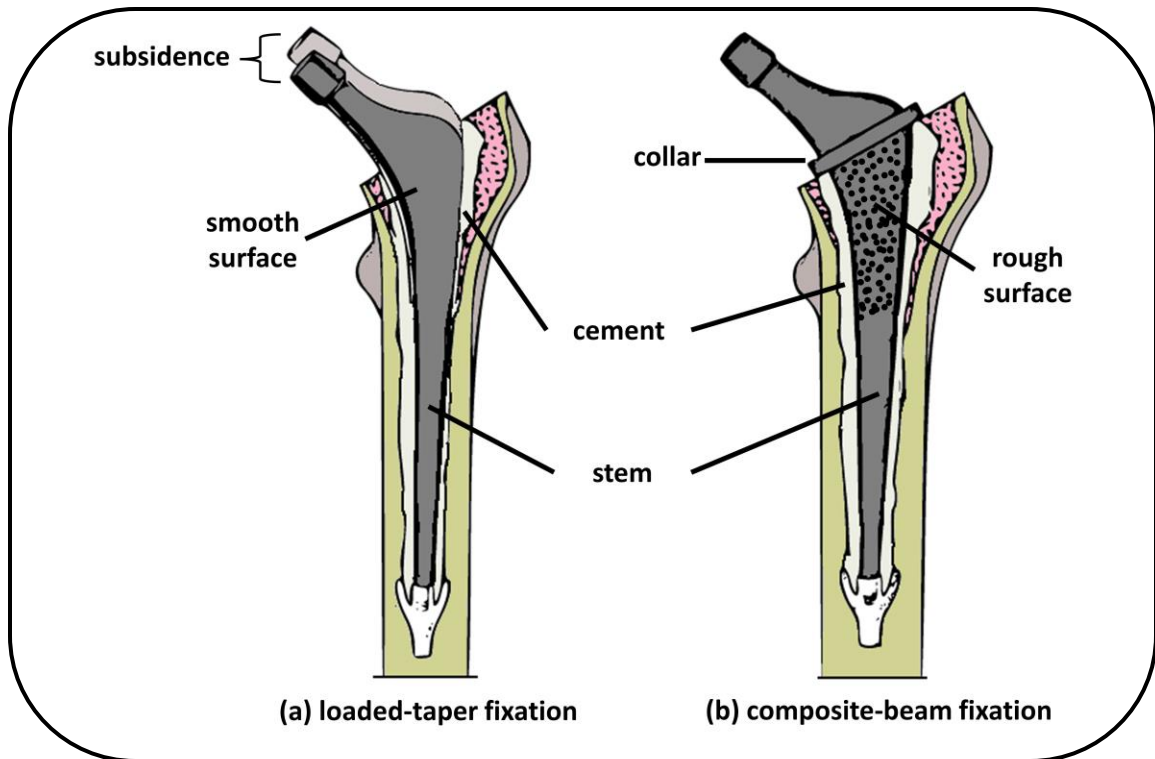


Figure 1. 5: Illustration of implant model in the concept of loaded-taper and composite-beam cement fixation

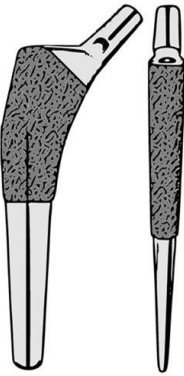
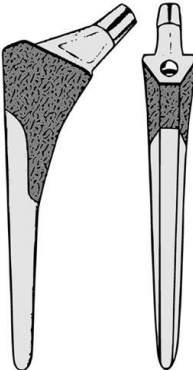
1.3.2 *Implant design in cementless total hip arthroplasty*

As mentioned earlier, the concept of stem fixation in cementless THA is mainly dependent on biological fixation known as osseointegration. Osseointegration can be achieved through bone ingrowth into the porous surface of the stem and bone ongrowth onto the roughened surface of the stem, resulting in a firm bone-stem fixation. Sufficient osseous contact and firm fixation will minimize the micromotion between the implant surface and the adjacent bone. On the other hand, micromotion of an implant that is less than 20 μm will result in predominantly bone formation after implantation, while

micromotion that is more than 150 μm will produce fibrous tissue formation [50]–[52]. In order for osseointegration to occur, a firm primary mechanical stability or primary fixation of the implant must be first achieved. Primary stability refers to the immediate stability of the implant after surgery, which is defined by the amount of movement between the implant and bone that occurs during loading. It can be influenced by several factors, including the design of the implant (geometry, roughness, and coating of the stem), preparation technique, and bone quality [53].

The shape of an implant is important in determining cortical contact and primary stability. Although there are a variety of cementless implant designs currently being manufactured, each design has a similar goal, which is to obtain primary stability and osseous contact. To achieve good primary stability, porous surfaces within a stem were designed and located in the desired area for fixation. Khanuja et al. introduced a classification system for cementless femoral stems, where the stems were classified into six different types [53]. These consist of type 1, type 2, type 3A, 3B and 3C, type 4, type 5 and type 6. Table 1.1 describes the information on each type of cementless stem.

Table 1. 1: Classification system of cementless implant design [53]

| Type 1 | | | |
|--|---|--|---|
|  | | | |
| Category | Geometry | Description | Location of fixation at bone |
| <ul style="list-style-type: none"> • Straight stem • Tapered proximal fixation | <ul style="list-style-type: none"> • Single wedge | <ul style="list-style-type: none"> • Narrows medially-laterally • Proximally coated • Flat stem • Thin in anterior-posterior plane | <ul style="list-style-type: none"> • Metaphyseal |
| Type 2 | | | |
|  | | | |
| Category | Geometry | Description | Location of fixation at bone |
| <ul style="list-style-type: none"> • Straight stem • Tapered proximal fixation | <ul style="list-style-type: none"> • Double wedge • Metaphyseal filling | <ul style="list-style-type: none"> • Narrows distally in both medial-lateral and anterior-posterior planes • Wider than Type 1 • Fills metaphyseal region | <ul style="list-style-type: none"> • Metaphyseal |

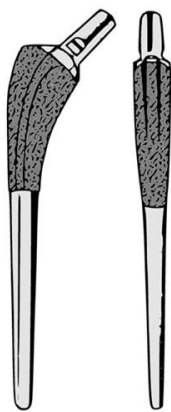
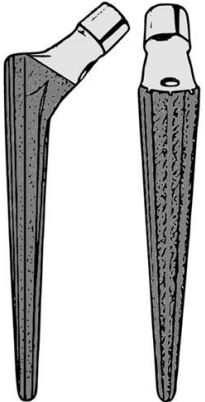
| Type 3A | | | |
|--|--|---|---|
|  | | | |
| Category | Geometry | Description | Location of fixation at bone |
| <ul style="list-style-type: none"> • Straight stem • Tapered proximal fixation | <ul style="list-style-type: none"> • Tapered • Round | <ul style="list-style-type: none"> • Rounded tapered conical stem • Porous coating at proximal two-thirds | <ul style="list-style-type: none"> • Metaphyseal-diaphyseal junction |
| Type 3B | | | |
|  | | | |
| Category | Geometry | Description | Location of fixation at bone |
| <ul style="list-style-type: none"> • Straight stem • Tapered distal fixation | <ul style="list-style-type: none"> • Tapered • Splined | <ul style="list-style-type: none"> • Conical taper • Longitudinal raised splines | <ul style="list-style-type: none"> • Metaphyseal-diaphyseal junction and proximal diaphyseal |

Table 1.1 (continued)

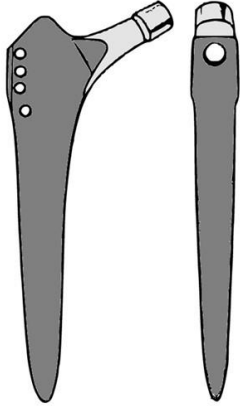
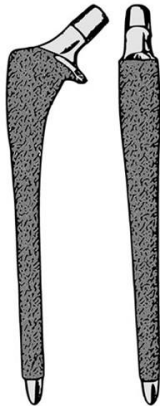
| Type 3C | | | |
|--|---|---|---|
|  | | | |
| Category | Geometry | Description | Location of fixation at bone |
| <ul style="list-style-type: none"> • Straight stem • Tapered distal fixation | <ul style="list-style-type: none"> • Tapered • Rectangular | <ul style="list-style-type: none"> • Rectangular cross section • Four-rotational support in metaphyseal-diaphyseal region | <ul style="list-style-type: none"> • Metaphyseal-diaphyseal junction and proximal diaphyseal |
| Type 4 | | | |
|  | | | |
| Category | Geometry | Description | Location of fixation at bone |
| <ul style="list-style-type: none"> • Straight stem • Distally fixed | <ul style="list-style-type: none"> • Cylindrical • Fully coated | <ul style="list-style-type: none"> • Extensive porous coating • Collar at proximal to enhance proximal bone loading and axial stability | <ul style="list-style-type: none"> • Primarily diaphyseal |

Table 1.1 (continued)

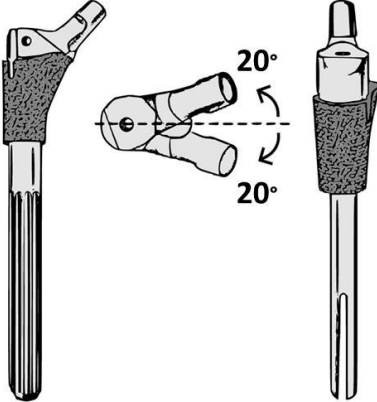
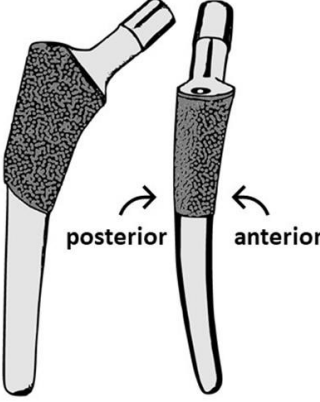
| Type 5 | | | |
|--|----------|--|--|
|  | | | |
| Category | Geometry | Description | Location of fixation at bone |
| <ul style="list-style-type: none"> • Modular | - | <ul style="list-style-type: none"> • Metaphyseal and diaphyseal components prepared independently | <ul style="list-style-type: none"> • Metaphyseal and diaphyseal |
| Type 6 | | | |
|  | | | |
| Category | Geometry | Description | Location of fixation at bone |
| <ul style="list-style-type: none"> • Curved stem • Anatomic stem | - | <ul style="list-style-type: none"> • Wide proximal portion in both lateral and posterior planes • Posterior bow in metaphysis • Anterior bow in diaphysis | <ul style="list-style-type: none"> • Metaphyseal |

Table 1.1 (continued)

In brief, the primary stability in Type 1 stem is obtained by three-point fixation along the stem length [54], which contacts the posterior, proximal, and distal areas inside the femoral canal, while the broad, flat shape of the implant ensures rotational stability. For Type 2, fixation is acquired through proximal contact in the anterior-posterior and medial-lateral planes, and some Type 2 designs require diaphyseal engagement for better rotational stability [55], [56].

In the case of Type 3, the fixation generally focuses more on the metaphyseal-diaphyseal junction rather than the metaphysis. For Type 3A, three-point fixation is obtained through porous coating located at the proximal two-thirds of the stem [57], [58], and the rotational stability is achieved by the existence of fins at the proximal region of the stem [59]. For Type 3B, fixation is gained from the longitudinally raised splines along the conical taper shape, and rotational stability is obtained through the sharp edges that cut into the bone [59]. For Type 3C, the rectangular cross-section of the stem provides three-point fixation in the proximal part of the diaphysis and in the metaphyseal-diaphyseal junction. Additionally, four-point rotational support is obtained through its rectangular cross-section [60].

For Type 4, fixation is obtained by creating ingrowth surface coatings throughout the entire prosthesis, engaging the cortical bone in the diaphysis. The existence of a collar in the proximal region improves axial stability. In Type 5, fixation is gained from the proximal and distal areas of the stem, and this stem is usually applied in complex operations due to patient abnormalities, such as hip dysplasia. Type 6 achieves stability through the distal curve and metaphyseal fill [61], [62], however, this type of stem is not commonly used.

Aside from geometry, surface and coating of the stem also play important roles in the design of cementless implants to ensure the process of bone ingrowth and ongrowth (osseointegration). For bone to grow inside the porous surface of a stem (bone ingrowth), the required pore size must be between 50 μm and 400 μm , and the absence of voids within the coating must be between 30% and 40% to preserve mechanical strength.

Ingrowth surfaces are created using sintered beads, fiber mesh, and porous metals, which create microscopic pores that allow bone to grow. Sintered beads consist of microspheres or powder of either titanium alloy or cobalt chromium that are attached to the surfaces of the stem through a heating process [63], [64]. Fiber mesh coatings, on the other hand, are metal pads that are attached to the stem by diffusion bonding [63], while porous metals provide a uniform three-dimensional network [65], which have higher porosity and void interconnectivity than both sintered beads and fiber metal coatings.

Meanwhile, the ongrowth surfaces are created through grit blasting or plasma spraying onto the implant to create a textured surface where bone can grow. In grit blasting, the textured surface is created by blasting the implant with small abrasive particles such as aluminum oxide, resulting in a surface roughness ranging from 3 μm to 5 μm [66], [67]. On the other hand, plasma spraying creates the textured surface by spraying a molten material onto the implant through a high-energy flame, using a mixture of metal powder and inert gas that is pressurized and ionized.

1.4 Complications after Total Hip Arthroplasty

1.4.1 *Aseptic/mechanical loosening*

Aseptic/mechanical loosening is known to be one of the major post-surgery complications and common reasons for revision surgery after THA. The mechanisms that induce this complication include the mechanical failure of the implant or cement, osteolysis caused by the introduction of wear debris into the bone and implant interface region, relative motion throughout the interface, and stress shielding in the bone [68], [69]. These mechanisms can lead to bone resorption and result in implant loosening, implant migration, implant failure, or periprosthetic fracture [70].

From a biomechanical perspective, stress shielding is an important factor that contributes to aseptic loosening. Stress shielding is a biomechanical phenomenon that causes adaptive changes in bone strength and stiffness, particularly in the bone region surrounding metallic implants or the bone-implant interface. This phenomenon occurs due to the different mechanical properties between the bone and the implant. The mismatch in elastic modulus between the bone and the implant alters the stress distribution in the bone. In post-operative conditions, the stiffer component, such as the implant, sustains most of the loads from the body weight, leaving fewer parts of the load to be carried by the bone [71]. This altered stress distribution leads to bone mineral loss at the bone-implant interface, resulting in reduced contact in that region and ultimately leading to implant loosening.

The stress distribution in the femur is largely affected by the mechanical properties of the prosthetic components. Therefore, the severity of the stress shielding effect depends

on the degree of stiffness mismatch between the implant and the natural bone. A stiffer prosthetic component will lead to a more pronounced stress shielding effect. Harrie et al. found that stem design variables such as elastic modulus, size, geometry, coating, and ingrowth conditions can influence the amount of stress shielding. Additionally, bone variables such as geometry, bone density distribution, and stem placement within the femur may also affect the severity of the phenomenon [72].

Currently, most THA implants are designed using metallic materials such as titanium alloys (Ti6Al4V, Ti-Mg), cobalt-chromium alloys, and 316L stainless steel. Among these metallic materials, titanium alloys are predominantly used due to their high mechanical strength and biocompatibility with bone [73]–[75]. However, these metallic materials still have much higher stiffness compared to femoral bone. For instance, the Young's modulus of cortical bone ranges between 10 to 30 GPa, while titanium alloy has a modulus of 110 GPa, which poses a high risk of stress shielding [76]. In the field of biomaterials, reducing the Young's modulus of the stem material, such as titanium alloy, is considered one of the most effective ways to prevent stress shielding. Several studies conducted by Niinomi et al. have aimed to improve the mechanical biocompatibility of titanium alloy, focusing on properties such as Young's modulus, fatigue strength, wear resistance, fracture toughness, and strength/ductility balance [77]–[79].

Currently, the modulus of titanium alloy has been successfully reduced to 50 GPa without significant changes in other mechanical properties. Computational analysis conducted by Todo simulated the effect of reduced Young's modulus titanium alloy in a hip joint with a THA stem. The study found that the strain energy density profiles within

the femur with a modulus of 50 GPa for titanium alloy were effectively increased compared to a modulus of 110 GPa, suggesting an improvement in mechanical stimulus [80].

Another factor that can affect the severity of stress shielding in the femur following arthroplasty is bone density distribution. Low bone density in the underlying trabecular bone is often associated with clinical failure of the femoral component and has been attributed to stress shielding [81]. Bone density is an important parameter for ensuring bone strength. When a stiffer material is inserted into a bone with low density, the effect of stress shielding may contribute to progressive loosening of the implant. Figure 1.6 illustrates an example of post-operative radiographs showing the effect of stress shielding from 0 to 6 years after surgery. It can be observed that the width of the cortical bone around the stem becomes thinner at year 6 after surgery, resulting in bone resorption and loss of bone mass.

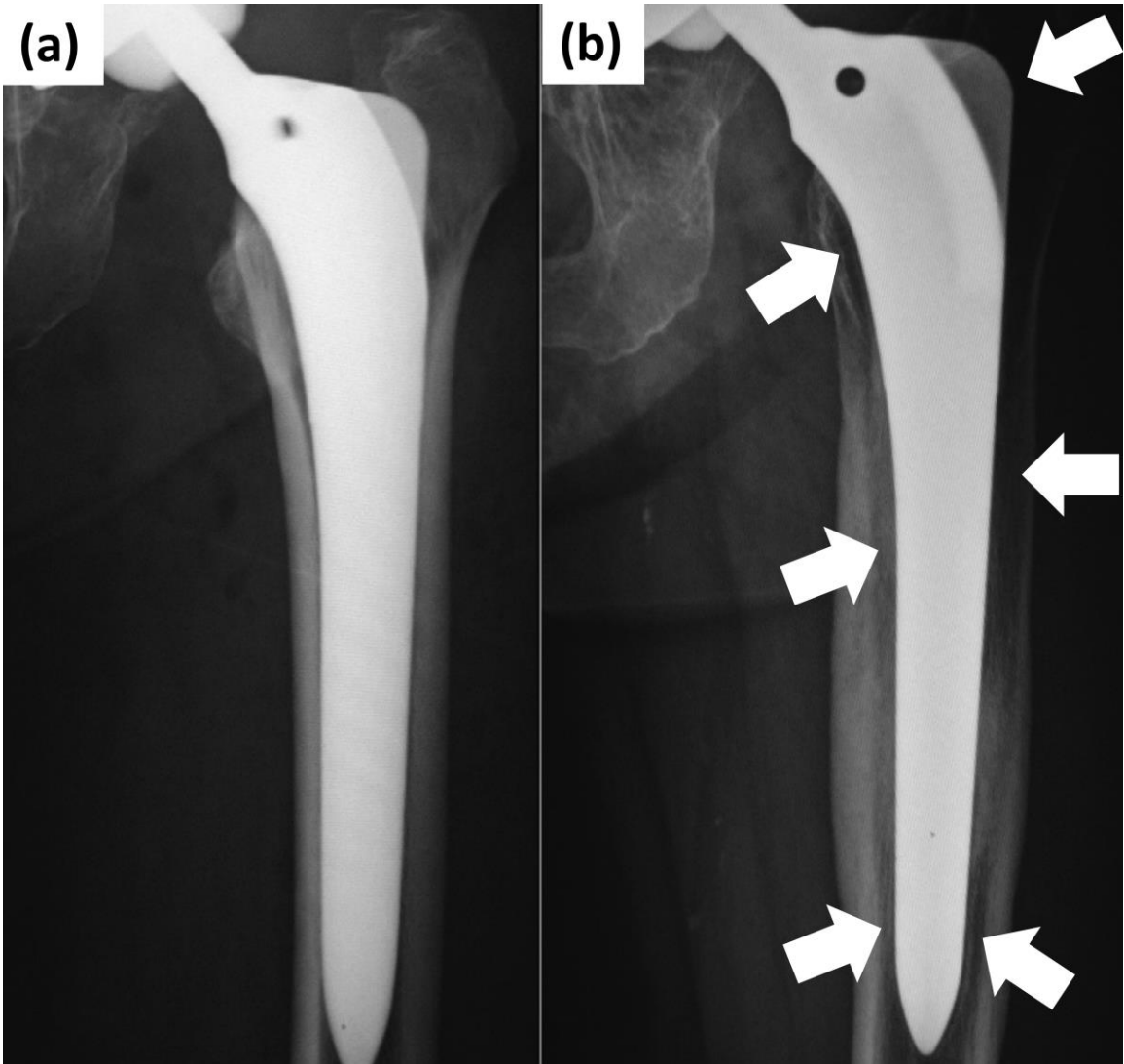


Figure 1. 6: Progressed stress shielding from (a) 0 year after surgery to (b) 6 years after surgery [82]

1.4.2 *Periprosthetic femoral fractures*

Periprosthetic femoral fracture (PFF) is another major complication that associated with THA. PFF can occur intraoperatively or postoperatively, and the frequency varies depending on the fixation method, whether cementless or cemented THA. Intraoperative PFF has a higher reported rate (0.1-27.8%) compared to postoperative PFF (0.07%-18%), and the incidence is more frequent in cementless THA than cemented THA, in both primary and revision surgery [83]–[85]. It is the third most common reason for revision surgery following THA, after aseptic loosening and infection [86], [87], and the mortality rate associated with this complication is alarmingly high [88].

Several risk factors contribute to intraoperative PFF, including female gender, age (higher risk in patients younger than 50 and older than 80 years), previous surgery on the same hip, bone disease, surgical technique, and technical errors during the operation [89]–[91]. On the other hand, post-operative PFF is related to the biomechanical issue. Risk factors for postoperative PFF include bone quality [92], [93], implant design [94], implant position [95], and minor trauma such as falls. According to the Swedish registry database, 75% of PFF cases occurred due to falls at the same level at which the patient had been standing or sitting [96].

Bone quality is a recognized risk factor for postoperative PFF. Poor-quality bone, such as osteoporotic bone, is associated with reduced bone strength and a higher risk of fracture. Osteoporosis is characterized by a gradual decrease in bone mass, resulting in the deterioration of bone structure and increased bone fragility. It is generally accepted as a risk factor for late PFF [83], [97], [98], although only a few studies have systematically

investigated the relationship between a patient's bone quality and fracture risk. For example, Wu et al. conducted a study to identify predictive indicators that could preoperatively recognize the risk of femoral fracture [99]. Using Singh's index of osteoporosis, they found that patients in the fracture group following cementless THA had poorer preoperative bone quality compared to the non-fracture group, suggesting that preoperative osteoporosis can be an important predictor of fracture risk. Additionally, bone variables such as cortical thickness of the femur, proximal femoral geometry, and bone diseases such as avascular necrosis and rheumatoid arthritis also contribute to the risk of PFF after THA [94], [100].

Implant design is another known risk factor for PFF. A systematic review conducted by Carli et al. observed a significantly increased risk of PFF with the use of cementless implants [94]. However, the rates of PFF varied between different types of implants, with type 1 and type 2 stems associated with increased rates of PFF, while lower rates were observed in the group consisting of type 3 and type 4 stems. Nevertheless, limitations in confounding factors may have affected the results, including age, gender, body mass index (BMI), bone quality (including metabolic bone disease or osteoporosis), surgical approach, and surgeon experience. Furthermore, the study highlights the need for more biomechanical investigations to compare modern implants and precisely clarify the contribution of implant design to the risk of PFF, as the study was limited to reports on PFF cases in different types of implants following THA.

The variety of different fracture configurations and patterns of periprosthetic femoral fractures (PFF) can present significant challenges in their treatment. Currently, the Vancouver classification system is widely used in clinical practice to classify and guide the

management of postoperative PFF following hip arthroplasty. This classification system, introduced by Duncan and Masri [101], categorizes fractures into three types: Type A, Type B, and Type C. Vancouver Type A fractures involve the trochanter area of the femur and are further divided into A_G for fractures occurring in the greater trochanter and A_L for fractures in the lesser trochanter. Type B fractures are located around the diaphysis of the femur, including those just distal to the tip of the stem. Type B fractures are subdivided into B₁, B₂, and B₃. Type B₁ fractures occur in a region with good bone stock and a well-fixed stem. Type B₂ fractures occur in a region with good bone stock but an unstable stem, while Type B₃ fractures occur in a region with poor bone stock and an unstable stem. Vancouver Type C fractures are located well below the stem. The Vancouver classification system provides a standardized framework for assessing and communicating PFF patterns, assisting orthopaedic surgeons in determining the appropriate treatment plan and management. Figure 1.7 illustrates the Vancouver classification for periprosthetic femoral fractures.

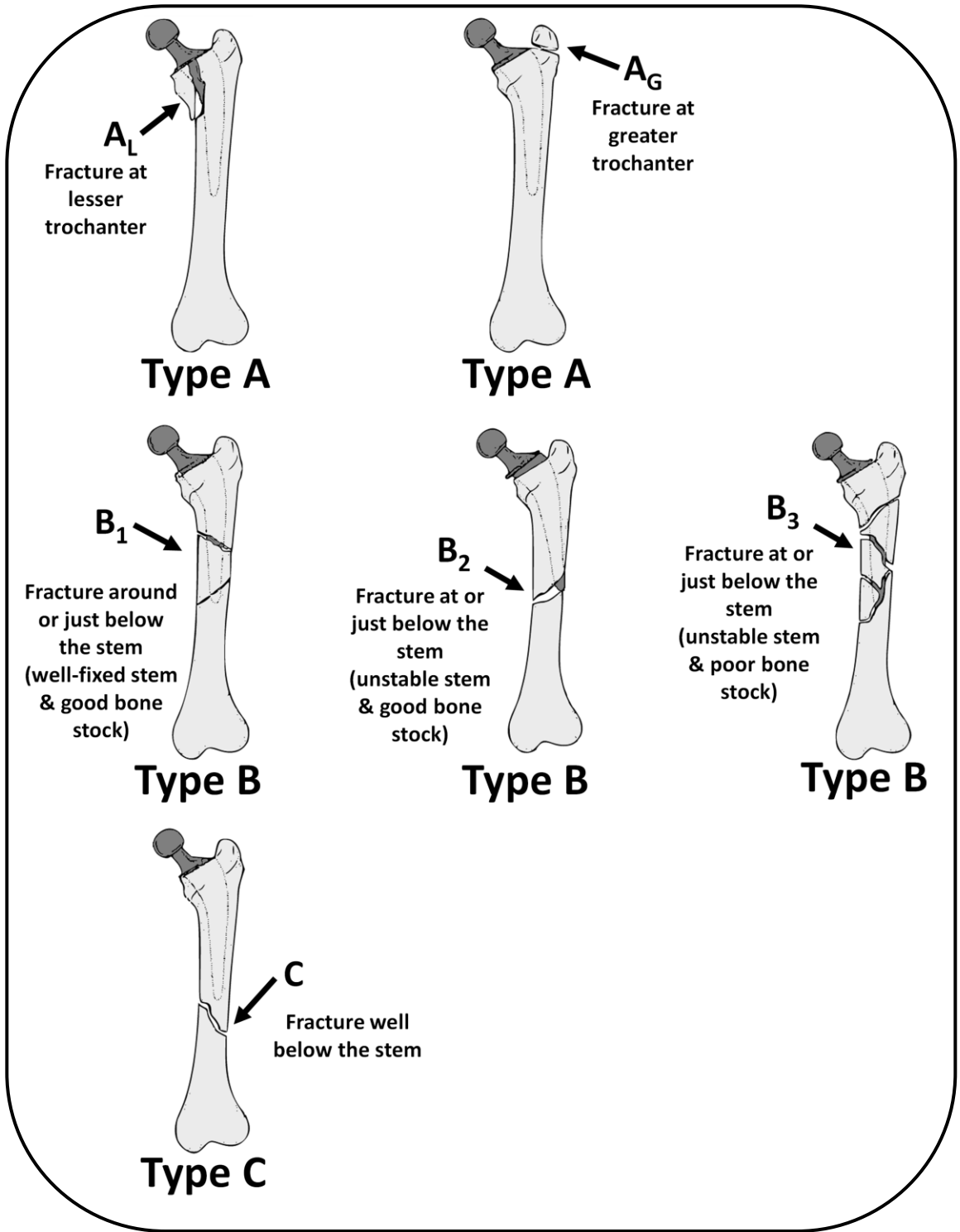


Figure 1. 7: Vancouver classification of periprosthetic femoral fractures [102]

1.5 Biomechanical study of Total Hip Arthroplasty

Over the years, biomechanical studies of THA have been widely performed to continuously improve the outcomes following THA. Biomechanical analyses are usually conducted using experimental or computational techniques, or a combination of both. Known risk factors for complications following THA, such as implant loosening (stress shielding) and periprosthetic fractures, are associated with implant design and bone variables including bone quality, strength, and geometry. Several biomechanical studies have been conducted in recent years, particularly using computational techniques such as finite element analysis (FEA), to investigate the relationship between these risk factors and complications, specifically in implant design. The common objectives of these studies include evaluating implant stability, strength, and wear resistance of different implant types and materials. These studies have provided valuable information to orthopaedic surgeons and researchers in their efforts to optimize the outcomes of THA, addressing the challenge of adapting to various bone quality characteristics.

The design features of THA implants, including geometry, size, dimensions, and materials, may influence the outcomes following THA. For instance, Sabatini et al. conducted a study using FEA to optimize THA stems with various cross-sections, namely circular, elliptical, trapezoid, and oval [103]. The study reported that the stem made of titanium alloy exhibited lower stress levels compared to cobalt-chromium and stainless steel. Furthermore, different stem cross-sections exhibited varying stress distributions along the length of the stem, with circular and elliptical cross-sections showing more even distribution of von Mises stress compared to oval and trapezoid cross-sections.

Another computational study investigating the influence of stem geometry on the performance of THA was conducted by Senalp et al. [104]. The study analysed stems with straight geometry, notched geometry, and curved geometry to assess their fatigue behaviour under static and dynamic loading conditions. The results revealed that different stem designs exhibited varying safety factors for fatigue life. Specifically, stem-3, constructed with titanium alloy (Ti-6Al-4V), demonstrated the most favourable shape for fatigue resistance under both static and dynamic loading, as determined by Soderberg, Gerber, and Goodman fatigue theories.

On another note, Reimeringer et al. conducted a study investigating the influence of different stem designs and lengths in cementless femoral stems on their primary stability after THA [105]. Two distinct implant designs, consisting of a straight stem and a curved stem, were implanted into a finite element model of a composite sawbones. Both the straight and curved implant designs were developed in five and four different lengths, respectively. The study found that the average micromotion increased from 17 μm to 52 μm as the length of the straight stem decreased from 146 mm to 54 mm during fast-walking conditions. Similarly, in the curved stem, comparable findings were observed, with the average micromotion increasing from 10 μm to 29 μm as the length of the stem decreased from 105 mm to 54 mm. The study concludes that different stem designs and lengths directly influence the primary stability in the THA procedure and can potentially impact the process of osseointegration.

Although several biomechanical studies have been conducted successfully, highlighting the influence of implant design on the outcomes following THA, these studies have been limited to homogeneous bone models. In other words, constant material

properties such as elastic modulus and Poisson's ratio were assigned to every element forming the geometry of the cortical and cancellous bone. However, in reality, the material properties of bone are not homogeneous due to the anisotropic nature of bone tissue, which means its behaviour changes depending on the load direction. As a result, biomechanical analyses focusing on the outcomes after THA, specifically related to bone variables such as bone quality, bone strength, and bone geometry, have rarely been investigated.

In a computational study conducted by Kwak et al., the possibility of periprosthetic femoral fracture was predicted using a finite element (FE) bone model, assuming a homogeneous and isotropic linear structure [106]. The elastic modulus for the cortical and cancellous bone was set to 17,000 MPa and 920 MPa, respectively, while the Poisson's ratio was set to 0.3 and 0.2 for the cortical and cancellous bone, respectively. The prediction of bone fracture was based on the peak von Mises stress and mean stress measured at the cortical bone, with the yield strength of the cortical bone set at 107.9 MPa. It is worth noting that although the von Mises equivalent stress has been adopted as the criterion for the bone's yield strength, such a criterion may be more appropriate for ductile materials. Bone, being a brittle material, has a smaller tensile strength compared to its compressive strength [107]. Therefore, the influence of hydrostatic stress should be taken into consideration as a yield criterion. The von Mises yield criterion does not account for the effect of hydrostatic stresses since the yielding of ductile materials, such as metals, is primarily affected by shear deformation. Hence, a more suitable failure theory should be employed to predict the failure of brittle materials like bone.

Due to the heterogeneous nature of bone, biomechanical studies, even with the use of computational methods, have been limited. However, Bessho et al. conducted a study to

address this limitation by creating a simulation model capable of accurately predicting important variables in proximal femoral bone, such as strength and surface strains, using a computed tomography-based finite element method (CT-based FEM) [108]. The accuracy of the FE model was verified by load testing fresh frozen cadaver specimens through quasi-static compression tests. The study found a significant correlation between the predictions of principal strains, yield loads, and fracture loads from the FE model and the corresponding experimental measurements ($r = 0.963, 0.941, 0.979$). Additionally, the study introduced the Drucker-Prager equivalent stress as the yield criterion, which is more suitable for brittle materials. This yield criterion requires a larger external load to cause compressive yielding of the bone element. Moreover, each element forming the bone's geometry in the FE model had different material properties, computed from the Hounsfield unit values derived from the CT images, thus accounting for the heterogeneity of the bone structure. The aggregation of compressive failure elements in the CT-based finite element model was found to be located in the subcapital region of the femur, similar to the experimental fracture site.

1.6 Problem statement

Recent years, CT-image based finite element method (CT-FEM) has been utilized to understand the biomechanical problems in the orthopaedical field [80], [109]–[114]. Although the bone mineral density (BMD) has become the primary clinical parameter to assess the fracture risk of bones, recently it was found that an average value of BMD cannot be the single parameter which mainly controls the fracture risk in the case of vertebral compression fracture [113]. CT-FEM can convert the inhomogeneous distribution of BMD into the distribution of Young's modulus, hence able to predict the risk of bone fracture with high accuracy introducing the damage mechanics into the non-linear finite element analysis. This unique and effective computational method has been implemented in a field of bone biomechanics where the bone strength and fracture sites were successfully predicted [80], [108]–[112], [114], [115], while in several classical computational biomechanical studies, the risk of bone fracture associated with THA was predicted through the evaluation of the stress and strain fields with the assumption of unrealistic homogeneous bone structures [106], [116], [117]. Meanwhile, the experimental studies with the use of cadavers could give us some realistic information of external fracture modes [118]–[120]; however, it was impossible to perform the internal analysis and visualization. Information on the internal bone region such as bone micro-damage is crucial in the effort to minimize the risk of complications such as stem loosening and bone fracture through the development of advanced THA implants. To the best of our knowledge, the study on the internal bone damage related to bone variables and different implant design has not yet been done previously and may contribute to the improvement of THA procedure.

1.7 Research objectives

The aim of this study is to investigate the effect of parameters related to total hip arthroplasty, such as bone variables and implant designs, on the risk of complications following THA by studying the mechanism of bone damage formation using CT-FEM. This aim leads to the following objectives:

- (1) To assess the influence of bone variables, including bone quality, strength and geometry, on the formation and progression of bone damage in THA femurs.
- (2) To investigate the impact of different implant designs, such as stem size, type, and geometry, on the development of femoral bone damage from the internal and external bone region.

1.8 Scope and limitations

- (1) The three-dimensional (3D) inhomogeneous FE femoral bone models were developed only from CT images of avascular necrosis patients.
- (2) The developed THA femoral bone models in this study only adheres to the cementless fixation method.
- (3) The loading and boundary conditions in predicting the formation of bone damage were presented only to investigate the effect of bone variables and implant design related to THA that deviate from typical daily physiological activities.

CHAPTER 2: DAMAGE MECHANISMS UNDER LATERAL BENDING AND TORSIONAL CONDITIONS

2.1 Overview

In order to understand the biomechanical effects of bone quality and THA stem designs to the outcomes following THA, the development of a realistic finite element bone model is crucial. Therefore, two inhomogeneous femoral bone models were developed from the CT images of 61 and 87-year-old patients, and three types of stems were introduced to represent the corresponding cementless THA models. Cementless THA model was adopted in this study since it has higher reported cases on implant loosening and periprosthetic femoral fractures based on the literatures. Finite element analyses with a nonlinear damage analysis were then performed under two boundary conditions, i.e., lateral bending and torsional conditions. The mechanism of bone micro-damage formation from the internal region of the bone and fracture formation from the external region of the bone in both models were then compared.

2.2 Construction of intact femoral models

Quantitative CT images of two female patients of 61 and 87-year-old, obtained from the Fukuoka University Hospital, Japan were used to develop computational models. Both patients were diagnosed with stage three of avascular necrosis at the head of the right femur. Both CT images had a slice thickness of 0.5 mm. CT-FEM software, Mechanical Finder version 11.0 (Research Centre for Computational Mechanics Inc., Tokyo, Japan), was used to develop the three-dimensional FE models of the right femurs. Two-dimensional femoral bone region of interest (ROI) was selected from each slice of the CT images, where the bone region had higher CT values than that of the soft tissues such as muscle, ligament and adipose tissues. The selected ROI at each CT image was vertically stacked to finally form the 3D geometry of the femur. Next, the FE model of the intact femur was meshed with 2-mm tetrahedral elements for the cancellous bone and inner cortical bone, whereas 2-mm triangular shell elements with a thickness of 0.3 mm were assigned to the outer surface of the cortical bone. The surface shell elements were assigned to express the stiffest layer of the cortical bone that cannot be expressed from the CT images [108]. The FE models of the 61 and 87-year-old patient were thereafter denoted with bone X and Y, respectively. The numbers of solid and shell elements of the intact model of bone X and Y were 156509, 191478, and 73698, 84954, respectively. The inhomogeneous BMD values were introduced into every element by converting the Hounsfield unit (HU) into BMD using a linear formula as follows [108]:

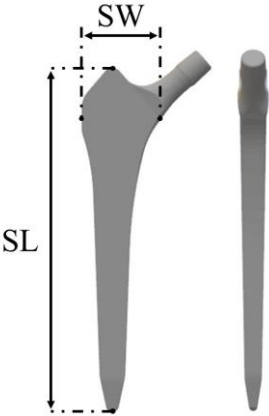
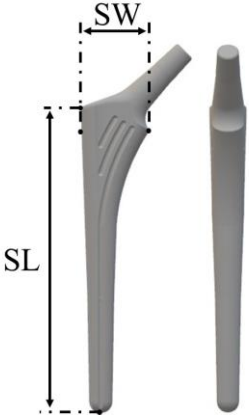
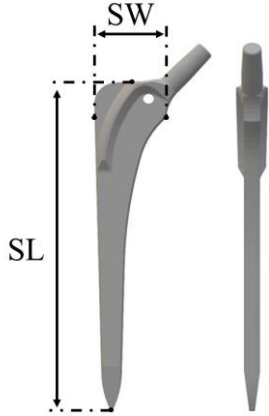
$$\rho \text{ (g/cm}^3\text{)} = [\text{HU} \pm 1.4246] \times 0.001 / 1.058 \text{ [HU value} > - 1]$$

$$\rho \text{ (g/cm}^3\text{)} = 0 \text{ [HU value} \leq - 1]$$

2.3 Construction of THA models

Three different types of femoral stem were introduced in this study and denoted by stem I, stem II, and stem III. Each stem came with a different design and geometry. The illustration and description of the stems were shown in Table 2.1. In reconstructing the virtual hip arthroplasty, the femoral bone head was osteotomized based on the intertrochanteric line to approximately 1 cm above the lesser trochanter. The osteotomy of the femoral head was performed by considering the stem geometry, i.e., the medial offset, vertical height, and neck length. The stem was then properly aligned into the femoral canal by referring to the mapping view from the CT images to replicate the original position of the femoral head. The THA models of bone X and Y implanted with stem I, II, and III are shown in Figure 2.1. The FE models of bone X implanted with stem I, II and III were constructed with 162,710, 155,220, 139,579 of tetrahedron solid elements and 62,628, 61,533, 62,547 of triangular shell elements, respectively. For bone Y, 189,777, 185,391, 175,221 of solid elements and 74,766, 74,190, 75,165 of shell elements were used with stem I, II, and III. The materials of the stem and femoral ball were assumed to be Titanium alloy and Alumina ceramic, respectively. Table 2.2 summarized the mechanical properties of the assigned materials [121]. The interface between the bone and stem was assumed to be perfectly bonded to mimic the complete process of osseointegration [42].

Table 2. 1: Illustration of stem I, stem II, and stem III

| (a) Stem I | Description |
|---|---|
|  | <ul style="list-style-type: none"> • Zweymuller (Teijin Nakashima Medical Co., LTD) • Shoulder width (SW) = 35 mm • Stem length (SL) = 120 mm • Rectangular cross-sectional shape |
| (b) Stem II | Description |
|  | <ul style="list-style-type: none"> • Perfix (Kyocera Medical Tech.) • Shoulder width (SW) = 25 mm • Stem length (SL) = 115 mm • Round cross-sectional shape |
| (c) Stem III | Description |
|  | <ul style="list-style-type: none"> • Aesculap (B. Braun Healthcare) • Shoulder width (SW) = 30 mm • Stem length (SL) = 140 mm • Rectangular cross-sectional shape |

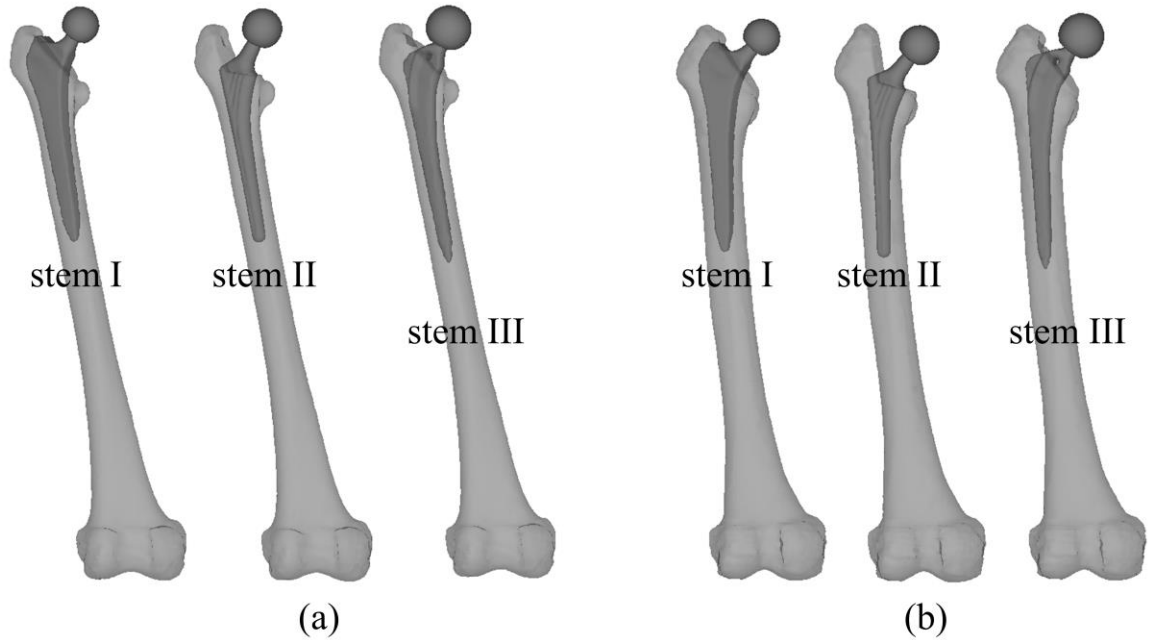


Figure 2. 1: THA model of (a) bone X and (b) bone Y implanted with stem I, stem II and stem III

Table 2. 2: Mechanical properties of THA implant [121]

| Properties | Titanium alloy | Alumina ceramic |
|------------------------------|-----------------------|------------------------|
| Elastic modulus (GPa) | 114 | 370 |
| Poisson ratio | 0.34 | 0.22 |
| Critical stress (GPa) | 0.88 | 0.40 |
| Yield stress (GPa) | 0.97 | 3.00 |
| Density (g/cm ³) | 4.43 | 3.96 |

2.4 Loading and boundary conditions

Two different loading and boundary conditions were introduced into the nonlinear FE analysis in order to predict the damage formations of the two types of femoral bone. These conditions were implemented on the basis of the validated and well-established testing protocol for periprosthetic femoral shaft fixation [122]–[126]. In the loading and boundary conditions, two different types of configurations were introduced, and they were thereafter denoted as lateral bending condition (LBC) and torsional condition (TC). The loading direction was set based on the angle of α and β , which represent the long axis of the femur in the frontal and sagittal plane, respectively. The orientation of loading direction for LBC was $\alpha = 90^\circ$, $\beta = 0^\circ$, and for TC, $\alpha = 90^\circ$, $\beta = 90^\circ$. The boundary conditions, LBC and TC, are shown in Figure 2.2. For both LBC and TC, the magnitude of applied load was set to be increased stepwise in 20 steps, ranging from 0 N to 1500 N with 75 N increment per step, until the failure of 1000 shell elements as the critical condition for analysis termination. The selected range of loading magnitude was found to be sufficient to demonstrate the damage mechanisms in femoral fracture under the same conditions in the previous study [114].

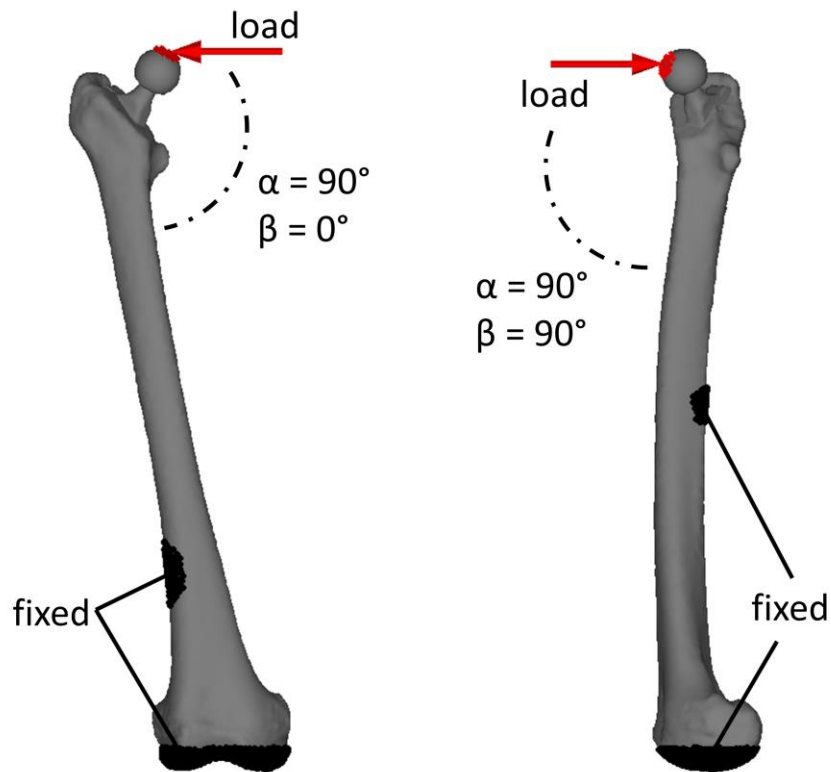


Figure 2. 2: Loading and boundary conditions: (a) lateral bending (LBC) and (b) torsional (TC)

2.5 Mechanical theories and material properties

The tensile deformation of all the elements constructing the femoral models was assumed to be expressed by the linear elastic response, in which the stress-strain relation was characterized by two material constants such as Young's modulus and Poisson's ratio. On the contrary, the compressive deformation of the elements was assumed to be expressed by the bi-linear elastic-plastic response, in which the stress-strain relation was

characterized by Young's modulus and Poisson's ratio under the linear-elastic behavior and the yield stress and the work hardening coefficient under the plastic behavior. The Drucker-Prager yield condition was used to assess the onset of yielding [108]. Yielding was assumed to take place when the Drucker-Prager equivalent stress reached the compressive yield stress. Young's modulus and the compressive yield stress of a solid element were calculated from the corresponding BMD value of the element using the empirical formulae proposed by Keyak et al. [127] and Keller [128] as shown in Table 2.3. Poisson's ratio and the work hardening coefficient of all the solid elements were set to 0.4 and 0.05, respectively. Those properties of each of the shell elements were chosen so that they were equivalent to those of the adjacent solid element located under its position.

Table 2. 3: Relationship between BMD and the material properties [127], [128]

| Bone mineral density (g/cm³) | Young's modulus (E) |
|--|----------------------------|
| $\rho = 0$ | 0.001 |
| $0 < \rho \leq 0.27$ | $33,900\rho^{2.20}$ |
| $0.27 < \rho \leq 0.6$ | $5307\rho + 469$ |
| $0.6 < \rho$ | $10,200\rho^{2.01}$ |
| Bone mineral density (g/cm³) | Yield stress (MPa) |
| $\rho < 0.317$ | $137\rho^{1.88}$ |
| $0.317 \leq \rho$ | $114\rho^{1.72}$ |

The tensile fracture of a solid or a shell element was assumed to take place when the maximum principal stress reached the tensile strength which was equal to 0.8 times the compressive yield stress of the element [129], [130]. On the other hand, the compressive fracture of the element was assumed to occur when the minimum principal strain reached the fracture strain which was equal to -3,000 micro-strain [130], [131]. Those criterions are summarized in Table 2.4. Aggregation of shell element failures is usually needed to express the femoral fracture of the outer cortical surface and compare the fracture behaviour between the intact and the THA models. Therefore, in this study, a critical condition was set on the basis of the number of failure elements. 1000 shell element failures were chosen as the condition and the analyses were terminated when the total number of shell element failures reached 1000 under either tensile stress or compressive stress state. The stress-strain responses of titanium alloy and alumina ceramic were assumed to be linear elastic. Young's modulus and Poisson's ratio were chosen to be 114 GPa and 0.34 for titanium alloy and 370 GPa and 0.22 for alumina ceramic [121].

Table 2. 4: Failure criterions under tensile and compressive stress states

| Stress state | | Criterion |
|---------------------|-----------------------------|---------------------------|
| Tensile | Initiation of failure | $\sigma_p = 0.8 \sigma_r$ |
| Compressive | Transition to yielded state | $\sigma_D = \sigma_r$ |
| | Initiation of failure | $\epsilon_p = -3000$ |

σ_p = maximum principal stress
 σ_r = yield stress
 σ_D = Drucker-Prager equivalent stress
 ϵ_p = minimum principal strain

2.6 Results and Discussion

2.6.1 *Distribution of bone mineral density*

Figure 2.3 (a) and (b) illustrate the inhomogeneous distribution of BMD in bone X and bone Y, respectively. The head and neck areas of the femurs were vertically cut to have cross-sectional views of the areas. For each bone model, the extraction points were selected at every threshold of the contours along the line from distal (D) to proximal (P), and the average BMD values were extracted. The BMD distributions along the lines are shown in Figure 2.4. Point A to B and F to G indicate the distal cortical bone area of bone X and bone Y, respectively. Point B to C and G to H correspond to the areas of bone marrow, C to D and H to I are the areas of cancellous bone, while D to E and I to J are the areas of cortical bone at the proximal femur for both bones, respectively. The distance of bone X and Y measured from D to P was approximately 83.2 mm and 89.1 mm, respectively. It was found that BMD values of bone X were greater than bone Y in every bone segment, e.g., cortical and cancellous bone throughout the distance. A notable difference of BMD was observed in the distal cortical, cancellous, and proximal cortical bone, i.e., 0.31 g/cm^3 , 0.13 g/cm^3 , and 0.43 g/cm^3 , respectively. Obviously aging was thought to be the key factor of this finding, where the increased porosity of the elder bone reduced its density and mass [132].

Figure 2.5 (a) and (b) shows the comparison of the density distribution and Young's modulus between both bones from the cross-section of the anterior view. It can be observed that the density of bone Y at the proximal and diaphyseal areas is much lower compared to bone X, suggesting bone stock deficiency. In terms of bone structure, a slight bend towards

the medial side of the femur was noticed at the diaphyseal segment of bone Y, while bone X has a straight geometry. Also, bone X was observed to have a greater thickness of cortical bone compared to bone Y at that respective segment. Since the cortical bone is important for providing strength and stiffness, the thickness and density of the cortical bone may affect those mechanical properties.

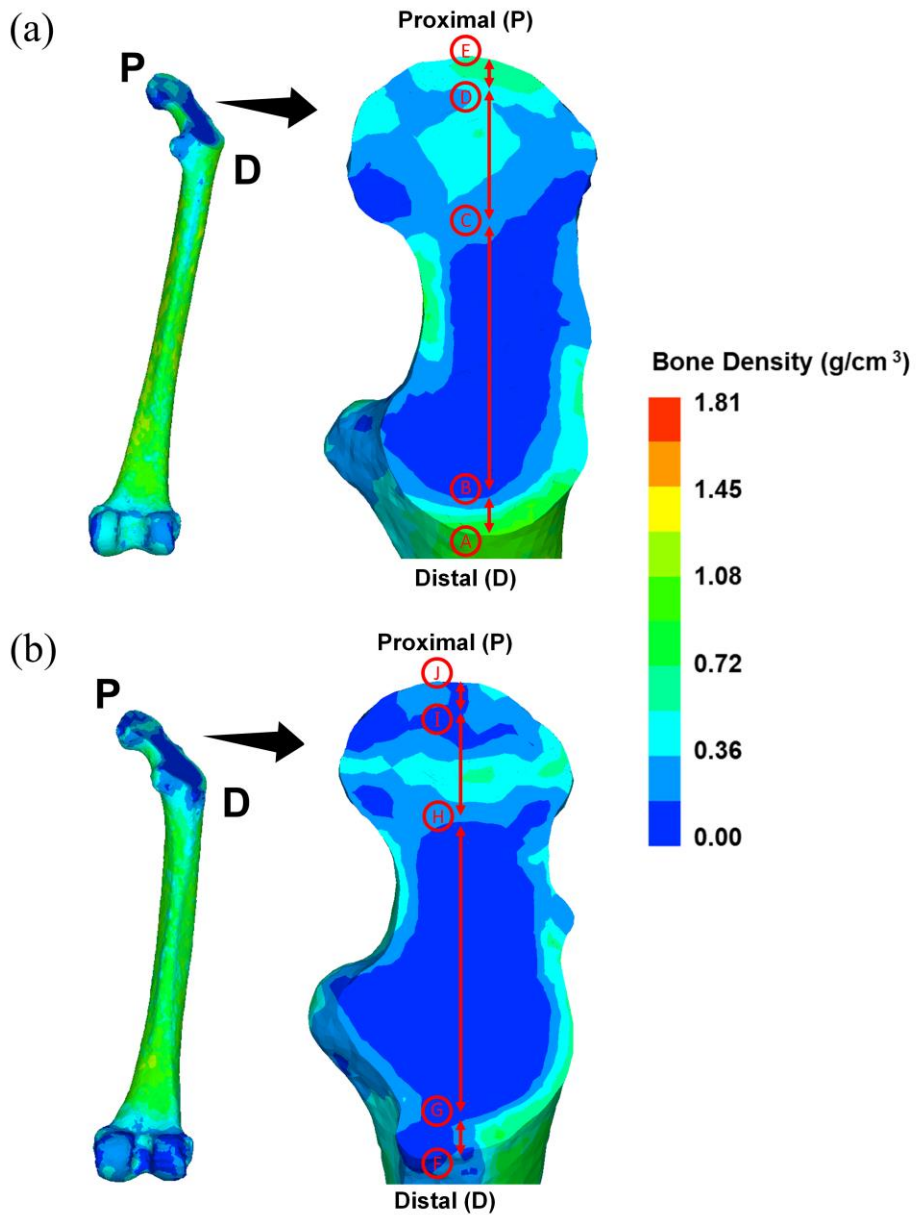


Figure 2. 3: Inhomogeneous distribution of BMD: (a) bone X and (b) bone Y

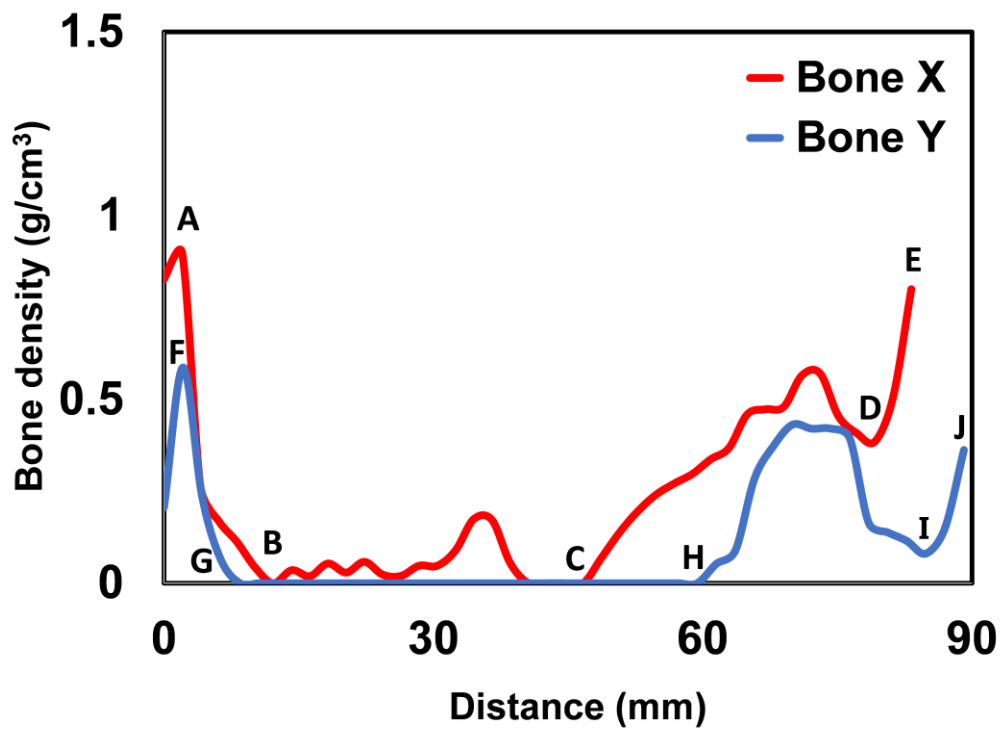


Figure 2. 4: Comparison of volumetric bone mineral density (vBMD) distribution of bone X and bone Y. Point A-B and F-G: Distal cortical bone area. Point B-C and G-H: Area of bone marrow. Point C-D and H-I: Cancellous bone area. Point D-E and I-J: Proximal cortical bone area of bone X and Y, respectively

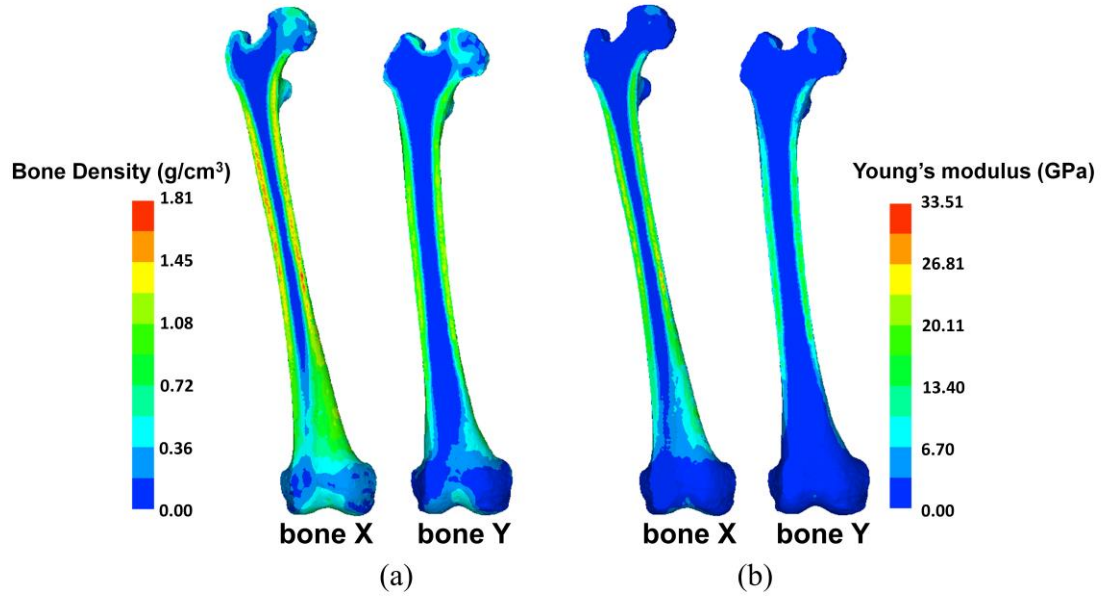


Figure 2. 5: Anterior cross-sectional view of bone X and Y: (a) bone density and (b) young's modulus

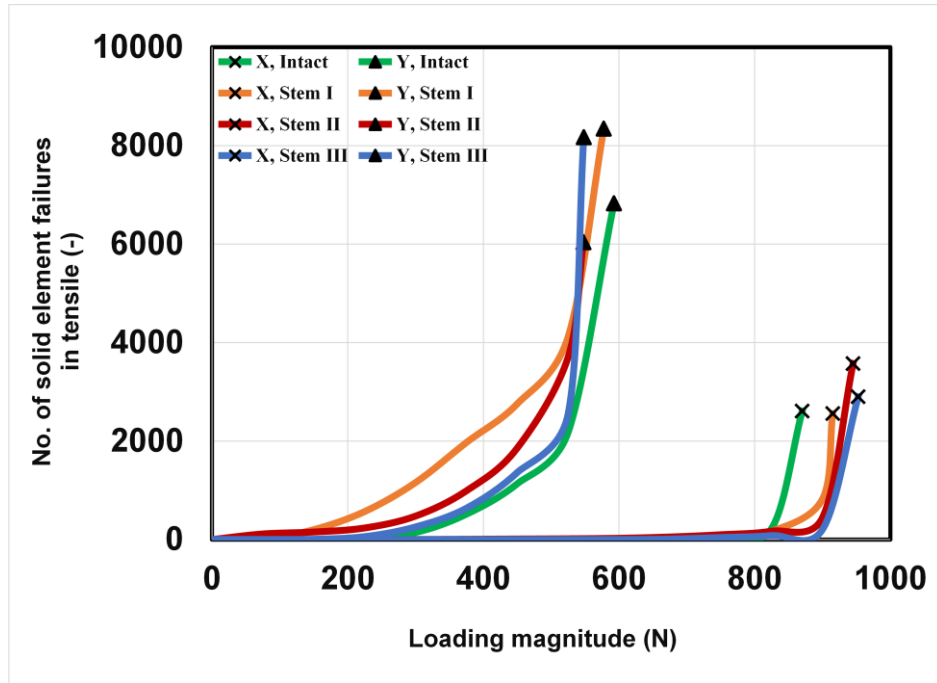
2.6.2 Accumulation of element failures as bone micro-damage

Figure 2.6 and Figure 2.7 show the cumulative numbers of solid element failures under LBC and TC, respectively. Figures (a) and (b) corresponded to the element failures generated under tensile and compressive conditions, respectively. It can be seen that the solid element failures under the tensile stress state were dominant compared to the compressive state for both LBC and TC, suggesting that the strength of the bone is lesser under tensile compared to compressive. The cumulative numbers tended to gradually increase up to the final load level, and rapidly increase at the final load under both LBC and TC. It should be noted that the final levels of load of bone X models were much higher than those of bone Y models, suggesting that the strength of bone X at the final bone

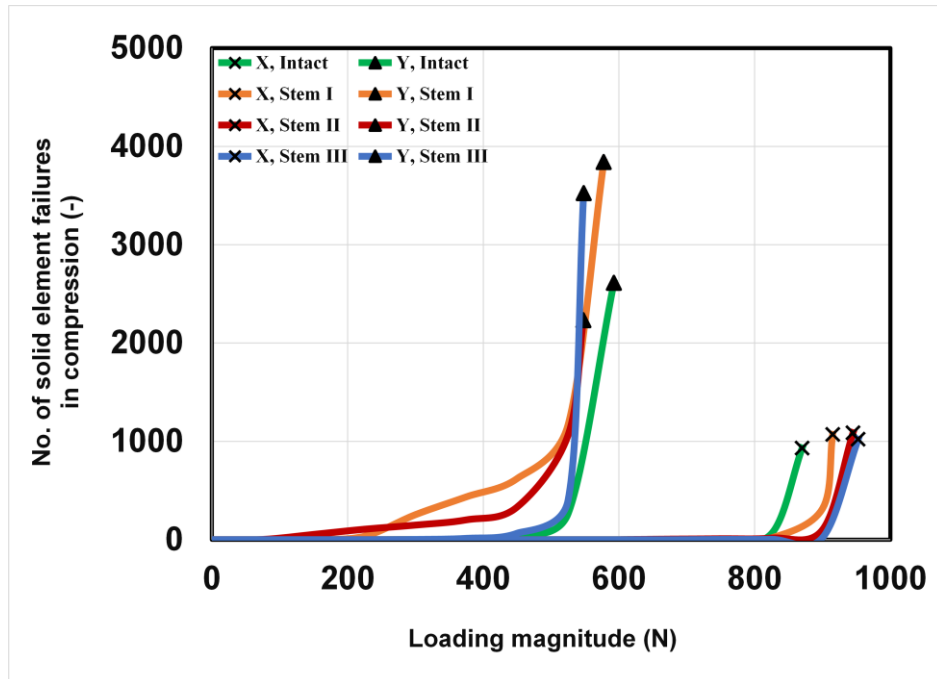
fracture was much greater than that of bone Y. It is important to see that in bone Y, the stem insertion tended to lower the bone strength, while in bone X, the bone strength tended to increase due to the stem insertion.

The effect of stem geometry and design on the internal bone damage, i.e., solid element failures, can be seen in bone X under TC. Based on Figure 2.7 (a), each stem exhibited different behaviour of solid element failures which occurred between the load 900 N and 1200 N. Bone X with stem II initially experienced the increasing trend, followed by stem III and stem I. This behaviour might be related to the different design of stem shoulder. Stem I has the widest shoulder width with a rectangular cross-section, while stem III also has a rectangular cross-section with smaller shoulder width. The shoulder width of stem II is comparable to stem III, however, with a circular cross-sectional shape. Differences in the shoulder size and the cross-sectional shape of the stem might affect the formation of internal bone damage. From the observation, smaller shoulder sizes tend to have early increments of bone damage compared to the stem with wider shoulders. A wider shoulder with a rectangular cross-sectional shape could produce a much higher torsional resistance when the implant is surrounded by cancellous bones with higher strength.

The cumulative numbers of shell element failures under LBC and TC are also shown in Figures 2.8 and 2.9, respectively. Similar to the solid element failures, the tensile failures tended to be more dominant than the compressive failures. Under LBC, for both bone X and bone Y, the numbers of shell element failures under tension and compression rapidly increased at the final stage of loading. Thus, the element failures were led by the solid elements and then finally the shell element failures took place. It is also clearly seen that bone X is much stronger than bone Y for both intact and stem insertion models.

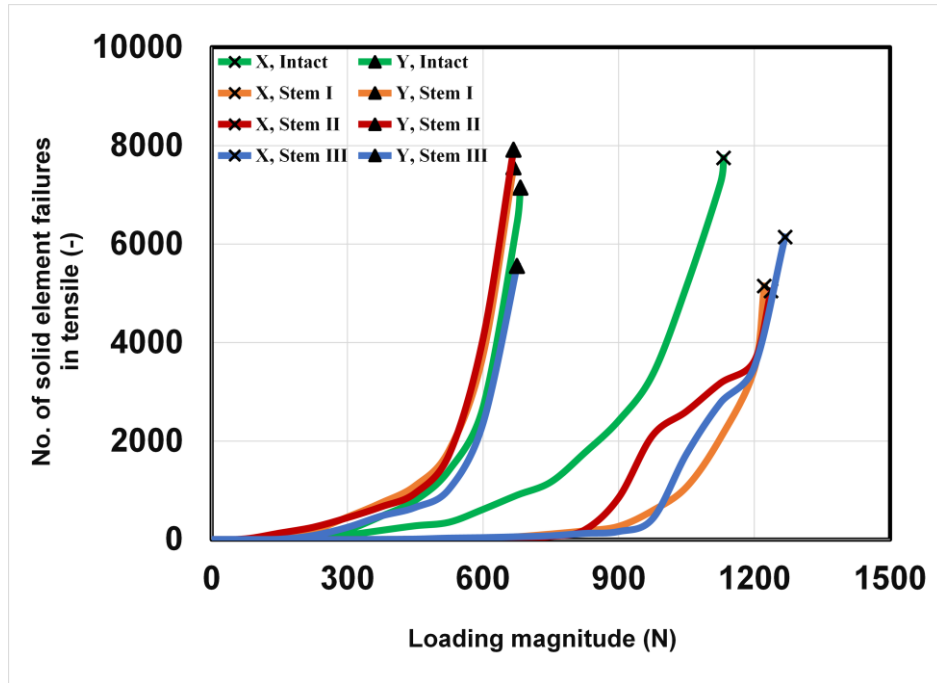


(a) Tensile failure

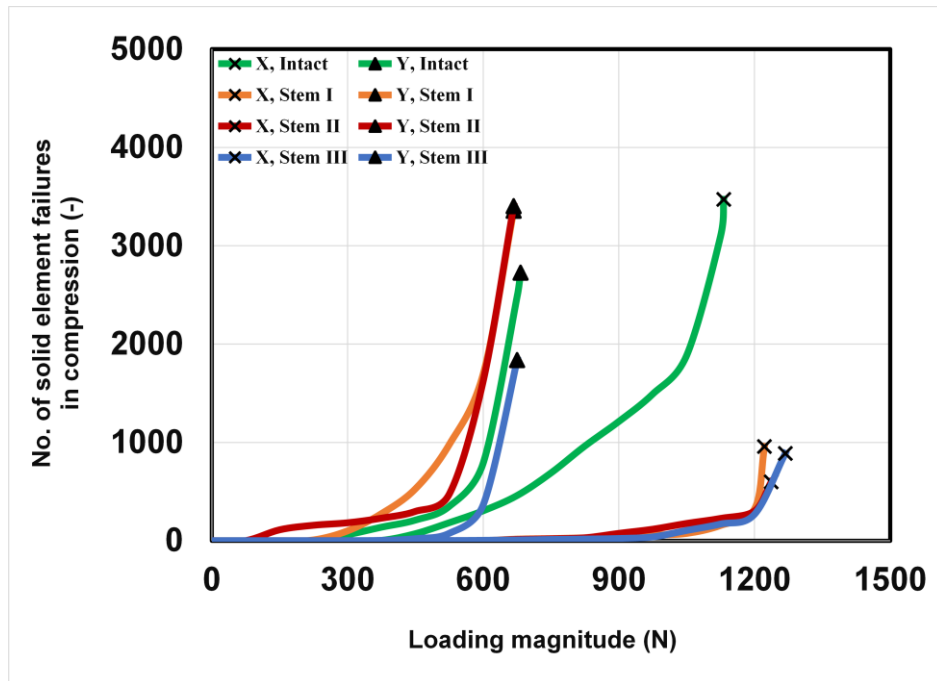


(b) Compressive failure

Figure 2. 6: Number of solid element failures under LBC condition

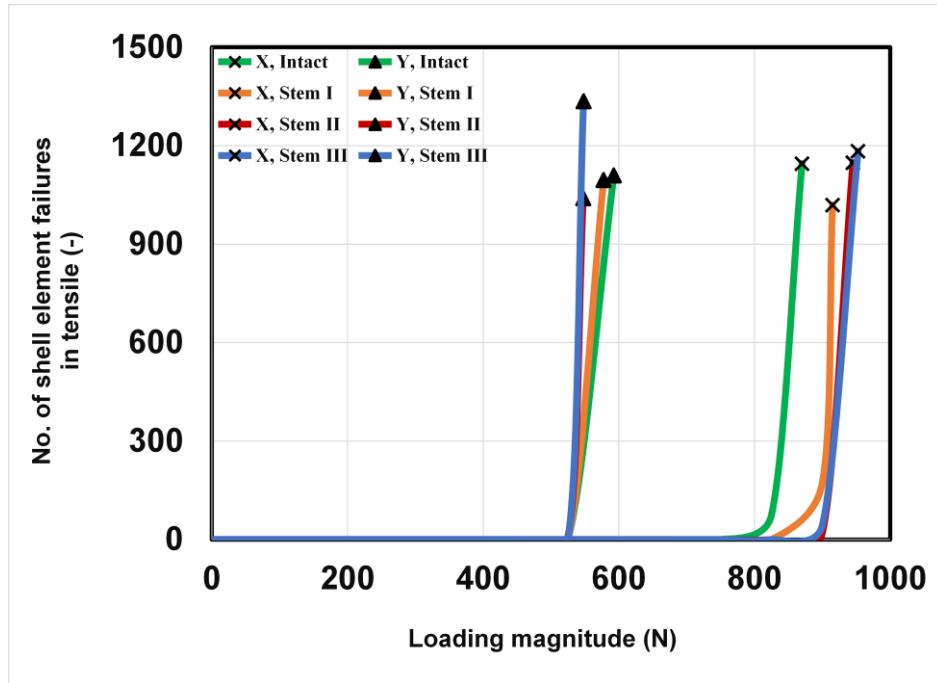


(a) Tensile failure

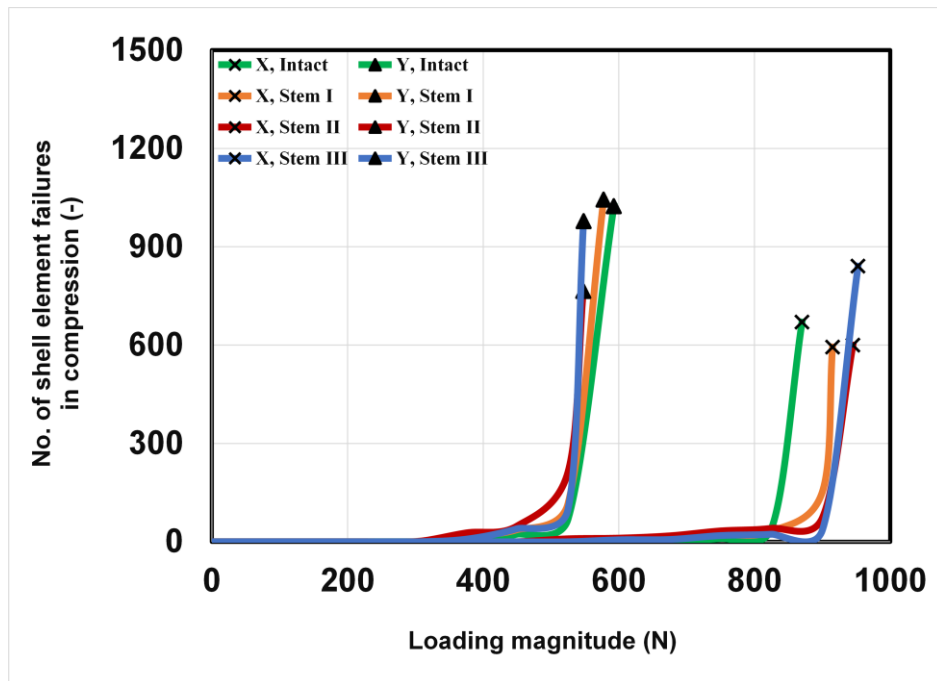


(b) Compressive failure

Figure 2. 7: Number of solid element failures under TC condition

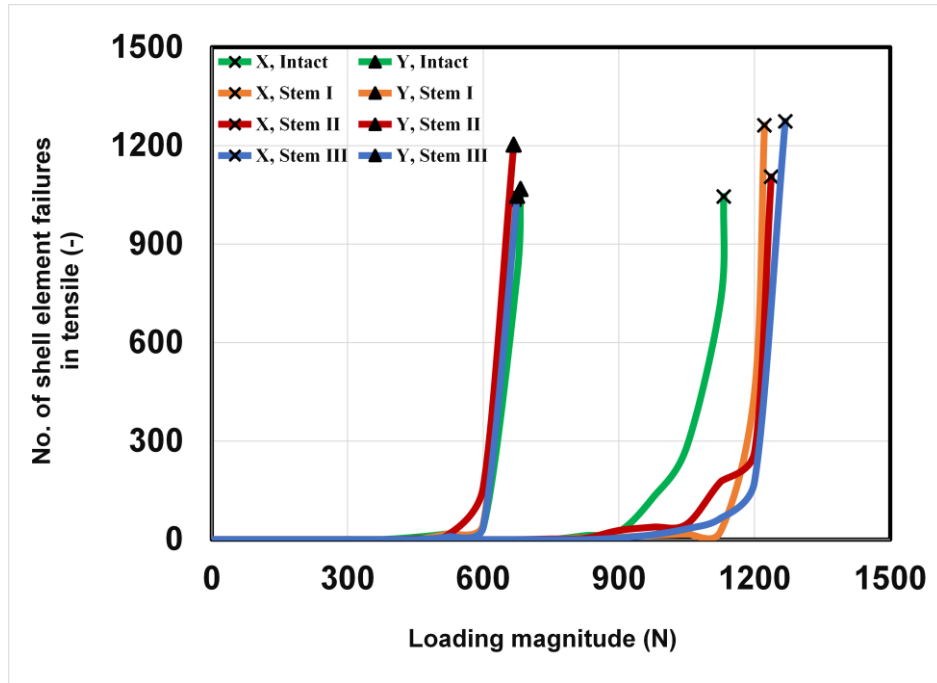


(a) Tensile failure

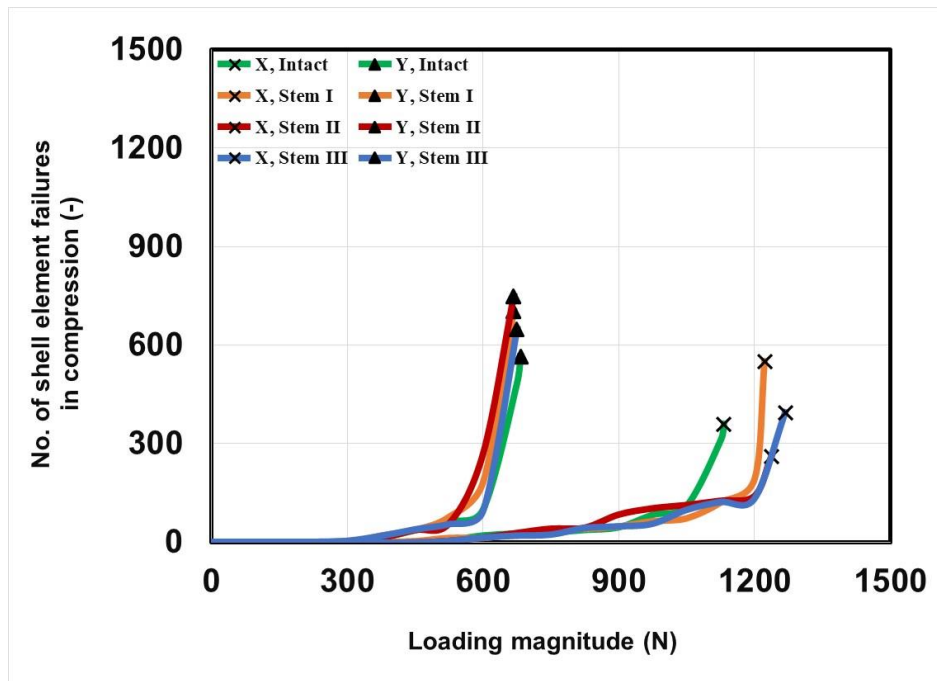


(b) Compressive failure

Figure 2. 8: Number of shell element failures under LBC condition



(a) Tensile failure



(b) Compressive failure

Figure 2. 9: Number of shell element failures under TC condition

Table 2.5 summarizes data of bone X and bone Y under configurations of LBC and TC. The data were obtained based on the three stages of damage under both configurations after the stepwise load was applied. Those stages consist of the damage at the initiation stage, damage at critical load, and complete failure. The damage at the initiation and critical load stages was represented by the number of solid element failures which explains the damage at the internal region of the bone since, during these stages, the outer cortical surface of the bone was still intact. In the stage of complete failure, the number of shell element failures was obtained which explains the aggregation failure elements that indicate bone fracture. It was observed that bone X could withstand a much higher load in both configurations when compared to bone Y in both the critical and complete failure stages. This result suggested that the strength of bone X was higher than bone Y in both pre-operative and post-operative conditions, as shown by the final load obtained by the intact and THA models of bone X.

Table 2. 5: Data summarization of bone X and bone Y under LBC and TC

| <i>Configuration: LBC</i> | | | | | | | |
|---------------------------|----------|----------------------------|--------------------|------------------------|------------------------------|--------------------|------------------------|
| Bone | Model | Solid element | | | Shell element | | |
| | | Load at critical stage (N) | Failure in tensile | Failure in compressive | Load at complete failure (N) | Failure in tensile | Failure in compressive |
| X | Intact | 825 | 231 | 63 | 870 | 1145 | 670 |
| | Stem I | 900 | 823 | 315 | 915 | 1019 | 594 |
| | Stem II | 900 | 447 | 101 | 945 | 1148 | 600 |
| | Stem III | 900 | 207 | 21 | 952.5 | 1183 | 841 |
| Y | Intact | 525 | 2183 | 266 | 592.5 | 1109 | 1024 |
| | Stem I | 525 | 4122 | 1169 | 577.5 | 1095 | 1044 |
| | Stem II | 525 | 3704 | 1062 | 547.5 | 1040 | 765 |
| | Stem III | 525 | 2548 | 398 | 548 | 1335 | 978 |

| <i>Configuration: TC</i> | | | | | | | |
|--------------------------|----------|----------------------------|--------------------|------------------------|------------------------------|--------------------|------------------------|
| Bone | Model | Solid element | | | Shell element | | |
| | | Load at critical stage (N) | Failure in tensile | Failure in compressive | Load at complete failure (N) | Failure in tensile | Failure in compressive |
| X | Intact | 1125 | 7243 | 3096 | 1132 | 1045 | 359 |
| | Stem I | 1200 | 3464 | 324 | 1222 | 1262 | 551 |
| | Stem II | 1200 | 3629 | 303 | 1237 | 1105 | 260 |
| | Stem III | 1200 | 3507 | 269 | 1268 | 1274 | 394 |
| Y | Intact | 675 | 6410 | 2479 | 682.5 | 1068 | 566 |
| | Stem I | 600 | 3746 | 1696 | 667.5 | 1038 | 704 |
| | Stem II | 600 | 4081 | 1624 | 667.5 | 1203 | 749 |
| | Stem III | 600 | 2365 | 367 | 675 | 1047 | 648 |

2.6.3 *Distribution of solid and shell element failures*

Distribution patterns of element failures as bone micro-damages are shown in Figures 2.10 and 2.11 for LBC and TC, respectively. In those images, distributions of solid element failures at the damage initiation and the critical load stages, corresponding to the final bone fracture, are presented, along with the distributions of shell element failures at the final bone fracture (called ‘complete failure’). It is clearly seen that bone Y had greater internal bone damages than bone X in both damage initiation and critical load stages. In the intact models, solid element failures are mainly generated in the femoral neck region and the distal side close to the knee joint under LBC. On the other hand, solid element failures generated in the femoral neck and the middle region of diaphysis under TC. It is worth noting that the distal side and the middle region corresponded to the fixed regions set as the boundary conditions under LBC and TC, respectively. Also, shell element failures at the complete failure are mainly generated in those regions.

When a stiffer metallic stem was inserted into the femoral bone, it subsequently changes the mechanical environment of the bone. From the figures, the presence of stem easily damaged the cancellous bones that surrounded the stem in bone Y compared to bone X, where quite noticeable damage was seen even in the lower loading magnitude as illustrated in the damage initiation stage. Such severe bone damage that appeared along the bone-stem interface of bone Y may affect the primary stability of the implant after the arthroplasty. Without primary stability, the process of osseointegration may probably be delayed. In addition, the high number of failure elements at the bone-stem interface may contribute to the risk of implant loosening due to the failure of the cancellous bones surrounding the stem. This phenomenon may also contribute to the risk of periprosthetic

fracture after THA where loosening of the stem was known as one of the risk factors [86], [133]–[136].

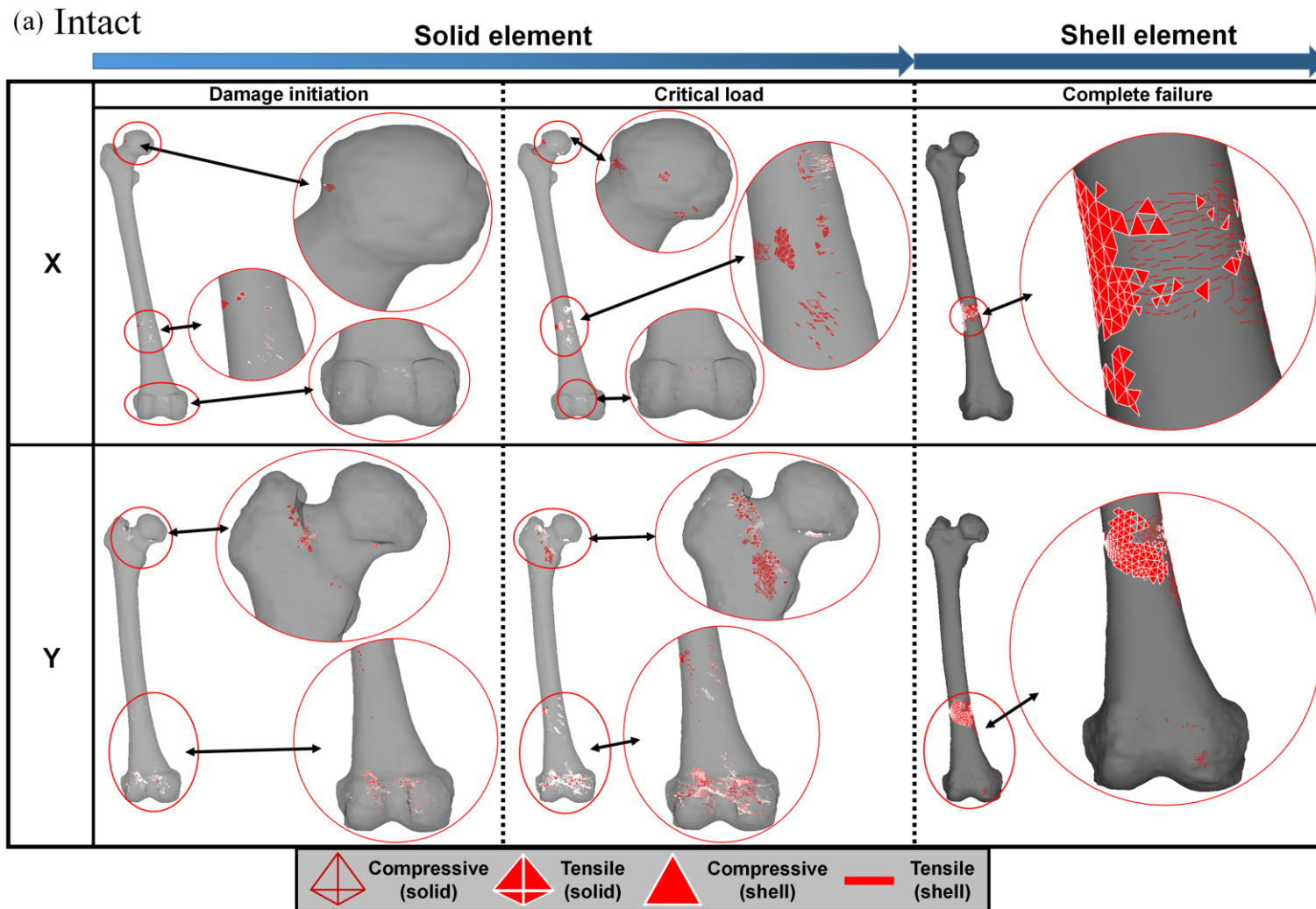


Figure 2. 10: Distribution of element failures under LBC: (a) intact, (b) stem I, (c) stem II and (d) stem III

(b) Stem I

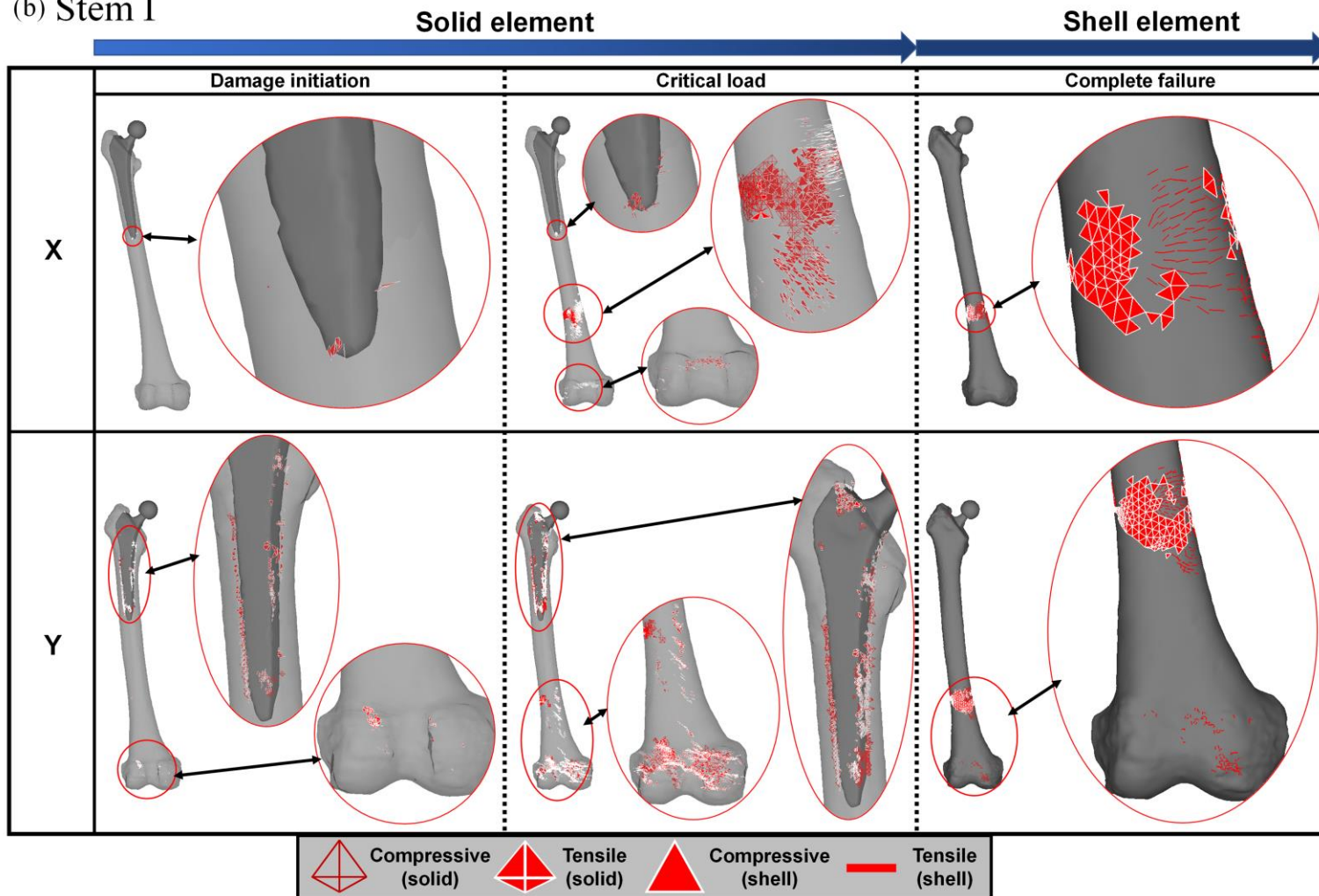


Figure 2.10 (continued)

(c) Stem II

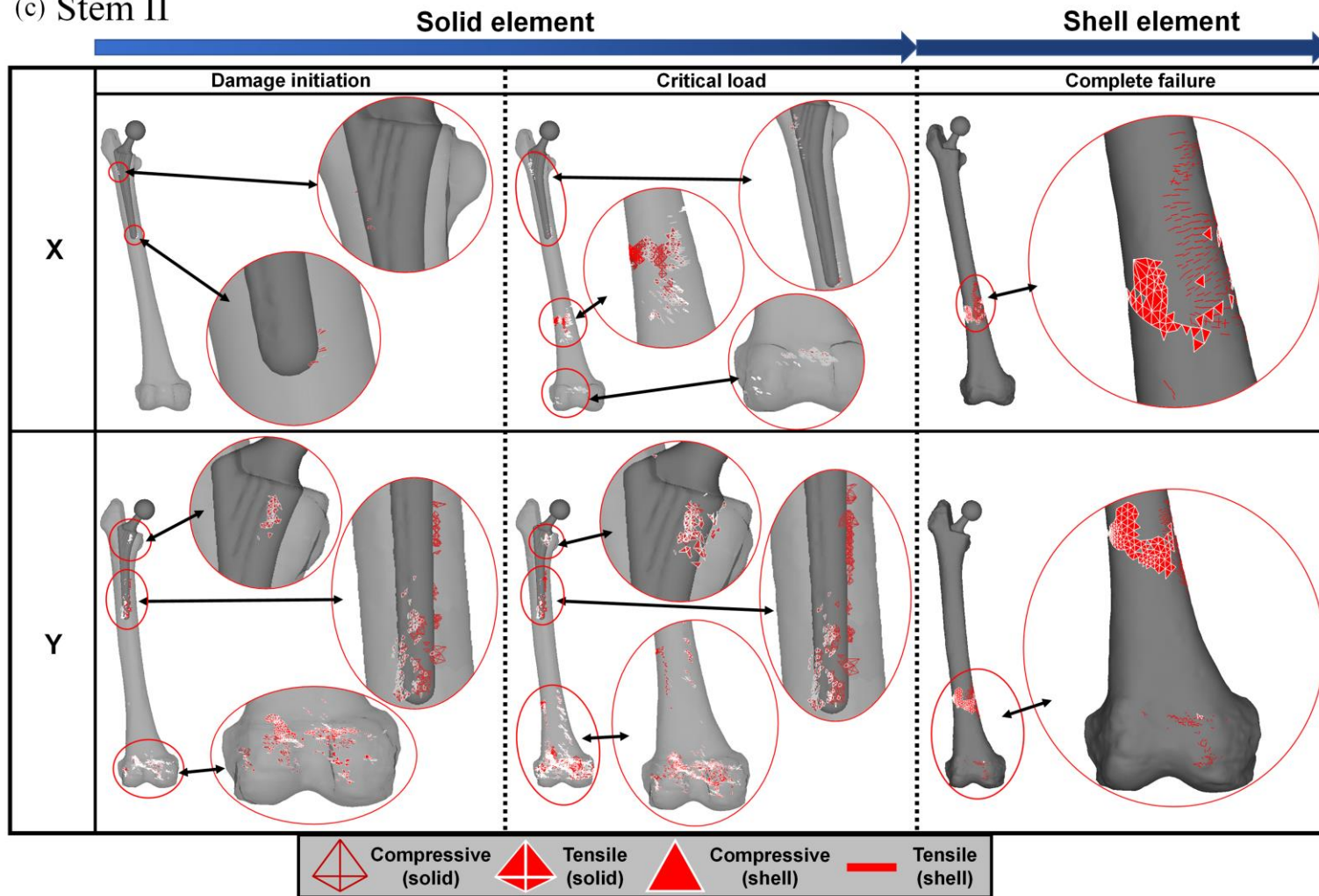


Figure 2.10 (continued)

(d) Stem III

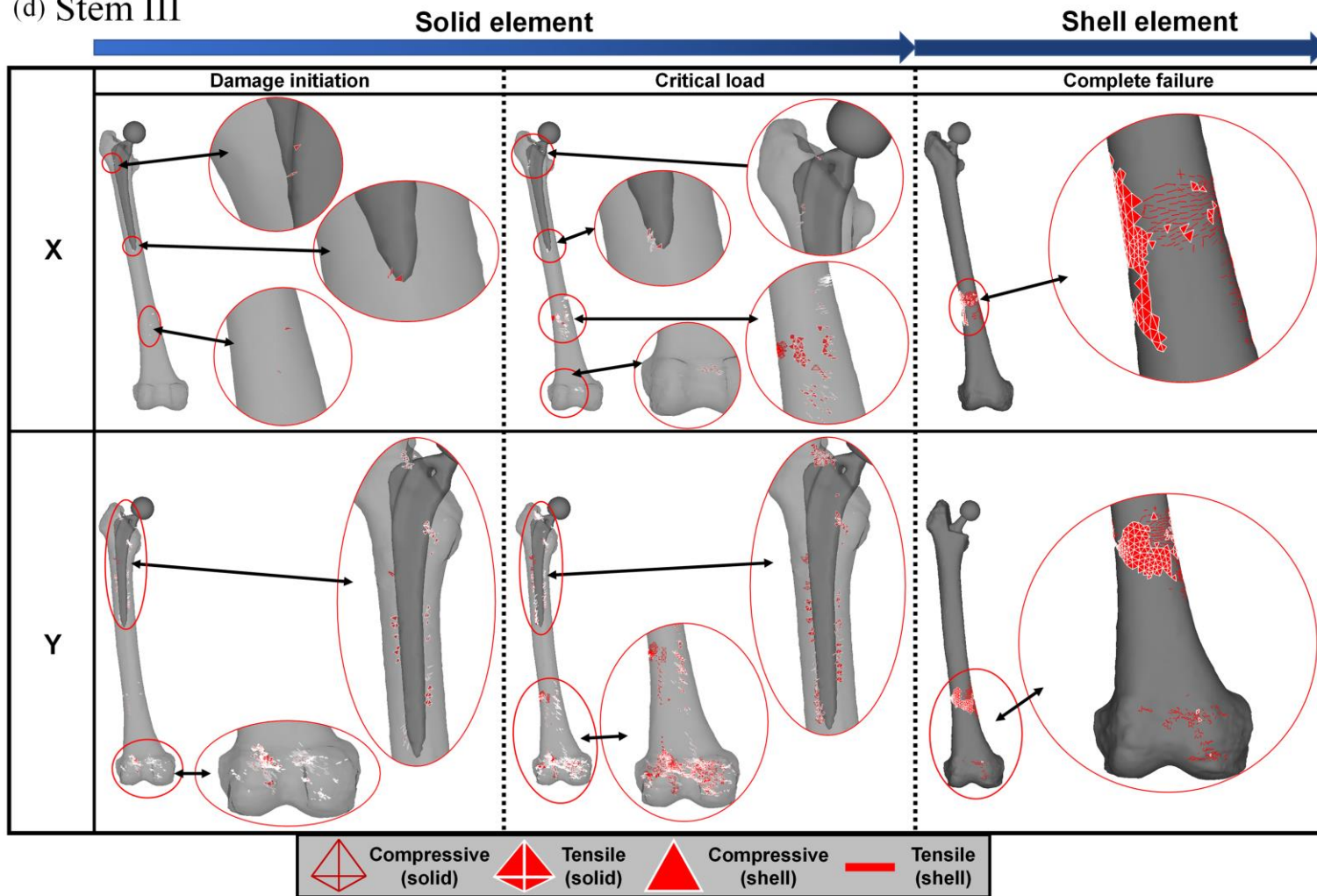


Figure 2.10 (continued)

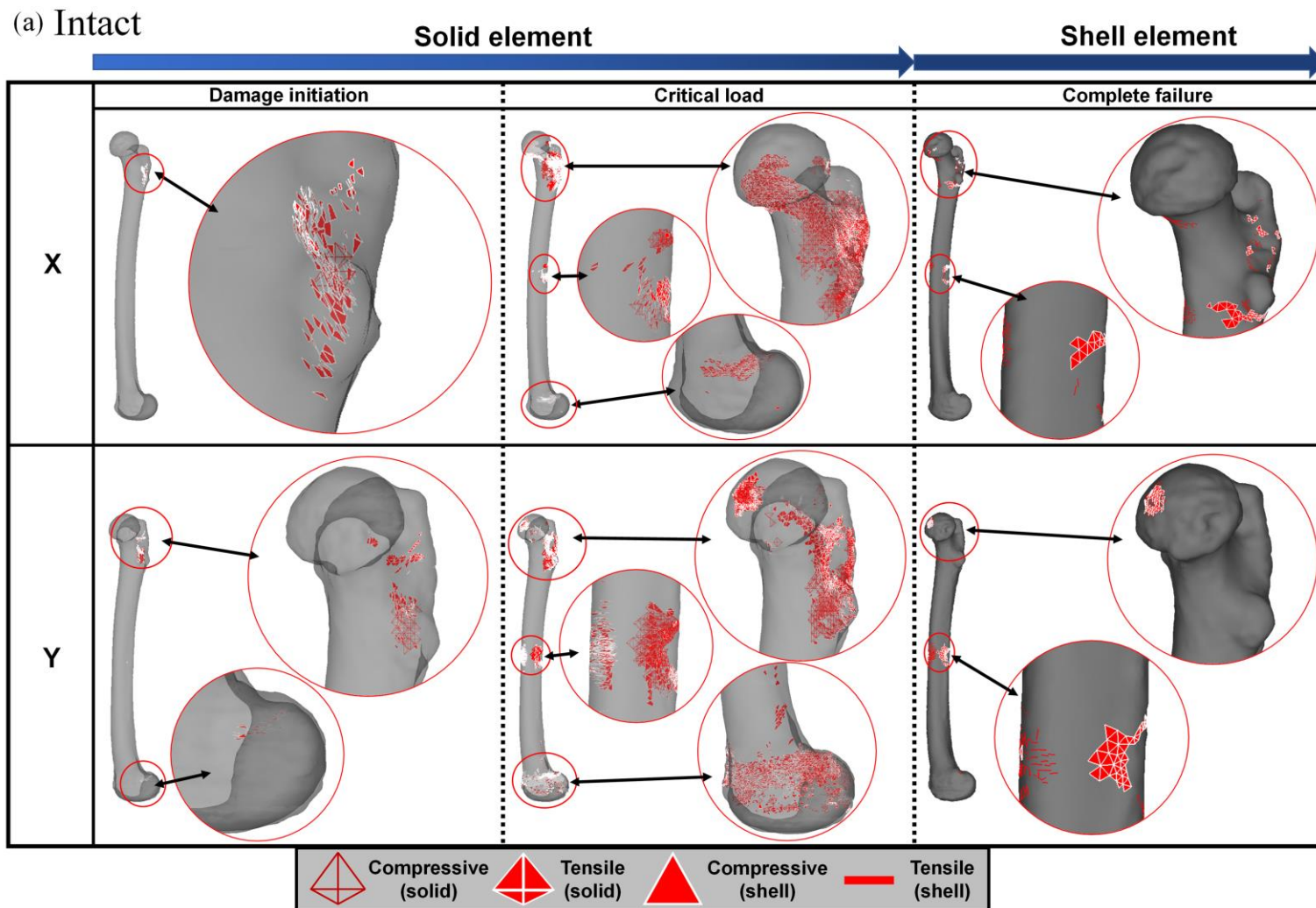


Figure 2. 11: Distribution of element failures under TC: (a) intact, (b) stem I, (c) stem II and (d) stem III

(b) Stem I

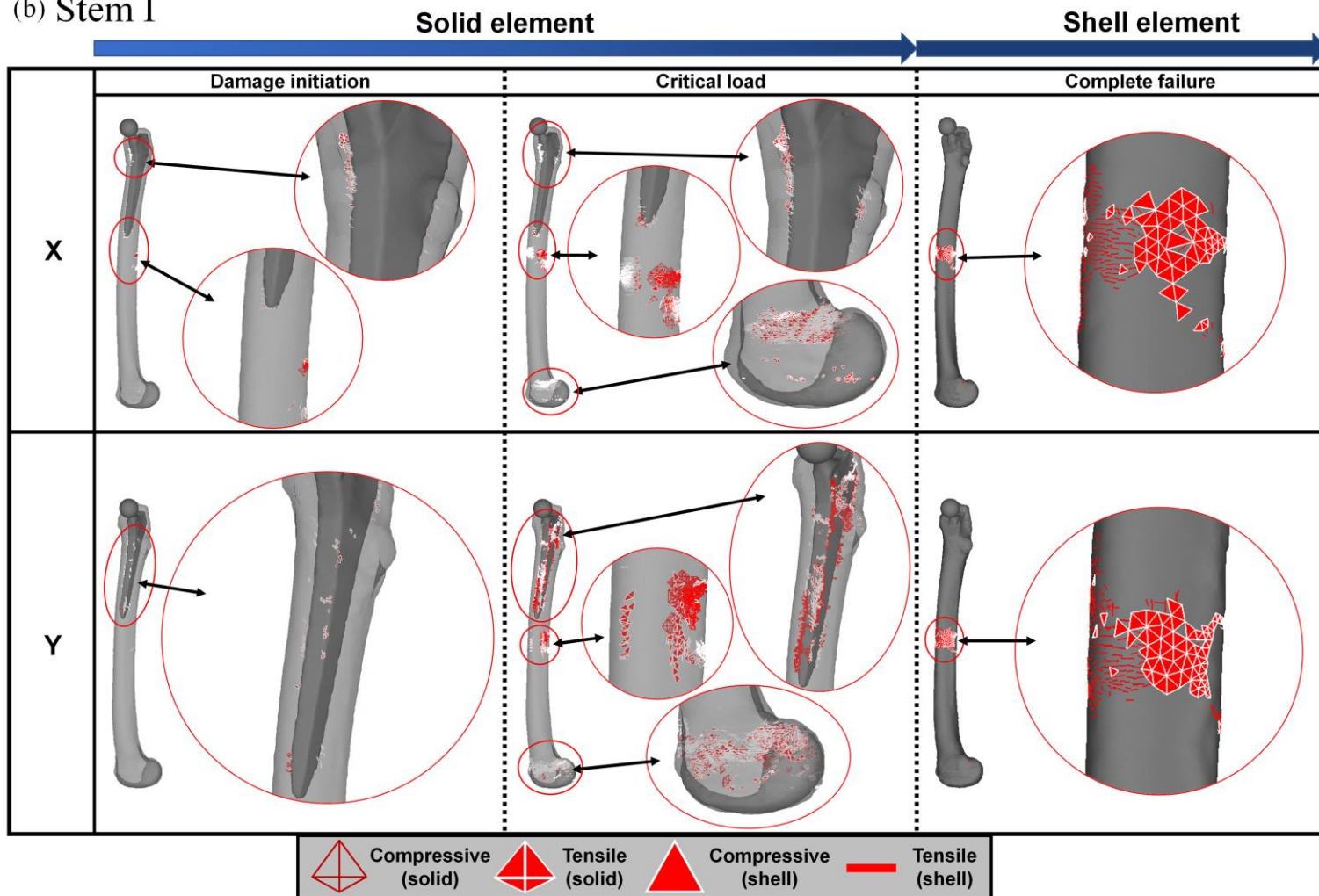


Figure 2.11 (continued)

(c) Stem II

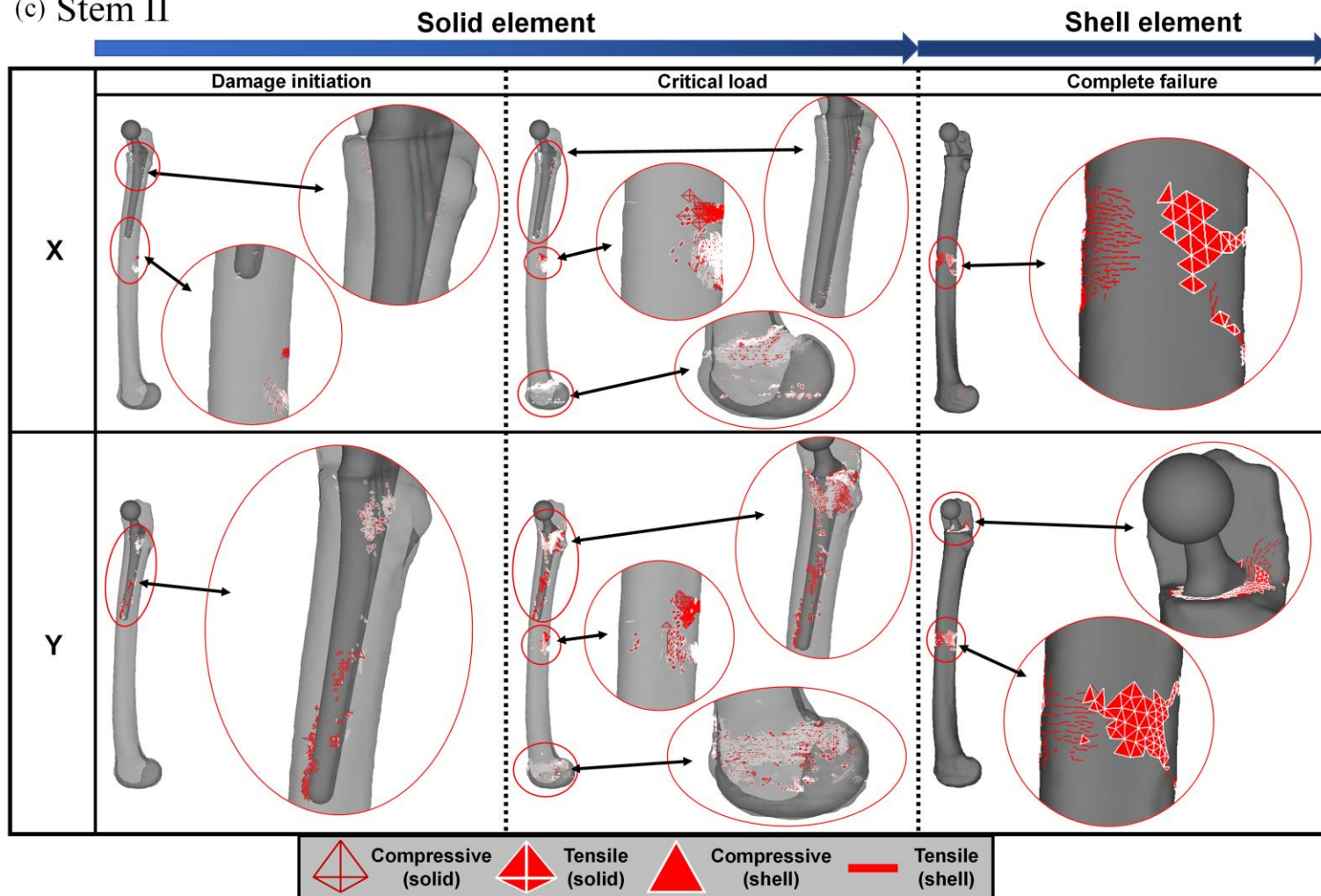


Figure 2.11 (continued)

(d) Stem III

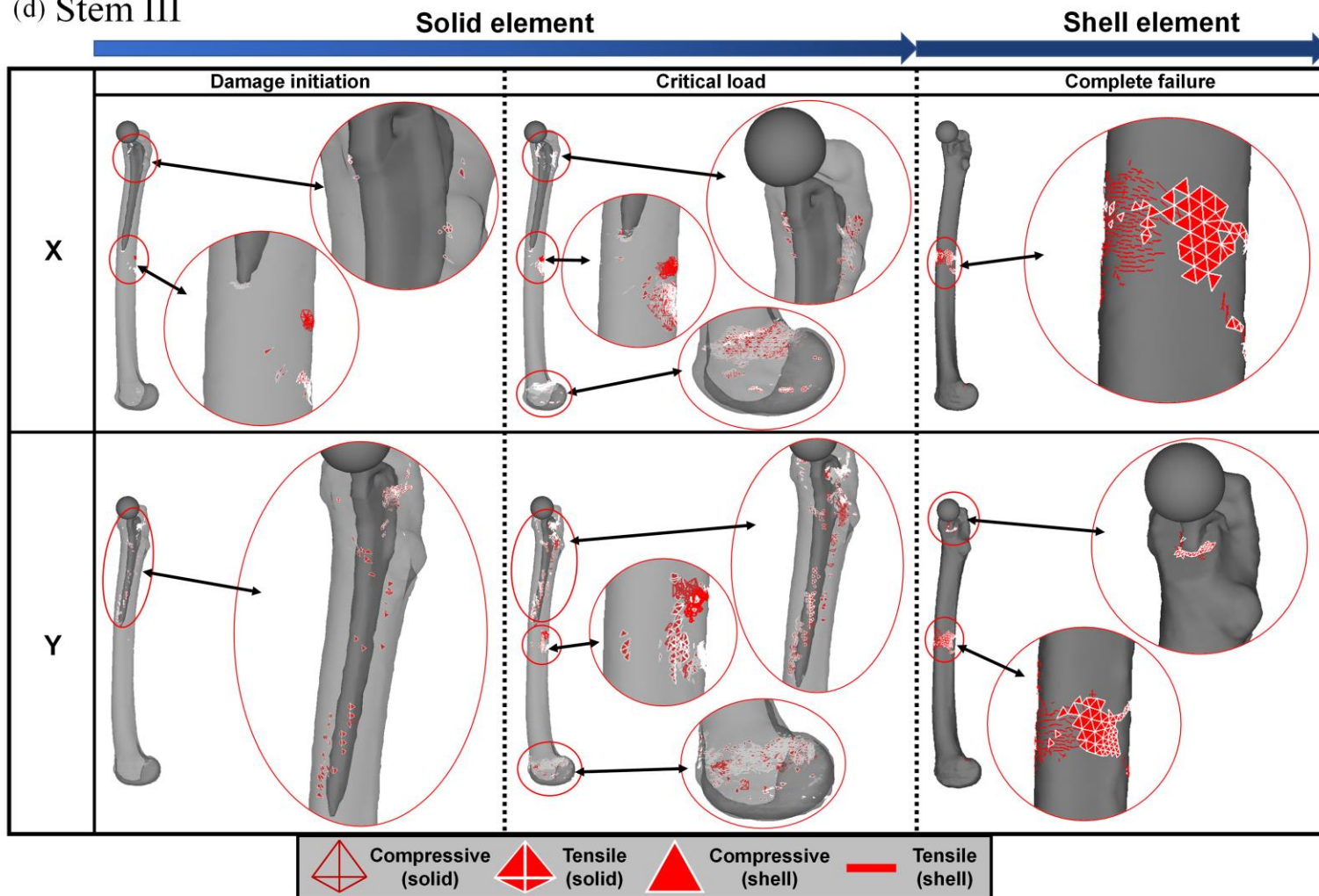
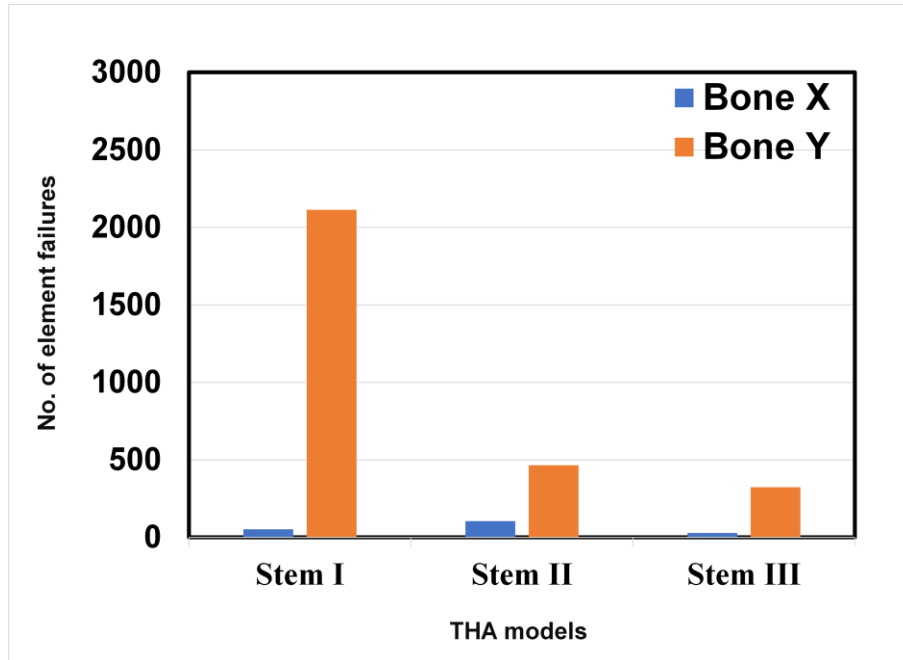


Figure 2.11 (continued)

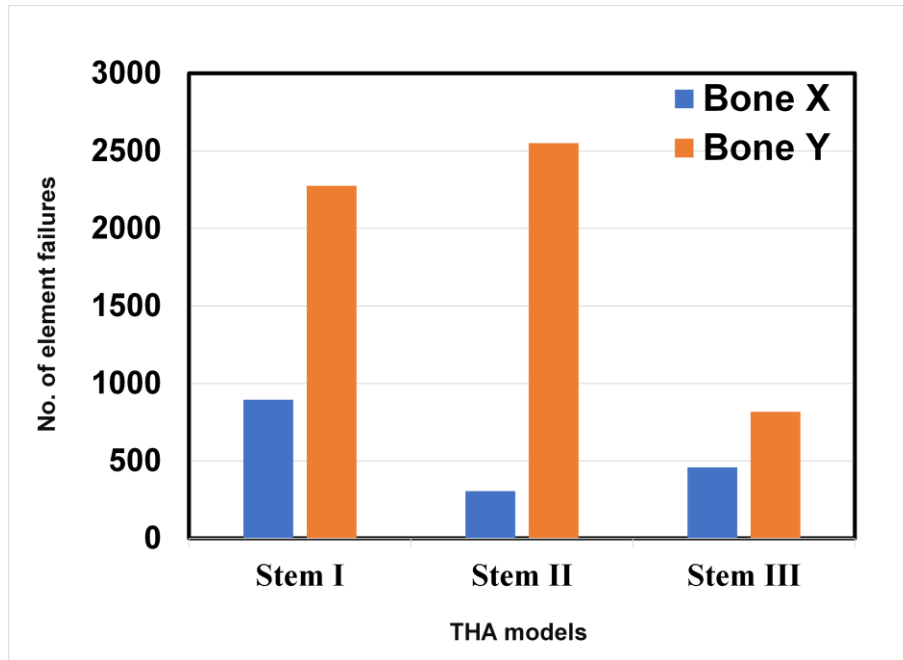
2.6.4 *Solid element failures within the bone-stem interface at the critical stage*

The numbers of solid element failures within the bone-stem interface at the critical stage are shown in Figure 2.12. A similar extraction size of 70 mm × 70 mm × 180 mm was applied to all models that enclosed the area of the bone and the stem. It is clearly seen that the number of element failures of bone X was much lower than that of bone Y for all stem types. From this finding, it is understood that bone with poor quality will experience greater internal bone damage specifically at the interfacial area of bone and stem. The small number of element failures suggests that bone X may have greater primary stability with stem, allowing the osseointegration process to occur. For bone Y, the highest number of element failures was obtained at stem I model. From this result, it can be said that the stem with larger dimensions may produce major damage to the cancellous bones. The bones with low strength due to lower BMD may easily be damaged when they are in contact with stiffer material, hence resulting in the significant number of element failures in stem I model compared to stem II and III models.

It is understood from Figure 2.12 (b) that bone X with stem I had the highest number of element failures at the critical stage under TC. This was similar to bone Y with stem I under LBC condition. In the case of bone Y, however, stem I and stem II shared almost similar numbers of element failures. The lowest number of element failures was obtained by stem III. This phenomenon might be related to the factor of stem length. In this study, both loading configurations of LBC and TC will lead the bone to experience the bending process, thus, the factor of longer stem length will affect the bending behaviour of the bone.



(a) LBC



(b) TC

Figure 2. 12: Number of solid element failures in the bone-stem interface region at the critical stage

2.6.5 *Classification of femoral fractures following total hip arthroplasty*

The assessment of the femoral bone fractures was based on the resulting failure of shell elements in the THA models. The fracture classification of the bone following THA was based on the Vancouver Classification and the AO Foundation/Orthopaedic Trauma Association (AO/OTA) [101], [137]. In the case of LBC, the fracture of bone X was located only at the distal diaphyseal segment of the femur, while for bone Y, two locations were identified, i.e., distal diaphyseal and distal end segment of the femur as shown in Figure 2.10 (b)-(d), complete failure of shell element. The fracture located at the distal diaphyseal segment drew a parallel view to the Vancouver classification type C. An oblique fracture pattern was observed in both bones. In regard to the fracture located at the distal end segment of bone Y, the view is almost similar to type 33-A-2.3, extra-articular, simple fracture with a transverse pattern from the AO/OTA classification. This fracture type was observed to occur at all of the THA models of bone Y.

Shell element failures of Figure 2.11 (b)-(d) illustrate the prediction of bone fracture under TC. The THA models of bone X fractured only at the middle diaphyseal segment, while two locations were observed for the THA models of bone Y, namely, the middle diaphyseal and trochanteric region. The fracture predicted at the middle diaphyseal segment was correlated to type B₂ in the Vancouver classification. It is observed that the THA models of bone X had a spiral fracture pattern, while the THA models of bone Y were similar to the transverse pattern. On the other hand, quite noticeable fractures were seen at the trochanteric regions of bone Y implanted with Stem II and III, which suggests the possibility of Vancouver classification type A_G.

2.7 Conclusion

In this chapter, two different bones implanted with three different stem designs were successfully developed. Then, finite element analysis with non-linear damage analysis was conducted under two different boundary conditions namely lateral bending and torsional condition. The conclusions were obtained as follows:

- (1) The quality of the two bones was successfully evaluated based on the quantitative comparison of bone mineral density at the proximal region of the intact femur i.e., head and neck. It was found that bone X, developed from CT image of 61-year-old patient had higher BMD value in every bone segment i.e., distal cortical, cancellous and proximal cortical bone, compared to bone Y, which developed from CT image of 87-year-old. The BMD difference in every segment was 0.31 g/cm^3 , 0.13 g/cm^3 , and 0.43 g/cm^3 , respectively. It is concluded that age had become a factor of reduction of BMD with higher age produces lesser BMD.
- (2) The mechanism of bone micro-damage at the internal bone region was successfully depicted through the cumulative number of solid element failures. It was found that the implant geometry had influenced the micro-damage behaviour of the bone from the internal region, especially in bone in bone X under TC, however, the difference was found to be small between each stem design under both LBC and TC for bone Y. It is then concluded that the size of the stem shoulder and its cross-sectional shape had influenced the behaviour of internal bone damage of bone with good quality (bone X), where stem with small shoulder and round cross-sectional shape produce early and higher bone damage under the torsional condition compared to stem with

bigger shoulder and rectangular cross-sectional shape. This finding may be useful in the development of advanced THA implant design.

- (3) The effect of bone quality on the internal bone damage at the interfacial area of bone and stem was identified. It was found that bone X had lesser bone damage at the bone and stem interface compared to bone Y. It is then concluded that bone with poor quality may not be suitable to undergo THA with cementless fixation since the stiffer material i.e., THA stem, was found to easily damage the internal region of the bone which potentially lead to loosening of the implant, and the findings were consistent despite implanted with different stem design.
- (4) The strength of the bone was successfully determined based on the cumulative failure of 1000 shell elements. It was found that bone X can withstand a much higher load compared to bone Y. The stem insertion was found to increase the strength of bone X, while decrease the strength of bone Y, which was compared to the strength of the intact model. It is concluded that bone with good quality has a higher strength at the diaphyseal bone region (femoral shaft) compared to the proximal region (femoral head and neck) in which influenced the number of bone element failures in intact model. Hence, removing the proximal region of the bone would result in the increment of bone strength. Meanwhile, bone with poor quality had a similar strength at both the proximal and diaphyseal, resulting in a reduction of bone strength after the implantation.
- (5) Different boundary conditions were found to affect the strength of the bone. It was observed that the strength of the bone is higher in TC compared to LBC.

CHAPTER 3: DAMAGE MECHANISMS UNDER FALLING CONDITIONS

3.1 Overview

Falling has been acknowledged as one of the leading causes of PFF following THA. To further extend the study in chapter 2, another loading and boundary condition had been introduced in this chapter which simulate different types of falling configurations from the lateral to posterolateral side by using the bone model from 61 and 87-year-old patients. Three different stem designs were implanted into the femur consisting of stem I, stem II, and stem III. Finite element analyses with a nonlinear damage analysis were then performed and the mechanism of bone micro-damage formation from the internal region of the bone and fracture formation from the external region of the bone in both models were then compared.

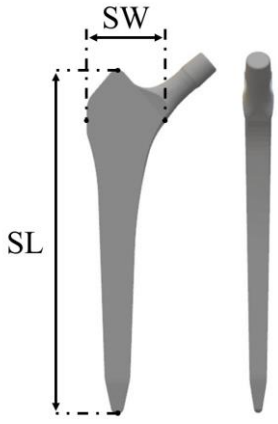
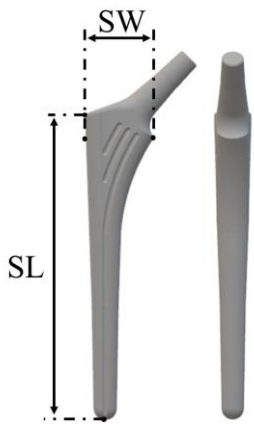
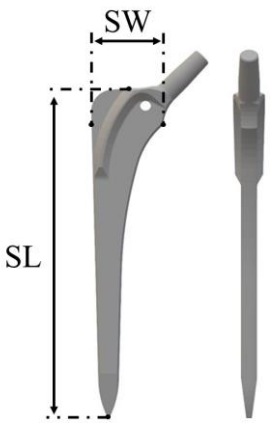
3.2 Construction of intact femoral model

To create computational models, CT images of two female patients (aged 61 and 87) diagnosed with stage three avascular necrosis in the right femur were obtained at Fukuoka University Hospital, Japan. Both CT images had slice thickness of 0.5 mm. CT-FEM software (Mechanical Finder version 11.0) was used to develop three-dimensional finite element (FE) models of the right femurs. To construct the models, a two-dimensional femoral bone region of interest (ROI) was selected from each CT image, with a higher CT value than that of the surrounding soft tissues. The ROIs were vertically stacked to create the three-dimensional geometry of the femur. The intact femur FE model was meshed with 2-mm tetrahedral elements for the cancellous and inner cortical bone, and 2-mm triangular shell elements with a 0.3 mm thickness were assigned to the outer surface of the cortical bone. These parameters were assigned based on the results from convergence test of previous study, where the 2 mm mesh size produces the most accurate value of total strain energy compared to 3 and 4mm [108]. Additionally, the surface shell elements were assigned to express the stiffest layer of the cortical bone that cannot be expressed from the CT images [108]. The computational models of the 61 and 87-year-old patients were labeled as bone X and Y, respectively. The intact model of bone X consisted of 156,509 solid elements and 191,478 shell elements, while the intact model of bone Y comprised 73,698 solid elements and 84,954 shell elements. Inhomogeneous bone mineral density (BMD) values were assigned to each element by converting the Hounsfield unit (HU) to BMD using a linear formula [108].

3.3 Construction of THA models

In this study, three distinct femoral stem types, referred to as stem I, stem II, and stem III, were introduced, each with its own unique design and geometry, as described in Table 3.1. The virtual hip arthroplasty procedure involved removal of the femoral bone head based on the intertrochanteric line, approximately 1 cm above the lesser trochanter. The stem was then aligned properly into the femoral canal, with the mapping view from the CT images used to replicate the original position of the femoral head. The resulting total hip arthroplasty (THA) models of bone X and Y with stem I, II, and III are depicted in Figure 3.1. Specifically, the FE models of bone X implanted with stem I, II, and III consisted of 162,710, 155,220, and 139,579 tetrahedral solid elements, and 62,628, 61,533, and 62,547 triangular shell elements, respectively. For bone Y, the FE models comprised 189,777, 185,391, and 175,221 solid elements, and 74,766, 74,190, and 75,165 shell elements for stem I, II, and III, respectively. Lastly, the materials used for the stem and femoral ball were assumed to be titanium alloy and alumina ceramic, respectively. Table 3.2 presents a summary of the mechanical properties of the materials that were used in the study. [121]. It is noted that the interface between the bone and stem was assumed to be perfectly bonded to mimic the complete process of osseointegration of the total hip stem, which ideally achieve a stable and secure fixation to the bone, hence produce no relative movement between the implant and bone interface [42].

Table 3. 1: Illustration of stem I, stem II and stem III

| (a) Stem I | Description |
|---|---|
|  | <ul style="list-style-type: none"> • Zweymuller (Teijin Nakashima Medical Co., LTD) • Shoulder width (SW) = 35 mm • Stem length (SL) = 120 mm • Rectangular cross-sectional shape |
| (b) Stem II | Description |
|  | <ul style="list-style-type: none"> • Perfix (Kyocera Medical Tech.) • Shoulder width (SW) = 25 mm • Stem length (SL) = 115 mm • Round cross-sectional shape |
| (c) Stem III | Description |
|  | <ul style="list-style-type: none"> • Aesculap (B. Braun Healthcare) • Shoulder width (SW) = 30 mm • Stem length (SL) = 140 mm • Rectangular cross-sectional shape |

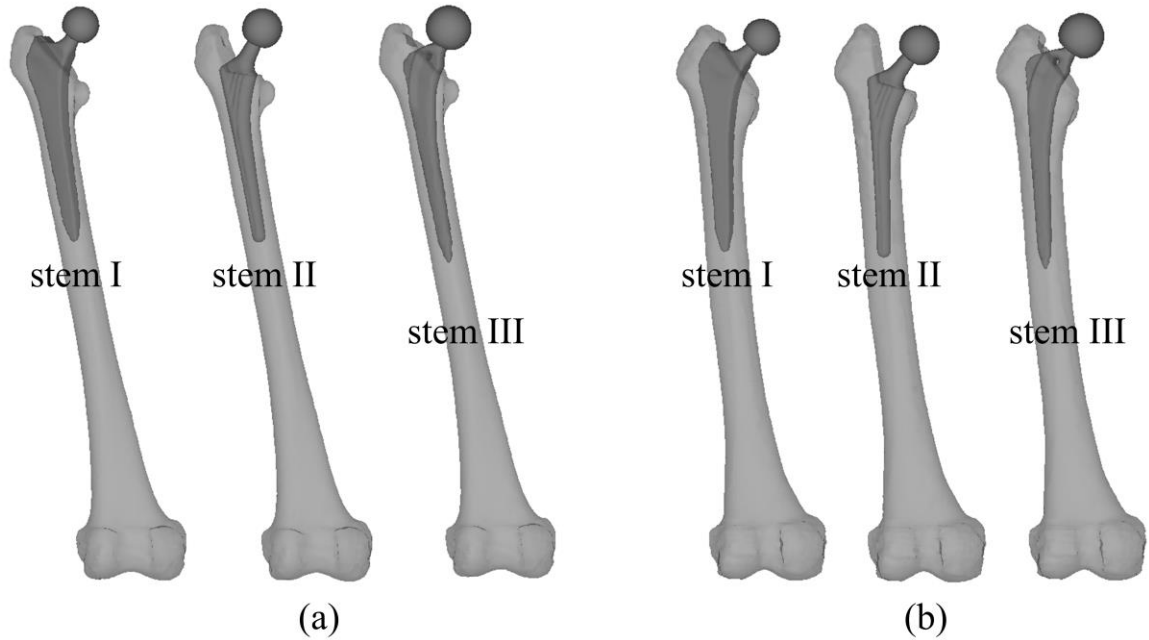


Figure 3. 1: THA model of (a) bone X and (b) bone Y implanted with stem I, stem II, and stem III

Table 3. 2: Mechanical properties of THA implant [121]

| Properties | Titanium alloy | Alumina ceramic |
|------------------------------|-----------------------|------------------------|
| Elastic modulus (GPa) | 114 | 370 |
| Poisson ratio | 0.34 | 0.22 |
| Critical stress (GPa) | 0.88 | 0.40 |
| Yield stress (GPa) | 0.97 | 3.00 |
| Density (g/cm ³) | 4.43 | 3.96 |

3.4 Loading and boundary conditions

Four different loading and boundary conditions were introduced into the nonlinear FE analysis in order to predict the damage formations of the two types of femoral bone. These conditions were adopted from the previous studies [114], [115]. In the loading and boundary conditions, four different types of falling configurations (FCs) were introduced, and they were thereafter denoted as falling configuration 1 (FC1), falling configuration 2 (FC2), falling configuration 3 (FC3) and falling configuration 4 (FC4). The loading direction was set based on the angle of α and β , which refers to the long axis of the femur in frontal plane and femoral neck axis in the transverse plane, respectively. The orientation of loading direction for FC1 was $\alpha = 120^\circ$, $\beta = 0^\circ$, FC2 was $\alpha = 60^\circ$, $\beta = 0^\circ$, FC3 was $\alpha = 60^\circ$, $\beta = 15^\circ$, and FC4 was $\alpha = 60^\circ$, $\beta = 45^\circ$. The boundary conditions of all FCs are shown in Figure 3.2. For all FCs, the magnitude of applied load was set to be increased stepwise, ranging from 0 N to 2500 N in 20 steps (125 N per step). The selected range of loading magnitude was found to be sufficient to demonstrate the damage mechanism in femoral fracture under the same conditions in the previous study [115].

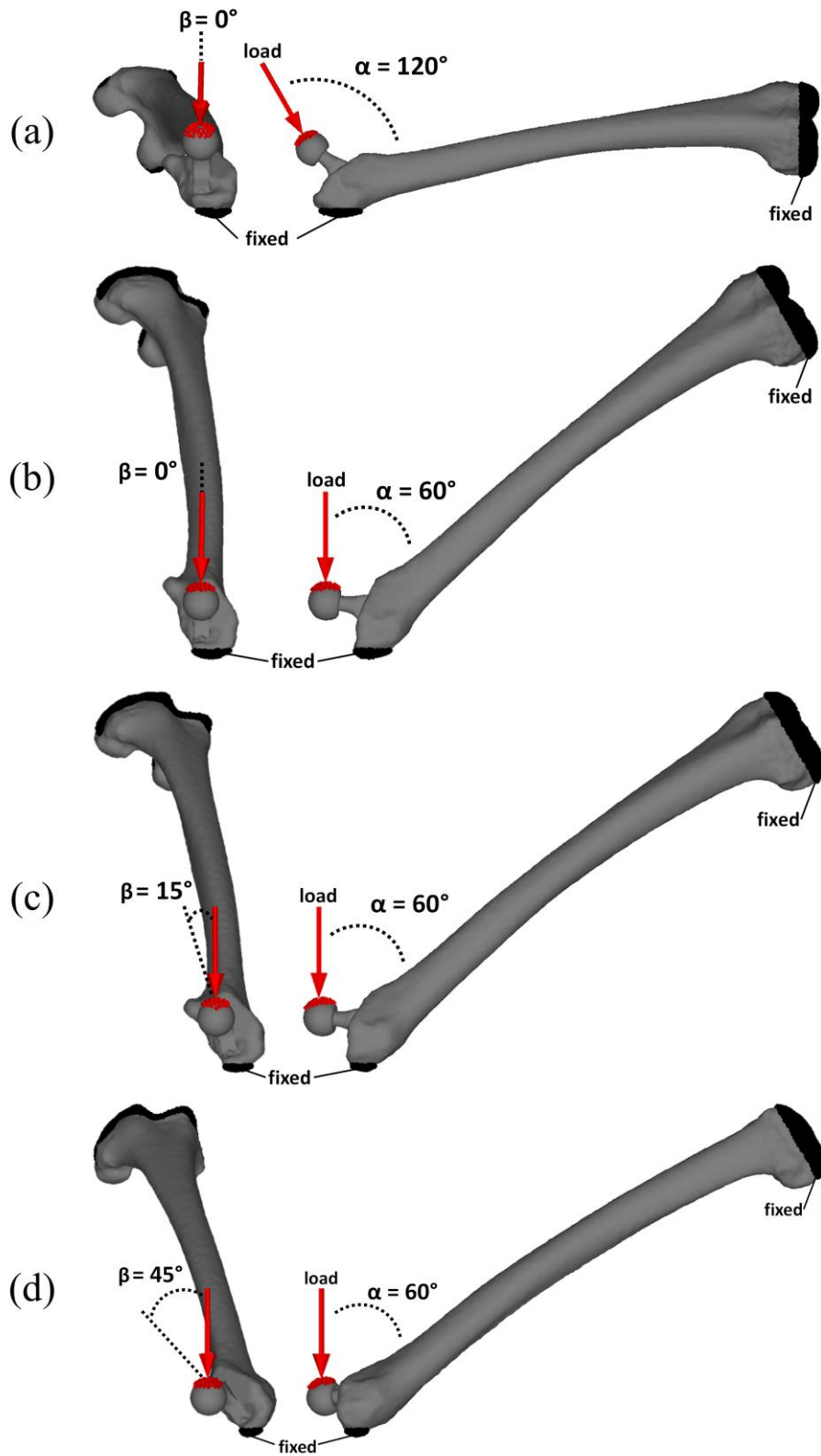


Figure 3. 2: Loading and boundary conditions (a) FC1, (b) FC2, (c) FC3 and (d) FC4

3.5 Mechanical theories and material properties

The tensile deformation of all the elements composing the femoral models was modeled using a linear elastic response, while the compressive deformation was modeled using a bi-linear elastic-plastic response. The stress-strain relationship for the linear-elastic behavior was characterized by Young's modulus and Poisson's ratio, while the plastic behavior was characterized by the yield stress and the work hardening coefficient. The Drucker-Prager yield condition was employed to determine the onset of yielding. [108]. Yielding was assumed to occur when the Drucker-Prager equivalent stress reaches the compressive yield stress, which is calculated based on Young's modulus and the corresponding BMD value of the solid element. The empirical formulae proposed by Keyak et al. [127] and Keller [128] were used to calculate Young's modulus and compressive yield stress, as presented in Table 3.3. Poisson's ratio and the work hardening coefficient of all solid elements were set at 0.4 and 0.05, respectively. Additionally, properties of each shell element were chosen to be equivalent to those of the adjacent solid element situated below it.

It was assumed that the maximum principal stress reaching the tensile strength (equal to 0.8 times the compressive yield stress) of a solid or shell element would result in tensile fracture [129], [130]. Conversely, compressive fracture of the element was assumed to occur when the minimum principal strain reached the fracture strain of -3,000 micro-strain [130], [131]. The criteria for failure are summarized in Table 3.4. It should be noted that in order to evaluate the femoral fracture of the outer cortical surface and compare fracture behavior between intact and THA models, aggregation of shell element failures is typically required. Thus, in this study, a critical condition was established based on the number of

shell element failures, with a limit of 300 failures chosen as the threshold. The analysis was terminated when the total number of shell element failures reached 300 under either tensile or compressive stress state. The stress-strain responses of titanium alloy and alumina ceramic were assumed to be linear elastic, with Young's modulus and Poisson's ratio chosen to be 114 GPa and 0.34 for titanium alloy and 370 GPa and 0.22 for alumina ceramic, respectively, based on previous studies [121].

Table 3. 3 Relationship between BMD and the material properties [127], [128]

| Bone mineral density (g/cm³) | Young's modulus (E) |
|--|----------------------------|
| $\rho = 0$ | 0.001 |
| $0 < \rho \leq 0.27$ | $33,900\rho^{2.20}$ |
| $0.27 < \rho \leq 0.6$ | $5307\rho + 469$ |
| $0.6 < \rho$ | $10,200\rho^{2.01}$ |
| Bone mineral density (g/cm³) | Yield stress (MPa) |
| $\rho < 0.317$ | $137\rho^{1.88}$ |
| $0.317 \leq \rho$ | $114\rho^{1.72}$ |

Table 3. 4: Failure criterions under tensile and compressive stress states

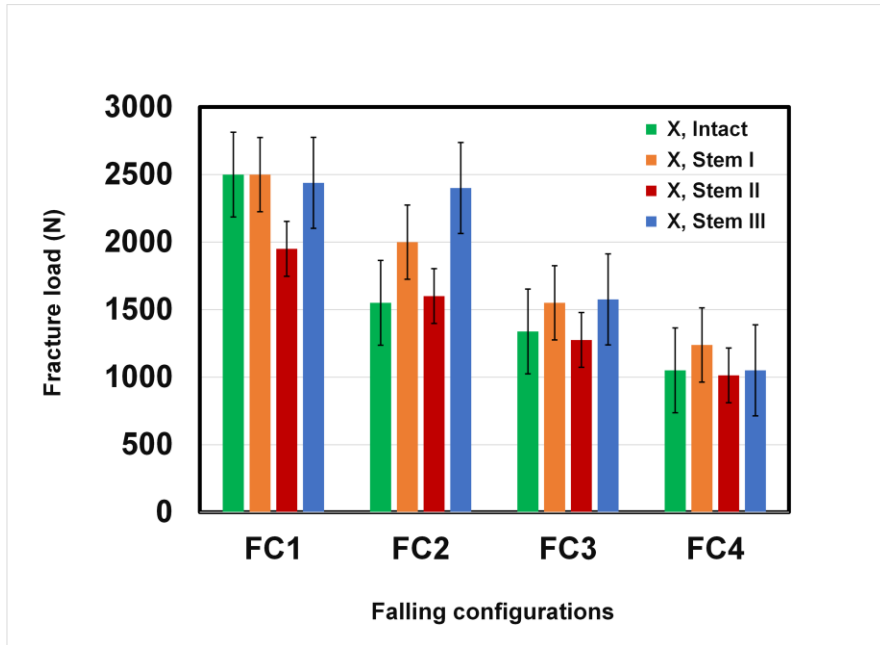
| Stress state | | Criterion |
|---------------------|-----------------------------|---------------------------|
| Tensile | Initiation of failure | $\sigma_p = 0.8 \sigma_r$ |
| Compressive | Transition to yielded state | $\sigma_D = \sigma_r$ |
| | Initiation of failure | $\epsilon_p = -3000$ |

σ_p = maximum principal stress
 σ_r = yield stress
 σ_D = Drucker-Prager equivalent stress
 ϵ_p = minimum principal strain

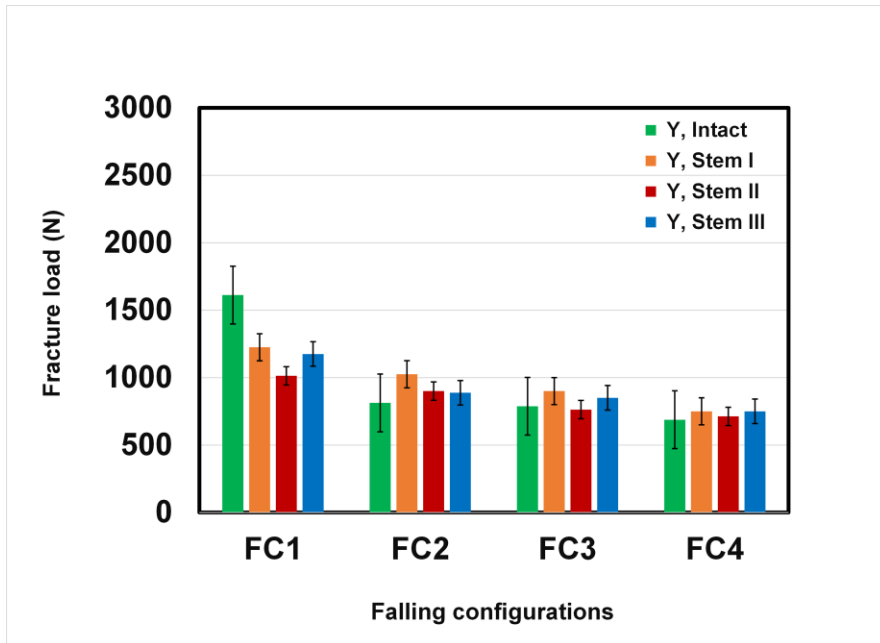
3.6 Results and Discussion

3.6.1 Fracture load under different falling configuration

Figure. 3.3 shows the fracture load of the intact and THA models of bone X and Y in all falling configurations. A decreasing trend was observed in the fracture load of each model of both bones when different loading and boundary conditions were applied, where FC1 has the highest fracture load compared to others. In addition, the design of the stem was observed to affect the fracture load of bone X, especially on FC1 and FC2, but the influence was negligible to bone Y. Despite having the same downward trend, bone X however, possessed a greater fracture load in all falling conditions compared to bone Y as a result of greater bone quality. It is important to note that the fracture load in every model was determined after the failure of 300 shell elements.



(a) Bone X



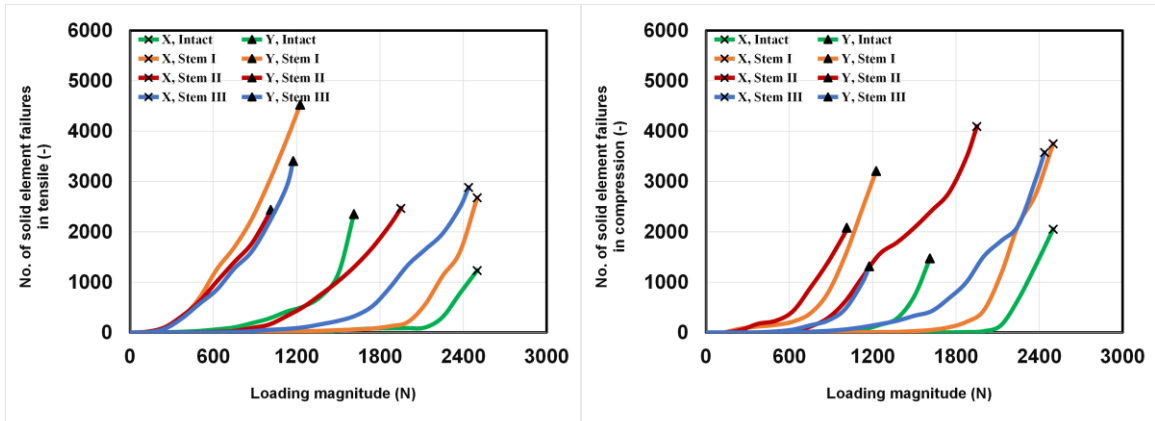
(b) Bone Y

Figure 3. 3: Fracture load of intact and THA models of bone X and Y in all falling configurations

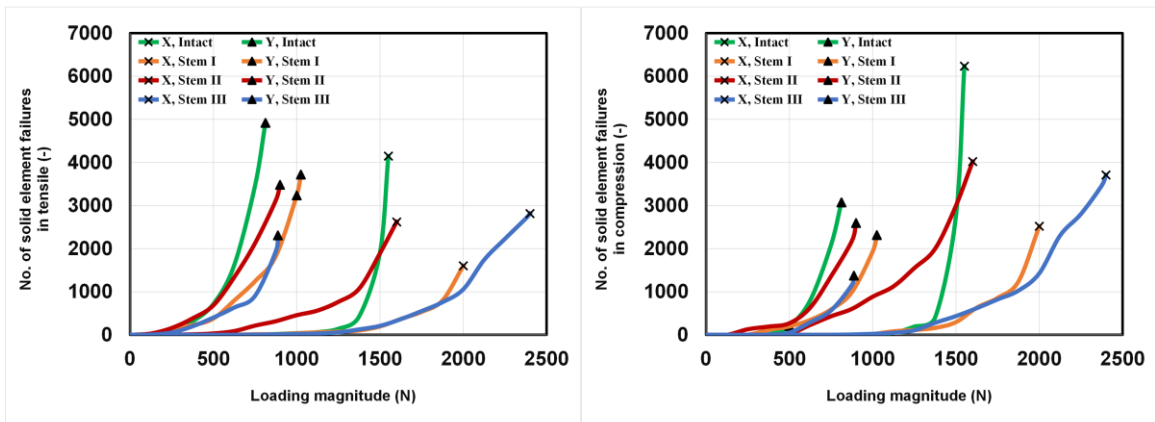
3.6.2 *Accumulation of element failures as bone micro-damage*

Figures 3.4 and 3.5 show the cumulative numbers of solid element failures in tensile and compressive state under all FCs. Upon fracture, it was observed that the compressive failures were dominant for bone X, while tensile failures were dominant for bone Y. The pattern was consistent in all FCs. The cumulative number of solid element failures tended to gradually increase until the final load level, and rapidly increase as it reached the final load in all FCs, and the pattern was observed to be similar in each model. On the other hand, the stem design was seen to affect the internal bone micro-damage, especially to bone X. For example, observation on FC1, FC2 and FC3 showed that bone X implanted with stem II tended to experience early bone damage compared to stem I and III, while bone X with stem III experience early damage in FC1 compared to stem I. For bone Y, the effect of stem design to the internal bone micro-damage were found to be small.

Figures 3.6 and 3.7 show the cumulative numbers of shell element failures. The finding was found to be similar as in the failures of solid element, where the tensile failures were dominant for bone Y, while compressive failures were dominant in bone X. The cumulative number of shell element failures tended to rapidly increase at the final load level, where similar pattern was observed in each model. Similar to solid element, the effect of stem design was found to affect the strength of bone X implanted with stem II, where the failure of shell elements was observed to appear at lower load levels compared to stem I and III, which can be observed in FC1, FC2 and FC3. This finding suggested that bone X with stem II had experienced early bone cracking compared to other models, before experiencing complete fracture. For bone Y, the effect of stem design to the mechanism of bone damage was found to be small, except for intact model under FC1.

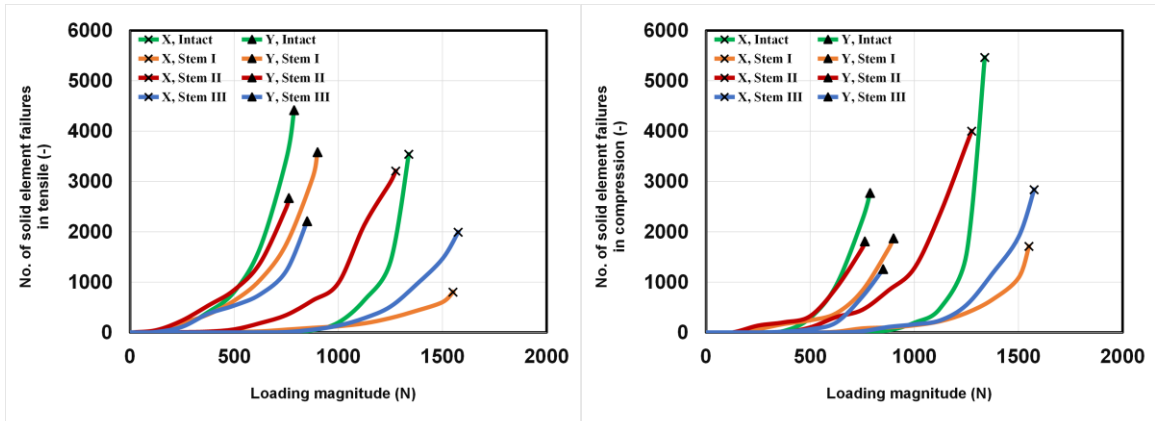


(a)

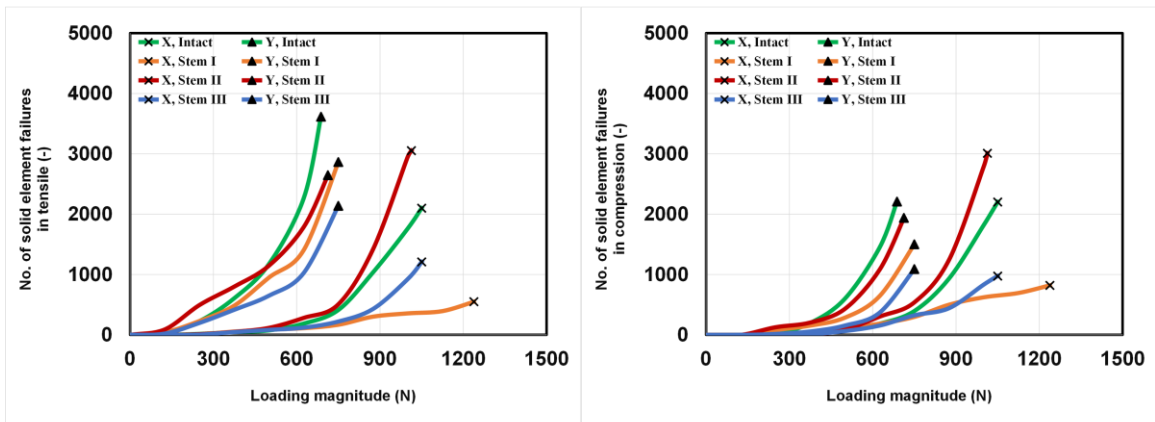


(b)

Figure 3. 4: Number of solid element failures in tensile (left) and compressive (right) under (a) FC1 and (b) FC2

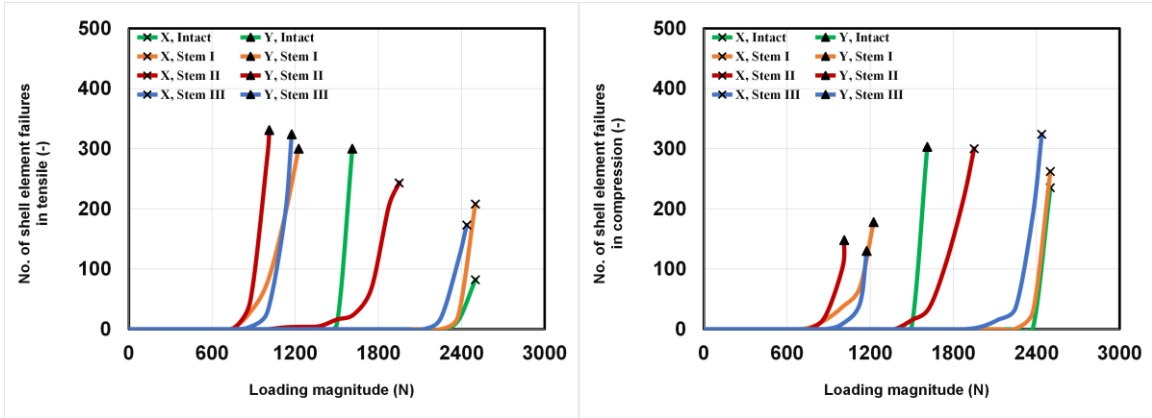


(a)

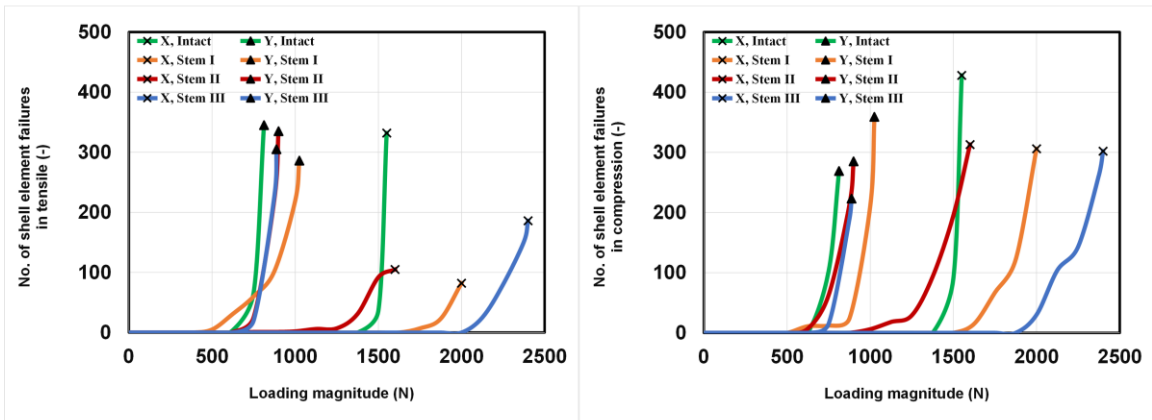


(b)

Figure 3. 5: Number of solid element failures in tensile (left) and compressive (right) under (a) FC3 and (b) FC4

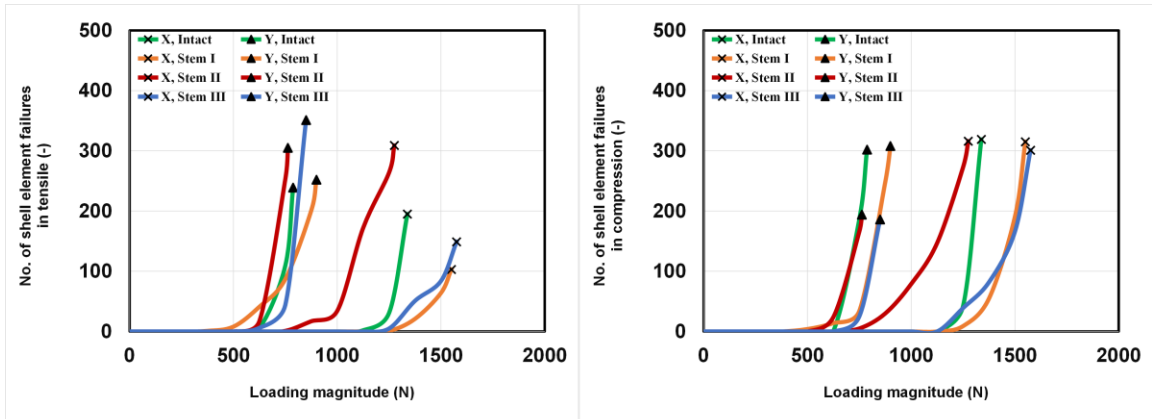


(a)

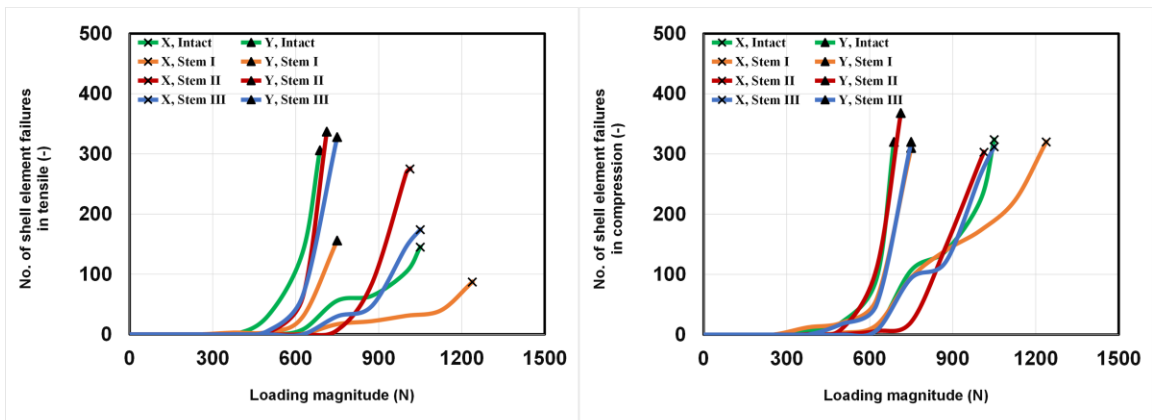


(b)

Figure 3. 6: Number of shell element failures in tensile (left) and compressive (right) under (a) FC1 and (b) FC2



(a)



(b)

Figure 3. 7: Number of shell element failures in tensile (left) and compressive (right)

under (a) FC3 and (b) FC4

Table 3.5 summarizes the total number of solid and shell element failures at final load level (bone fracture) of THA models. Based on the data, bone X implanted with stem I, stem II, and stem III shared an almost similar number of solid element failures in FC1. As the configuration shifted towards the posterolateral side of the femur, the element failures between each model showed a gap. This can be observed based on the calculation of percentage difference between the highest and lowest number of element failures from those models as shown in Eqn. (1). For example, the percentage difference of solid element failures of bone X in FC 1 was 2.03 %, but the numbers were increasing as the configuration change to FC 2, FC 3 and FC 4 with percentage difference of 46.84 %, 96.64 % and 126.23 %, respectively. This phenomenon may be due to the effect of stem design. Additionally, it can be noticed that the lowest number of solid element failures in all FCs was obtained when bone X implanted with stem I.

$$\frac{|V_1 - V_2|}{\frac{(V_1 + V_2)}{2}} \times 100 \quad (1)$$

This phenomenon might be correlated with the design of stem I and the variations in the degree of falling from the lateral to posterolateral side of the bone. There are two possible reasons to consider. First, to relate with the falling configurations that do not involve any rotational effect on the bone-stem interface, i.e., FC1 and FC2. It was noted that stem I has been designed with a larger size on its proximal region (shoulder of the stem). This design allows a larger bone area to be accommodated by the implant stem. Consequently, the number of bone elements within the shoulder region of bone X, when implanted with stem I, may be significantly lower than in the other two models designed with a smaller shoulder size. As a result, the number of bone element failures in bone X

implanted with stem I was smaller compared to stem II and stem III. In other words, when a larger bone area is taken up by the stem, it subsequently reduces the number of bone elements, hence influencing the number of bone element failures.

Secondly, in the case of falling configurations that involve a rotational effect on the bone-stem interface, i.e., FC3 and FC4, high values of bone density at the proximal region of bone X may enable a strong rotational stability to be obtained from the design of stem I. The rectangular cross-section with four corners embedded into the endosteal bone could be fully utilized since the implant is surrounded by bones with higher strength. Additionally, it can be observed that the percentage difference of element failures shows an increasing gap between stem I and the other two stems as the falling configuration changes from FC1 to FC4, which may support the relationship between the stem design and internal bone damage

However, for the case of bone Y, the solid element failures obtained in the model showed almost no correlation between the design of the THA stem and the falling configuration. For example, in the condition of falling onto the lateral direction, stem II has the lowest number of total element failures in FC1 with 4518 element failures, but highest in FC2 with 6077 element failures. Another example, in the case of falling onto the posterolateral direction, bone Y with stem I has the highest number of element failures in FC3 (5452 element failures), but not in FC4. Since the stem design and element failures showed no correlation, thus, the possible reason might be due to the weaker trabecular bones of bone Y at the proximal region of the femur, where the THA implant is introduced. The stiffer materials from the implant would easily damage the internal bone elements in

any configuration since the bone elements that surrounded the implant surfaces were developed from the bone with low-density values.

The number of shell element failures was also tabulated in Table 3.5. It was noted that the design of the stem had influenced the fracture load of the bone as shown in Figure 3.3, however, the fracture severity might be important to discuss as well. Therefore, the number of shell element failures here suggests the severity of bone fracture under a different THA stem design. There are many reasons which may influence the severity of bone fracture especially when involves different types of THA stem. Bone quality, stem design, applied forces, and different loading and boundary conditions may become the contributing factors as presented in this study. However, in comparison to the other stems, the fracture was observed to be more severe on both bones when implanted with stem II. From Figure 3.3, it can be observed that the fracture load of bone X and bone Y implanted with stem II consistently exhibited lower values than the other models but experiencing a comparable number of shell element failures. The post-operative geometry of the bone to suit the design of stem II is thought to be the reason for this phenomenon. Based on the illustration of THA model shown in Figure 3.1, it is worth noting that the bone model implanted with stem II had an excessive bone removal at the proximal area in order to suit the design of stem II, which has a longer neck length. Without excessive bone removal, the stem will subside into the bone. Aside from giving insight to the THA implant designer, this finding may be useful to the current surgical context, in which highlighting the importance of femoral osteotomy as it can influence the severity of bone fractures in traumatic incidents.

Table 3. 5: Data summarization of element failures under all FCs

| <i>Configuration: FC1</i> | | | |
|---------------------------|-----------|--|--|
| Bone | THA model | total number of solid element failures | total number of shell element failures |
| X | stem I | 6426 | 470 |
| | stem II | 6558 | 543 |
| | stem III | 6457 | 497 |
| Percentage difference (%) | | 2.03 | 14.41 |
| Y | stem I | 7731 | 478 |
| | stem II | 4518 | 479 |
| | stem III | 4721 | 454 |
| Percentage difference (%) | | 52.46 | 5.35 |
| <i>Configuration: FC2</i> | | | |
| X | stem I | 4120 | 388 |
| | stem II | 6640 | 418 |
| | stem III | 6522 | 488 |
| Percentage difference (%) | | 46.84 | 22.83 |
| Y | stem I | 6032 | 645 |
| | stem II | 6077 | 620 |
| | stem III | 3683 | 528 |
| Percentage difference (%) | | 49.05 | 19.94 |
| <i>Configuration: FC3</i> | | | |
| X | stem I | 2511 | 418 |
| | stem II | 7207 | 625 |
| | stem III | 4830 | 450 |
| Percentage difference (%) | | 96.64 | 39.69 |
| Y | stem I | 5452 | 560 |
| | stem II | 4480 | 499 |
| | stem III | 3469 | 537 |
| Percentage difference (%) | | 44.45 | 11.52 |
| <i>Configuration: FC4</i> | | | |
| X | stem I | 1371 | 407 |
| | stem II | 6063 | 578 |
| | stem III | 2184 | 486 |
| Percentage difference (%) | | 126.23 | 34.72 |
| Y | stem I | 4364 | 466 |
| | stem II | 4584 | 705 |
| | stem III | 3229 | 648 |
| Percentage difference (%) | | 34.68 | 40.81 |

3.6.3 *Distribution of solid and shell element failures*

The distribution of solid element failures within the bone and stem interface at final load level was evaluated using the Gruen zone system. The extraction size of zones 1, 2, 4, 6, and 7 was similar in all stems, but the extraction size of zones 3 and 5 was based on the length of the stem. The results were presented in Figures 3.8 and 3.9.

Figure 3.8 shows the distribution of solid element failures for bone X implanted with stem I, II and III, under all FCs. Most of the damaged elements were seen to be concentrated in zone 1 and zone 7. The pattern was seen to be consistent in every stem model and FCs. In zone 1, the damaged elements were dominated by the compressive failure elements labeled in red colour whereas, in zone 7, the tensile failure elements were dominant, labeled in white colour. It was observed that the number of element failures is higher in zone 1 compared to zone 7, results in falling onto the trochanteric region of the femur.

A different scenario was observed in bone Y. Based on Figure 3.9, it can be seen that the damaged elements were scattered throughout the zones, except for zone 4. The pattern was seen to be consistent in all of the THA models and FCs. At the proximal region, the element failures were accumulated mostly at zone 1 compared to zone 7. In the middle region, element failures in zone 6 were slightly higher compared to zone 2, and at the distal region, element failures in zone 5 were slightly higher than zone 3. This pattern is consistent at THA models of bone Y in all FCs. Factors of poor bone quality and the effect of stem bending may influence the results. Nonetheless, greater bone damage at zone 1, was the results of falling onto the trochanteric region at the lateral side of the bone.

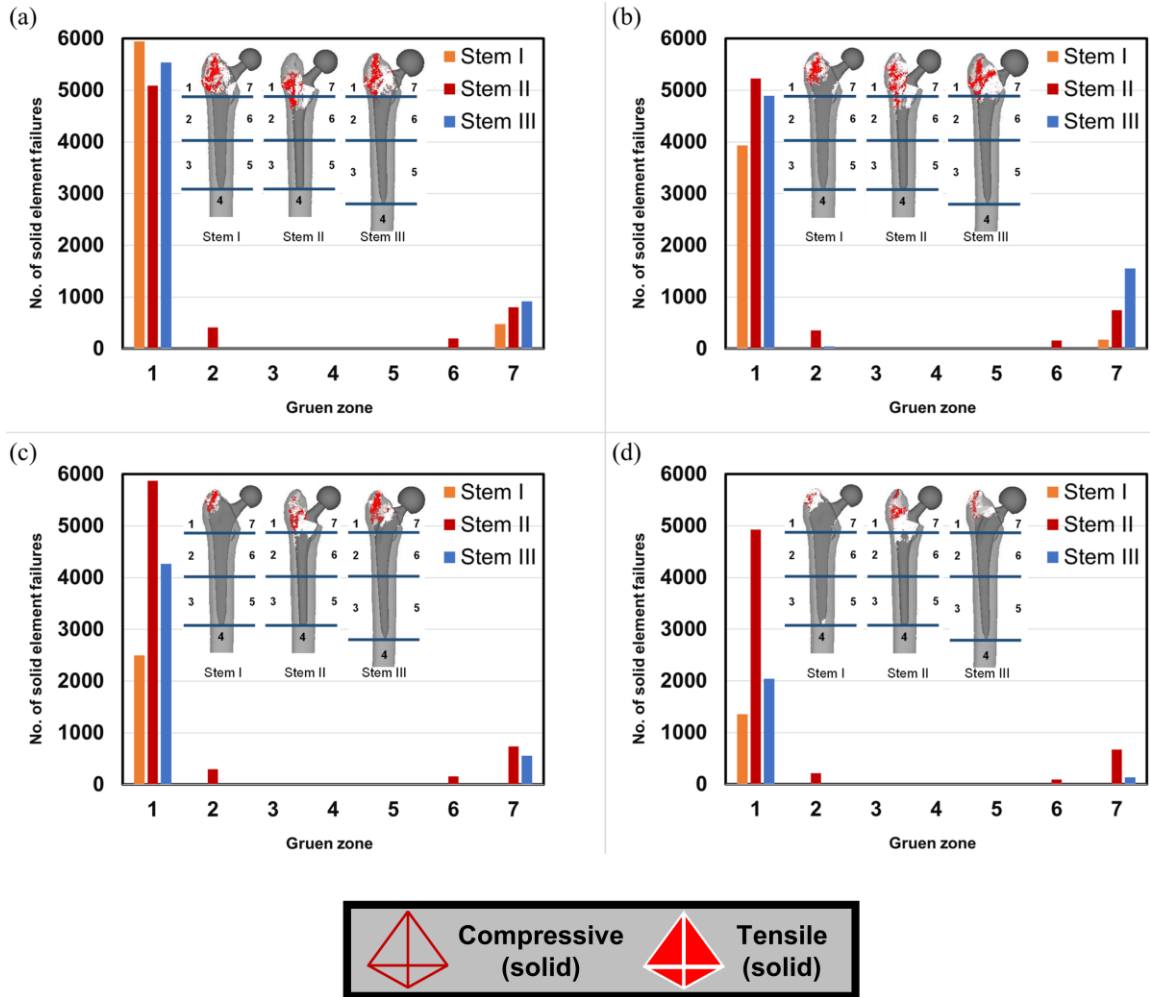


Figure 3. 8: Distribution of solid element failures in bone X based on Gruen zone under

(a) FC1, (b) FC2, (c) FC3 and (d) FC4

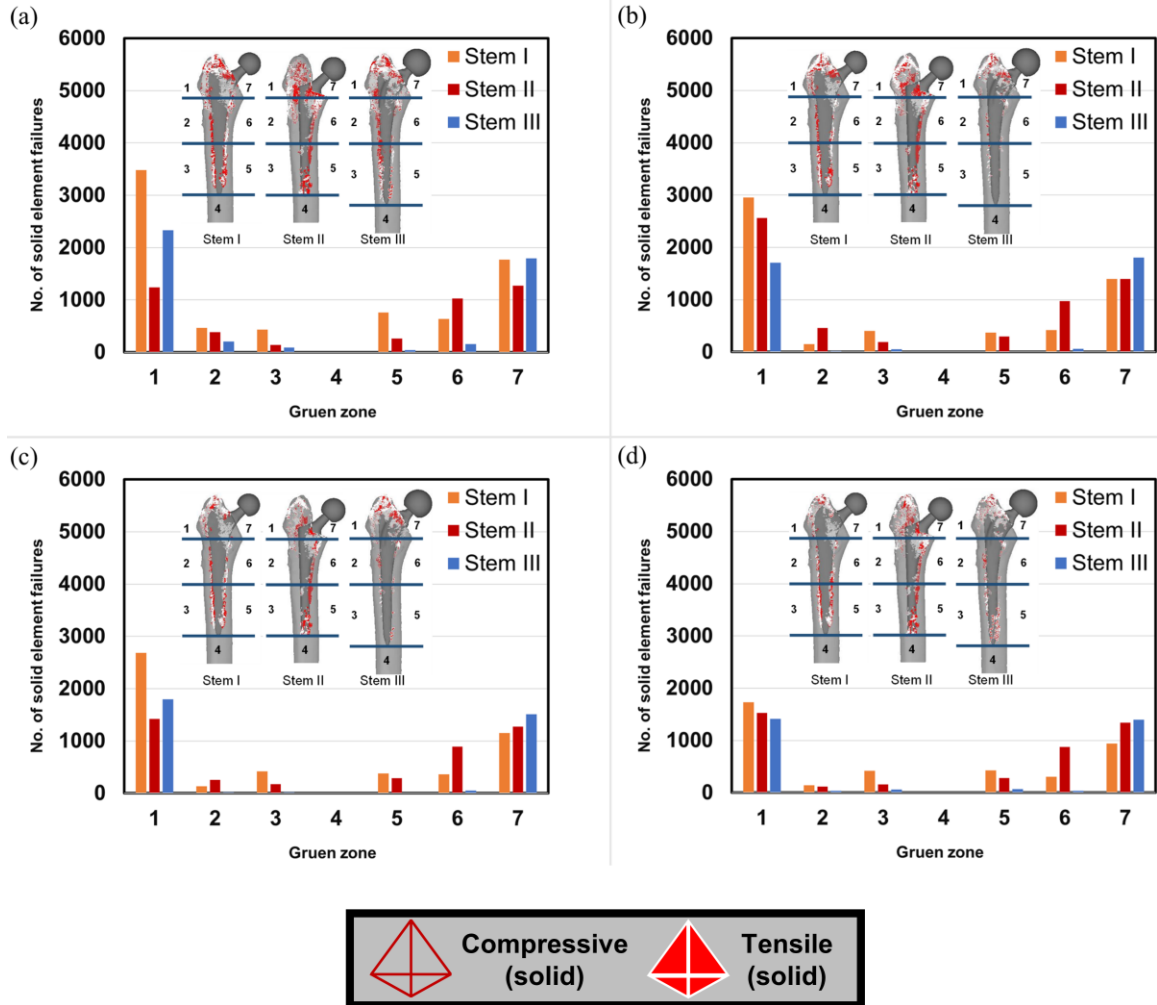


Figure 3. 9: Distribution of solid element failures in bone Y based on Gruen zone under (a) FC1, (b) FC2, (c) FC3 and (d) FC4

Distribution of shell element failures in intact and THA models of both bones were shown in Figure 3.10 – Figure 3.13, along with the distribution pattern of solid element failures at the damage initiation and fracture stages. It was found that the location of shell element failures was similar in each model under all FCs, which located at the trochanteric region of the femur, except for intact model under FC1. In FC1, the distribution of shell failures occurred at the femoral head and neck region.

(a) Intact

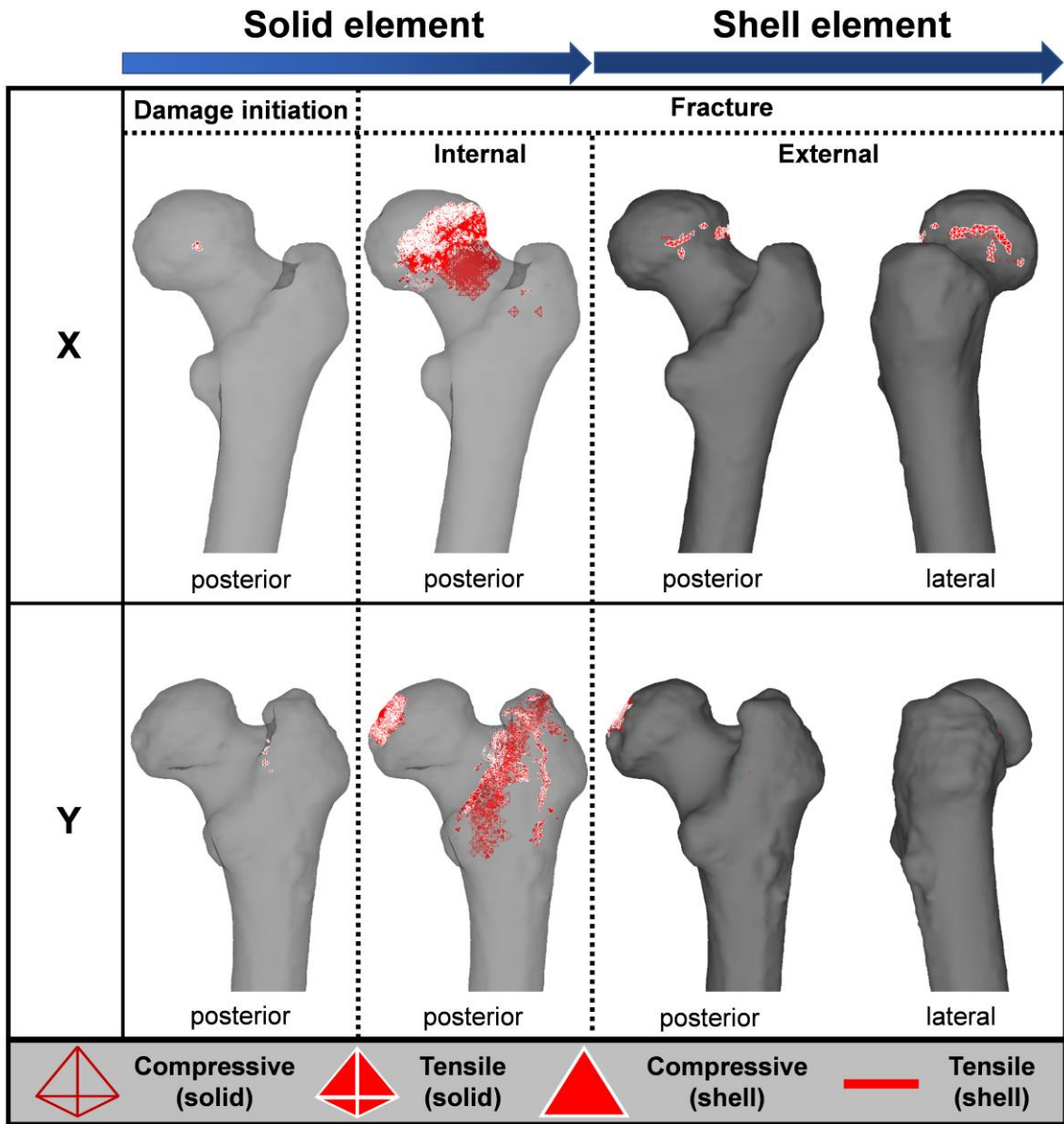


Figure 3. 10: Distribution of solid and shell element failures under FC1: (a) intact, (b) stem I, (c) stem II and (d) stem III

(b) Stem I

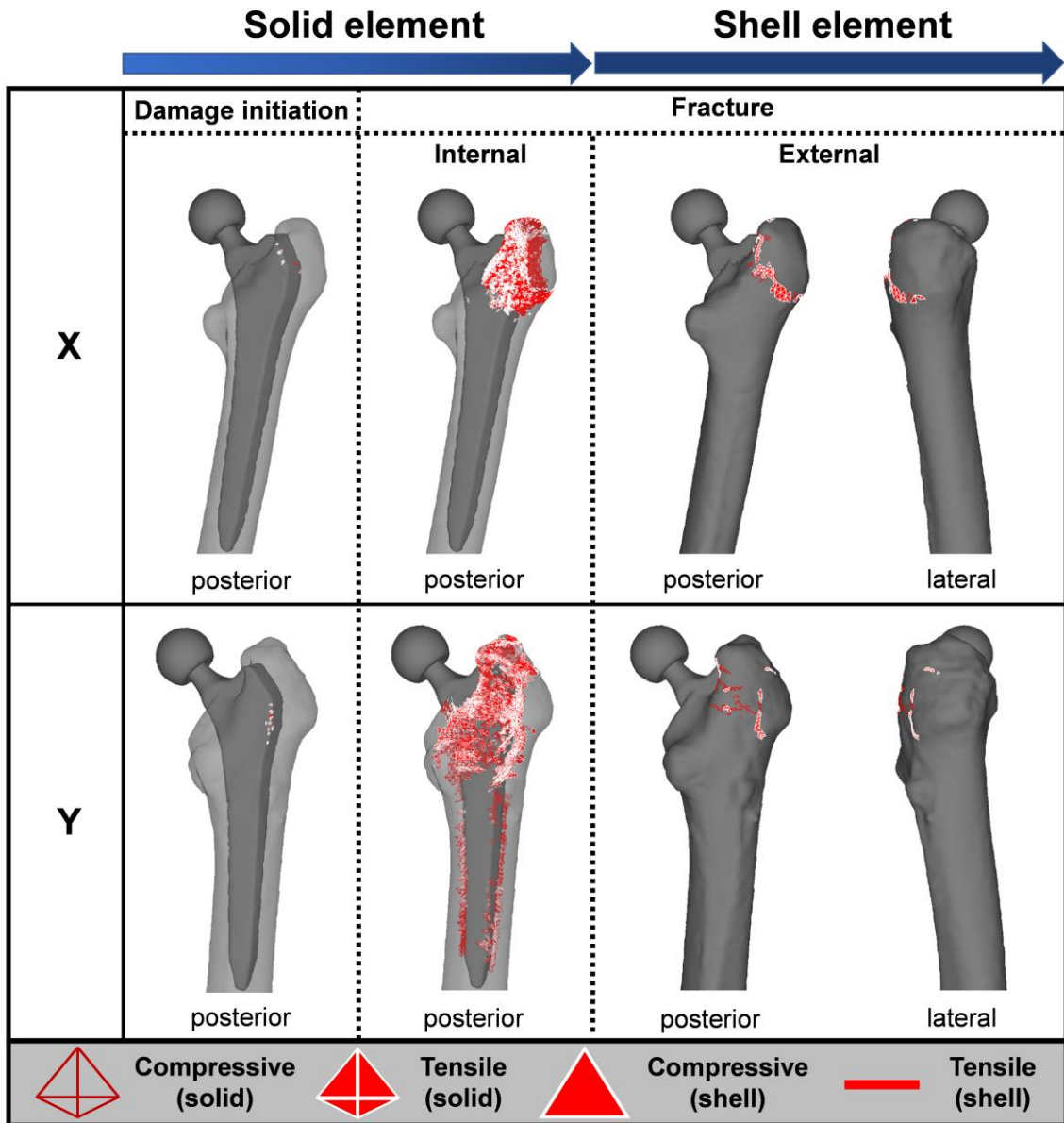


Figure 3.10 (continued)

(c) Stem II

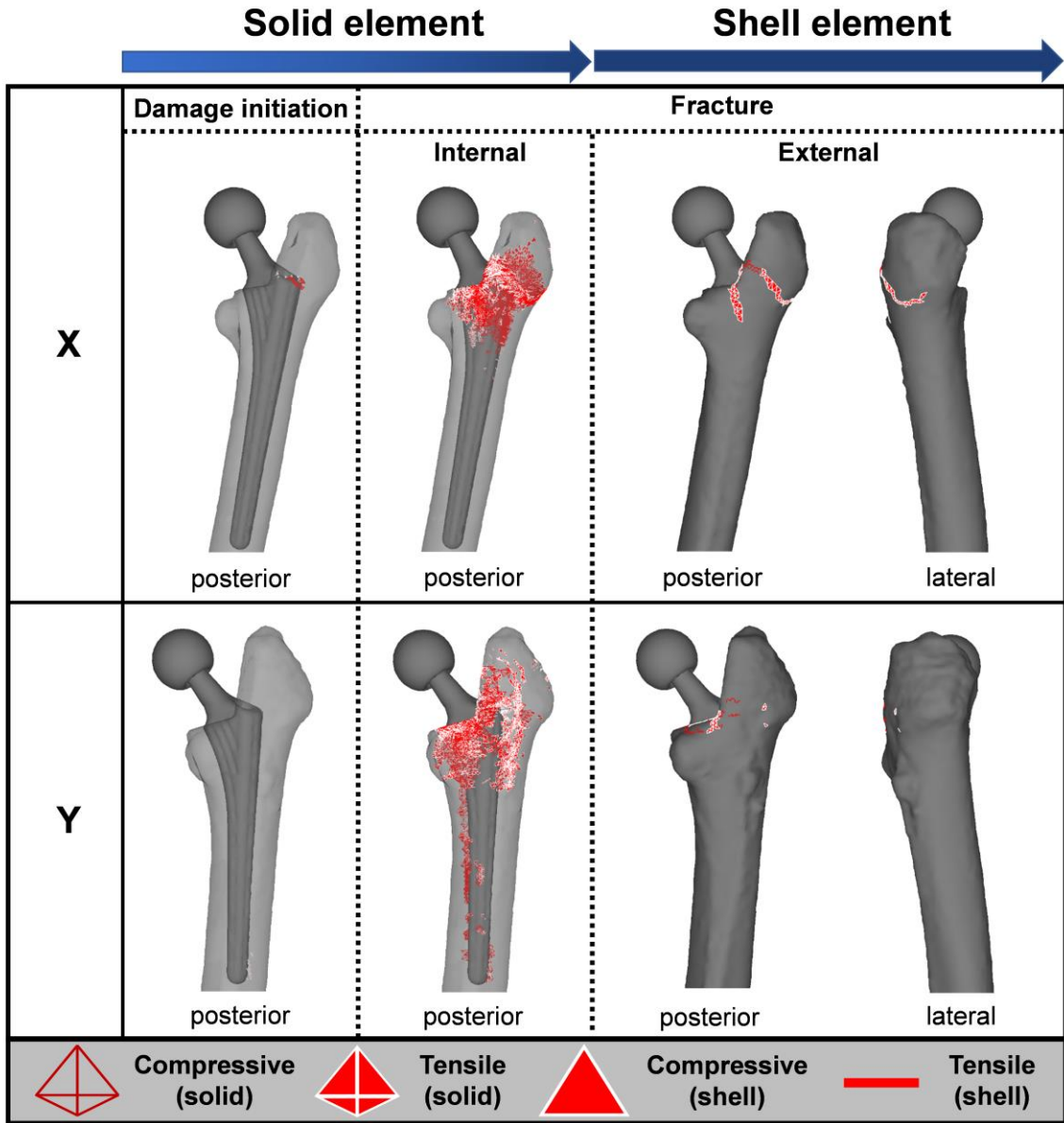


Figure 3.10 (continued)

(d) Stem III

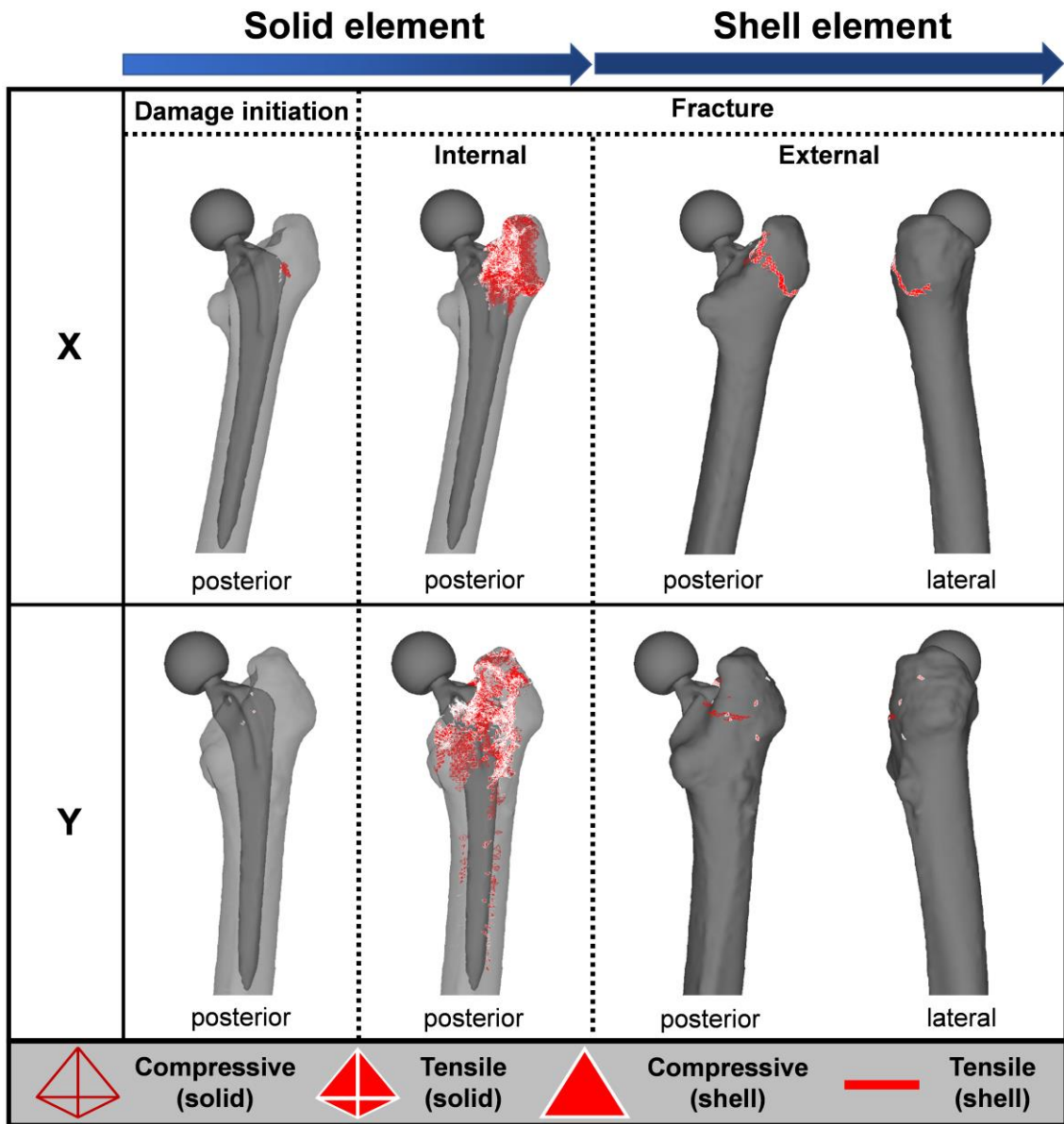


Figure 3.10 (continued)

(a) Intact

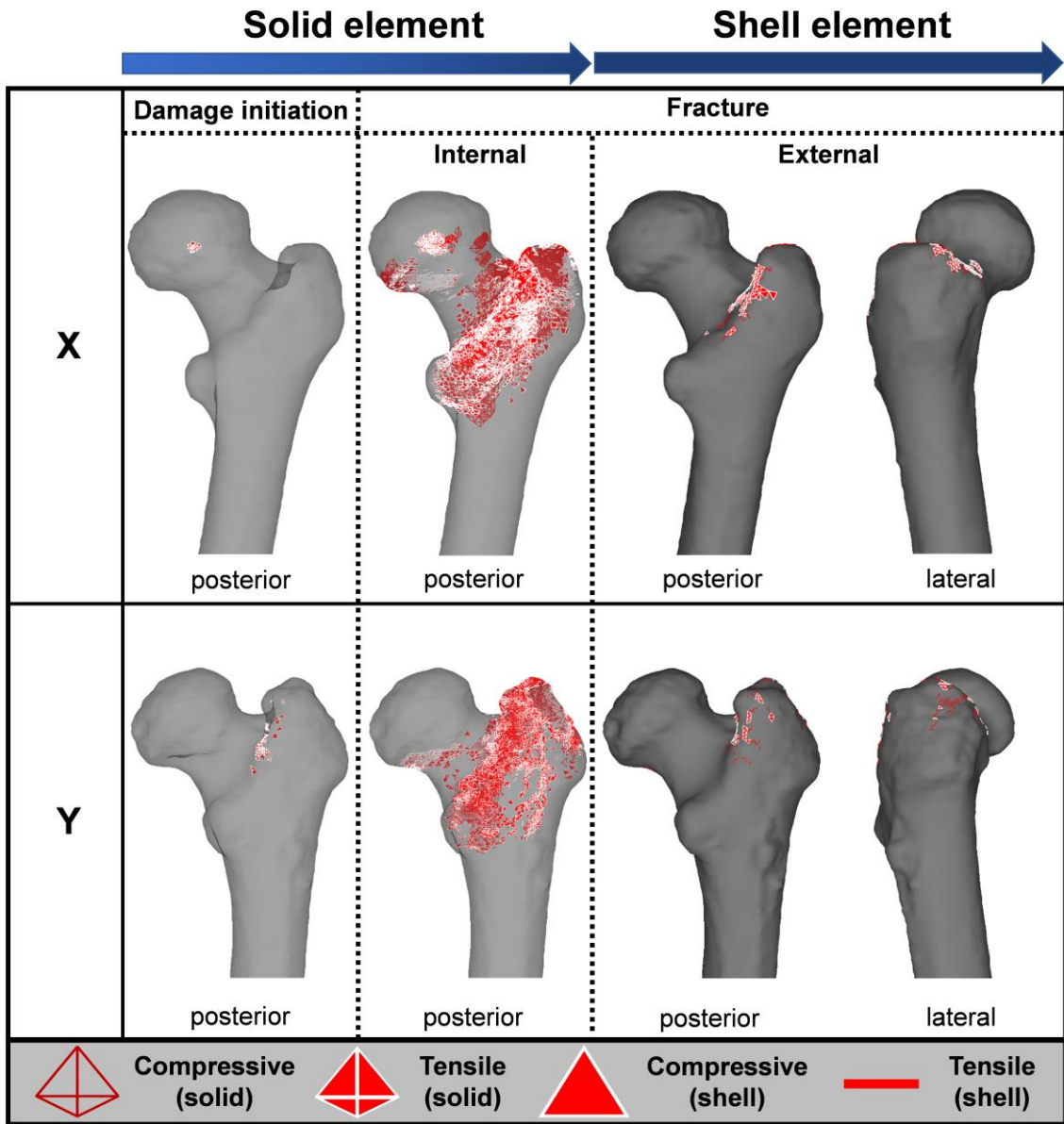


Figure 3. 11: Distribution of solid and shell element failures under FC2: (a) intact, (b) stem I, (c) stem II and (d) stem III

(b) Stem I

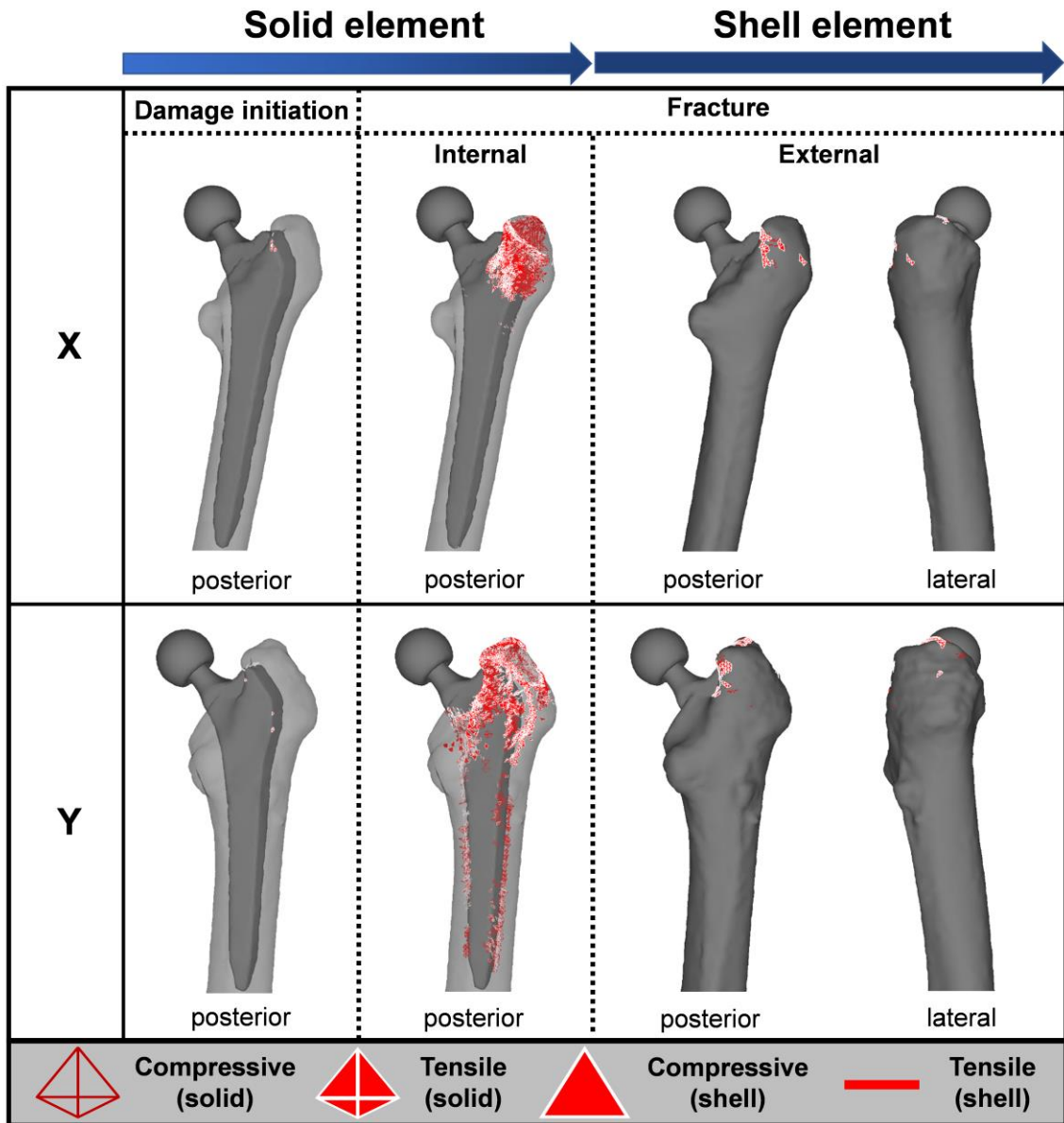


Figure 3.11 (continued)

(c) Stem II

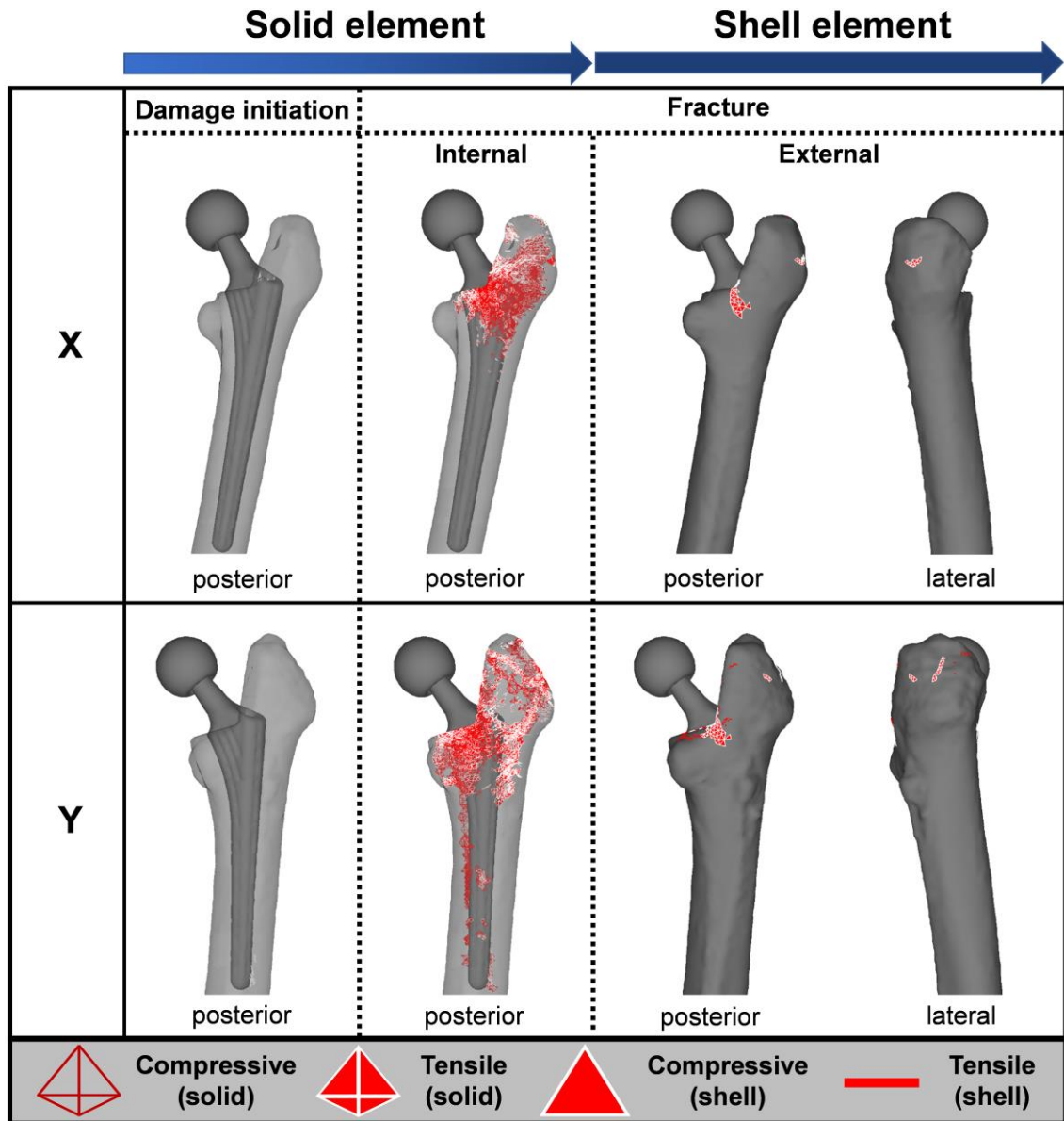


Figure 3.11 (continued)

(d) Stem III

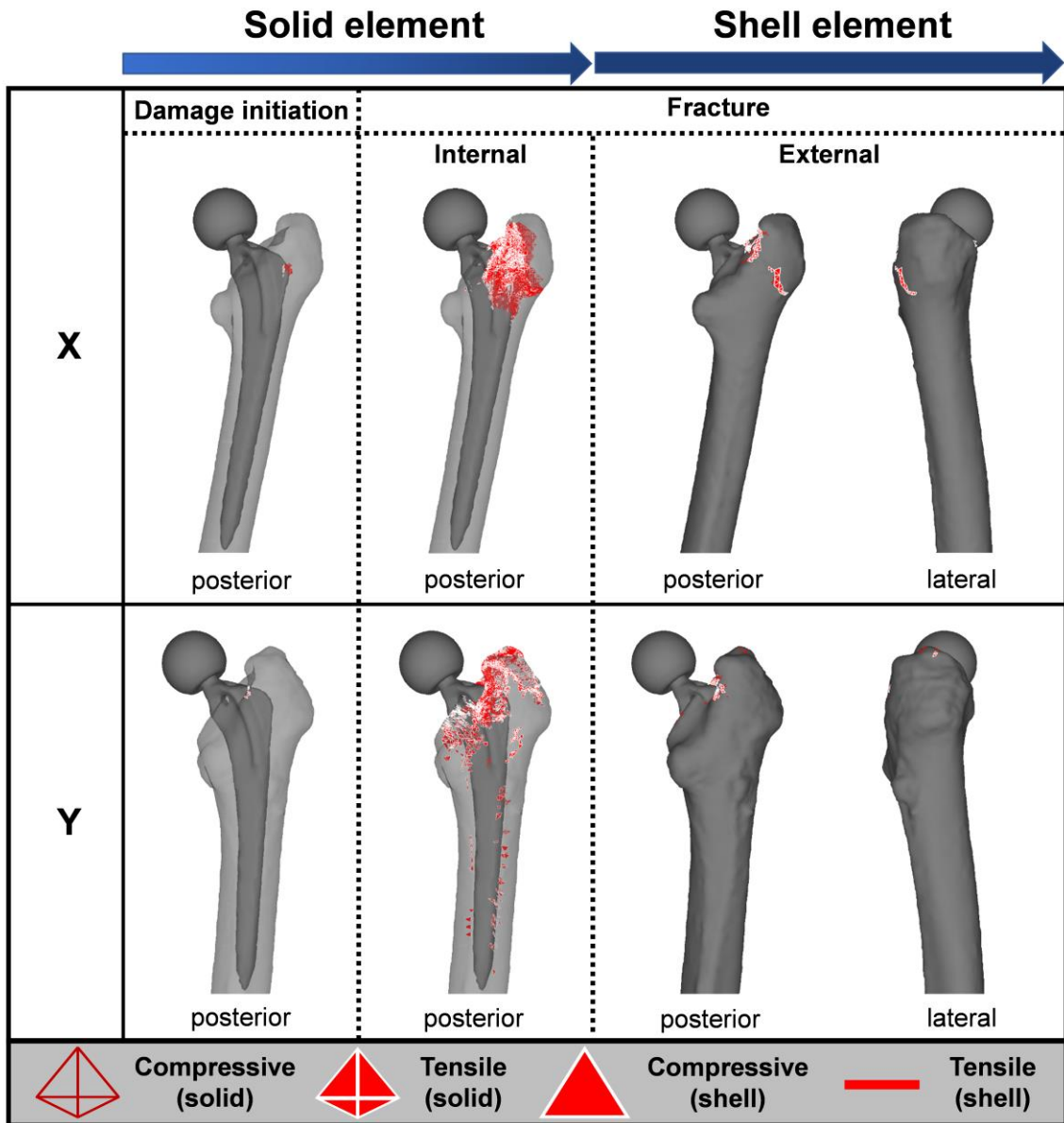


Figure 3.11 (continued)

(a) Intact

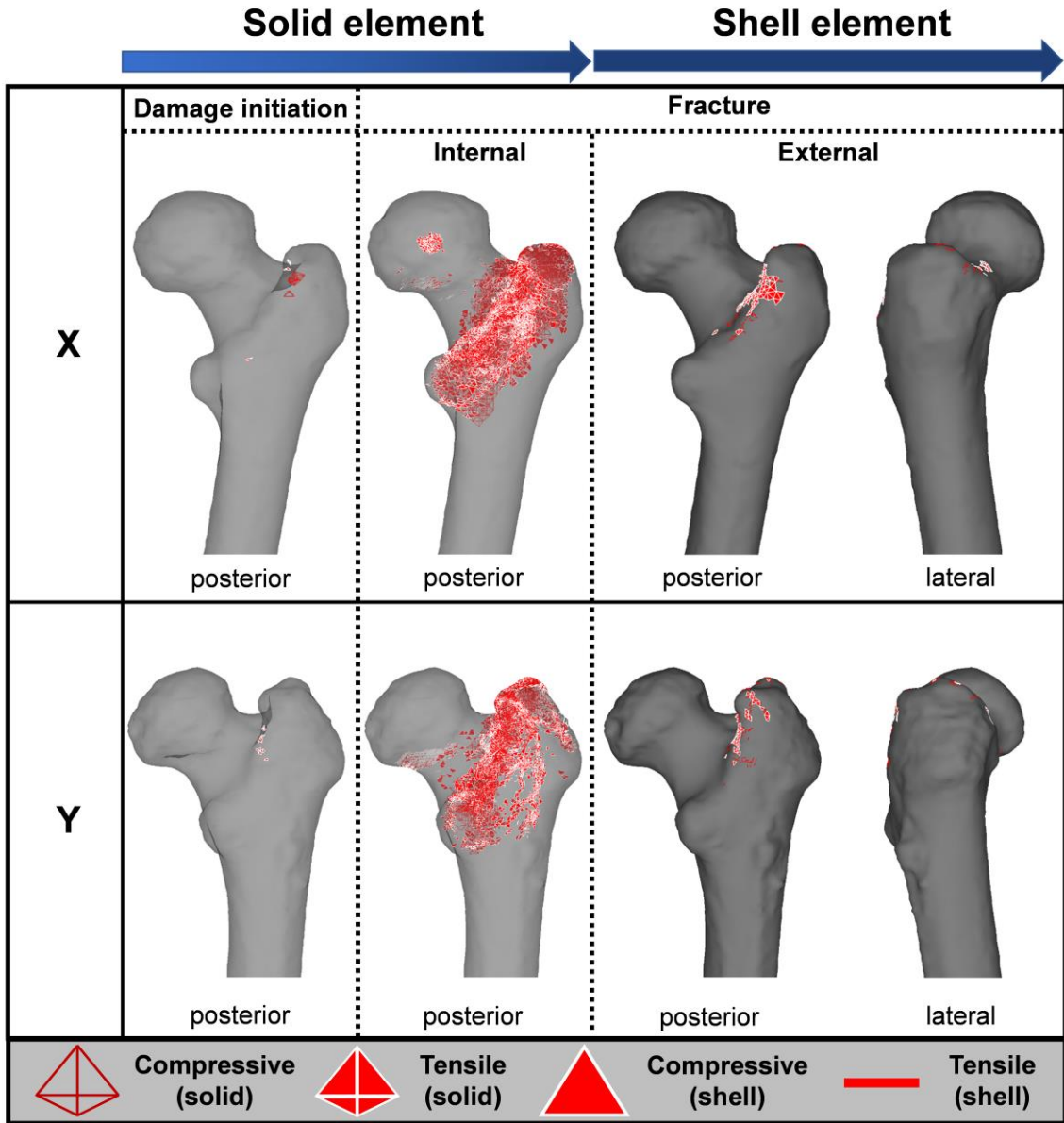


Figure 3. 12: Distribution of solid and shell element failures under FC3: (a) intact, (b) stem I, (c) stem II and (d) stem III

(b) Stem I

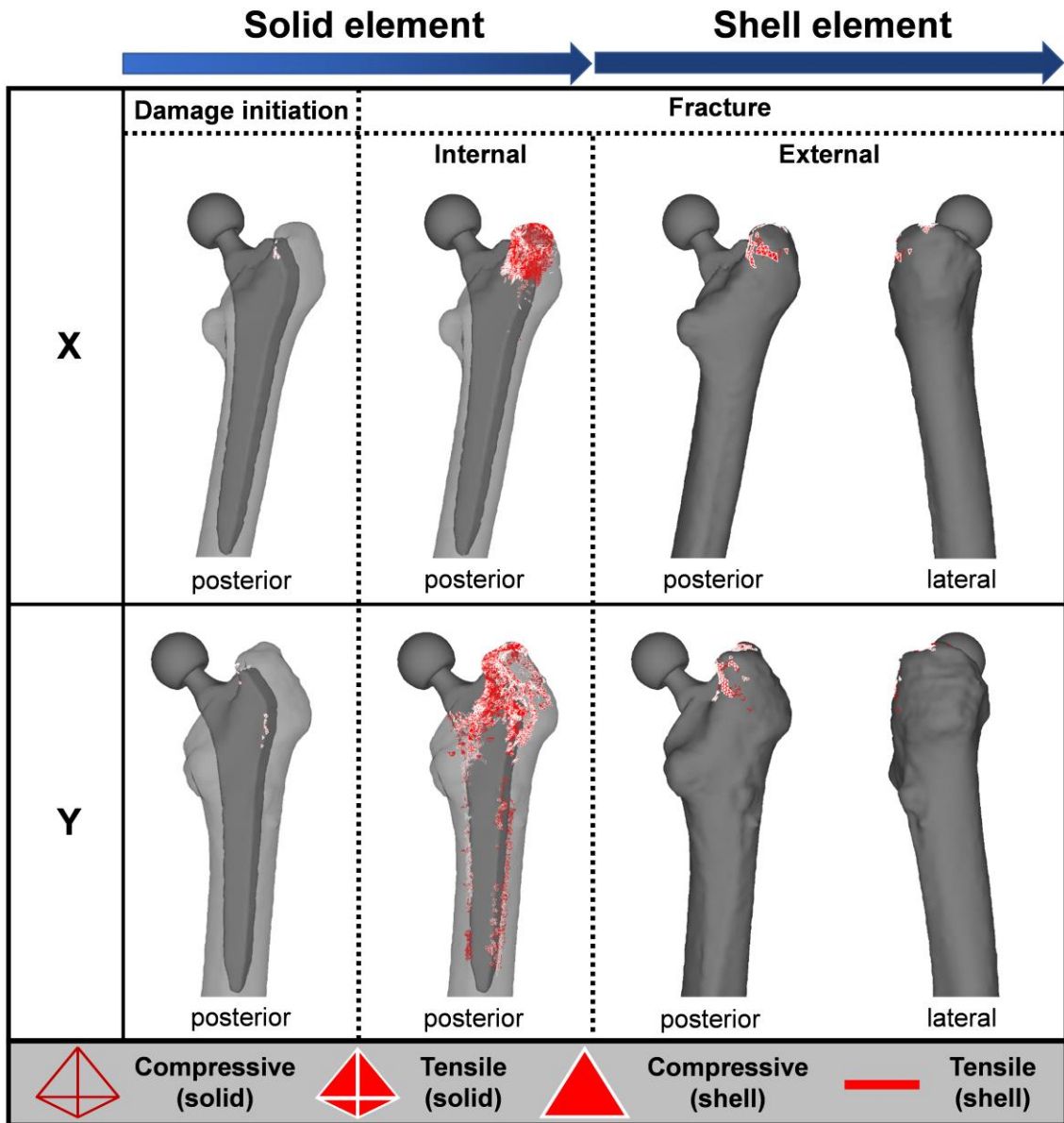


Figure 3.12 (continued)

(c) Stem II

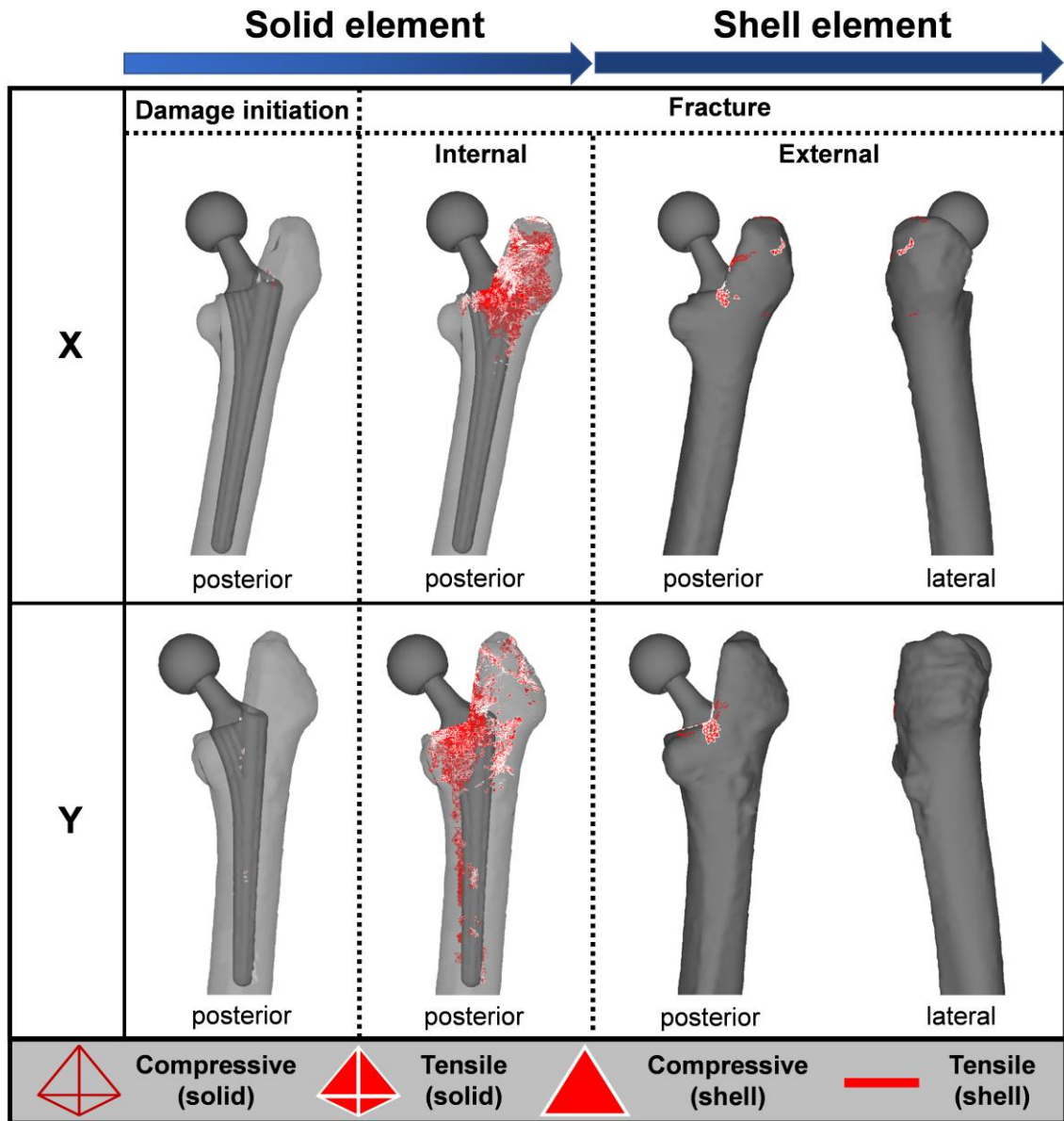


Figure 3.12 (continued)

(d) Stem III

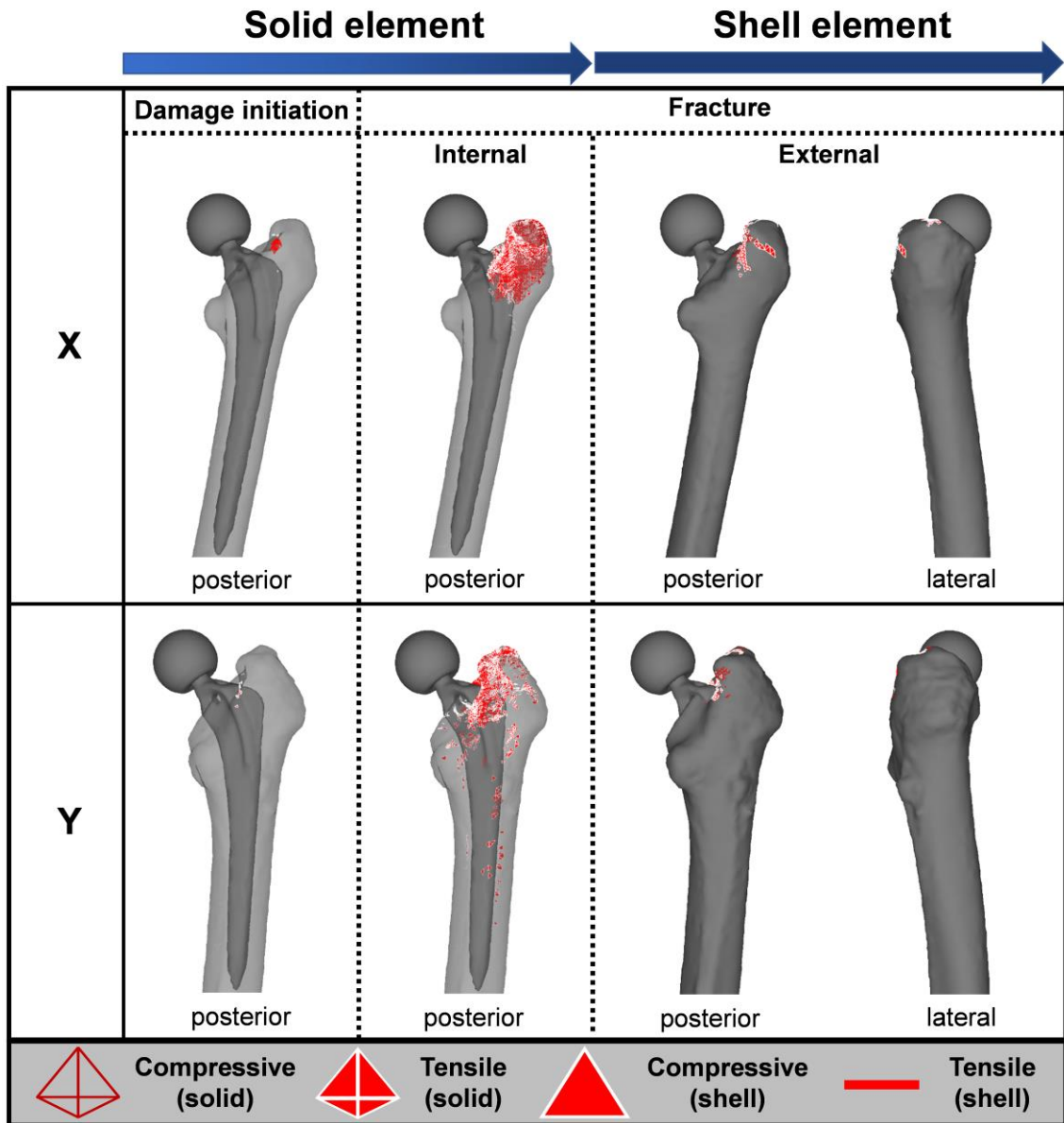


Figure 3.12 (continued)

(a) Intact

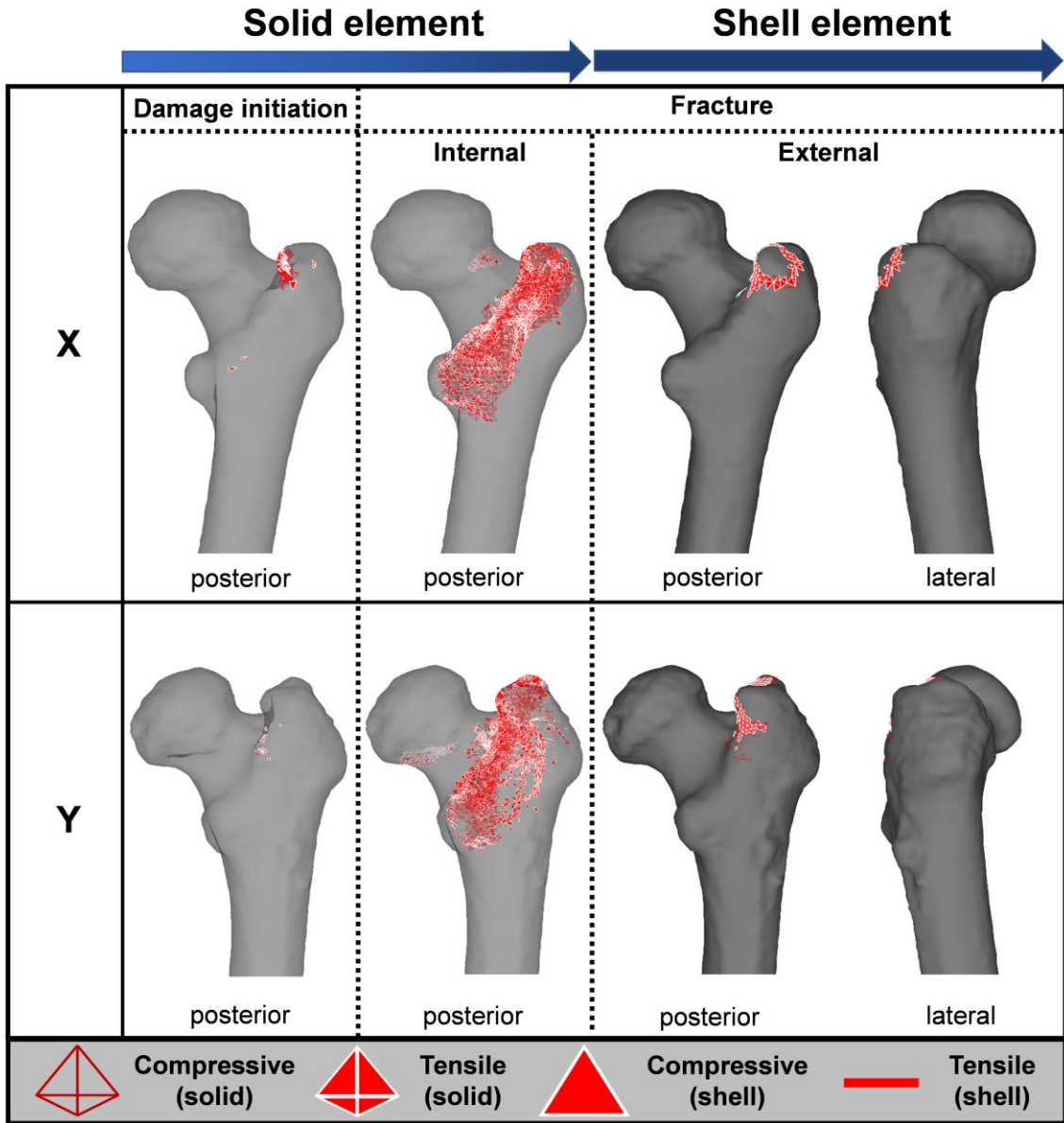


Figure 3. 13: Distribution of solid and shell element failures under FC4: (a) intact, (b) stem I, (c) stem II and (d) stem III

(b) Stem I

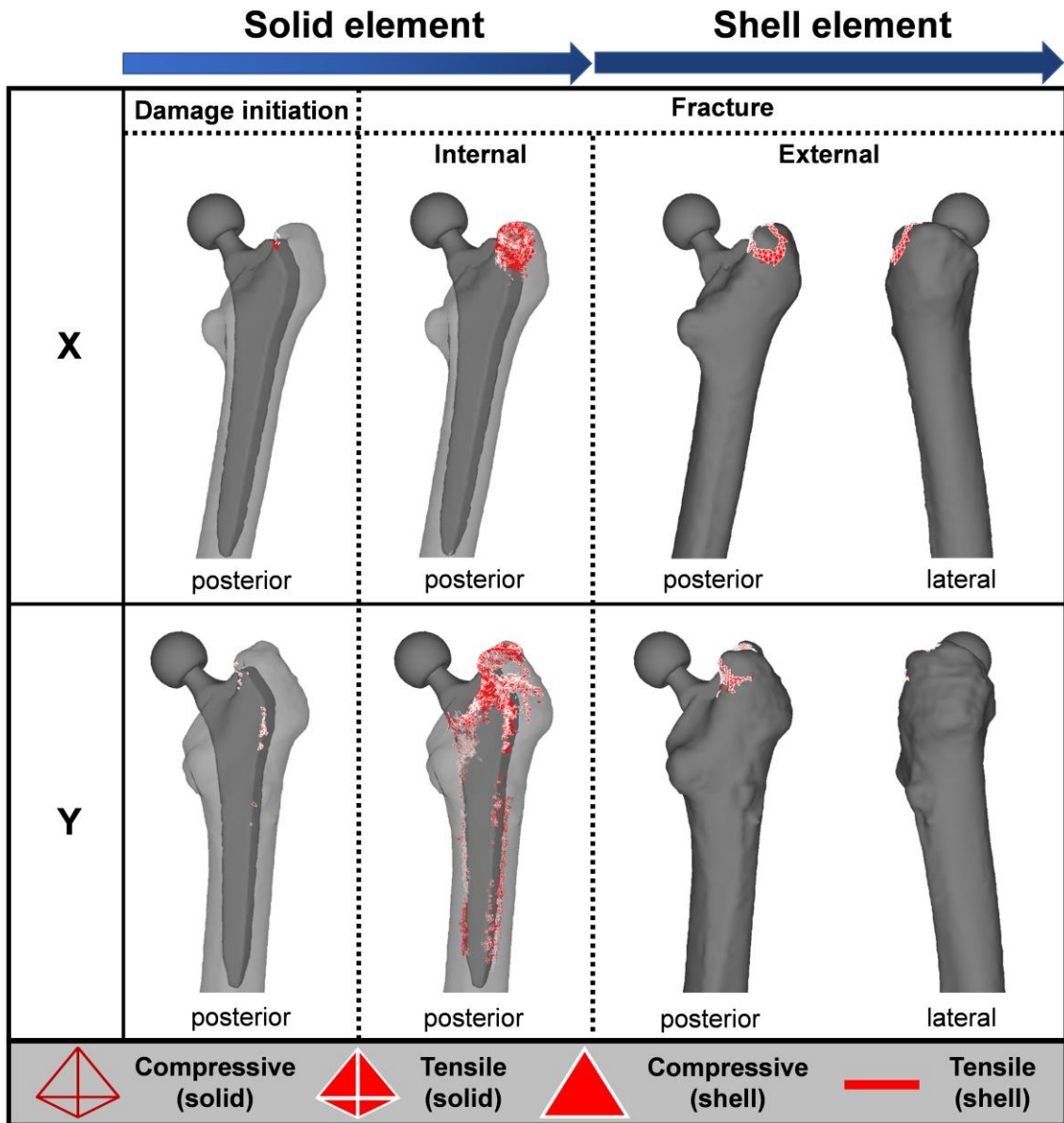


Figure 3.13 (continued)

(c) Stem II

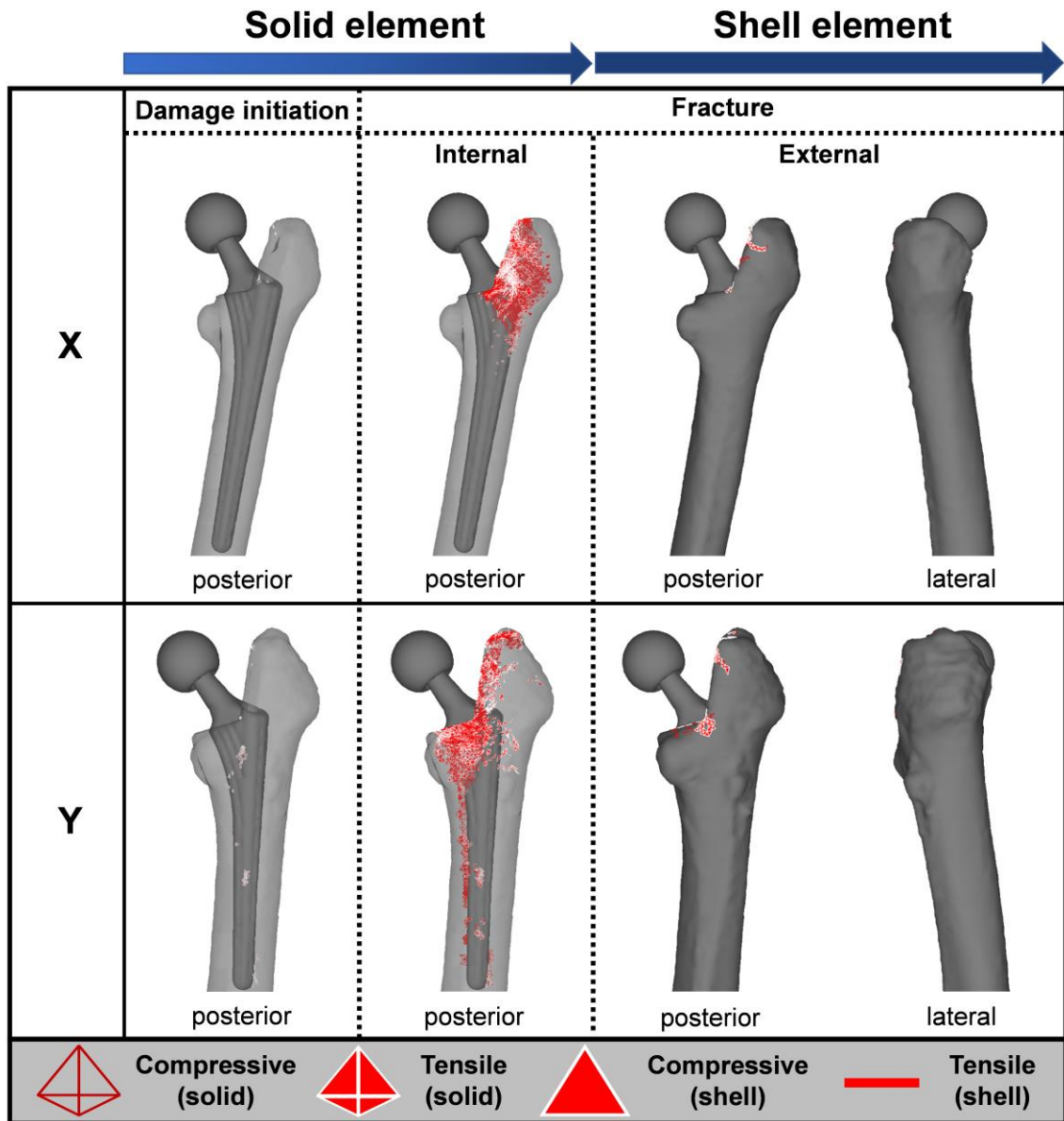


Figure 3.13 (continued)

(d) Stem III

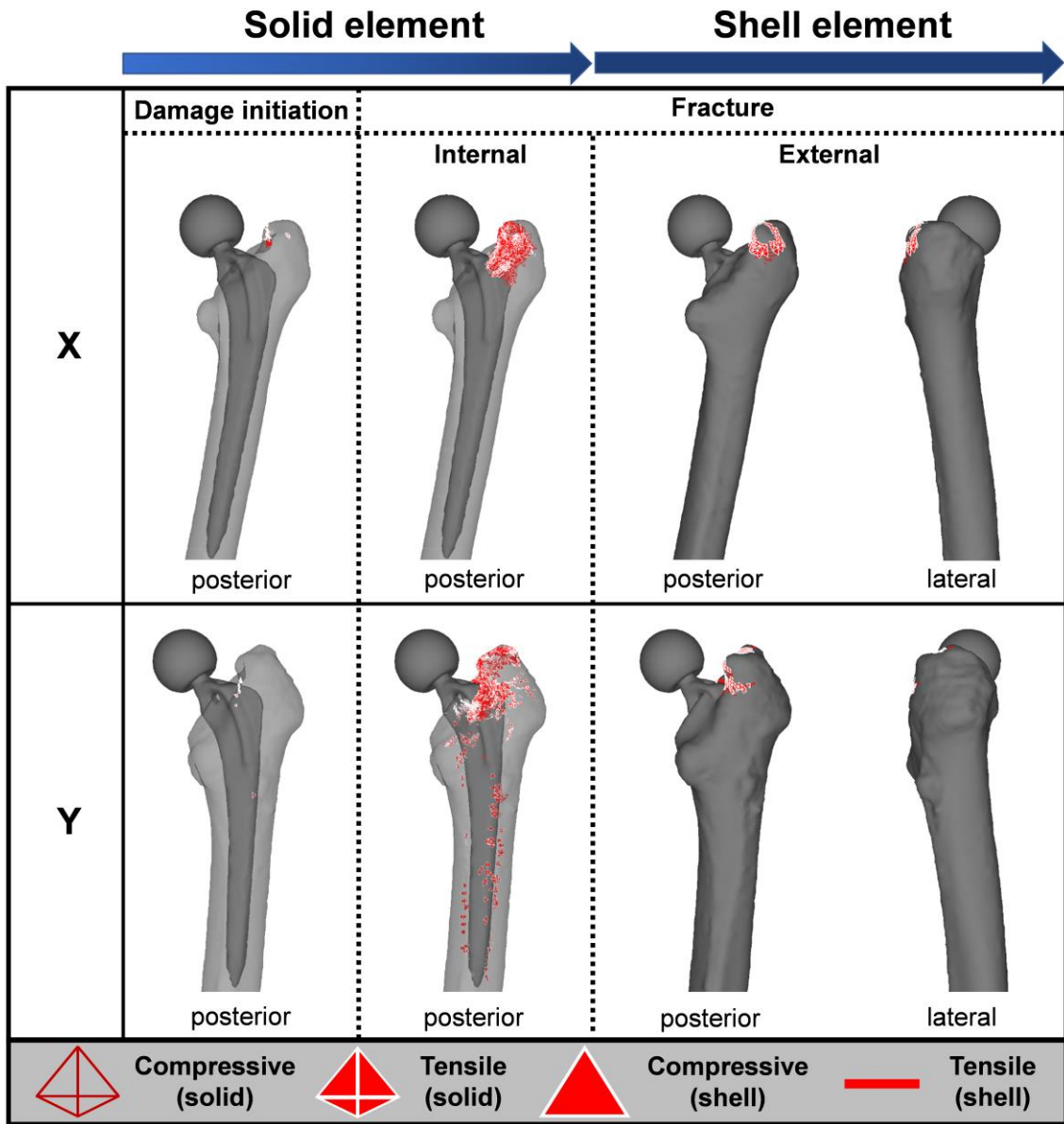


Figure 3.13 (continued)

3.7 Conclusion

Two different bones implanted with three different stem designs were successfully developed. Finite element analysis with non-linear damage analysis was conducted under four different types of falling configuration. The conclusions were obtained as follows:

- (1) The fracture load in both intact and THA models developed from bone X and Y was successfully obtained based on the failure of 300 shell elements. It was found that the fracture load reduces accordingly from FC1 to FC4. The stem design was observed to affect the fracture load of bone X, but the impact was small in bone Y. It is then concluded that the risk of bone fracture is more vulnerable when falling onto the posterolateral side compared to lateral side as obtained by the lower fracture load in FC3 and FC4 compared to FC1 and FC2.
- (2) The stem design was found to affect the internal bone micro-damage of bone X, where early bone damage was seen in stem II and stem III under FC1, FC2, and FC3 compared to stem I. Meanwhile, the effect was insignificant to bone Y. It is then concluded that bigger stem shoulder could produce lesser bone damage when falling onto the lateral side (FC1 and FC2) due to the larger bone area taken up by the stem, while under posterolateral side (FC3 and FC4), bigger stem shoulder with rectangular cross-section could enable strong rotational stability resulting from the four corners embedded into the endosteal bone with high strength.
- (3) The design of the stem had influenced the strength of bone X, as the initiation of bone fracture occurred at much lower load levels when the bone was implanted with stem II compared to stem I and III under FC1, FC2, and FC3. However, in bone Y,

the design of the stem had a negligible impact. It is concluded that the stem design with longer neck length had to undergo excessive bone removal which could influence the severity of bone fractures in traumatic incidents such as sideways fall, which highlighting the importance of femoral osteotomy to the current surgical practise.

- (4) Major bone damages were found only in Gruen zones 1 and 7 in all THA models of bone X, with zone 1 exhibiting higher damage compared to zone 7. In all models of bone Y, damages were found in all Gruen zones except for zone 4. Comparison on proximal, middle and distal bone areas showed that damage in zones 1, 6, and 5 were higher compared to zones 7, 2, and 3, respectively, which was consistent in all falling configurations. It is concluded that bone with greater quality could have lesser risk of implant loosening when experienced traumatic incidents.

CHAPTER 4: EFFECTS OF BONE VARIABLES AND IMPLANT POSITION

4.1 Overview

Study on the effect of bone variables such as bone density, bone geometry, angle of femoral torsion and thickness of femoral bone to the outcomes following THA are rarely be investigated due to limitation in developing a realistic finite element bone model. In this chapter, further investigation on the relationship between bone variables and bone damage mechanism following cementless THA was conducted. Finite element analyses with a nonlinear damage analysis were then performed under three different loading conditions i.e., stance, lateral bending, and torsion. In addition, the placement of the THA stem that being inserted into the implanted femurs was based on its original femoral torsion of the femoral head, in order to investigate the effect of implant position to the mechanism of bone micro-damage formation.

4.2 Construction of intact femoral models

28 patients diagnosed with avascular necrosis (AVN) were included in this study, with their ages ranging from 19 to 87 years old. Quantitative CT images were obtained from the Fukuoka University Hospital and imported into the CT-FEM software, Mechanical Finder version 11.0 (Research Centre for Computational Mechanics Inc., Tokyo, Japan) for the purpose of modelling. A two-dimensional region of interest was selected from each CT image slice, with the bone region having higher CT values than that of the surrounding soft tissues. These selected regions of interest were then stacked to form a three-dimensional geometry of the femur. The femoral models were meshed with 2-mm tetrahedral elements for the cancellous and inner cortical bone, and 2-mm triangular shell elements with a thickness of 0.3 mm were assigned to the outer surface of the cortical bone. The surface shell elements were assigned to represent the stiffest layer of the cortical bone, which cannot be accurately expressed from the CT images [108]. A linear formula was utilized to convert the Hounsfield unit (HU) into bone mineral density (BMD), thereby introducing inhomogeneous BMD values into each element as shown below [108]:

$$\rho \text{ (g/cm}^3\text{)} = [\text{HU} \pm 1.4246] \times 0.001 / 1.058 \text{ [HU value} > - 1\text{]}$$

$$\rho \text{ (g/cm}^3\text{)} = 0 \text{ [HU value} \leq - 1\text{]}$$

4.3 Construction of THA models

The femoral head and neck of the femur was removed based on the intertrochanteric line to approximately 1 cm above the lesser trochanter. Zweymuller stem was chosen to be inserted into selected femurs, since it is known as one of the commonly used stems in the clinical institution worldwide. The stem was shown in Figure 4.1. The placement of the implant was carefully inserted into the femoral canal through templating from the CT-images while considering the medial offset, vertical height, and angle of torsion to replicate the femoral torsion of the original femoral head as shown in Figure 4.2. The materials of the stem and femoral ball were assumed to be titanium alloy and alumina ceramic, respectively. Table 4.1 summarized the mechanical properties of the assigned materials [121]. It is noted that the interface between the bone and stem was assumed to be perfectly bonded to mimic the complete process of osseointegration [42].



Figure 4. 1: Zweymuller stem

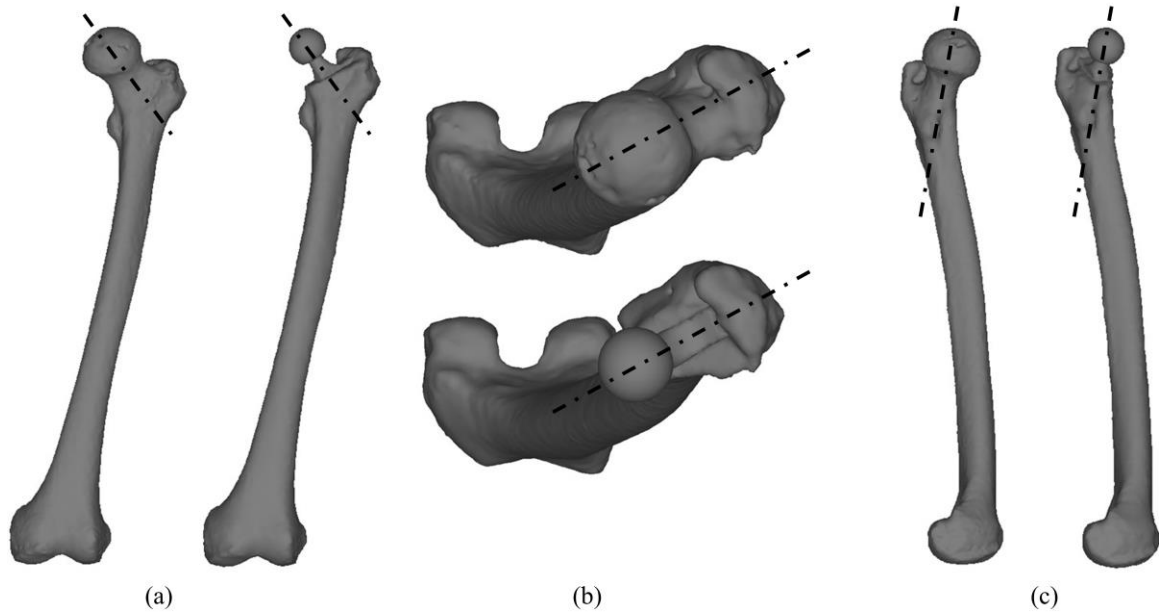


Figure 4. 2: Comparison on the placement of THA implant and original femoral head from (a) anterior view (b) superior view and (c) lateral view

Table 4. 1: Mechanical properties of THA implant

| Properties | Titanium alloy | Alumina ceramic |
|------------------------------|-----------------------|------------------------|
| Elastic modulus (GPa) | 114 | 370 |
| Poisson ratio | 0.34 | 0.22 |
| Critical stress (GPa) | 0.88 | 0.40 |
| Yield stress (GPa) | 0.97 | 3.00 |
| Density (g/cm ³) | 4.43 | 3.96 |

4.4 Loading and boundary conditions

Three different loading and boundary conditions were introduced into the nonlinear FE analysis in order to predict the damage formations of the THA femoral bones. These conditions were implemented on the basis of the validated and well-established testing protocol for periprosthetic femoral shaft fixation [122]–[126]. Those three loading and boundary conditions were denoted as stance condition (SC), lateral bending condition (LBC), and torsional condition (TC). The loading direction was set based on the angle of α and β , which represent the long axis of the femur in the frontal and sagittal plane, respectively. The orientation of loading direction for SC was $\alpha=160^\circ$, $\beta=0^\circ$, for LBC was $\alpha=90^\circ$, $\beta=0^\circ$, and for TC was $\alpha=90^\circ$, $\beta=90^\circ$. Before assigning the boundary condition, the orientation of the bone in x, y, and z-axis was carefully adjusted to mimic the standing position. The boundary conditions, SC, LBC, and TC are shown in Figure 4.3. For all conditions, the magnitude of applied load was set to be increased stepwise with 10 N increment per step until the failure of 1000 shell elements. The analysis was terminated after the failure of shell elements, and the value of the final load was recorded as the fracture load of the THA models.

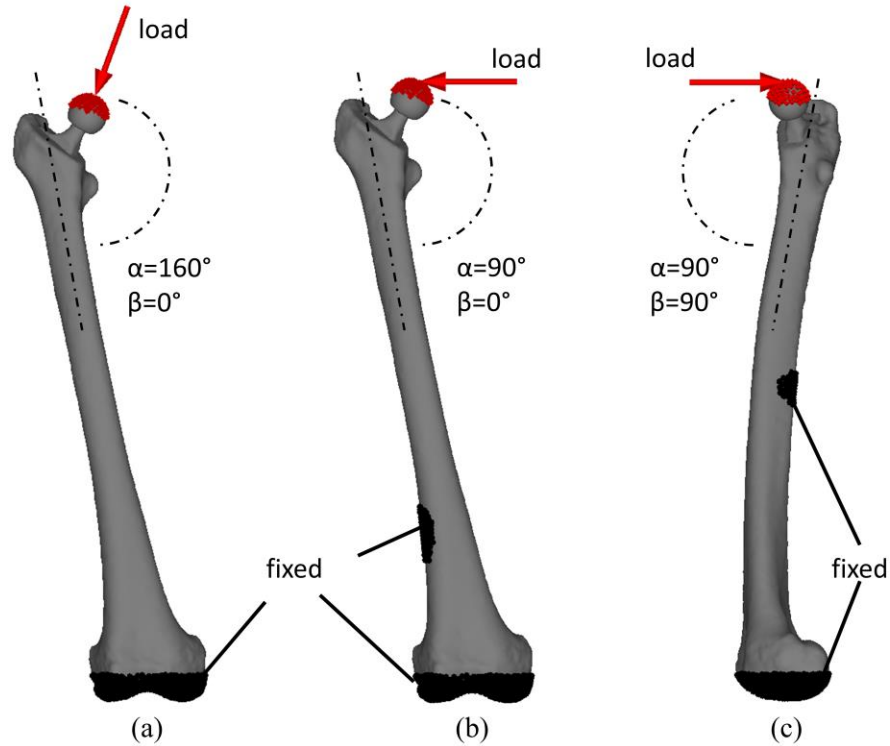


Figure 4. 3: Loading and boundary conditions: (a) stance condition (SC), (b) lateral bending condition (LBC) and (c) torsion condition (TC)

4.5 Mechanical theories and material properties

The tensile deformation of all the elements constructing the femoral models was assumed to be expressed by the linear elastic response, in which the stress-strain relation was characterized by two material constants such as Young's modulus and Poisson's ratio. On the contrary, the compressive deformation of the elements was assumed to be expressed by the bi-linear elastic-plastic response, in which the stress-strain relation was characterized by Young's modulus and Poisson's ratio under the linear-elastic behaviour and the yield stress and the work hardening coefficient under the plastic behaviour. The

Drucker-Prager yield condition was used to assess the onset of yielding [108]. Yielding was assumed to take place when the Drucker-Prager equivalent stress reached the compressive yield stress. Young's modulus and the compressive yield stress of a solid element were calculated from the corresponding BMD value of the element using the empirical formulae proposed by Keyak et al. [127] and Keller [128]. Poisson's ratio and the work hardening coefficient of all the solid elements were set to 0.4 and 0.05, respectively. Those properties of each of the shell elements were chosen so that they were equivalent to those of the adjacent solid element located under its position.

The tensile fracture of a solid or a shell element was assumed to take place when the maximum principal stress reached the tensile strength which was equal to 0.8 times the compressive yield stress of the element [129], [130]. On the other hand, the compressive fracture of the element was assumed to occur when the minimum principal strain reached the fracture strain which was equal to -3,000 micro-strain [130], [131]. Aggregation of shell element failures is usually needed to express the femoral fracture of the outer cortical surface and compare the fracture behaviour between the intact and the THA models. Therefore, in this study, a critical condition was set on the basis of the number of failure elements. 1000 shell element failures were chosen as the condition and the analyses were terminated when the total number of shell element failures reached 1000 under either tensile stress or compressive stress state. The stress-strain responses of titanium alloy and alumina ceramic were assumed to be linear elastic. Young's modulus and Poisson's ratio were chosen to be 114 GPa and 0.34 for titanium alloy and 370 GPa and 0.22 for alumina ceramic [121].

4.6 Results and Discussion

4.6.1 Relationship between age and bone density

The average value of bone density within the head and neck region of the intact femur was extracted from all the 28 models. Figure 4.4 shows the relationship between age (years old) and bone density (g/cm^3). The results showed a moderate negative correlation ($r = -0.69$) which indicates that there is a relationship between these two variables, with higher age being associated with lower bone density.

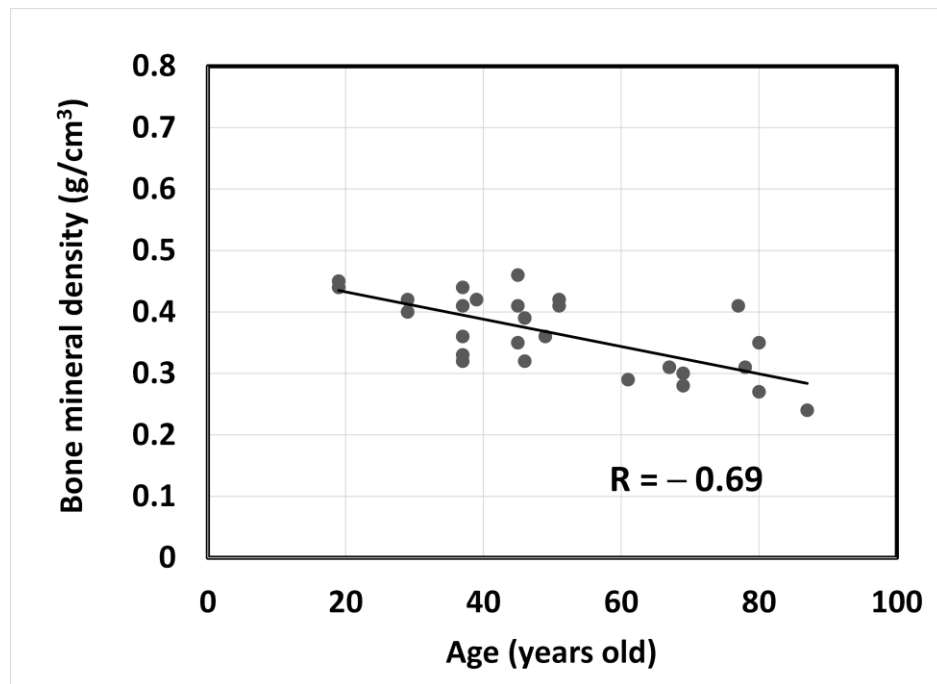


Figure 4. 4: Correlation coefficient between age and bone density in 28 femurs

In order to further investigate the relationship between bone variables and damage mechanism following THA, a total of 10 femoral models were selected and categorized into two groups of the highest (H) and lowest (L) BMD among the 28 models. The BMD and age of those 10 models ranged between 0.24 g/cm³ to 0.46 g/cm³ and 19 to 87-year-old, respectively. Those selected models were then implanted with the Zweymuller stem. Table 4.2 summarizes information on the selected intact femoral models.

Table 4. 2: Selected intact femoral model for implantation

| Model | Age (years old) | Gender | Femur | Average BMD at femoral head and neck (g/cm ³) |
|-------|-----------------|--------|-------|---|
| H1 | 45 | male | right | 0.46 |
| H2 | 19 | female | right | 0.44 |
| H3 | 77 | female | right | 0.41 |
| H4 | 37 | male | right | 0.41 |
| H5 | 51 | female | right | 0.42 |
| L1 | 78 | female | left | 0.31 |
| L2 | 87 | female | right | 0.24 |
| L3 | 80 | female | right | 0.27 |
| L4 | 69 | female | right | 0.28 |
| L5 | 61 | female | right | 0.29 |

4.6.2 Correlation of bone density and element failures in THA models

Figure 4.5 shows the correlation between bone density and fracture load in all the THA models under SC, LBC, and TC, respectively. In this section, the average BMD value throughout the entire bone structure was extracted for the comparison which ranging from 0.26 g/cm^3 to 0.60 g/cm^3 . Based on the results, the mean (\pm standard error) predicted fracture load of those THA models was found to be $1093 \pm 174 \text{ N}$ in SC, $667 \pm 61 \text{ N}$ in LBC, and $950 \pm 95 \text{ N}$ in TC. A strong positive correlation was observed between BMD and fracture load, which found to be consistent in all three boundary conditions (SC, $r = 0.74$), (LBC, $r = 0.79$), (TC, $r = 0.88$). The presence of a strong correlation coefficient implies that there is a significant statistical relationship between these two variables, with higher BMD being associated with higher fracture load. These findings suggested that bone with higher density will have a greater bone strength and resistance to fracture from the outer cortical region, despite being implanted with the metallic stem and assigned with different boundary conditions.

On another note, Figure 4.6 shows the correlation between bone density and solid element failures. From the results, a moderate negative correlation was observed between these two variables which seen to be consistent in all boundary conditions (SC, $r = -0.40$), (LBC, $r = -0.51$), (TC, $r = -0.48$). It should be noted that the cumulative numbers of solid element failures were taken at the final load value of the model which represents the bone damage from the internal bone region.

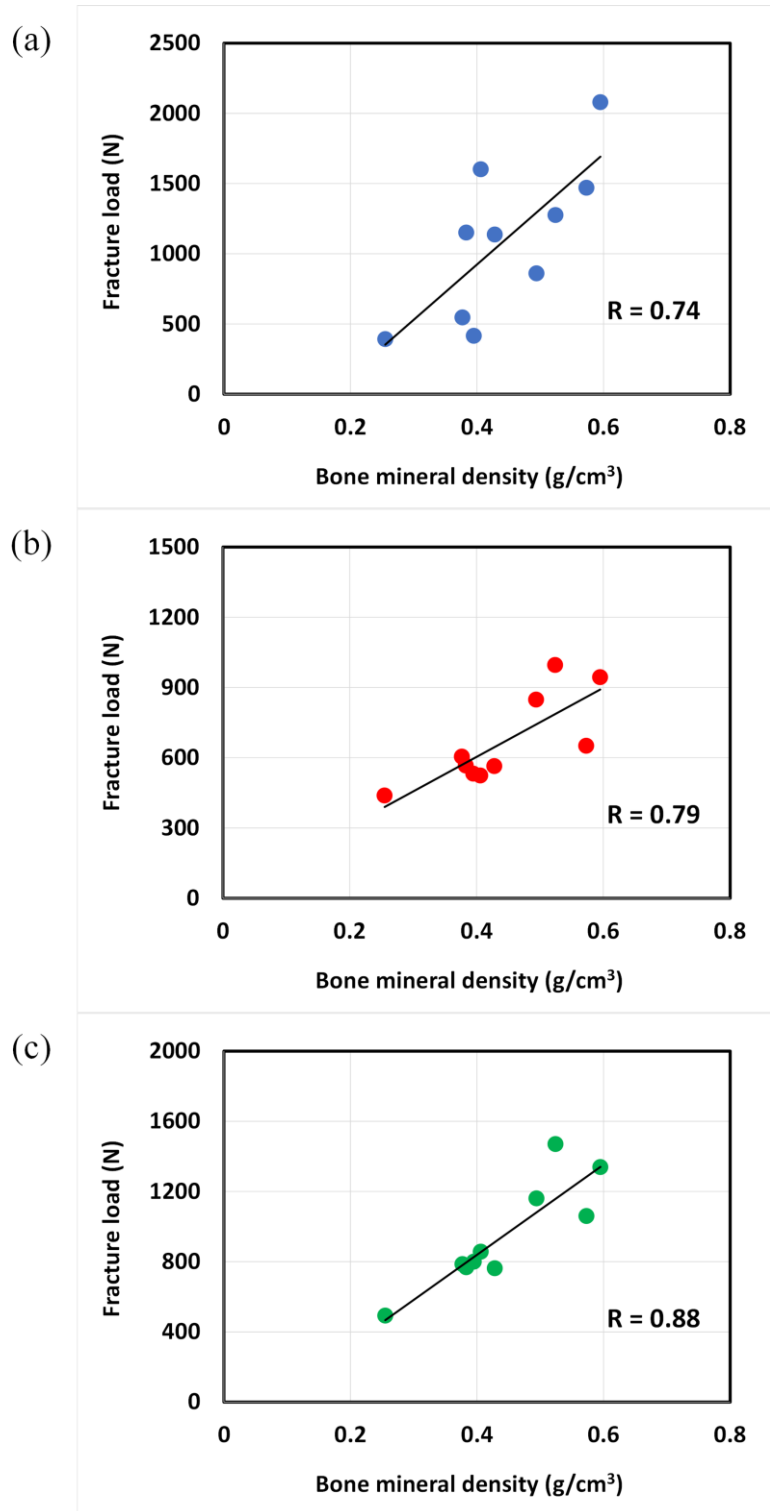


Figure 4. 5: Correlation coefficient between BMD and fracture load of THA models under (a) SC, (b) LBC and (c) TC

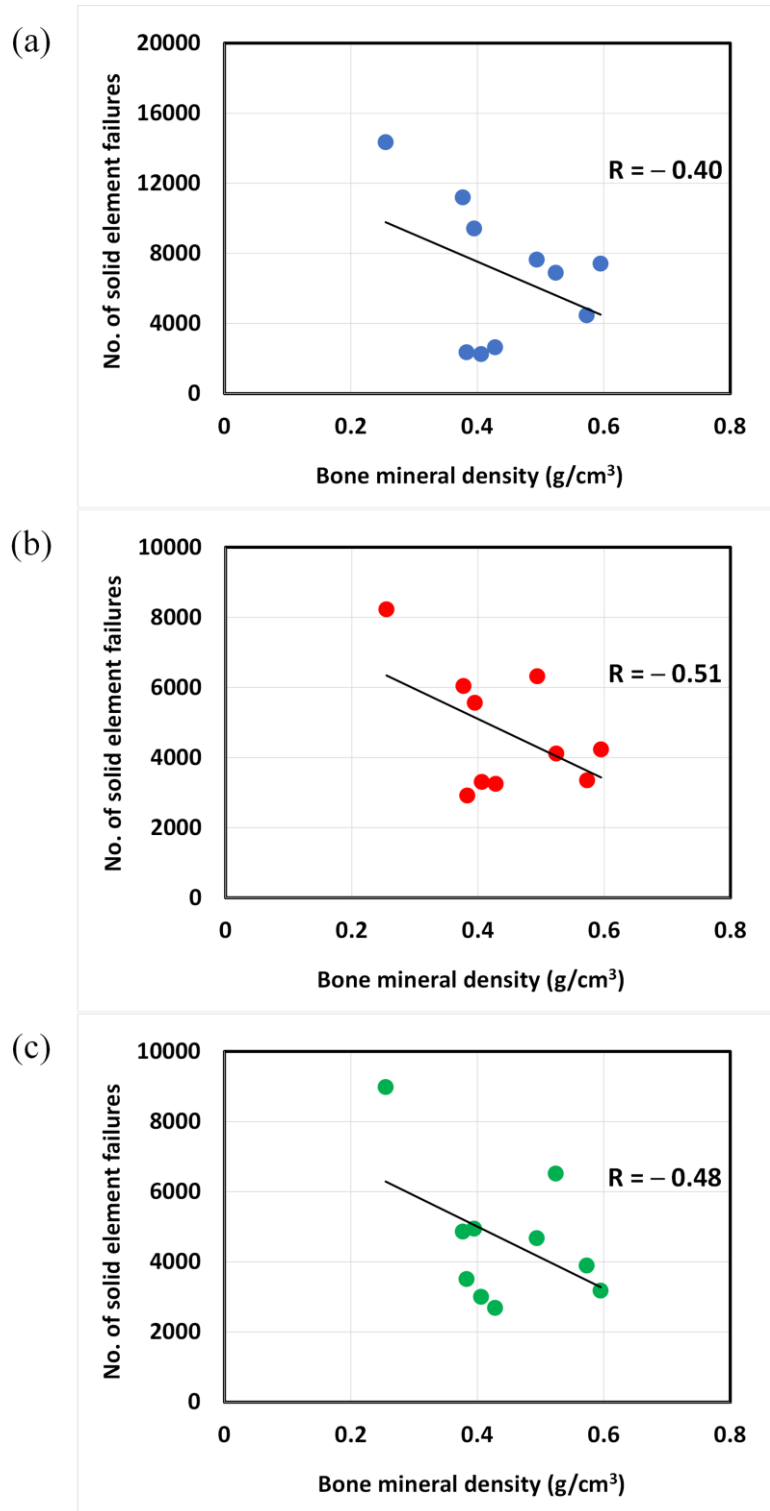


Figure 4. 6: Correlation coefficient between BMD and solid element failures of THA models under (a) SC, (b) LBC and (c) TC

While bone density is generally recognized as an important parameter for measuring bone strength, it is worth noting that the moderate correlation between BMD and the failure of solid elements suggests that bone strength in the internal bone region does not solely depend on BMD. Other factors may also play a role, particularly since the mechanical environment of the femoral bone is altered by the presence of a metallic stem. Therefore, to further investigate the potential impact of other factors on bone damage, especially at the interfacial area between the bone and stem, the number of solid element failures within that region was extracted and compared among all the models.

4.6.3 *Effect of bone variables and implant position to bone damage formation*

Figure 4.7 shows the number of solid element failures at the bone and stem interface in all models under the three different boundary conditions. The number was extracted at the final load in each model. In SC (Figure 4.7 (a)), model L2 had the highest number of solid element failures, followed by H1 and L3. In LBC (Figure 4.7 (b)), the highest number of solid element failures still obtained by L2, followed by L4 and H1, while in TC (Figure 4.7 (c)), L2 had the highest, followed by H1 and L4.

It is important to note that models L2 and H1 were constantly experienced greater bone damage in all three boundary conditions. Major bone damage occurred at the interfacial areas of bone and stem in L2 may be the results of thin cortices and substantial bone loss at the proximal femur. The cortical thickness of L2 model is comparable to the type C of Dorr classification [138], which refers to wide canal diameter that often found in elderly and female patient. Figure 4.8 shows the cross-sectional view of model L2 compared to model L5, which thought to be the reason of greater bone damage.

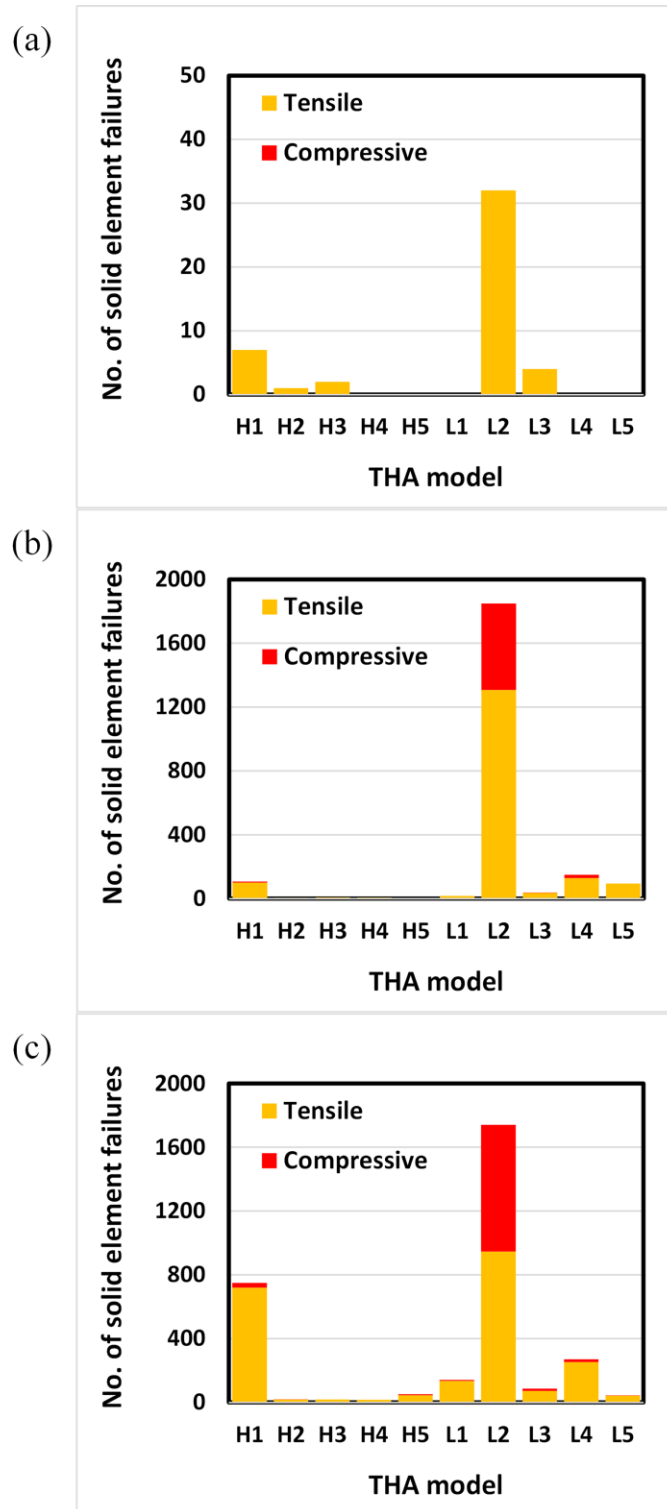


Figure 4. 7: Solid element failures within the interfacial areas of bone and stem at final

load under (a) SC, (b) LBC and (c) TC

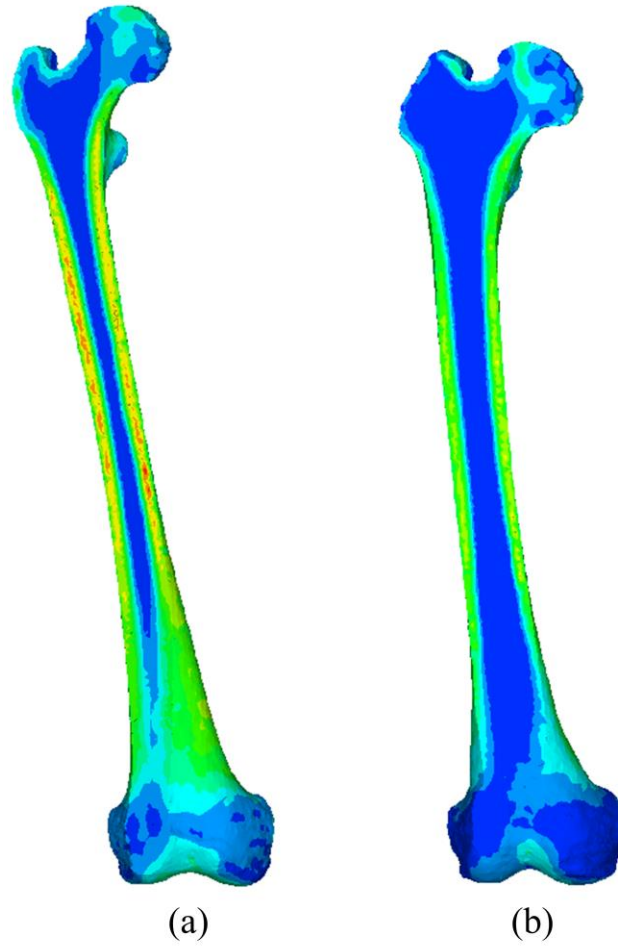


Figure 4. 8: Comparison between (a) thick femoral cortices, L5 and (b) thin femoral cortices, L2

Meanwhile, the high bone damage in H1 may be the result of implant positioning. Figure 4.9 illustrates the comparison of implant positions between the H1 model and another model. It can be seen that the implant in H1 was retroverted, which is believed to affect the cumulative number of bone damage. For instance, under the TC condition, an implant positioned with normal anteversion is expected to result in less bone damage

compared to retroversion after loading, considering the moment effect due to the shorter distance, d , as depicted in Figure 4.9. It should be noted that the stem placement was based on the femoral torsion of the original femoral head. Thus, it is evident that the risk of complications after THA can be influenced by other factors, such as implant position, even in a bone with high BMD, as observed in H1.

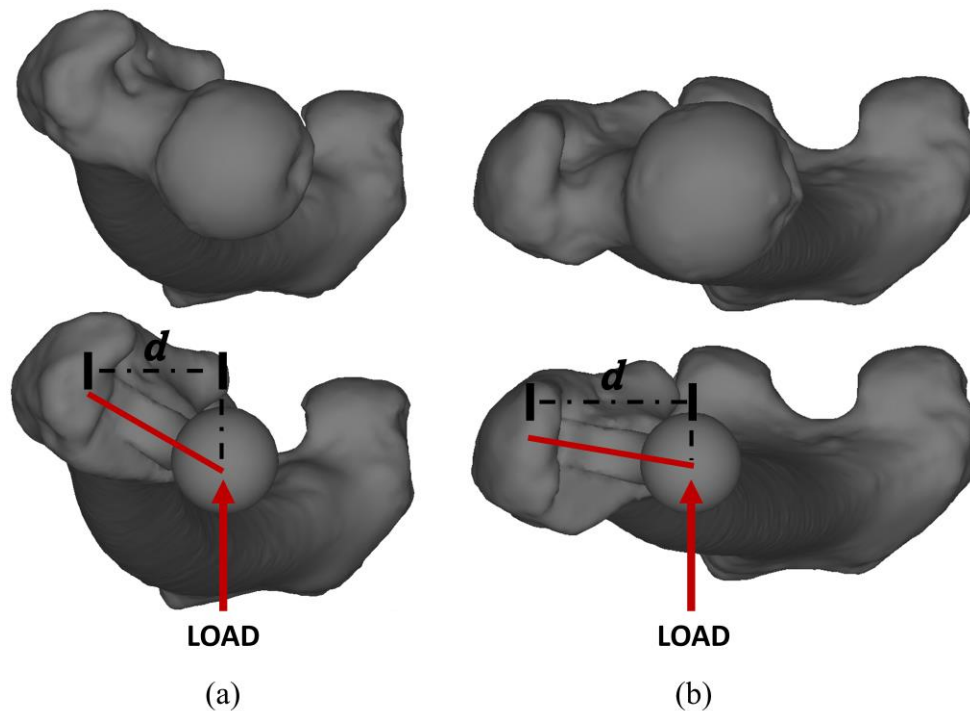


Figure 4. 9: Implant placement (a) normal anteversion and (b) retroversion

On the other hand, the geometry of the bone was thought to be the contributing factor in the formation of bone damage under boundary conditions that involve bending to the bone, such as LBC and TC. It was found that model L4 consistently experienced greater damage in both boundary conditions. The bend geometry of the femoral shaft may be the reason for the increased formation of bone damage in L4, as shown in Figure 4.10. It can

be observed that the element failures accumulated at the distal end of the stem in L4, in comparison to the H2 model with a straight femoral shaft geometry. Additionally, it can be observed that most of the femurs in the L group had bend femoral shaft geometry, which contributes to the greater formation of bone damage.

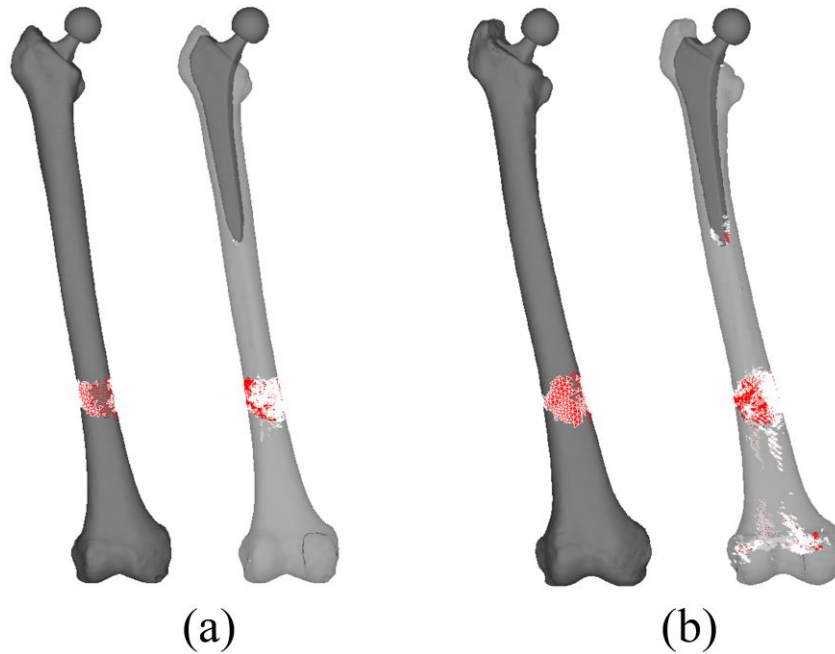


Figure 4. 10: Comparison of bone geometry and bone damage formation from external and internal region: (a) straight shaft, H2 and (b) bend shaft, L4

Distribution patterns of element failures as bone micro-damages for all 10 models under SC, LBC, and TC are shown in Figures 4.11 – 4.13, respectively. In those images, distributions of solid element failures at the damage initiation and internal damage at fracture are presented, along with the distributions of shell element failures indicate external formation of bone fracture.

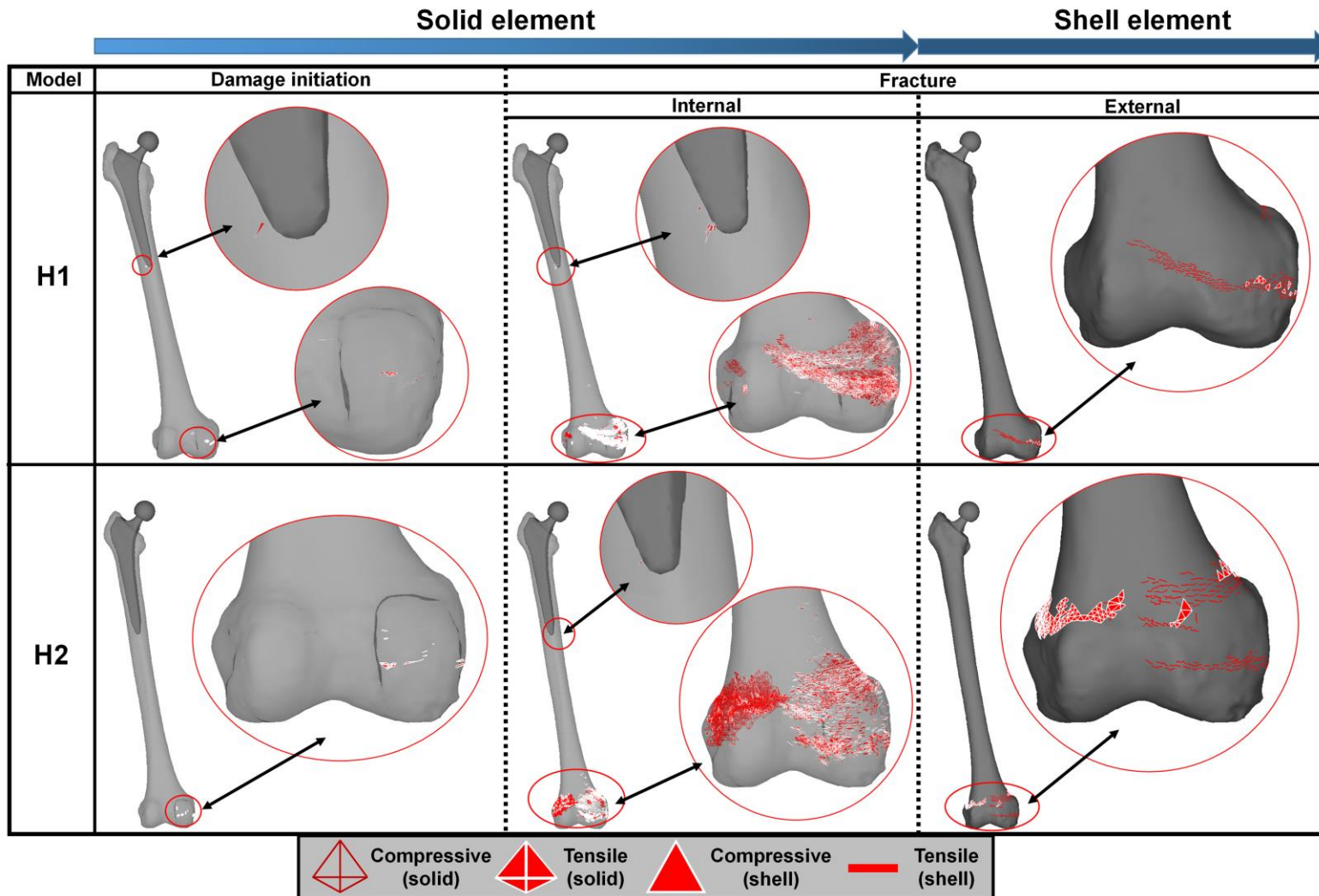


Figure 4. 11: Distribution of element failures under SC

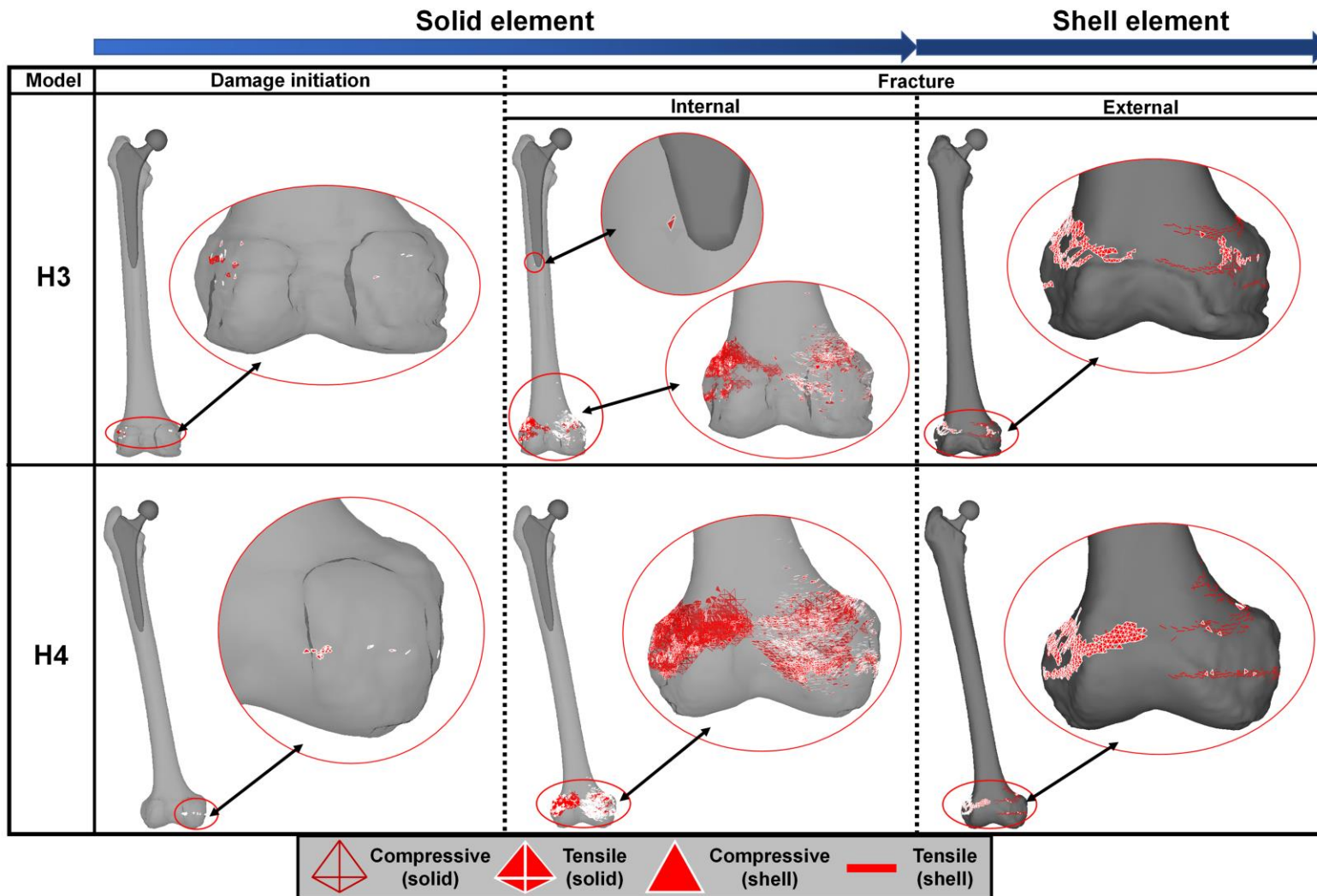


Figure 4.11 (continued)

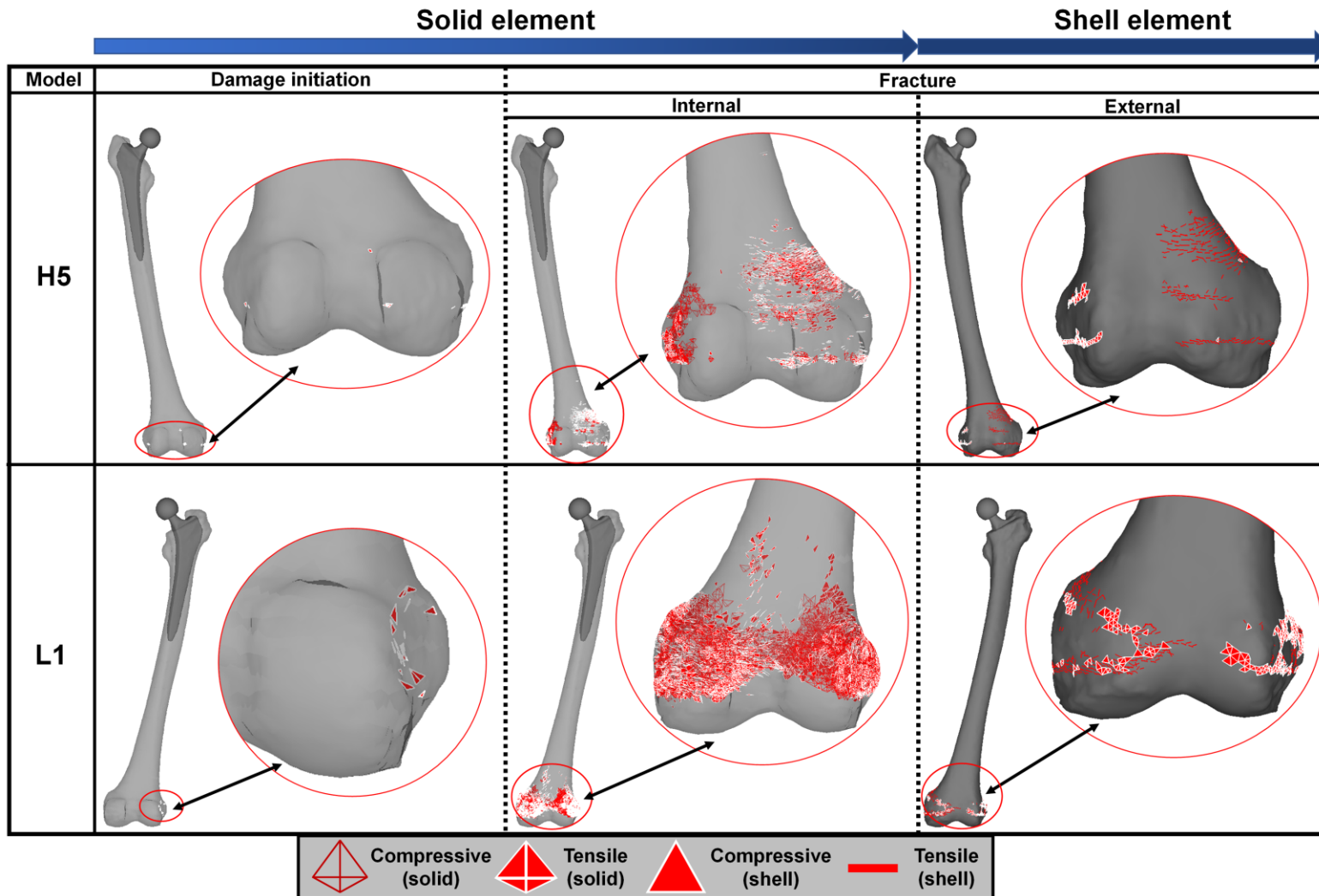


Figure 4.11 (continued)

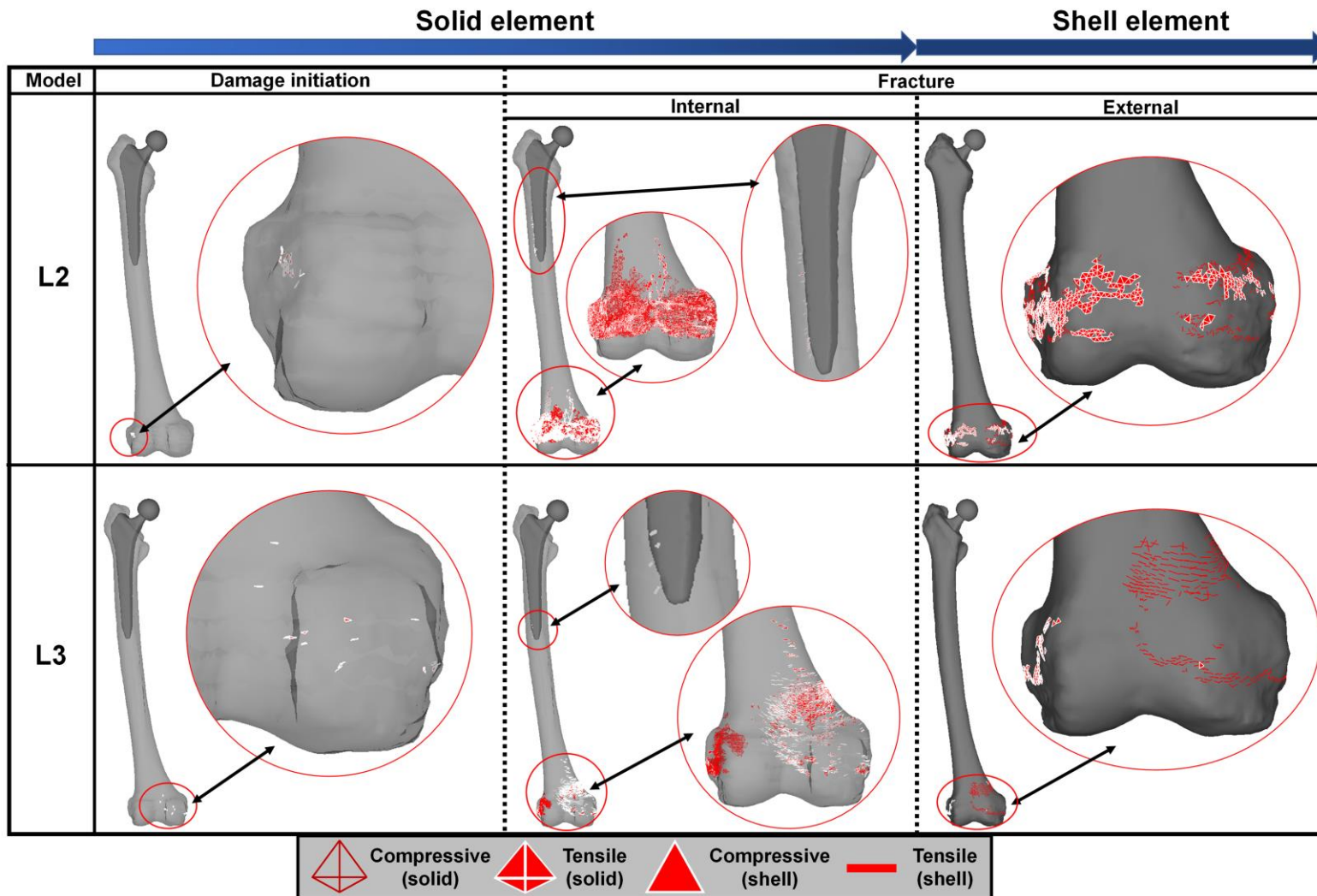


Figure 4.11 (continued)

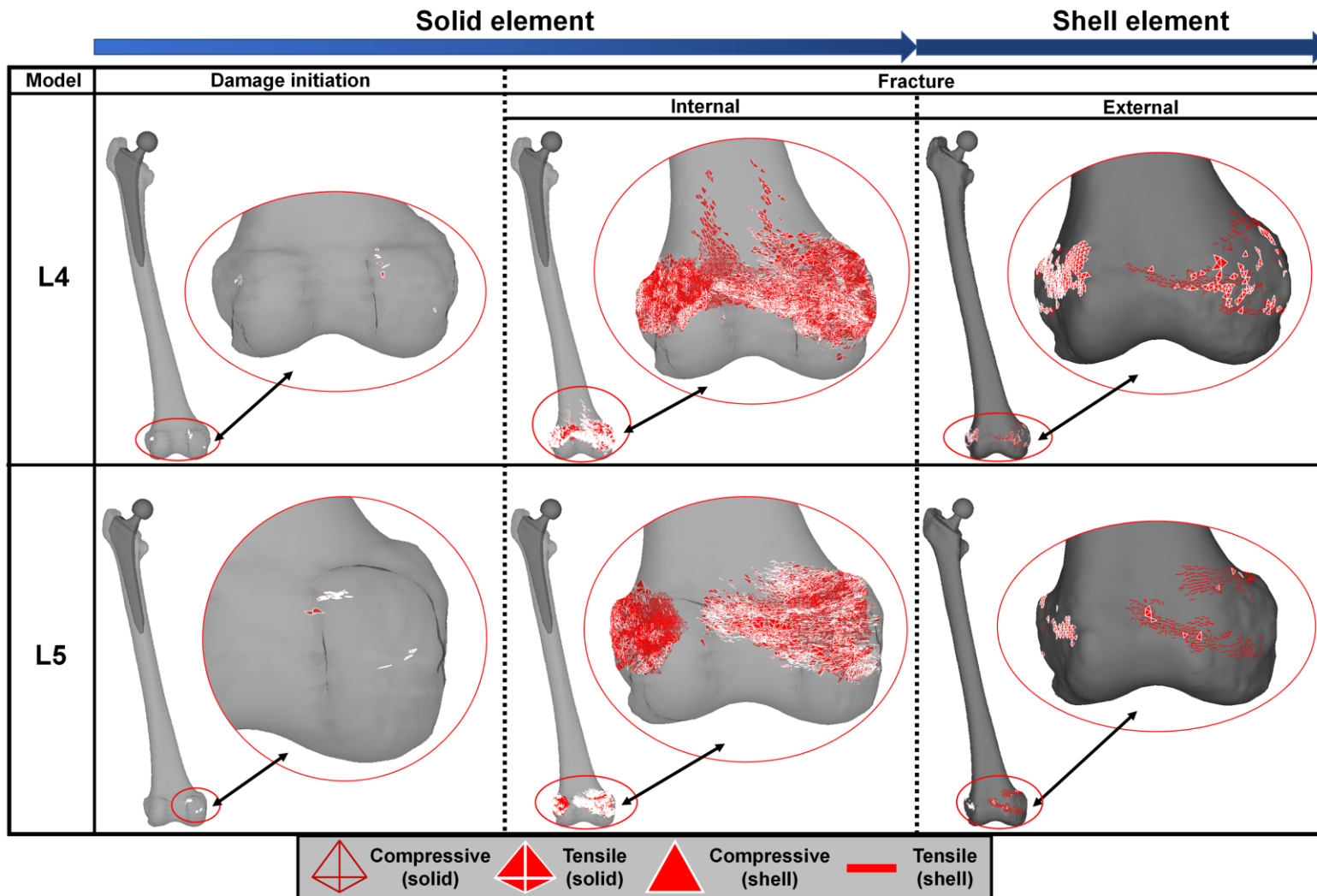


Figure 4.11 (continued)

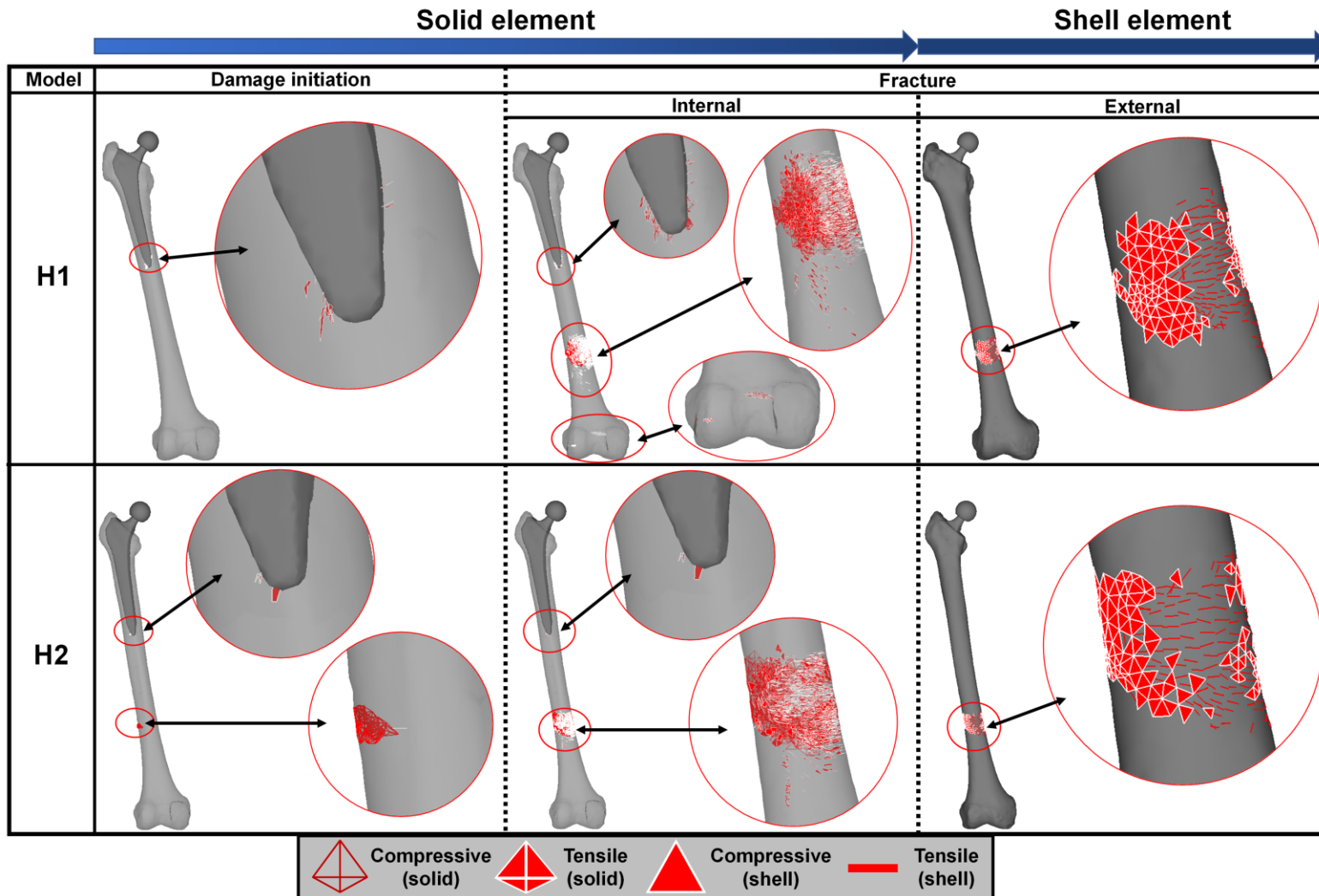


Figure 4. 12: Distribution of element failures under LBC

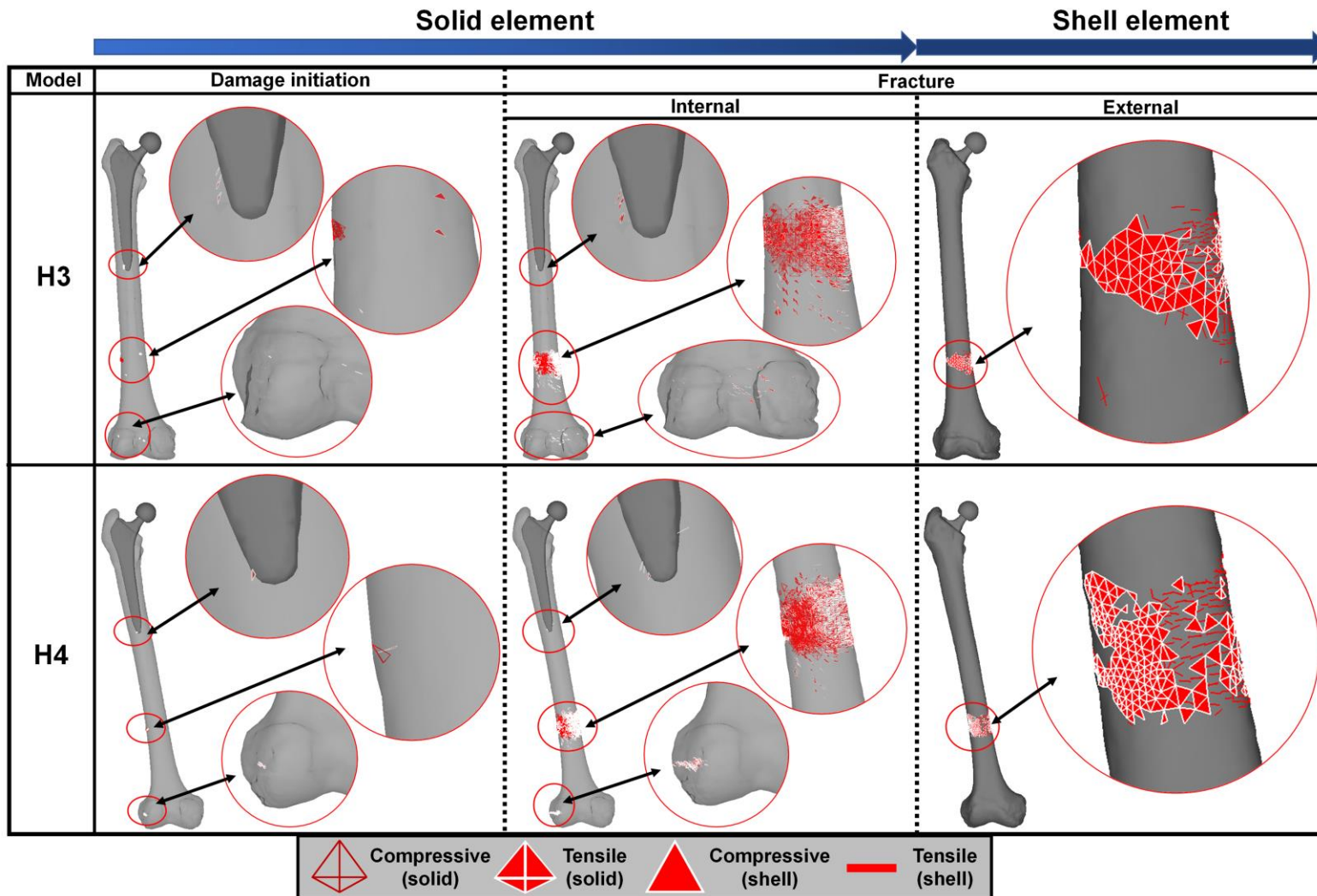


Figure 4.12 (continued)

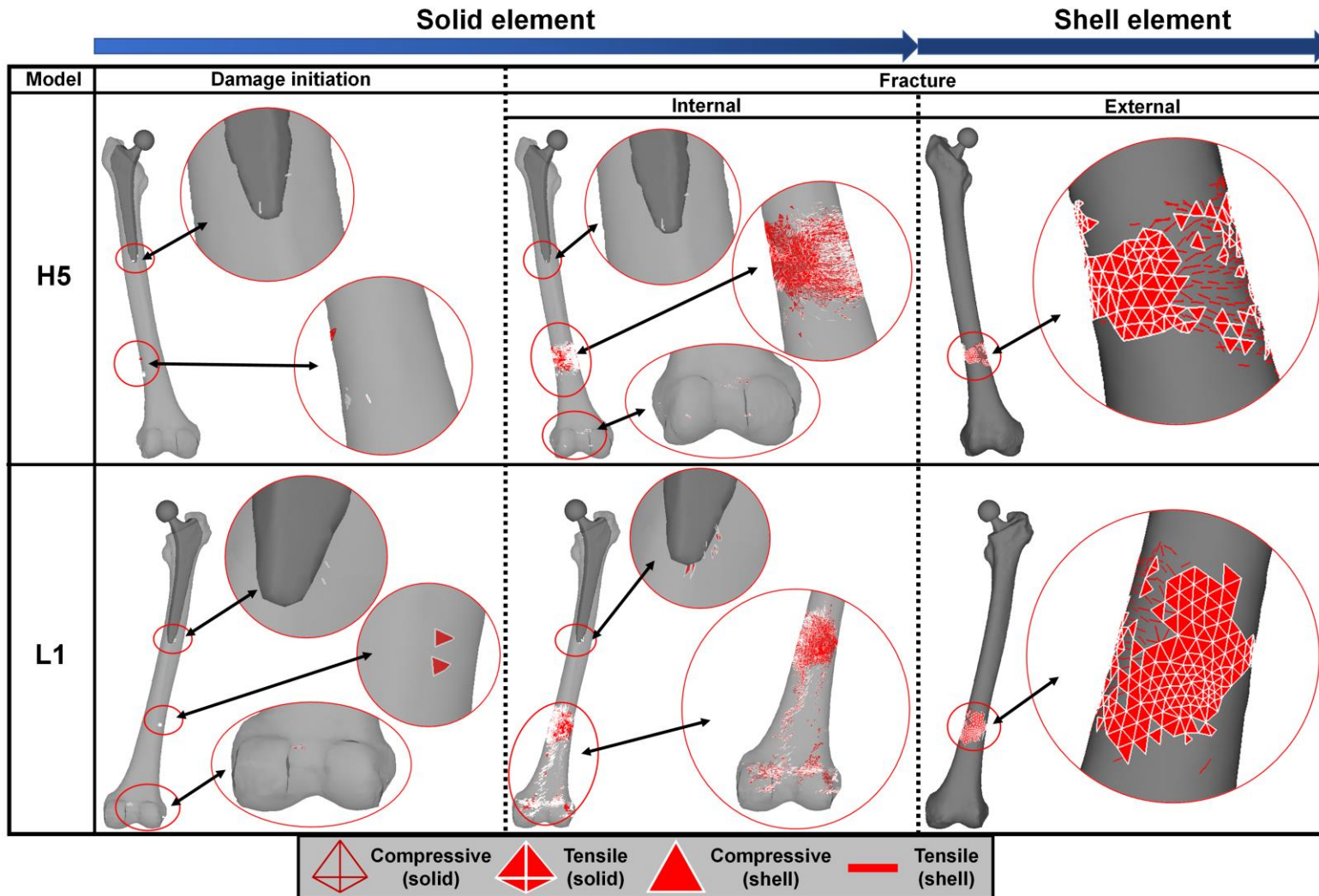


Figure 4.12 (continued)

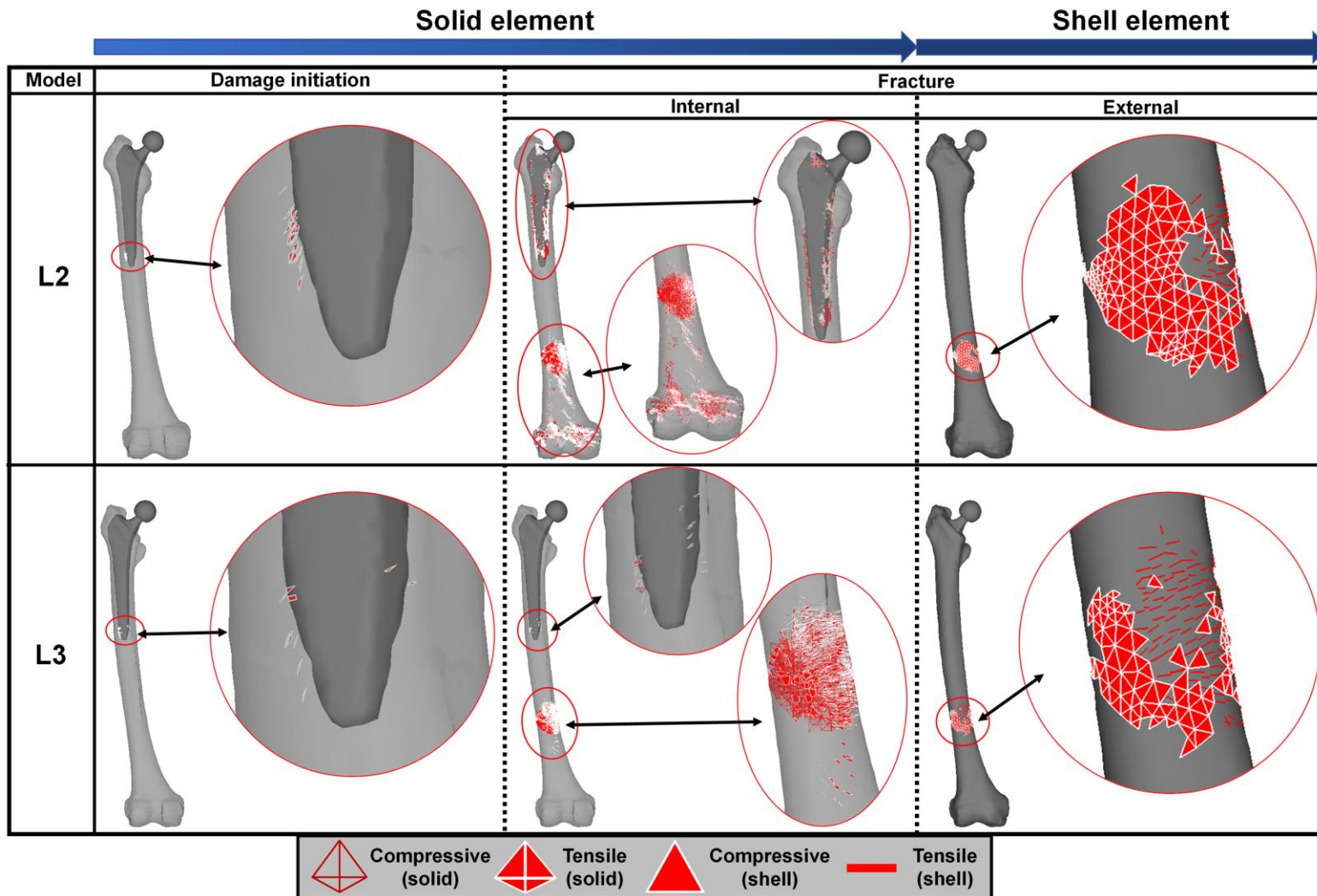


Figure 4.12 (continued)

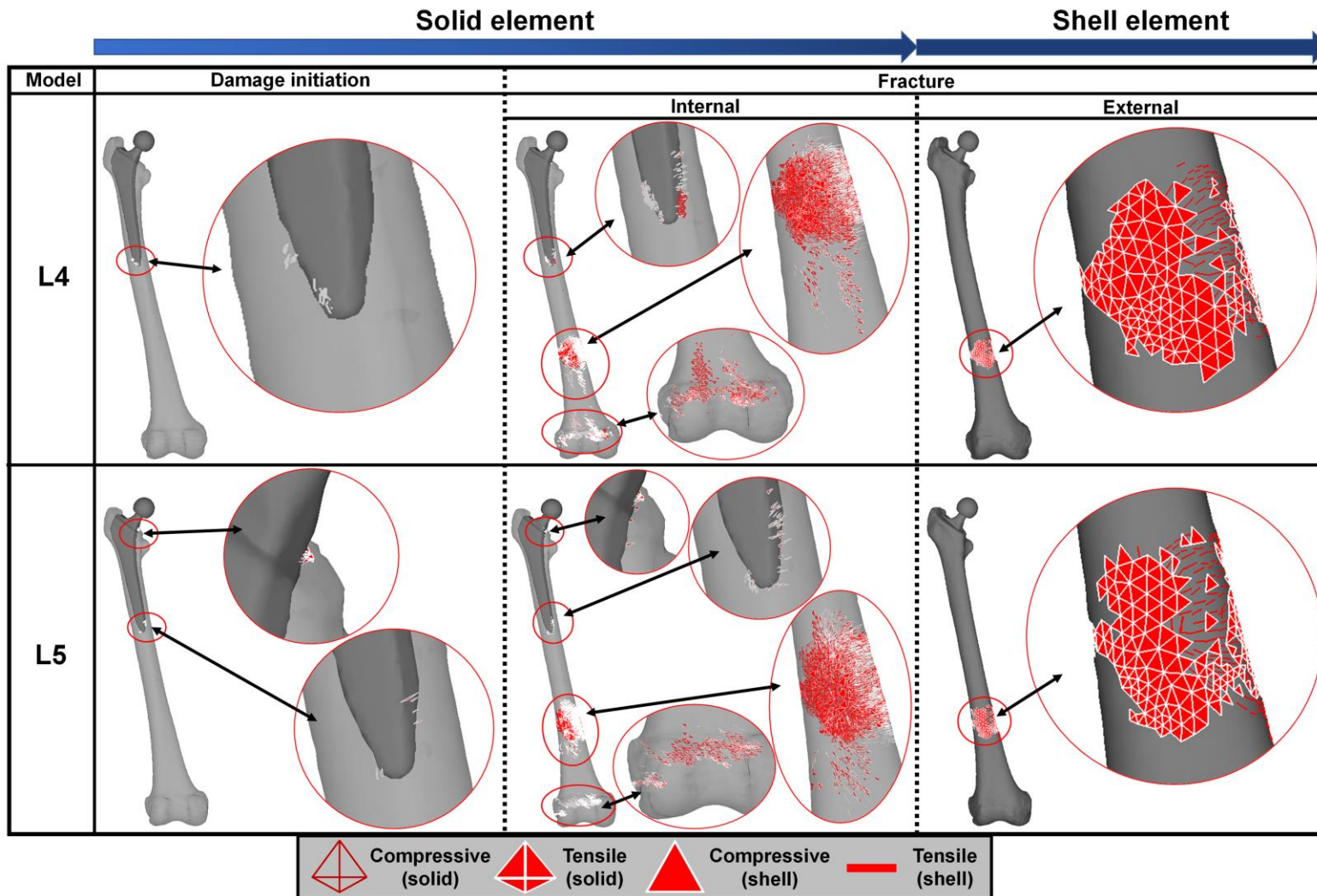


Figure 4.12 (continued)

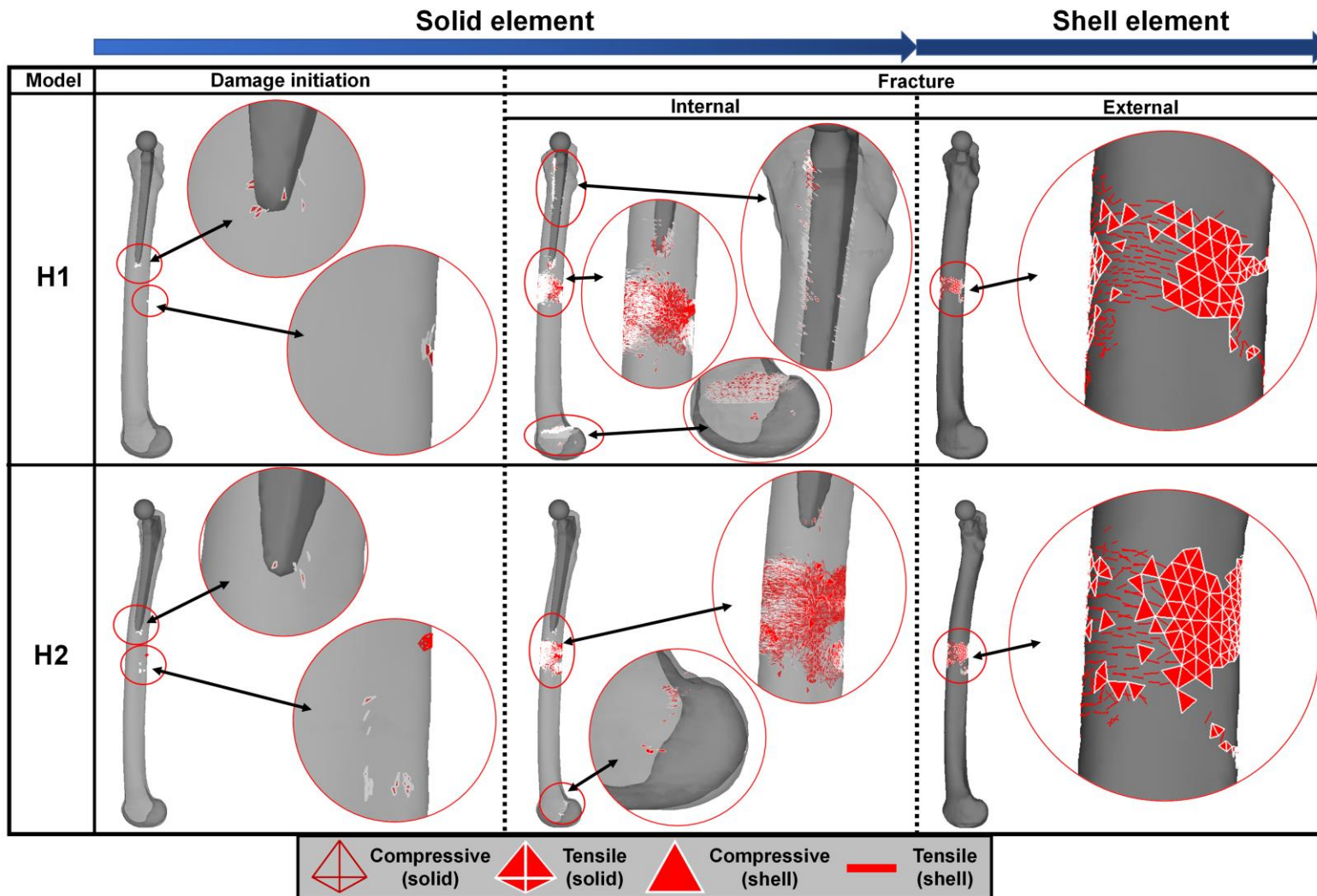


Figure 4.13: Distribution of element failures under TC

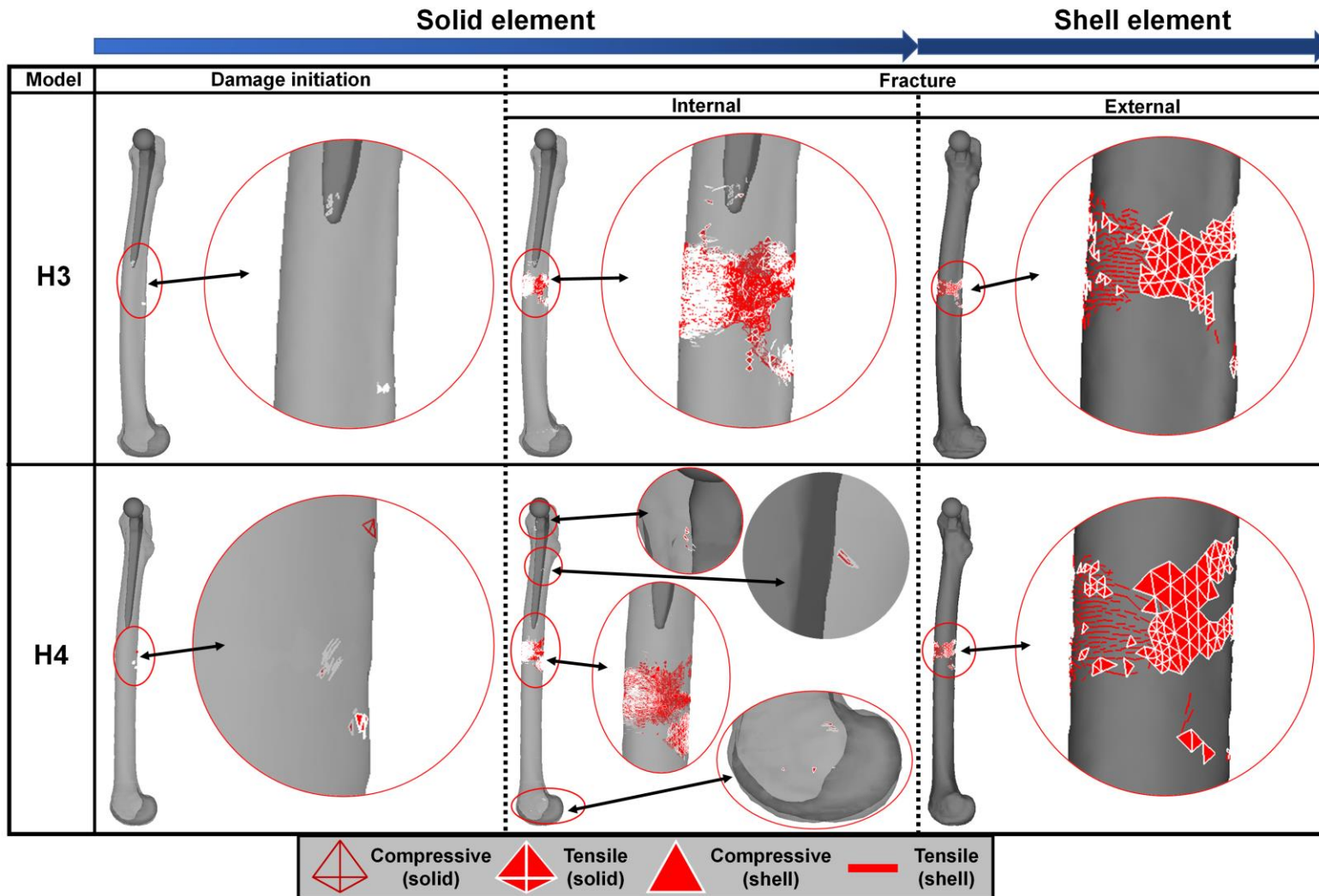


Figure 4.13 (continued)

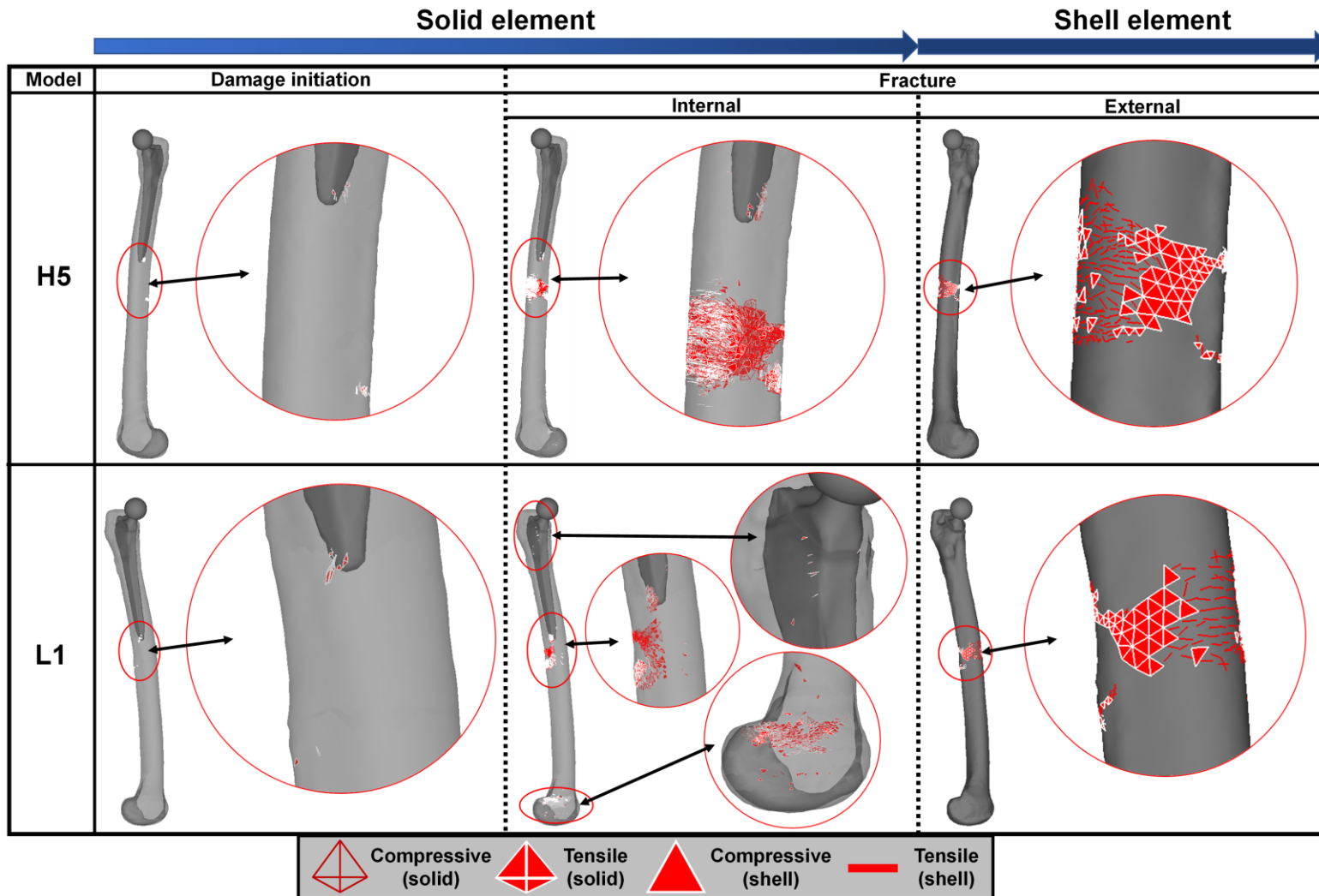


Figure 4.13 (continued)

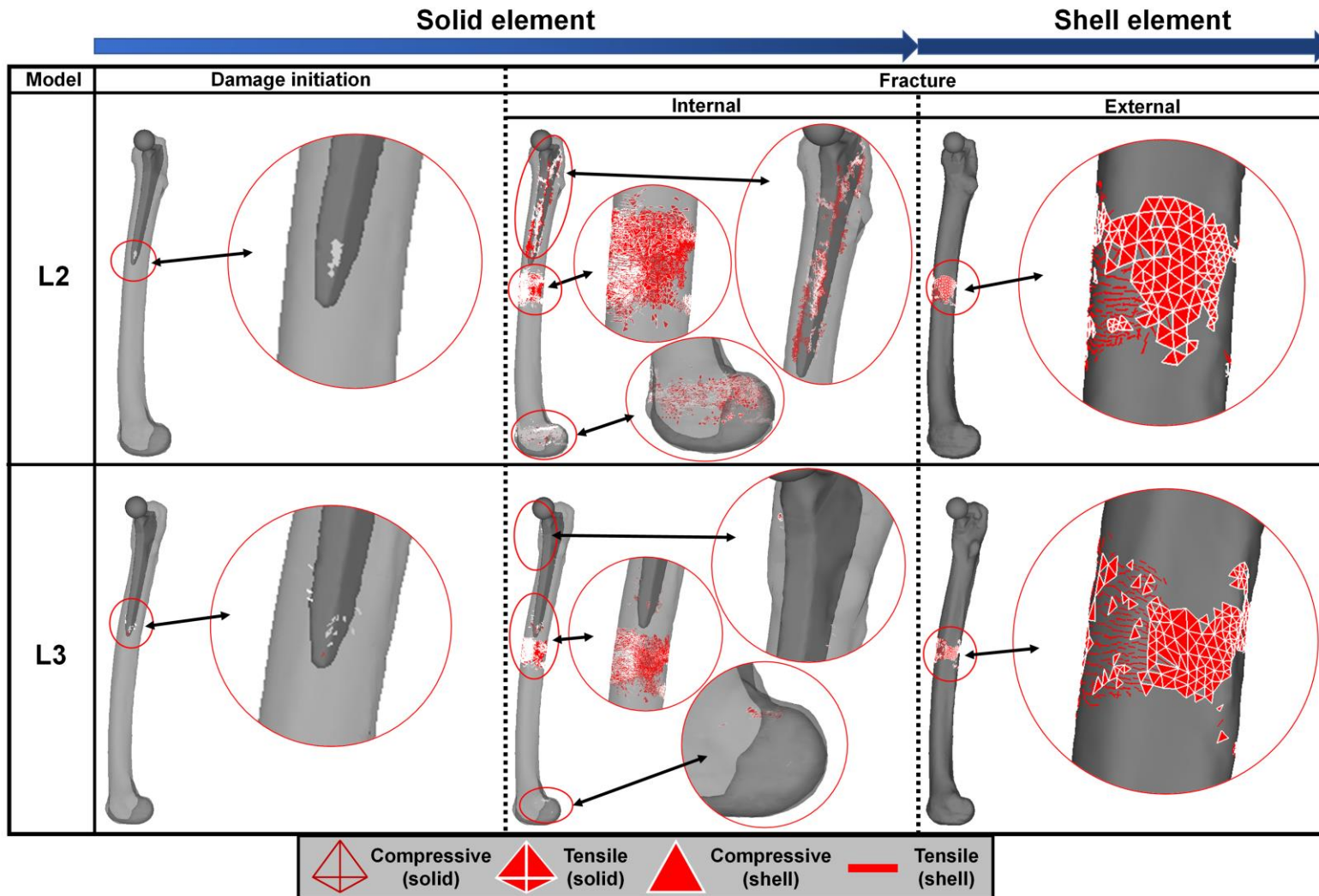


Figure 4.13 (continued)

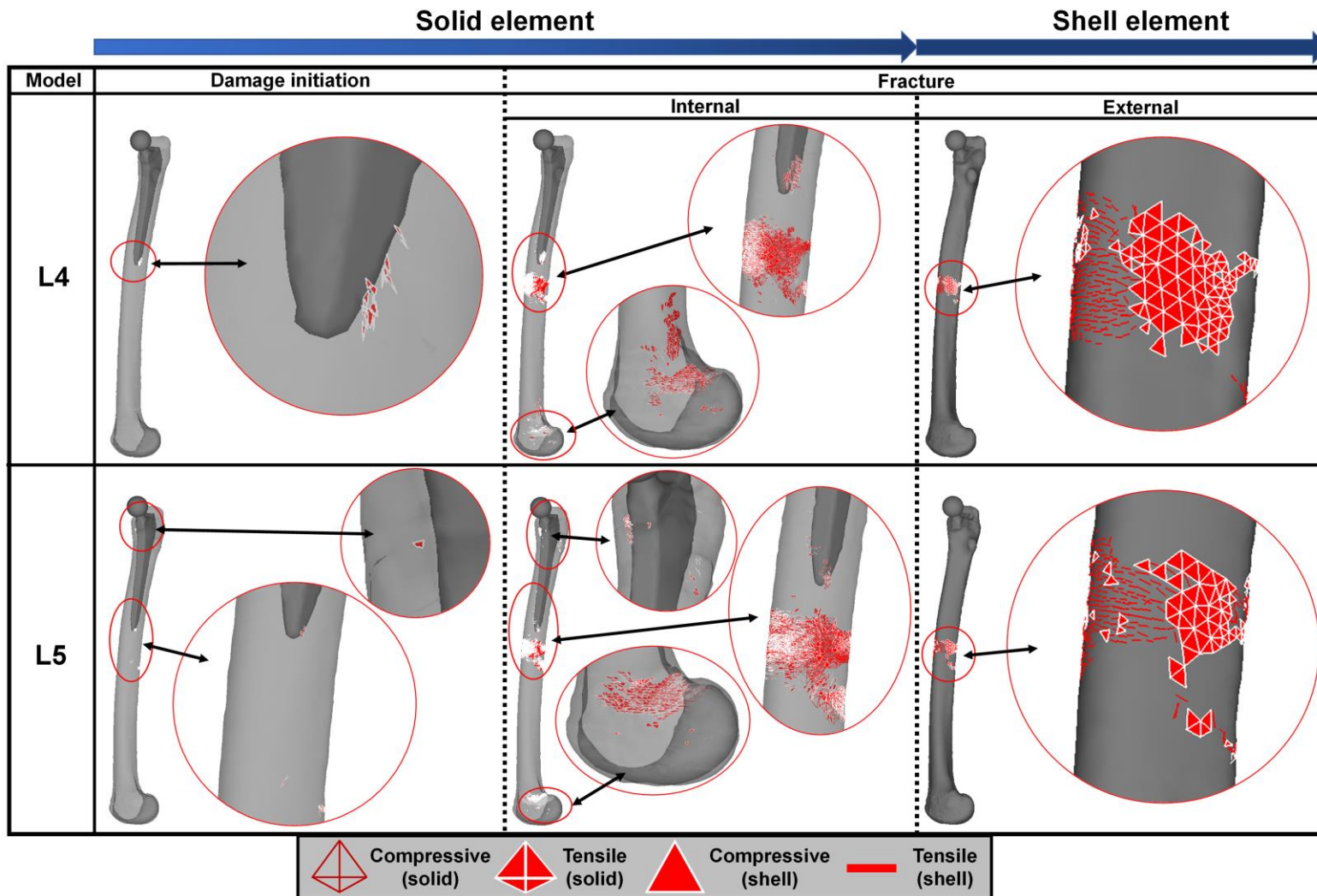


Figure 4.13 (continued)

4.7 Conclusion

In this chapter, 28 FE femoral bone models were developed from CT images of avascular necrosis patients, before selecting 10 femurs to be implanted with Zweymuller stem. Then, finite element analysis with non-linear damage analysis was performed under three different types of boundary conditions, namely stance, lateral bending, and torsion. The conclusions were obtained as follows:

- (1) The relationship between age and bone density was successfully determined. A moderated negative correlation was obtained ($r = -0.69$) suggesting the influence of age on the reduction of BMD.
- (2) It was found that bones with higher BMD had greater strength and high resistance to fracture in the outer cortical bone in all boundary conditions, despite implanted with a metallic stem. A strong correlation was observed between bone density and fracture load in all boundary conditions of the THA models (SC, $r = 0.74$), (LBC, $r = 0.79$), (TC, $r = 0.88$).
- (3) The strength of the bone in the internal region was found to have a low correlation with BMD, suggesting that bone micro-damage was influenced by other factors. A moderate relationship was observed between BMD and the number of solid element failures in all boundary conditions: (SC, $r = -0.40$), (LBC, $r = -0.51$), (TC, $r = -0.48$).
- (4) It was found that factors such as thin cortices of the cortical bone, bend geometry of the femoral shaft, and the position of the THA stem had a substantial effect on the mechanism of bone micro-damage formation in the internal region of the bone.

CHAPTER 5: COMPARISON OF COLLARLESS AND COLLARED STEM DESIGNS

5.1 Overview

The most crucial part in the procedure of cementless total hip arthroplasty is to achieve biological fixation or osseointegration, in which primary stability of the implant is known to be one of the important factors in promoting the process. Excessive micromotion of the stem after loaded may produce micro-damage to the interfacial of bone and stem, thus delaying or prevent the osseointegration. Several known factors that influence the primary stability was the design of the implant. In this chapter, collarless and collared versions of a similar cementless femoral stem were implanted into a computational femoral bone model, developed from the CT images of 61-year-old patient. The distribution of strain within the bone and the mechanism of bone micro-damage formation from those collarless and collared stem versions were then compared under two different boundary conditions.

5.2 Construction of intact femoral model

Quantitative CT images of a 61-year-old patient with AVN were obtained from the Fukuoka University Hospital. To model the femur, each CT image was imported into the CT-FEM software, Mechanical Finder version 11.0 (Research Centre for Computational Mechanics Inc., Tokyo, Japan). A two-dimensional region of interest was selected from each CT slice where the bone region had higher CT values compared to surrounding soft tissues, such as muscle, ligament, and adipose tissues. These selected regions were vertically stacked to form a three-dimensional geometry of the femur. To mesh the intact femoral models, 2-mm tetrahedral elements were assigned for cancellous bone and inner cortical bone, while 2-mm triangular shell elements with a thickness of 0.3 mm were used for the outer surface of the cortical bone. The surface shell elements were employed to represent the stiffest layer of the cortical bone, which could not be discerned from the CT images [108]. The Hounsfield unit (HU) values were converted into bone mineral density (BMD) by applying a linear formula [108], thereby introducing inhomogeneous BMD values into each element.

5.3 Construction of THA model

The femoral head and neck of the femur was removed based on the intertrochanteric line to approximately 1 cm above the lesser trochanter. The collarless and collared version of a similar cementless stem was obtained from Teijin Nakashima Medical Co., LTD, and was carefully inserted into the femoral canal of the 61-year-old-patient. The placement of the implant was carefully inserted into the femoral canal through templating from the CT-images while considering the medial offset, vertical height, and angle of torsion to replicate the femoral torsion of the original femoral head. Figures 5.1 and 5.2 show the illustration of both stem versions and the THA femoral bone models, respectively. The materials of the stem and femoral ball were assumed to be titanium alloy and alumina ceramic, respectively [121]. To allow the non-bonding characteristic between the interface of stem and internal bone area, a frictional coefficient of 0.4 was set at the contact surface between the two elements [139].

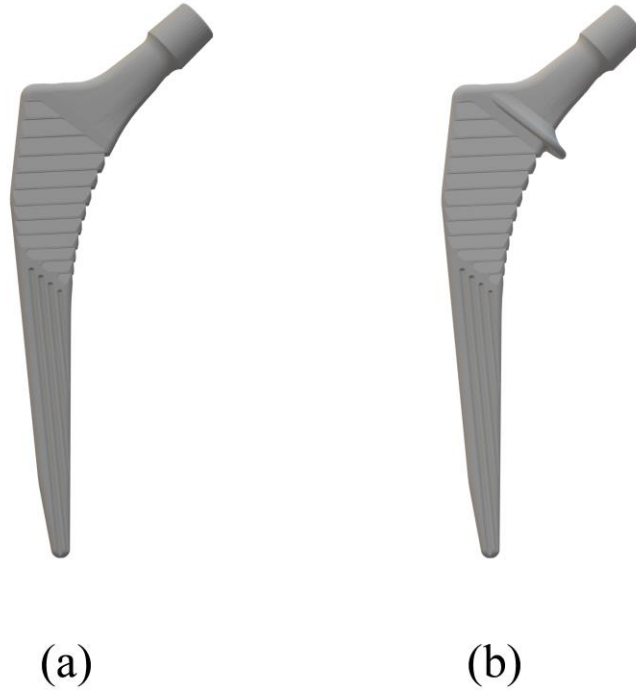


Figure 5. 1: Version of (a) collarless and (b) collared stem

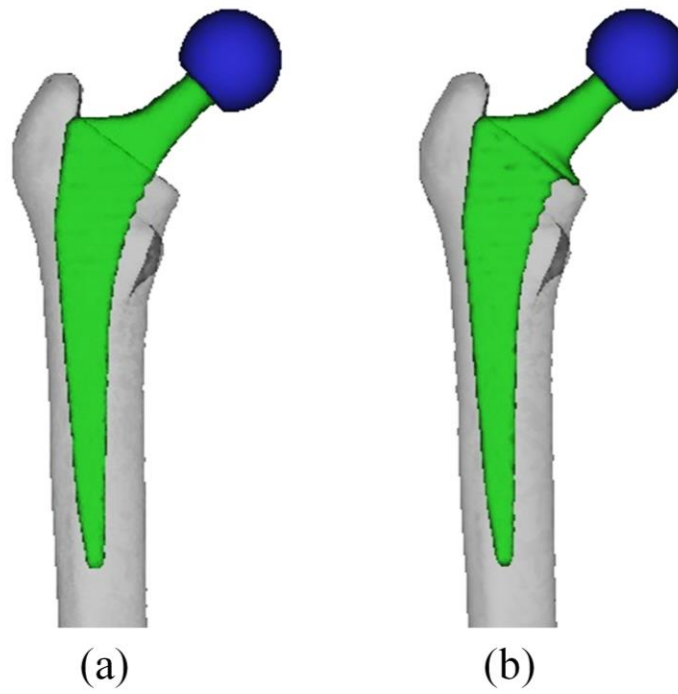


Figure 5. 2: THA model of (a) collarless and (b) collared stem

5.4 Loading and boundary conditions

Two different loading and boundary conditions were introduced into the nonlinear FE analysis in order to predict the damage formations of the THA femoral bones implanted with collarless and collared stem versions. Those conditions were denoted as axial compression condition (ACC) and torsional condition (TC). For ACC, the loading direction was set based on the angle of α and β , from the long axis of the femur in the frontal and sagittal plane, respectively. The orientation of the loading direction was $\alpha=180^\circ$, $\beta=0^\circ$. For TC, a realistic torsional behaviour on the femur was introduced where two loading directions were assigned at the proximal area of the stem i.e., femoral ball, that being covered with a hemispheric resin ($E=2.64$ GPa, poisson's ratio=0.4), which sufficient to produce a rotational motion to the bone and stem. The orientation of the bone was set to be parallel with the z-axis of the stem. Figure 5.3 shows the boundary condition of ACC and TC. The load was increased stepwise in six steps ranging from 294 N to 1764 N, which was subjected to 0.5 to 3.0 of the patient's body weight (BW) to determine the subsidence, micromotion, and bone damage formation between the collarless and collared stem.

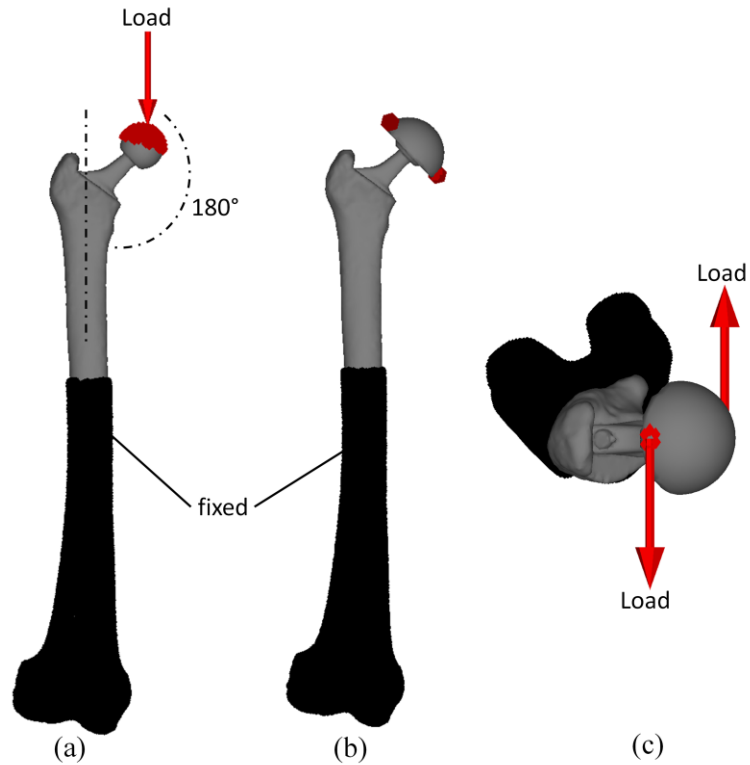


Figure 5. 3: Loading and boundary conditions: (a) axial compression condition (ACC), (b) anterior view of torsional condition (TC) and (c) superior view of torsion condition (TC)

5.5 Mechanical theories and material properties

The tensile deformation of all the elements constructing the femoral models was assumed to be expressed by the linear elastic response, in which the stress-strain relation was characterized by two material constants such as Young's modulus and Poisson's ratio. On the contrary, the compressive deformation of the elements was assumed to be expressed by the bi-linear elastic-plastic response, in which the stress-strain relation was characterized by Young's modulus and Poisson's ratio under the linear-elastic behaviour

and the yield stress and the work hardening coefficient under the plastic behaviour. The Drucker-Prager yield condition was used to assess the onset of yielding [108]. Yielding was assumed to take place when the Drucker-Prager equivalent stress reached the compressive yield stress. Young's modulus and the compressive yield stress of a solid element were calculated from the corresponding BMD value of the element using the empirical formulae proposed by Keyak et al. [127] and Keller [128]. Poisson's ratio and the work hardening coefficient of all the solid elements were set to 0.4 and 0.05, respectively. Those properties of each of the shell elements were chosen so that they were equivalent to those of the adjacent solid element located under its position.

The tensile fracture of a solid or a shell element was assumed to take place when the maximum principal stress reached the tensile strength which was equal to 0.8 times the compressive yield stress of the element [129], [130]. On the other hand, the compressive fracture of the element was assumed to occur when the minimum principal strain reached the fracture strain which was equal to -3,000 micro-strain [130], [131]. Aggregation of shell element failures is usually needed to express the femoral fracture of the outer cortical surface and compare the fracture behaviour between the intact and the THA models. Therefore, in this study, a critical condition was set on the basis of the number of failure elements. 1000 shell element failures were chosen as the condition and the analyses were terminated when the total number of shell element failures reached 1000 under either tensile stress or compressive stress state. The stress-strain responses of titanium alloy and alumina ceramic were assumed to be linear elastic. Young's modulus and Poisson's ratio were chosen to be 114 GPa and 0.34 for titanium alloy and 370 GPa and 0.22 for alumina ceramic [121].

5.6 Results and Discussion

5.6.1 Distribution of bone strain

Figures 5.4 and 5.5 show the maximum and minimum principal strain distribution at the bone areas surrounding the collarless and collared stem under ACC and TC, respectively. The illustration of strain distribution was compared at 1 BW load under a similar strain scale. The maximum and minimum principal strain refers to the bone deformation under the tensile and compressive state, respectively.

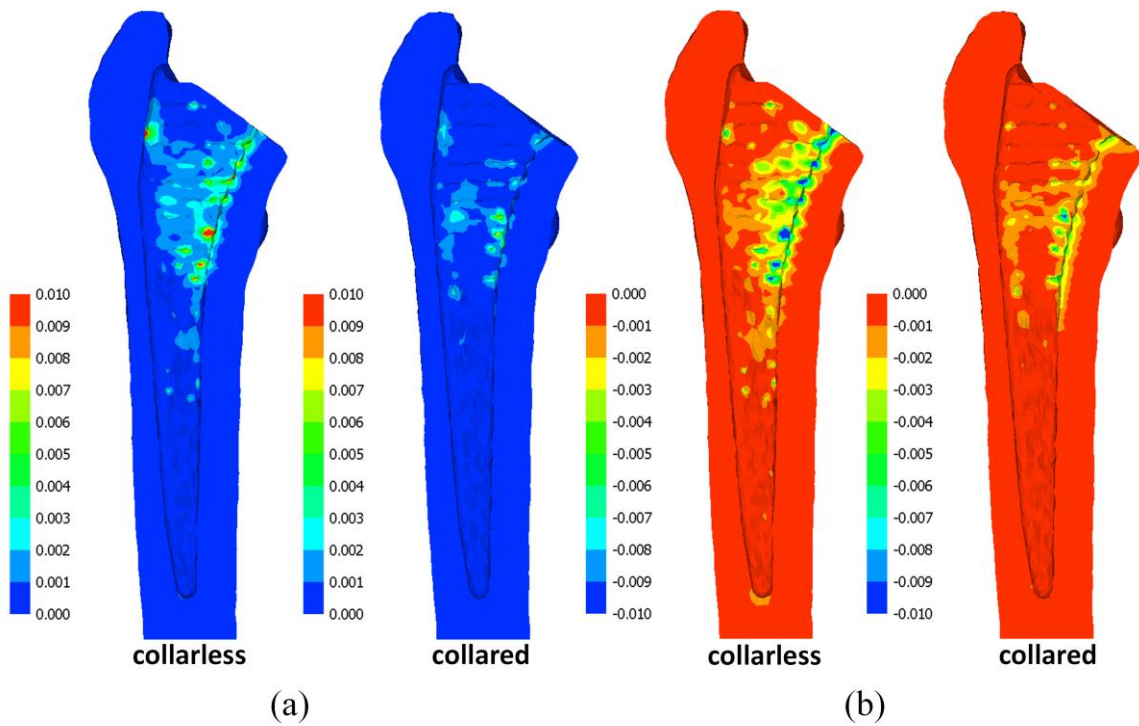


Figure 5. 4: Distribution of bone strain in (a) tensile and (b) compressive under ACC

In ACC, the distribution of tensile strain was located at the proximal bone areas for both the collarless and collared models. Larger strain value was observed in the collarless model than in the collared model. This can be seen in Figure 5.4 (a). In the case of compressive strain, higher values were noticed at the bone area located at the distal end of the collarless stem as shown in Figure 5.4 (b). In TC, the distribution pattern of bone strain was similar for both models under the tensile and compressive states, however, the collarless model exhibited higher strain values at the bone area compared to the collared model. The comparison can be observed in Figure 5.5 (a) and (b).

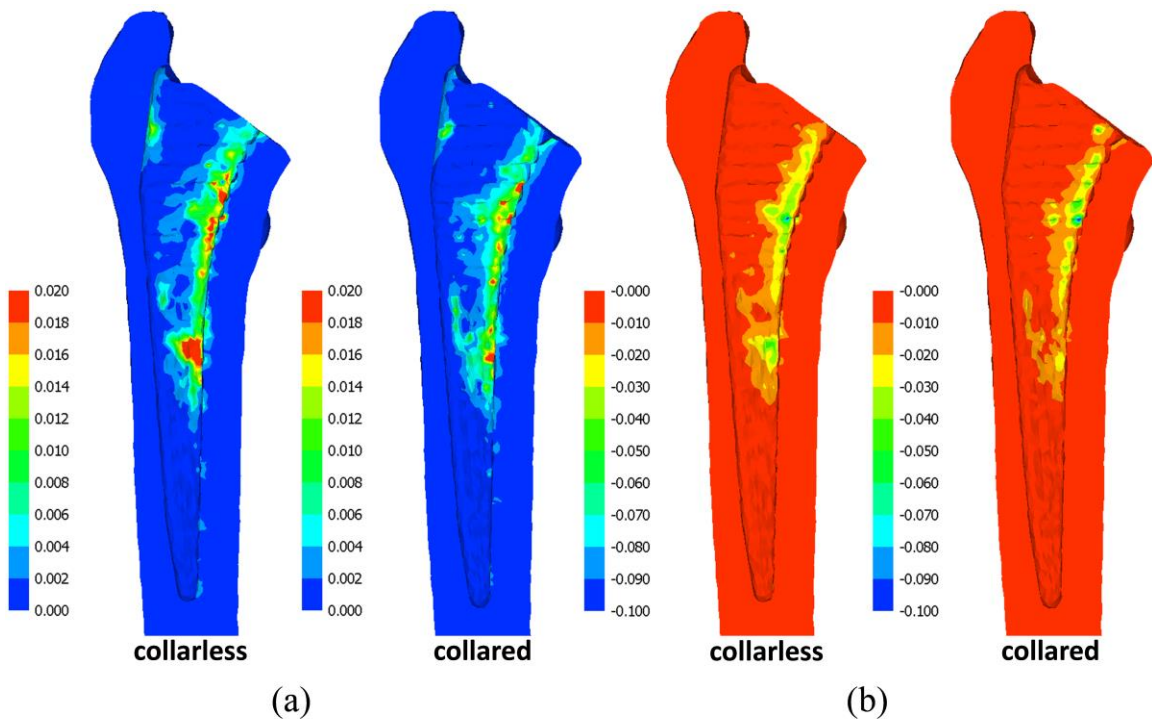


Figure 5. 5: Distribution of bone strain in (a) tensile and (b) compressive under TC

Figures 5.6 and 5.7 show a quantitative comparison of the average strain values in the bone for both stem versions under ACC and TC. The results indicate that the bone exhibited higher strain values with the collarless stem as compared to the collared stem in all load levels under both boundary conditions. The strain differences were more notable in ACC as compared to TC at lower load levels i.e., 0.5 BW to 2 BW, in both tensile and compressive state. This suggests that the presence of a collar has improved the axial stability of the stem but not the rotational stability. As a comparison, the percentage difference of maximum and minimum strain between both models at 1 BW under ACC was 23.64% and 18.92%, respectively, while under TC, the percentage difference was 4.74% and 7.67%, respectively. Significant differences were only noted at higher load levels under TC.

The proximal bone area within the femoral canal plays a critical role in providing the contact point for stem fixation to ensure implant stability and promotes osseointegration. Based on the results, the presence of a higher strain value at the bone area located at the fixation point of the stem indicates lesser implant stability, which could be due to the subsidence and micromotion of the implant after loaded. On the other hand, the results suggest that the presence of a collar has reduced the subsidence of the stem into the femoral canal, as high values of compressive strain were only noticed at the distal bone area of the collarless stem under ACC.

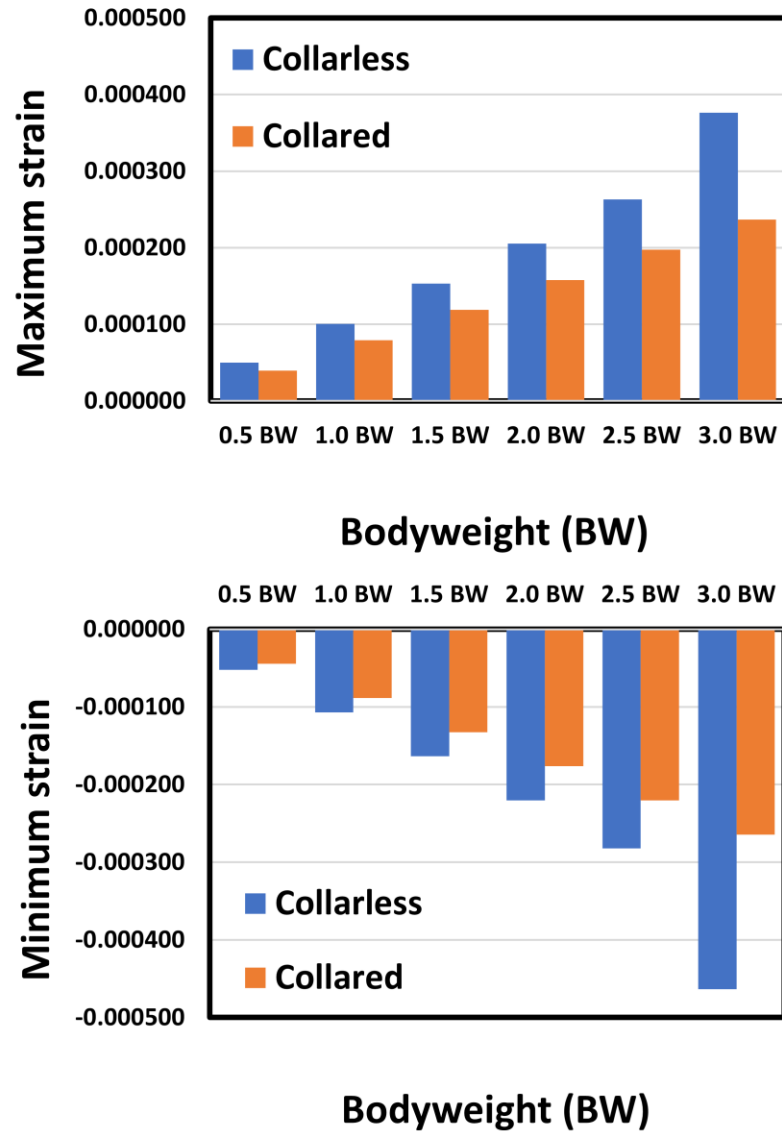


Figure 5. 6: Average value of maximum and minimum principal strain under ACC

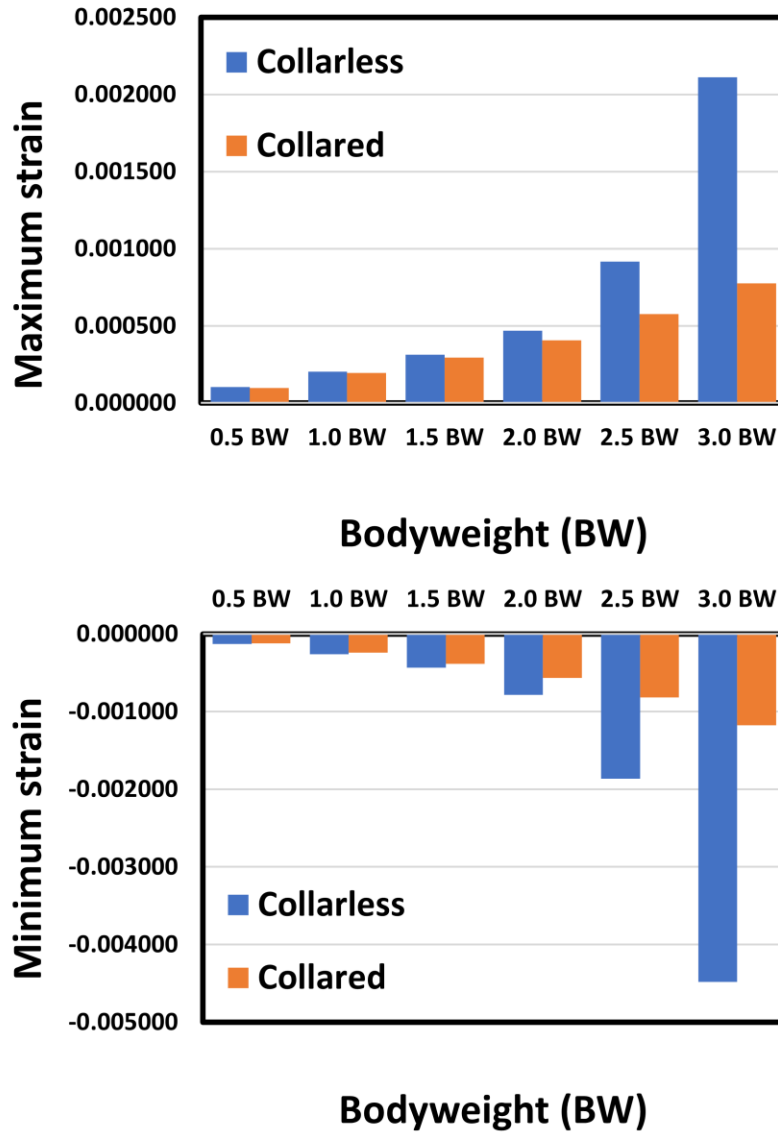


Figure 5. 7: Average value of maximum and minimum principal strain under TC

5.6.2 *Accumulation of bone element failures as bone micro-damage*

Figures 5.8 (a) and (b) show the cumulative number of solid failures under ACC and TC, respectively. Figures left and right corresponded to the element failures generated under tensile and compressive conditions, respectively. It can be seen that the solid element failures under compressive stress state were dominant compared to the tensile state for both ACC and TC. On the other hand, the number of solid element failures was seen to be higher in collarless stem compared to collared stem in every load level. The effects were much notable in ACC compared to TC. In ACC, the cumulative numbers of solid element failures in collarless stem tended to gradually increase until 2.5 BW, and rapidly increase at 3 BW. Meanwhile, the cumulative numbers in collared stem was seen to increase slowly until the final load levels. Under TC, the cumulative numbers tended to increase steadily until the final load levels. The pattern was similar in both stem models.

The cumulative numbers of shell element failures under ACC and TC are also shown in Figures 5.9 (a) and (b), respectively. Similar to the solid element failures, the compressive failures tended to be more dominant than the tensile failures in both boundary conditions. It is important to see that under ACC, only collarless model had experienced the shell element failures. Thus, the presence of collar tended to increase the bone strength under this boundary condition. The number of shell element failures under tension and compression was rapidly increased only at the final stage of loading i.e., 3 BW. In the case of TC, both models were seen to experience bone fracture. The cumulative pattern was seen to vary between the tensile and compressive conditions. In tensile condition, the cumulative numbers tended to increase, remain steady and increase again until final load levels, while, in compressive condition, the cumulative numbers tended to increase steadily

until the final load. The presence of collar has affected the strength of the bone, where in both tensile and compressive, the shell element failures in collared model tended to appear at higher load level compared to the collarless stem. In addition, the total number of shell element failures was higher in collarless than in collared under this boundary condition.

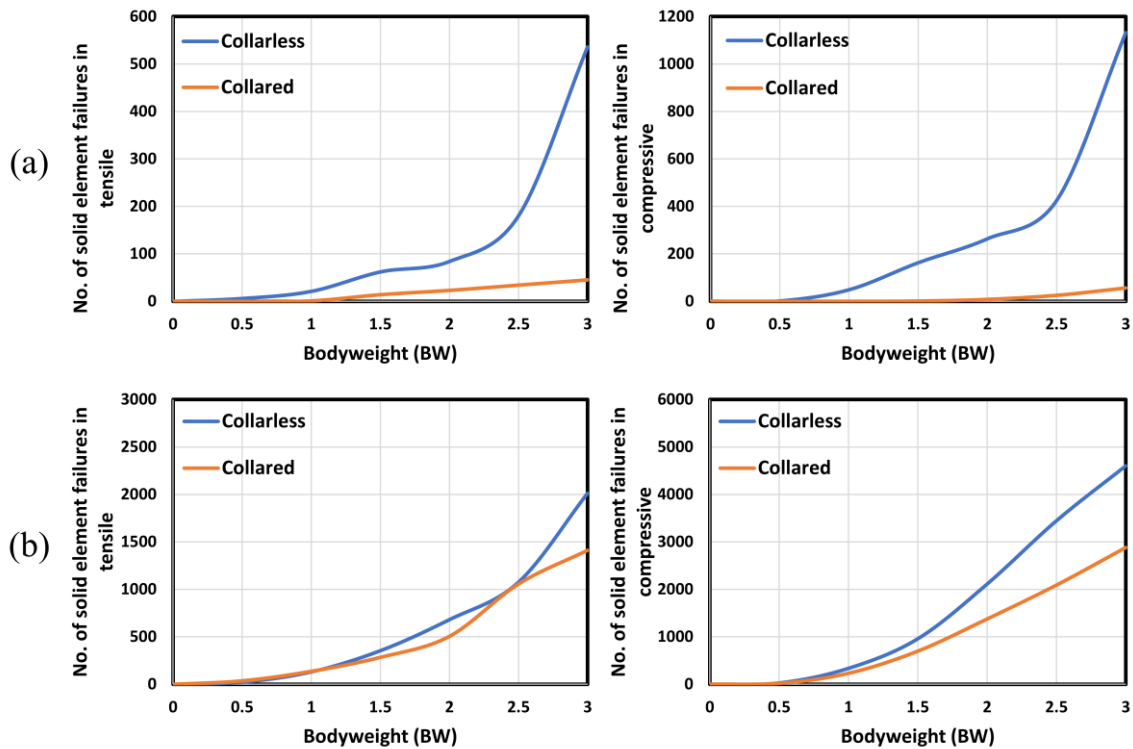


Figure 5. 8: Number of solid element failures in tensile (left) and compressive (right)

under (a) ACC and (b) TC

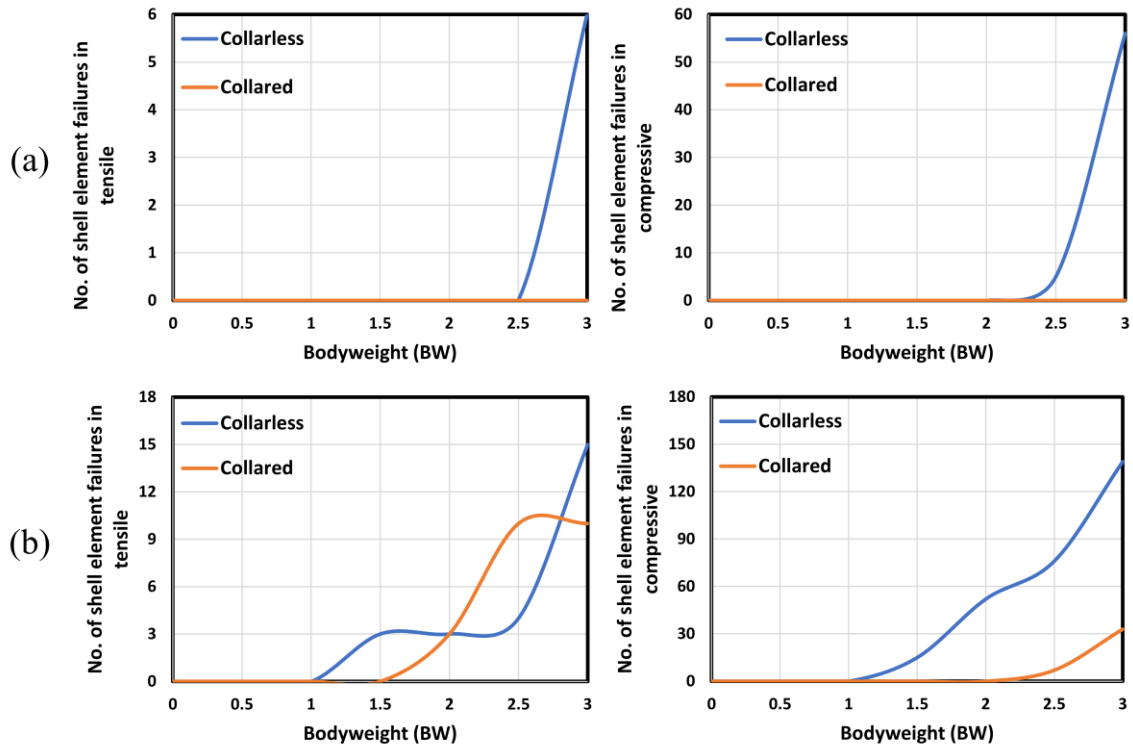


Figure 5. 9: Number of shell element failures in tensile (left) and compressive (right) under (a) ACC and (b) TC

5.6.3 Distribution of solid and shell element failures

Distribution patterns of solid element failures from 0.5 BW to 3 BW under ACC and TC were shown in Figures 5.10 and 5.11, respectively. The collarless and collared stems were represented by figures (a) and (b), respectively. Under ACC, it is clearly seen that the collarless model had greater internal bone damage than collared model in every load levels. Major element failures were observed to be accumulated at Gruen zone 7 while minor failures were noticed at Gruen zones 1 and 4 of the collarless model. On the other hand, the accumulation of element failures in collared model were only located at Gruen zone 7.

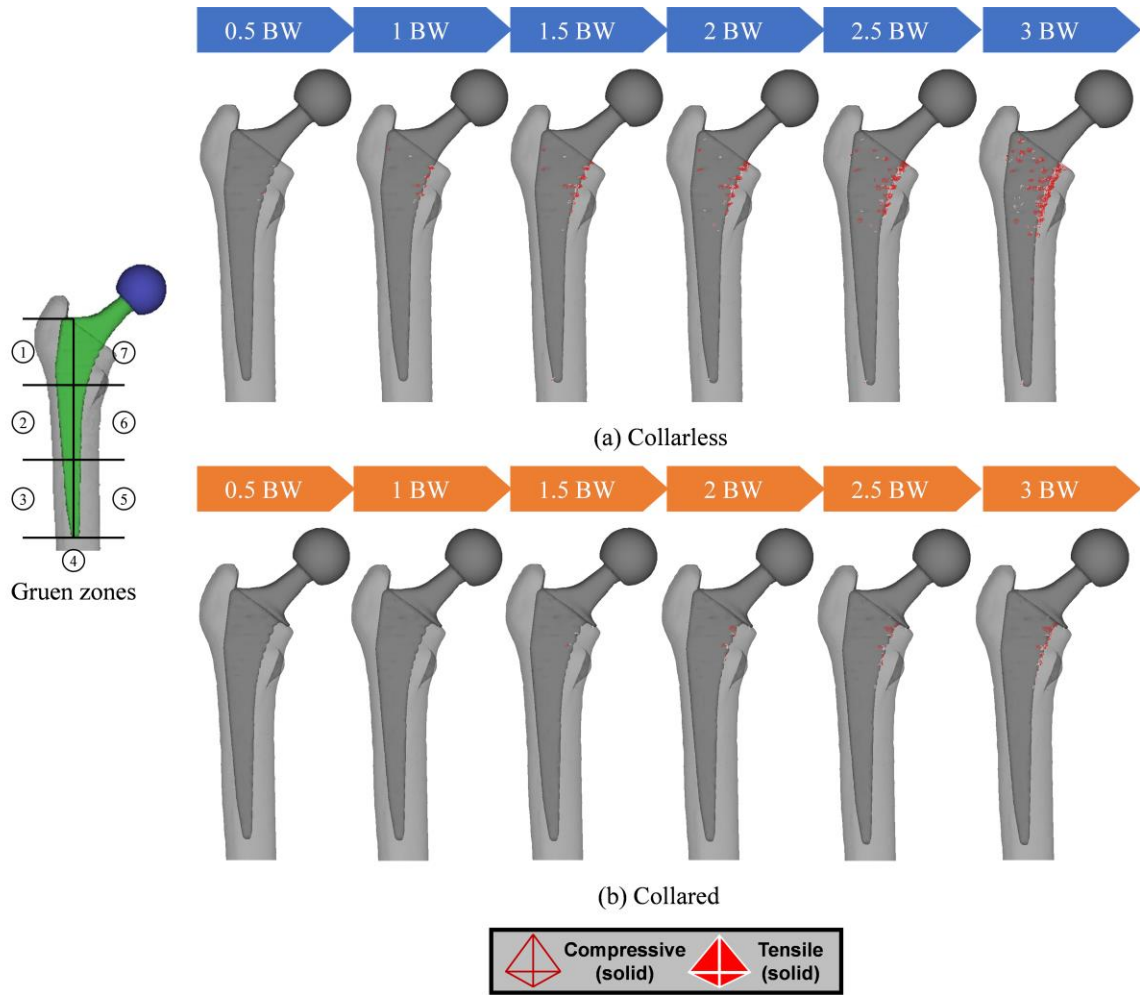


Figure 5. 10: Distribution of solid element failures under ACC

From the observation in TC, the element failures were initiated at Gruen zone 1, 6, and 7 in both collarless and collared models. This can be seen at 1 BW load. As the load increases, greater bone damages were accumulated at those respective regions. However, the distribution of element failures exhibited some variations at higher loads. Specifically, at 3 BW, the collarless model showed a notable accumulation of element failures in Gruen

zone 2, in contrast to the collared model, which experienced greater damage in Gruen zone 1 compared to the collarless model.

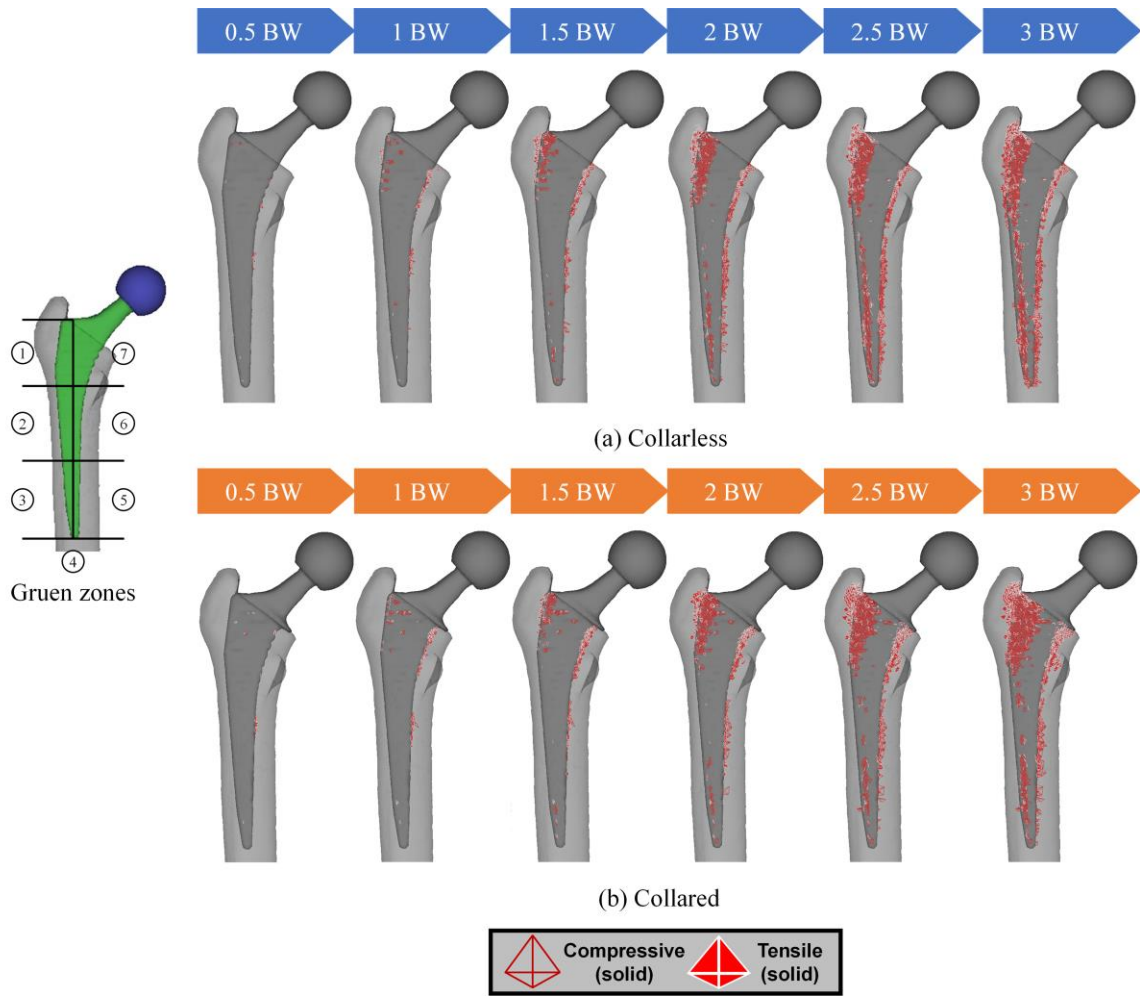


Figure 5. 11: Distribution of solid element failures under TC

The distribution of shell element failures was illustrated in Figures 5.12. Figures (a) and (b) corresponded to the condition of ACC and TC, respectively. In ACC, only the collarless model has experienced shell failures while in TC, the element failures occurred in both models. It was observed that the location of element failures under both boundary conditions were similar in both models which occurred at the proximal region of the bone.

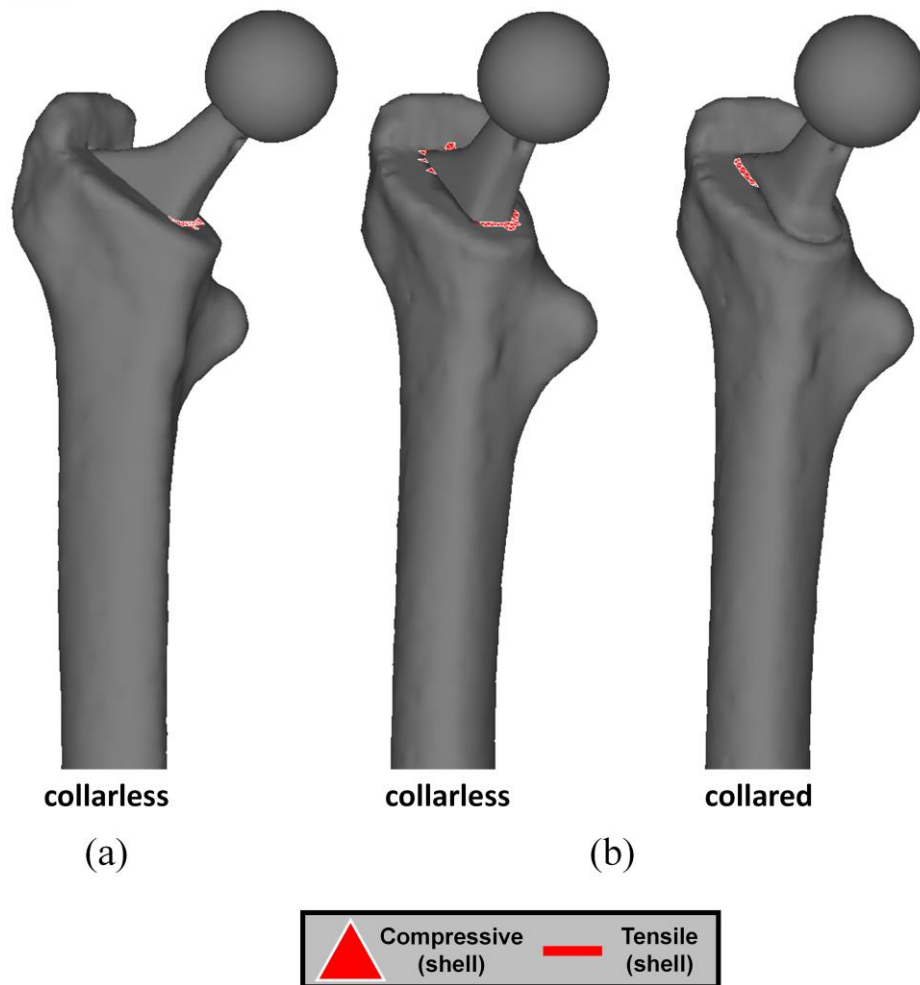


Figure 5. 12: Formation of shell element failures under (a) ACC and (b) TC

5.7 Conclusion

A collarless and collared versions of a similar THA stem were implanted into a FE bone model developed from CT image of 61-year-old patient with avascular necrosis. Finite element analysis with non-linear damage analysis was performed under axial compression (ACC) and torsional conditions (TC). The conclusions were obtained as follows:

- (1) The bone strain was found to be higher in the collarless stem compared to the collared stem in both tensile and compressive states. The difference was more significant under ACC, where the percentage difference in bone strain between the collarless and collared stems at a 1 BW load was 23.64% and 18.92% for the tensile and compressive states, respectively. Under TC, a much smaller percentage difference was observed with 4.74% and 7.67% for the tensile and compressive states, respectively. It is concluded that the presence of collar had improved the implant stability especially under axial loading.
- (2) The cumulative number of solid element failures in the collarless stem was much higher than in the collared stem in both boundary conditions and at all load levels. This difference was more significant under ACC compared to TC. It is concluded that implant with better stability could produce lesser damage as shown by the model with collared stem.
- (3) Under ACC, significant bone damage was found to accumulate at Gruen zone 7 in the internal region of the collarless model. Minor damage was also observed in Gruen zones 1 and 4 under the same conditions. In contrast, the collared model exhibited

bone damage only in Gruen zone 7. It is concluded that the risk of implant loosening after THA could be higher when implanted with collarless stem due to bone damages at several locations within the bone and stem interface.

- (4) Under TC, the initiation of bone damage was found in Gruen zones 1, 6, and 7 in both models. At a higher load, specifically 3 BW, a greater accumulation of element failures was observed in Gruen zone 2 for the collarless model and in Gruen zone 1 for the collared model.
- (5) Shell element failures were found to occur only in the collarless model under ACC. Under TC, shell failures occurred in both the collarless and collared models. It was observed that the bone in the collarless model experienced fractures at lower load levels compared to the collared model. The location of bone fracture was similar in both models. It is concluded that the presence of collar could increase the strength of the bone when implanted with collared stem, specifically under axial loading.

CHAPTER 6: GENERAL CONCLUSIONS

In this study, inhomogeneous FE bone models were successfully developed from the CT-images of avascular necrosis patients and those models were implanted with several types of THA stem. Non-linear finite element analyses with elemental damage models were then conducted to investigate the mechanism of bone damage formation in each of the femoral bone, simulated under several types of boundary conditions. The results of this work can be summarized as follows:

1. In Chapter 2, two inhomogeneous femoral bone models from CT-image of avascular necrosis patients were successfully developed, and denoted with bone X and bone Y. The quality between the two bones were successfully evaluated through the quantitative comparison of BMD distribution at the head and neck region of both femurs. It was found that the BMD distribution in the head and neck region showed a similar pattern, but different BMD values were obtained from the two bones. Therefore, it is understood that different bones will have different qualities. The mechanism of bone micro-damage in the internal bone region was successfully depicted by analysing the cumulative number of solid element failures under two types of isometric loadings namely, lateral bending (LBC) and torsional conditions (TC). It was found that the cumulative number of element failures could explain the effect of stem design on the internal condition of the bone, including its internal strength and severity of bone damage, especially in bone with good quality. However, the effect of stem design was found to be small for poor bone quality under the two boundary conditions, i.e., LBC and TC. This research highlights the pivotal role of

the stem shoulder size and cross-sectional shape in shaping the internal bone damage of high-quality bone (bone X). Notably, stems with smaller shoulder sizes and round cross-sectional shapes exhibited early and higher levels of bone damage under torsional conditions when compared to stems with larger shoulders and rectangular cross-sectional shapes. These discoveries hold valuable implications for the advancement of THA implant design. By understanding the influence of stem geometry on bone micro-damage, designers and researchers can tailor their approaches to optimize implant designs for improved clinical outcomes. Future research endeavours may focus on conducting comparative studies with a broader range of implant designs to enhance our understanding of bone micro-damage patterns across various bone qualities.

2. In Chapter 3, similar bone models of bone X and bone Y were used to investigate the effect of bone quality and implant design under several falling configurations, which simulated falls onto the lateral and posterolateral sides of the femur. By applying a similar concept as in Chapter 2, it was found that the effect of stem design influenced the mechanism of bone micro-damage in the internal region of high-quality bone (bone X) during falls. The bone damage in bone X was observed to initiate at different load levels when implanted with different stem design. However, the influence was found to be insignificant in bone Y. Overall, these findings underscore the importance of stem design in the context of bone fracture vulnerability and internal bone micro-damage. The results of this study may have practical implications for the development of THA implants, particularly in enhancing rotational stability and minimizing bone damage risks in traumatic incidents, such as

sideways falls. The significance of femoral osteotomy in current surgical practices is highlighted as a means to mitigate excessive bone removal when employing stems with longer neck lengths. Additionally, bone quality was found to have notable influence on the formation of bone damage. Thus, future research could delve deeper into the specific factors influencing fracture load and bone micro-damage, considering variations in patient characteristics and implant materials and designs.

3. In Chapter 4, further analysis was conducted to determine other potential factors that could affect the performance of a THA femur, through the bone damage analysis. The relationship between age and BMD was determined based on 28 FE femoral models developed from AVN patients, which results in moderate correlation ($r = -0.69$). Here, it is understood that age alone is not an absolute indicator of lower BMD, but it does influence on the reduction of BMD. From the 28 femurs, 10 were selected for implantation. Again, the relationship between BMD and fracture load was investigated. All implanted models were assigned with three different boundary conditions namely, stance (SC), lateral bending (LBC), and torsional (TC) conditions and a monotonic load with 10 N load increment was assigned to all models until bone fracture. Strong correlations between BMD and fracture load were observed in all boundary conditions (SC, $r = 0.74$), (LBC, $r = 0.79$), (TC, $r = 0.88$), suggesting that BMD is an important factor in assessing fracture risk from the outer cortical bone. However, moderate correlation was observed between BMD and bone strength from the internal region of the bone (SC, $r = -0.40$), (LBC, $r = -0.51$), (TC, $r = -0.48$), suggesting the performance after THA can be influenced by other factors. In conclusion, the findings from the study highlight crucial considerations for THA in

patients with varying bone qualities. Specifically, bones with thin cortical cortices present a higher risk of complications due to significant bone damage at the bone and stem interface, suggesting that these cases may not be suitable for undergoing cementless THA. Additionally, in femurs without thin cortices, factors such as bent femoral shaft geometry and retroversion implant placement contribute to elevated bone damage. To address these challenges and improve THA outcomes, future research should focus on several key areas. Mechanistic studies are warranted to understand the biomechanical forces acting on bones with thin cortical cortices during THA, facilitating the development of personalized implant designs and surgical strategies. Patient-specific preoperative planning tools, incorporating advanced imaging and modeling techniques, hold promise for optimizing implant selection and placement based on individual bone properties. On the other hand, to address the challenges of femoral shaft geometry, in-depth biomechanical analyses should be conducted to comprehend how bent femoral shafts impact load distribution, stress patterns, and stability during THA. Advanced computational modeling and in vitro testing can provide valuable insights. Meanwhile, adjustable implants specifically at the neck region may be useful to mitigate the problem with retroverted femoral head, to avoid retroversion placement of the THA stem.

4. In Chapter 5, collarless and collared versions of a similar stem were implanted into a finite element (FE) model developed from CT images of a 61-year-old patient with AVN. The primary stability between these two designs was investigated based on bone strain analysis under two different boundary conditions: axial compression (ACC) and torsional conditions (TC). It was found that the bone strain surrounding

the collarless stem was much higher than that surrounding the collared stem, suggesting that the collarless stem produced higher micromotion. The results were more pronounced in ACC compared to TC, indicating that the presence of a collar improved the axial stability of the THA stem. Furthermore, less bone micro-damage formation was observed in the internal bone region when the bone was implanted with the collared stem, and the presence of the collar increased the bone strength under ACC. In TC, it was found that the presence of the collar did influence the reduction of bone micro-damage in the internal bone region and increase the bone strength; however, the difference was small compared to the collarless stem. This discovery provides evidence that a basic modification to the THA stem, specifically the addition of a collar, has the potential to enhance postoperative results following THA. Moreover, it offers valuable insights for the development of more sophisticated implant designs.

REFERENCES

- [1] M. Fu, H. Zhou, Y. Li, H. Jin, and X. Liu, “Global, regional, and national burdens of hip osteoarthritis from 1990 to 2019: estimates from the 2019 Global Burden of Disease Study,” *Arthritis Research and Therapy*, vol. 24, no. 1, pp. 1–11, 2022, doi: 10.1186/s13075-021-02705-6.
- [2] E. W. Karlson, L. A. Mandl, G. N. Aweh, O. Sangha, M. H. Liang, and F. Grodstein, “Total hip replacement due to osteoarthritis: The importance of age, obesity, and other modifiable risk factors,” *American Journal of Medicine*, vol. 114, no. 2, pp. 93–98, 2003, doi: 10.1016/S0002-9343(02)01447-X.
- [3] C. Y. Chung, M. S. Park, K. M. Lee, S. H. Lee, T. K. Kim, K. W. Kim, J. H. Park, and J. J. Lee, “Hip osteoarthritis and risk factors in elderly Korean population,” *Osteoarthritis and Cartilage*, vol. 18, no. 3, pp. 312–316, 2010, doi: 10.1016/j.joca.2009.11.004.
- [4] R. K. Chaganti and N. E. Lane, “Risk factors for incident osteoarthritis of the hip and knee,” *Current Reviews in Musculoskeletal Medicine*, vol. 4, no. 3, pp. 99–104, 2011, doi: 10.1007/s12178-011-9088-5.
- [5] S. M. Kurtz, E. Lau, K. Ong, K. Zhao, M. Kelly, and K. J. Bozic, “Future young patient demand for primary and revision joint replacement: National projections from 2010 to 2030,” *Clinical Orthopaedics and Related Research*, vol. 467, no. 10, pp. 2606–2612, 2009, doi: 10.1007/s11999-009-0834-6.

- [6] A. A. Kiadaliri, G. Rinaldi, L. S. Lohmander, I. F. Petersson, and M. Englund, “Temporal trend and regional disparity in osteoarthritis hospitalisations in Sweden 1998–2015,” *Scandinavian Journal of Public Health*, vol. 47, no. 1, pp. 53–60, 2019, doi: 10.1177/1403494818766785.
- [7] I. N. Ackerman, J. L. Kemp, K. M. Crossley, A. G. Culvenor, and R. S. Hinman, “Hip and knee osteoarthritis affects younger people, too,” *Journal of Orthopaedic and Sports Physical Therapy*, vol. 47, no. 2, pp. 67–79, 2017, doi: 10.2519/jospt.2017.7286.
- [8] P. Dieppe, “Developments in osteoarthritis,” *Rheumatology*, vol. 50, no. 2, pp. 245–247, 2011, doi: 10.1093/rheumatology/keq373.
- [9] J. Parvizi and R. Ganz, “Hip Osteoarthritis,” *Orthopedics*, vol. 26, no. 11, pp. 1099–1109, 2003, doi: 10.3928/0147-7447-20031101-04.
- [10] B. H. Yoon, M. A. Mont, K. H. Koo, C. H. Chen, E. Y. Cheng, Q. Cui, W. Drescher, V. Ganji, S. B. Goodman, Y. C. Ha, P. Hernigou, M. W. Hungerford, R. Iorio, W. L. Jo, L. C. Jones, V. Khanduja, H. K. W. Kim, S. Y. Kim, T. Y. Kim, H. Y. Lee, M. S. Lee, Y. K. Lee, Y. J. Lee, J. Nakamura, J. Parvizi, T. Sakai, N. Sugano, M. Takao, T. Yamamoto, D. W. Zhao, “The 2019 Revised Version of Association Research Circulation Osseous Staging System of Osteonecrosis of the Femoral Head,” *Journal of Arthroplasty*, vol. 35, no. 4, pp. 933–940, 2020, doi: 10.1016/j.arth.2019.11.029.
- [11] G. J. M. L. Gary, “Osteonecrosis of the Femoral Head,” *Journalism*, vol. 11, no. 3,

pp. 369–373, 2010, doi: 10.1177/1461444810365020.

- [12] M. A. Mont, L. C. Jones, and D. S. Hungerford, “Current concepts review - Nontraumatic osteonecrosis of the femoral head: Ten years later,” *Journal of Bone and Joint Surgery*, vol. 88, no. 5, pp. 1117–1132, 2006, doi: 10.2106/JBJS.E.01041.
- [13] M. A. Mont, M. G. Zywiell, D. R. Marker, M. S. McGrath, and R. E. Delanois, “The natural history of untreated asymptomatic osteonecrosis of the femoral head: A systematic literature review,” *Journal of Bone and Joint Surgery*, vol. 92, no. 12, pp. 2165–2170, 2010, doi: 10.2106/JBJS.I.00575.
- [14] M. A. Mont, J. J. Cherian, R. J. Sierra, L. C. Jones, and J. R. Lieberman, “Nontraumatic osteonecrosis of the femoral head: Where do we stand today? A ten-year update,” *Journal of Bone and Joint Surgery - American Volume*, vol. 97, no. 19, pp. 1604–1627, 2014, doi: 10.2106/JBJS.O.00071.
- [15] K. Ikeuchi, Y. Hasegawa, T. Seki, Y. Takegami, T. Amano, and N. Ishiguro, “Epidemiology of nontraumatic osteonecrosis of the femoral head in Japan,” *Modern Rheumatology*, vol. 25, no. 2, pp. 278–281, 2015, doi: 10.3109/14397595.2014.932038.
- [16] J. S. Kang, K. H. Moon, D. G. Kwon, B. K. Shin, and M. S. Woo, “The natural history of asymptomatic osteonecrosis of the femoral head.” *International orthopaedics*, vol. 37, no. 3, pp. 379–384, 2013, doi: 10.1007/s00264-013-1775-y.
- [17] D. Petek, D. Hannouche, and D. Suva, “Osteonecrosis of the femoral head: Pathophysiology and current concepts of treatment,” *EFORT Open Reviews*, vol. 4,

no. 3, pp. 85–97, 2019, doi: 10.1302/2058-5241.4.180036.

- [18] L. Wells, N. P. Sheth, J. R. H. Foran, M. D. Miller, “Osteonecrosis of the Hip,” *orthoinfo.aaos.org*. <https://orthoinfo.aaos.org/en/diseases-conditions/osteonecrosis-of-the-hip> (accessed May 15, 2023).
- [19] S. Fransen, M; McConnell, S; Hernandez-Molina, G; Reichenbach, “Exercise for osteoarthritis of the hip and knee,” *Annual Review of Gerontology and Geriatrics*, vol. 36, no. 1, pp. 155–168, 2016, doi: 10.1891/0198-8794.36.155.
- [20] W. Zhang, M. Doherty, N. Arden, B. Bannwarth, J., Bijlsma, K-P. Gunther, H. J. Hauselmann, G. Herrero-Beaumont, K. Jordan, P. Kaklamanis, B. Leeb, M. Lequesne, S.Lohmander, B. Mazieres, E. Martin-Mola, K. Pavelka, A. Pendleton, L. Punzi, B. Swoboda, R. Varatojo, G. Verbruggen, I, Zimmermann-Gorska, M. Dougados, “EULAR evidence based recommendations for the management of hip osteoarthritis: Report of a task force of the EULAR Standing Committee for International Clinical Studies Including Therapeutics (ESCISIT),” *Annals of the Rheumatic Diseases*, vol. 64, no. 5, pp. 669–681, 2005, doi: 10.1136/ard.2004.028886.
- [21] C. Reyes, K. M. Leyland, G. Peat, C. Cooper, N. K. Arden, and D. Prieto-Alhambra, “Association Between Overweight and Obesity and Risk of Clinically Diagnosed Knee, Hip, and Hand Osteoarthritis: A Population-Based Cohort Study,” *Arthritis and Rheumatology*, vol. 68, no. 8, pp. 1869–1875, 2016, doi: 10.1002/art.39707.
- [22] M. C. Hochberg, R. D. Altman, K. T. April, M. Benkhalti, G. Guyatt, J. McGowan,

- T. Towheed, V. Welch, G. Wells, P. Tugwell, “American College of Rheumatology 2012 recommendations for the use of nonpharmacologic and pharmacologic therapies in osteoarthritis of the hand, hip, and knee,” *Arthritis Care and Research*, vol. 64, no. 4, pp. 465–474, 2012, doi: 10.1002/acr.21596.
- [23] L. Shan, B. Shan, D. Graham, and A. Saxena, “Total hip replacement: A systematic review and meta-analysis on mid-term quality of life,” *Osteoarthritis and Cartilage*, vol. 22, no. 3, pp. 389–406, 2014, doi: 10.1016/j.joca.2013.12.006.
- [24] G. G. Polkowski, J. J. Callaghan, M. A. Mont, and J. C. Clohisy, “Total hip arthroplasty in the very young patient,” *Journal of the American Academy of Orthopaedic Surgeons*, vol. 20, no. 8, pp. 487–497, 2012, doi: 10.5435/JAAOS-20-08-487.
- [25] R. Pivec, A. J. Johnson, S. C. Mears, and M. A. Mont, “Hip arthroplasty,” *The Lancet*, vol. 380, no. 9855, pp. 1768–1777, Nov. 2012, doi: 10.1016/S0140-6736(12)60607-2.
- [26] R. J. Ferguson, A. J. Palmer, A. Taylor, M. L. Porter, H. Malchau, and S. Glyn-Jones, “Hip replacement,” *The Lancet*, vol. 392, no. 10158, pp. 1662–1671, 2018, doi: 10.1016/S0140-6736(18)31777-X.
- [27] H. Jared, R; Foran, “Total Hip Replacement,” *orthoinfo.aaos.org*. <https://orthoinfo.aaos.org/en/treatment/total-hip-replacement/> (accessed May 15, 2023).
- [28] H. Katano, N. Ozeki, Y. Kohno, Y. Nakagawa, H. Koga, T. Watanabe, T. Jinno, and

- I. Sekiya, "Trends in arthroplasty in Japan by a complete survey, 2014–2017," *Journal of Orthopaedic Science*, vol. 26, no. 5, pp. 812–822, 2021, doi: 10.1016/j.jos.2020.07.022.
- [29] C. Pabinger, H. Lothaller, N. Portner, and A. Geissler, "Projections of hip arthroplasty in OECD countries up to 2050," *HIP International*, vol. 28, no. 5, pp. 498–506, 2018, doi: 10.1177/1120700018757940.
- [30] Z. K. Wszolek and R. F. Pfeiffer, *Swedish Arthroplasty Register Annual report 2014.*, vol. 21, no. 5. 2015.
- [31] S. Kurtz, K. Ong, E. Lau, F. Mowat, and M. Halpern, "Projections of primary and revision hip and knee arthroplasty in the United States from 2005 to 2030," *Journal of Bone and Joint Surgery - Series A*, vol. 89, no. 4, pp. 780–785, 2007, doi: 10.2106/JBJS.F.00222.
- [32] K. J. Bozic, S. M. Kurtz, E. Lau, K. Ong, D. T. P. Vail, and D. J. Berry, "The epidemiology of revision total hip arthroplasty in the united states," *Journal of Bone and Joint Surgery*, vol. 91, no. 1, pp. 128–133, 2009, doi: 10.2106/JBJS.H.00155.
- [33] S. A. Lie, L. I. Havelin, O. N. Furnes, L. B. Engesæster, and S. E. Vollset, "Failure rates for 4762 revision total hip arthroplasties in the Norwegian arthroplasty register," *Journal of Bone and Joint Surgery - Series B*, vol. 86, no. 4, pp. 504–509, 2004, doi: 10.1302/0301-620x.86b4.14799.
- [34] N. N. Mahomed, J. A. Barrett, J. N. Katz, C. B. Phillips, E. Losina, R. A. Lew, E. Guadagnoli, W. H. Harris, R. Poss, J. A. Baron, "Rates and outcomes of primary

and revision total hip replacement in the united states medicare population,” *Journal of Bone and Joint Surgery*, vol. 85, no. 1, pp. 27–32, 2003, doi: 10.2106/00004623-200301000-00005.

- [35] D. Douglas A, “Revision total knee arthroplasty,” *AAOS Comprehensive Orthopaedic Review* 2, vol. 1, pp. 1305–1316, 2018.
- [36] A. K. Jaffer, W. K. Barsoum, V. Krebs, J. G. Hurbanek, N. Morra, and D. J. Brotman, “Duration of Anesthesia and Venous Thromboembolism After Hip and Knee Arthroplasty,” *Mayo Clinic Proceedings*, vol. 80, no. 6, pp. 732–738, 2005, doi: 10.4065/80.6.732.
- [37] M. Khatod, T. Barber, E. Paxton, R. Namba, and D. Fithian, “An analysis of the risk of hip dislocation with a contemporary total joint registry,” *Clinical Orthopaedics and Related Research*, vol. 447, no. 447, pp. 19–23, 2006, doi: 10.1097/01.blo.0000218752.22613.78.
- [38] G. Peersman, R. Laskin, J. Davis, and M. Peterson, “Infection in Total Knee Replacement,” *Clinical Orthopaedics and Related Research*, vol. 392, no. 392, pp. 15–23, 2001, doi: 10.1097/00003086-200111000-00003.
- [39] L. Pulido, J. Parvizi, M. Macgibeny, P. F. Sharkey, J. J. Purtill, R. H. Rothman, and W. J. Hozack, “In Hospital Complications After Total Joint Arthroplasty,” *Journal of Arthroplasty*, vol. 23, no. 6 SUPPL., pp. 139–145, 2008, doi: 10.1016/j.arth.2008.05.011.
- [40] A. Lübbecke, J. N. Katz, T. V. Perneger, and P. Hoffmeyer, “Primary and revision

hip arthroplasty: 5-Year outcomes and influence of age and comorbidity,” *Journal of Rheumatology*, vol. 34, no. 2, pp. 394–400, 2007.

- [41] S. Patil, D. S. Garbuz, N. V. Greidanus, B. A. Masri, and C. P. Duncan, “Quality of Life Outcomes in Revision vs Primary Total Hip Arthroplasty. A Prospective Cohort Study,” *Journal of Arthroplasty*, vol. 23, no. 4, pp. 550–553, 2008, doi: 10.1016/j.arth.2007.04.035.
- [42] A. F. Mavrogenis, R. Dimitriou, J. Parvizi, G. C. Babis, “Biology of implant osseointegration,” *University of Connecticut Health Center*, vol. 103, no. 2, pp. e22-5, 2011.
- [43] B. M. Wroblewski, P. D. Siney, and P. A. Fleming, “Triple taper polished cemented stem in total hip arthroplasty: Rationale for the design, surgical technique, and 7 years of clinical experience,” *Journal of Arthroplasty*, vol. 16, no. 8 SUPPL. 1, pp. 37–41, 2001, doi: 10.1054/arth.2001.28374.
- [44] E. T. Ek and P. F. M. Choong, “Comparison between triple-tapered and double-tapered cemented femoral stems in total hip arthroplasty: A prospective study comparing the c-stem versus the exeter universal early results after 5 years of clinical experience,” *Journal of Arthroplasty*, vol. 20, no. 1, pp. 94–100, 2005, doi: 10.1016/j.arth.2004.08.012.
- [45] A. Stefánsdóttir, H. Franzén, R. Johnsson, E. Ornstein, and M. Sundberg, “Movement pattern of the Exeter femoral stem: A radiostereometric analysis of 22 primary hip arthroplasties followed for 5 years,” *Acta Orthopaedica Scandinavica*,

vol. 75, no. 4, pp. 408–414, 2004, doi: 10.1080/00016470410001169-1.

- [46] H. W. J. Huiskes, R. Boeklagen, “Mathematical Shape Optimization of Hip Prosthesis Design,” *Journal of Biomechanics*, vol. 22, no. 8, pp. 793-804, 1989, doi: 10.1016/0021-9290(89)90063-8.
- [47] A. G. Della Valle, A. Zoppi, M. G. E. Peterson, and E. A. Salvati, “A rough surface finish adversely affects the survivorship of a cemented femoral stem,” *Clinical Orthopaedics and Related Research*, vol. 436, no. 436, pp. 158–163, 2005, doi: 10.1097/00003086-200507000-00024.
- [48] R. D. Crowninshield, J. D. Jennings, M. L. Laurent, and W. J. Maloney, “Cemented femoral component surface finish mechanics,” *Clinical Orthopaedics and Related Research*, vol. 355, no. 355, pp. 90–102, 1998, doi: 10.1097/00003086-199810000-00010.
- [49] A. Ong, K. L. Wong, M. Lai, J. P. Garino, and M. E. Steinberg, “Early Failure of Precoated Femoral Components in Primary Total Hip Arthroplasty,” *The Journal of Bone and Joint Surgery*, vol. 84, no. 5, pp. 786-792 , 2002, doi: 10.2106/00004623-200205000-00014.
- [50] C. A. Engh, D. O’Connor, M. Jasty, and H. H. William, “Quantification of Implant Micromotion, Strain Shielding, and Bone Resorption With Porous-Coated Anatomic Medullary Locking Femoral Prostheses,” *Clinical Orthopaedics and Related Research*, vol. 285, pp. 13-29, 1992, doi: <https://doi.org/10.1097/00003086-199212000-00005>.

- [51] R. M. Pilliar, J. M. Lee, and C. Maniopoulos, "Observations on the effect of movement on bone ingrowth into porous-surfaced implants," *Clinical Orthopaedics and Related Research*, vol. 208. pp. 108–113, 1986, doi: 10.1097/00003086-198607000-00023.
- [52] M. Jasty, C. Bragdon, D. Burke, D. O'Connor, J. Lowenstein, and W. H. Harris, "In vivo skeletal responses to porous-surfaced implants subjected to small induced motions," *Journal of Bone and Joint Surgery*, vol. 79, no. 5, pp. 707–714, 1997, doi: 10.2106/00004623-199705000-00010.
- [53] H. S. Khanuja, J. J. Vakil, M. S. Goddard, and M. A. Mont, "Cementless femoral fixation in total hip arthroplasty," *Journal of Bone and Joint Surgery*, vol. 93, no. 5, pp. 500–509, 2011, doi: 10.2106/JBJS.J.00774.
- [54] E. J. Vresilovic, W. J. Hozack, and R. H. Rothman, "Radiographic assessment of cementless femoral components. Correlation with intraoperative mechanical stability," *The Journal of Arthroplasty*, vol. 9, no. 2, pp. 137–141, 1994, doi: 10.1016/0883-5403(94)90062-0.
- [55] R. K. Sinha, D. S. Dungy, and H. B. Yeon, "Primary total hip arthroplasty with a proximally porous-coated femoral stem," *Journal of Bone and Joint Surgery*, vol. 86, no. 6, pp. 1254–1261, 2004, doi: 10.2106/00004623-200406000-00019.
- [56] J. W. H. Luites, M. Spruit, G. G. V. Hellemondts, W. G. Horstmann, and E. R. Valstar, "Failure of the uncoated titanium proxilock femoral hip prosthesis," *Clinical Orthopaedics and Related Research*, vol. 448, no. 448, pp. 79–86, 2006,

doi: 10.1097/01.blo.0000224011.12175.83.

- [57] A. V. Lombardi, K. R. Berend, T. H. Mallory, M. D. Skeels, and J. B. Adams, “Survivorship of 2000 tapered titanium porous plasma-sprayed femoral components,” *Clinical Orthopaedics and Related Research*, vol. 467, no. 1, pp. 146–154, 2009, doi: 10.1007/s11999-008-0568-x.
- [58] R. B. Bourne, C. H. Rorabeck, J. J. Patterson, and J. Guerin, “Tapered titanium cementless total hip replacements: A 10- to 13-year followup study,” *Clinical Orthopaedics and Related Research*, vol. 393, no. 393, pp. 112–120, 2001, doi: 10.1097/00003086-200112000-00013.
- [59] H. Wagner and M. Wagner, “Cone prosthesis for the hip joint,” *Archives of Orthopaedic and Trauma Surgery*, vol. 120, no. 1–2, pp. 88–95, 2000, doi: 10.1007/PL00021223.
- [60] K. Zweymüller and M. Semlitsch, “Concept and material properties of a cementless hip prosthesis system with Al₂O₃ ceramic ball heads and wrought Ti-6Al-4V Stems,” *Archives of Orthopaedic and Traumatic Surgery*, vol. 100, no. 4, pp. 229–236, 1982, doi: 10.1007/BF00381662.
- [61] J. J. Callaghan, “The clinical results and basic science of total hip arthroplasty with porous-coated prostheses,” *The Journal of Bone and Joint Surgery*, vol. 75, no. 2, pp. 299–236, 1993, doi: 10.2106/00004623-199302000-00020.
- [62] M. A. Mont, T. R. Yoon, K. A. Krackow, and D. S. Hungerford, “Clinical experience with a proximally porous-coated second-generation cementless total hip

- prosthesis: Minimum 5-year follow-up,” *Journal of Arthroplasty*, vol. 14, no. 8, pp. 930–939, 1999, doi: 10.1016/S0883-5403(99)90006-2.
- [63] R. B. Bourne, C. H. Rorabeck, B. C. Burkart, and P. G. Kirk, “Ingrowth surfaces: Plasma spray coating to titanium alloy hip replacements,” *Clinical Orthopaedics and Related Research*, vol. 298, no. 298, pp. 37–46, 1994, PMID: 8118992
- [64] R. M. Pilliar, “Powder metal-made orthopedic implants with porous surface for fixation by tissue ingrowth,” *Clinical Orthopaedics and Related Research*, vol. 176, pp. 42–51, 1983, doi: 10.1097/00003086-198306000-00007.
- [65] J. D. Bobyn, G. J. Stackpool, S. A. Hacking, M. Tanzer, and J. J. Krygier, “Characteristics of bone ingrowth and interface mechanics of a new porous tantalum biomaterial,” *Journal of Bone and Joint Surgery - Series B*, vol. 81, no. 5, pp. 907–914, 1999, doi: 10.1302/0301-620X.81B5.9283.
- [66] K. A. Zweymuller, F. K. Lintner, and M. F. Semlitsch, “Biologic fixation of a press-fit titanium hip joint endoprosthesis,” *Clinical Orthopaedics and Related Research*, no. 235, pp. 195–206, 1988, doi: 10.1097/00003086-198810000-00019.
- [67] S. A. Hacking, J. D. Bobyn, M. Tanzer, and J. J. Krygier, “The osseous response to corundum blasted implant surfaces in a canine hip model,” *Clinical Orthopaedics and Related Research*, vol. 364, no. 364, pp. 240–253, 1999, doi: 10.1097/00003086-199907000-00031.
- [68] M. G. Joshi, S. G. Advani, F. Miller, and M. H. Santare, “Analysis of a femoral hip prosthesis designed to reduce stress shielding,” *Journal of Biomechanics*, vol. 33,

no. 12, pp. 1655–1662, 2000, doi: 10.1016/S0021-9290(00)00110-X.

- [69] J. Jamari, M. I. Ammarullah, G. Santoso, S. Sugiharto, T. Supriyono, A. T. Prakoso, H. Basri, and E. van der Heide, “Computational Contact Pressure Prediction of CoCrMo, SS 316L and Ti6Al4V Femoral Head against UHMWPE Acetabular Cup under Gait Cycle,” *Journal of Functional Biomaterials*, vol. 13, no. 2, 2022, doi: 10.3390/jfb13020064.
- [70] P. I. Joseph, B. Richard A., B. Robert E., R. Richard H., C. Joy C., and P. Gary, “Aseptic Loosening After Total Hip Arthroplasty,” *The Journal of Arthroplasty*, vol. 1, pp. 99–107, 1986, doi: 10.1016/S0883-5403(86)80047-X.
- [71] R. Huiskes, H. Weinans, and B. Van Rietbergen, “The relationship between stress shielding and bone resorption around total hip stems and the effects of flexible materials,” *Clinical Orthopaedics and Related Research*, vol. 274, pp. 124–134, 1992, doi: 10.1097/00003086-199201000-00014.
- [72] H. Weinans, D. R. Sumner, R. Igloria, and R. N. Natarajan, “Sensitivity of periprosthetic stress-shielding to load and the bone density-modulus relationship in subject-specific finite element models,” *Journal of Biomechanics*, vol. 33, no. 7, pp. 809–817, 2000, doi: 10.1016/S0021-9290(00)00036-1.
- [73] M. Kaur and K. Singh, “Review on titanium and titanium based alloys as biomaterials for orthopaedic applications,” *Materials Science and Engineering C*, vol. 102, no. April, pp. 844–862, 2019, doi: 10.1016/j.msec.2019.04.064.
- [74] L. Guo, S. Ataollah Naghavi, Z. Wang, S. Nath Varma, Z. Han, Z. Yao, L. Wang,

- L. Wang, and C. Liu, "On the design evolution of hip implants: A review," *Materials and Design*, vol. 216, p. 110552, 2022, doi: 10.1016/j.matdes.2022.110552.
- [75] X. Gao, Y. Zhao, M. Wang, Z. Liu, and C. Liu, "Parametric Design of Hip Implant With Gradient Porous Structure," *Frontiers in Bioengineering and Biotechnology*, vol. 10, no. May, 2022, doi: 10.3389/fbioe.2022.850184.
- [76] X. Wang, S. Xu, S. Zhou, W. Xu, M. Leary, P. Choong, M. Qian, M. Brandt, and Y. M. Xie, "Topological design and additive manufacturing of porous metals for bone scaffolds and orthopaedic implants: A review," *Biomaterials*, vol. 83, pp. 127–141, 2016, doi: 10.1016/j.biomaterials.2016.01.012.
- [77] M. Niinomi, T. Hattori, K. Morikawa, T. Kasuga, A. Suzuki, H. Fukui, and S. Niwa, "Development of low rigidity β -type titanium alloy for biomedical applications," *Materials Transactions*, vol. 43, no. 12, pp. 2970–2977, 2002, doi: 10.2320/matertrans.43.2970.
- [78] M. Niinomi, "Mechanical biocompatibilities of titanium alloys for biomedical applications," *Journal of the Mechanical Behavior of Biomedical Materials*, vol. 1, no. 1, pp. 30–42, 2008, doi: 10.1016/j.jmbbm.2007.07.001.
- [79] M. Niinomi, M. Nakai, and J. Hieda, "Development of new metallic alloys for biomedical applications," *Acta Biomaterialia*, vol. 8, no. 11, pp. 3888–3903, 2012, doi: 10.1016/j.actbio.2012.06.037.
- [80] M. Todo, "Biomechanical Analysis of Hip Joint Arthroplasties using CT-Image Based Finite Element Method," *Journal of Surgery and Research*, vol. 01, no. 02,

pp. 34–41, 2018, doi: 10.26502/jsr.1002005.

- [81] J. D. Bobyn, E. S. Mortimer, A. H. Glassman, C. A. Engh, J. E. Miller, and C. E. Brooks, “Producing and avoiding stress shielding: Laboratory and clinical observations of noncemented total hip arthroplasty,” *Clinical Orthopaedics and Related Research*, no. 274, pp. 79–96, 1992.
- [82] M. Kanto, S. Fukunishi, T. Fukui, S. Nishio, Y. Fujihara, S. Okahisa, Y. Takeda, S. Yoshiya, and T. Tachibana, “Radiological Evaluation of the Relationship Between Cortical Hypertrophy and Stress Shielding After Total Hip Arthroplasty Using a Cementless Stem,” *Arthroplasty Today*, vol. 6, no. 4, pp. 894–900, 2020, doi: 10.1016/j.artd.2020.09.018.
- [83] F. Biggi, S. Di Fabio, C. D’Antimo, and S. Trevisani, “Periprosthetic fractures of the femur: The stability of the implant dictates the type of treatment,” *Journal of Orthopaedics and Traumatology*, vol. 11, no. 1, pp. 1–5, 2010, doi: 10.1007/s10195-010-0085-z.
- [84] A. N. Fleischman and A. F. Chen, “Periprosthetic fractures around the femoral stem: Overcoming challenges and avoiding pitfalls,” *Annals of Translational Medicine*, vol. 3, no. 16, pp. 1–13, 2015, doi: 10.3978/j.issn.2305-5839.2015.09.32.
- [85] K. Eustathios, E. Tsiridis, L. Necas, M. Rovnak, M. Buttaro, J. A. Scola, R. Schwarzkopf, J. M. Stutz, C. K. Ledford, R. T. Trousdale, “Periprosthetic Femoral Fractures (PFFs),” *The Adult Hip - Master Case Series and Techniques*, pp. 791–816, 2018, doi: 10.1007/978-3-319-64177-5.

- [86] H. Lindahl, G. Garellick, H. Regnér, P. Herberts, And H. Malchau, “Three Hundred and Twenty-One Periprosthetic Femoral Fractures,” *The Journal of Bone and Joint Surgery-American Volume*, vol. 88, no. 6, pp. 1215–1222, 2006, doi: 10.2106/00004623-200606000-00007.
- [87] D. Marsland and S. C. Mears, “A Review of Periprosthetic Femoral Fractures Associated With Total Hip Arthroplasty,” *Geriatric Orthopaedic Surgery & Rehabilitation*, vol. 3, no. 3, pp. 107–120, 2012, doi: 10.1177/2151458512462870.
- [88] T. Bhattacharyya, D. Chang, J. B. Meigs, D. M. Estok, and H. Malchau, “Mortality after periprosthetic fracture of the femur,” *Journal of Bone and Joint Surgery*, vol. 89 A, no. 12, pp. 2658–2662, 2007, doi: 10.2106/JBJS.F.01538.
- [89] J. N. Lamb, G. S. Matharu, A. Redmond, A. Judge, R. M. West, and H. G. Pandit, “Risk Factors for Intraoperative Periprosthetic Femoral Fractures During Primary Total Hip Arthroplasty. An Analysis From the National Joint Registry for England and Wales and the Isle of Man,” *Journal of Arthroplasty*, vol. 34, no. 12, pp. 3065-3073.e1, 2019, doi: 10.1016/j.arth.2019.06.062.
- [90] D. Davidson, J. Pike, D. Garbuz, C. P. Duncan, and B. A. Masri, “Intraoperative periprosthetic fractures during total hip arthroplasty: Evaluation and management,” *Journal of Bone and Joint Surgery*, vol. 90, no. 9, pp. 2000–2012, 2008, doi: 10.2106/JBJS.H.00331.
- [91] H. Brüggemann, I. Dalen, L. K. Bache-Mathiesen, A. M. Fenstad, G. Hallan, and L. Fosse, “Incidence and risk factors of intraoperative periprosthetic femoral fractures

during primary total hip arthroplasty: 218,423 cases reported to the Norwegian Arthroplasty Register between 1987 and 2020,” *Acta Orthopaedica*, vol. 93, pp. 405–412, 2022, doi: 10.2340/17453674.2022.2431.

- [92] C. C. Sidler-Maier and J. P. Waddell, “Incidence and predisposing factors of periprosthetic proximal femoral fractures: a literature review,” *International Orthopaedics*, vol. 39, no. 9, pp. 1673–1682, 2015, doi: 10.1007/s00264-015-2721-y.
- [93] J. Franklin and H. Malchau, “Risk factors for periprosthetic femoral fracture,” *Injury*, vol. 38, no. 6, pp. 655–660, 2007, doi: 10.1016/j.injury.2007.02.049.
- [94] A. V. Carli, J. J. Negus, and F. S. Haddad, “Periprosthetic femoral fractures and trying to avoid them what is the contribution of femoral component design to the increased risk of periprosthetic femoral fracture?,” *Bone and Joint Journal*, vol. 99B, no. 1, pp. 50–59, 2017, doi: 10.1302/0301-620X.99B1.BJJ-2016-0220.R1.
- [95] H. Lindahl, “Epidemiology of periprosthetic femur fracture around a total hip arthroplasty,” *Injury*, vol. 38, no. 6, pp. 651–654, 2007, doi: 10.1016/j.injury.2007.02.048.
- [96] H. Lindahl, H. Malchau, P. Herberts, and G. Garellick, “Periprosthetic femoral fractures: Classification and demographics of 1049 periprosthetic femoral fractures from the Swedish National Hip Arthroplasty Register,” *Journal of Arthroplasty*, vol. 20, no. 7, pp. 857–865, 2005, doi: 10.1016/j.arth.2005.02.001.
- [97] F. S. Haddad, B. A. Masri, D. S. Garbuz, and C. P. Duncan, “The prevention of

periprosthetic fractures in total hip and knee arthroplasty,” *Orthopedic Clinics of North America*, vol. 30, no. 2, pp. 191–207, 1999, doi: 10.1016/S0030-5898(05)70074-2.

- [98] I. D. Learmonth, “The management of periprosthetic fractures around the femoral stem,” *Journal of Bone and Joint Surgery - Series B*, vol. 86, no. 1, pp. 13–19, 2004, doi: 10.1302/0301-620x.86b1.14864.
- [99] Wu C.C., Au M.K., Wu S.S., Lin L.C., “Risk factors for postoperative femoral fracture in cementless hip arthroplasty,” *Journal of the Formosan Medical Association*, 1999 Mar;98(3):190-4. PMID: 10365538.
- [100] C. Rogmark and O. Leonardsson, “Hip arthroplasty for the treatment of displaced fractures of the femoral neck in elderly patients,” *Bone and Joint Journal*, vol. 98B, no. 3, pp. 291–297, 2016, doi: 10.1302/0301-620X.98B3.36515.
- [101] B. A. Masri, R. M. D. Meek, and C. P. Duncan, “Periprosthetic Fractures Evaluation and Treatment,” *Clinical Orthopaedics and Related Research*, vol. 420, no. 420, pp. 80–95, 2004, doi: 10.1097/00003086-200403000-00012.
- [102] R. Schwarzkopf, J. K. Oni, and S. E. Marwin, “Total Hip Arthroplasty Periprosthetic Femoral Fractures: a review of classification and current treatment,” *Bulletin of the Hospital for Joint Disease (2013)*, vol. 71, no. 1, pp. 68–78, 2013, PMID: 24032586.
- [103] A. L. Sabatini and T. Goswami, “Hip implants VII: Finite element analysis and optimization of cross-sections,” *Materials and Design*, vol. 29, no. 7, pp. 1438–1446, 2008, doi: 10.1016/j.matdes.2007.09.002.

- [104] A. Z. Senalp, O. Kayabasi, and H. Kurtaran, “Static, dynamic and fatigue behavior of newly designed stem shapes for hip prosthesis using finite element analysis,” *Materials and Design*, vol. 28, no. 5, pp. 1577–1583, 2007, doi: 10.1016/j.matdes.2006.02.015.
- [105] M. Reimeringer, N. Nuno, C. Desmarais-Trepanier, M. Lavigne, P. A. Vendittoli, “The influence of uncemented femoral stem length and design on its primary stability: a finite element analysis,” *Computer Methods in Biomechanics and Biomedical Engineering*, vol. 16, no. 11, pp. 1221–1231, 2013, doi: 10.1080/10255842.2012.662677.
- [106] D. K. Kwak, S. H. Bang, S.-J. Lee, J.-H. Park, and J.-H. Yoo, “Effect of stem position and length on bone-stem constructs after cementless hip arthroplasty,” *Bone and Joint Research*, vol. 10, no. 4, pp. 250–258, 2021, doi: 10.1302/2046-3758.104.BJR-2020-0043.R3.
- [107] J. Cordey and E. Gautier, “Strain gauges used in the mechanical testing of bones. Part I: Theoretical and technical aspects,” *Injury*, vol. 30, no. SUPPL. 1, 1999, doi: 10.1016/s0020-1383(99)00120-5.
- [108] M. Bessho, I. O. ã, J. Matsuyama, T. Matsumoto, and K. Imai, “Prediction of strength and strain of the proximal femur by a CT-based finite element method,” *Journal of Biomechanics*, vol. 40, pp. 1745–1753, 2007, doi: 10.1016/j.jbiomech.2006.08.003.
- [109] M. Todo and K. Fukuoka, “Biomechanical Analysis of Femur with THA and RHA

- implants using CT-Image Based Finite Element Method,” *Journal of Orthopaedics and Sports Medicine*, vol. 02, no. 02, pp. 89–107, 2020, doi: 10.26502/josm.511500024.
- [110] A. H. Abdullah and M. Mitsugu Todo, “Effects of Hip Arthroplasties on Bone Adaptation in Lower Limbs: A Computational Study,” *Journal of Biosciences and Medicines*, vol. 03, no. 04, pp. 1–7, 2015, doi: 10.4236/jbm.2015.34001.
- [111] A. H. Abdullah and M. Todo, “Stress Evaluation of Lower Limbs with Hip Osteoarthritis and Hip Arthroplasty,” *Journal of Medical and Bioengineering*, vol. 4, no. 2, pp. 100–104, 2015, doi: 10.12720/jomb.4.2.100-104.
- [112] A. H. Abdullah, M. Todo, Y. Nakashima, and Y. Iwamoto, “Risk of Femoral Bone Fractures in Hip Arthroplasties during Sideway Falls,” *International Journal of Applied Physics and Mathematics*, vol. 4, no. 4, pp. 286–289, 2014, doi: 10.7763/ijapm.2014.v4.300.
- [113] S. Wu, M. Todo, D. Umebayashi, and Y. Yamamoto, “Risk assessment of vertebral compressive fracture using bone mass index and strength predicted by computed tomography image based finite element analysis,” *Clinical Biomechanics*, vol. 85, no. March 2020, p. 105365, 2021, doi: 10.1016/j.clinbiomech.2021.105365.
- [114] A. H. Abdullah, M. Todo, and Y. Nakashima, “Prediction of damage formation in hip arthroplasties by finite element analysis using computed tomography images,” *Medical Engineering and Physics*, vol. 44, pp. 8–15, 2017, doi: 10.1016/j.medengphy.2017.03.006.

- [115] M. Bessho, I. Ohnishi, T. Matsumoto, S. Ohashi, J. Matsuyama, K. Tobita, M. Kaneko, and K. Nakamura, "Prediction of proximal femur strength using a CT-based nonlinear finite element method: Differences in predicted fracture load and site with changing load and boundary conditions," *Bone*, vol. 45, no. 2, pp. 226–231, 2009, doi: 10.1016/j.bone.2009.04.241.
- [116] N. F. Ismail, S. Shuib, M. A. Yahaya, A. Z. Romli, and A. A. Shokri, "Finite element analysis of uncemented total hip replacement: The effect of bone-implant interface," *International Journal of Engineering and Technology(UAE)*, vol. 7, no. 4, pp. 230–234, 2018, doi: 10.14419/ijet.v7i4.26.22173.
- [117] M. S. Yusof, N. Aznan, N. Fazli, A. Manan, S. H. Marwan, M. H. Mazlan, and A. H. Abdullah, "Effects of Varus and Sagittal Implant Positioning to the Stress Adaptation in Cementless Hip Arthroplasty," *Malaysian Journal of Medicine and Health Sciences*, vol. 17(SUPP13), no. 5, pp. 22–27, 2021.
- [118] J. N. Lamb, J. Baetz, B. H. Van Duren, A. Redmond, R. M. West, M. M. Morlock, and H. G. Pandit, "A calcar collar is protective against early periprosthetic femoral fracture around cementless femoral components in primary total hip arthroplasty A," pp. 779–786, doi: 10.1302/0301-620X.
- [119] E. Schwarz, G. Reinisch, A. Brandauer, S. Aharinejad, W. Scharf, and K. Trieb, "Load transfer and periprosthetic fractures after total hip arthroplasty: Comparison of periprosthetic fractures of femora implanted with cementless distal-load or proximal-load femoral components and measurement of the femoral strain at the time of implant," *Clinical Biomechanics*, vol. 54, no. July 2017, pp. 137–142, 2018,

doi: 10.1016/j.clinbiomech.2018.03.010.

- [120] T. Čengić, J. Kodvanj, T. Smoljanović, P. Adamović, A. Alerić, I. Bohaček, M. Milošević, S. Sabalić, and D. Delimar, “Impact of cementless zweymüller stem anteversion on resistance to periprosthetic fracture in total hip arthroplasty,” *Acta Clinica Croatica*, vol. 60, no. 3, pp. 429–434, 2021, doi: 10.20471/acc.2021.60.03.13.
- [121] M. I. Z. Ridzwan, S. Shuib, A. Y. Hassan, A. A. Shokri, and M. N. Mohammad Ibrahim, “Problem of stress shielding and improvement to the hip implant designs: A review,” *Journal of Medical Sciences*, vol. 7, no. 3, pp. 460–467, 2007, doi: 10.3923/jms.2007.460.467.
- [122] M. G. Dennis, J. A. Simon, F. J. Kummer, K. J. Koval, and P. E. Di Cesare, “Fixation of periprosthetic femoral shaft fractures: A biomechanical comparison of two techniques,” *Journal of Orthopaedic Trauma*, vol. 15, no. 3, pp. 177–180, 2001, doi: 10.1097/00005131-200103000-00005.
- [123] E. Fulkerson, K. Koval, C. F. Preston, K. Iesaka, F. J. Kummer, and K. A. Egol, “Fixation of Periprosthetic Femoral Shaft Fractures Associated With Cemented Femoral Stems,” *Journal of Orthopaedic Trauma*, vol. 20, no. 2, pp. 89–93, 2006, doi: 10.1097/01.bot.0000199119.38359.96.
- [124] M. Talbot, R. Zdero, and E. H. Schemitsch, “Cyclic loading of periprosthetic fracture fixation constructs,” *Journal of Trauma - Injury, Infection and Critical Care*, vol. 64, no. 5, pp. 1308–1312, 2008, doi: 10.1097/TA.0b013e31811ea244.

- [125] R. Zdero, R. Walker, J. P. Waddell, and E. H. Schemitsch, “Biomechanical evaluation of periprosthetic femoral fracture fixation,” *Journal of Bone and Joint Surgery - Series A*, vol. 90, no. 5, pp. 1068–1077, 2008, doi: 10.2106/JBJS.F.01561.
- [126] J. K. Choi, T. R. Gardner, E. Yoon, T. A. Morrison, W. B. Macaulay, and J. A. Geller, “The effect of fixation technique on the stiffness of comminuted vancouver B1 periprosthetic femur fractures,” *Journal of Arthroplasty*, vol. 25, no. SUPPL. 6, pp. 124–128, 2010, doi: 10.1016/j.arth.2010.04.009.
- [127] J. H. Keyak, S. A. Rossi, K. A. Jones, and H. B. Skinner, “Prediction of femoral fracture load using automated finite element modeling,” *Journal of Biomechanics*, vol. 31, no. 2, pp. 125–133, 1997, doi: 10.1016/S0021-9290(97)00123-1.
- [128] T. S. Keller, “Predicting the compressive mechanical behavior of bone,” *Journal of Biomechanics*, vol. 27, no. 9, pp. 1159–1168, 1994, doi: 10.1016/0021-9290(94)90056-6.
- [129] T. M. Keaveny, E. F. Wachtel, W. C. Hayes, and C. M. Ford, “Differences between the tensile and compressive strengths of bovine tibial trabecular bone depend on modulus,” *Journal of Biomechanics*, vol. 27, no. 9, pp. 1137–1146, 1994, doi: 10.1016/0021-9290(94)90054-x.
- [130] T. S. Kaneko, M. R. Pejcic, J. Tehranzadeh, and J. H. Keyak, “Relationships between material properties and CT scan data of cortical bone with and without metastatic lesions,” *Medical Engineering and Physics*, vol. 25, no. 6, pp. 445–454, 2003, doi: 10.1016/S1350-4533(03)00030-4.

- [131] L. Røhl, E. Larsen, F. Linde, A. Odgaard, and J. Jørgensen, “Tensile and compressive properties of cancellous bone,” *Journal of Biomechanics*, vol. 24, no. 12, pp. 1143–1149, 1991, doi: 10.1016/0021-9290(91)90006-9.
- [132] X. Wang, X. Shen, X. Li, and C. Mauli Agrawal, “Age-related changes in the collagen network and toughness of bone,” *Bone*, vol. 31, no. 1, pp. 1–7, 2002, doi: 10.1016/S8756-3282(01)00697-4.
- [133] J. S. Bethea, J. R. DeAndrade, L. L. Fleming, S. D. Lindenbaum, and R. B. Welch, “Proximal femoral fractures following total hip arthroplasty,” *Clinical Orthopaedics and Related Research*, vol. No. 170, pp. 95–106, 1982, doi: 10.1097/00003086-198210000-00013.
- [134] H. O. Fredin, H. Lindberg, and A. S. Carlsson, “Femoral fracture following hip arthroplasty,” *Acta Orthopaedica*, vol. 58, no. 1, pp. 20–22, 1987, doi: 10.3109/17453678709146336.
- [135] J. S. Jensen, G. Barfod, D. Hansen, E. Larsen, F. Linde, H. Menck, and B. Olsen, “Femoral shaft fracture after hip arthroplasty,” *Acta Orthopaedica*, vol. 59, no. 1, pp. 9–13, 1988, doi: 10.3109/17453678809149334.
- [136] M. J. Raschke and B. Schliemann, “Periprosthetic fractures,” *Chirurg*, vol. 91, no. 10, p. 793, 2020, doi: 10.1007/s00104-020-01269-6.
- [137] E. Meinberg, J. Agel, C. Roberts, M. Karam, and J. Kellam, “Fracture and Dislocation Classification Compendium—2018,” *Journal of Orthopaedic Trauma*, vol. 32, no. 1, pp. S1–S10, Jan. 2018, doi: 10.1097/BOT.0000000000001063.

- [138] J. Wilkerson and N. D. Fernando, “Classifications in Brief: The Dorr Classification of Femoral Bone,” *Clinical Orthopaedics and Related Research*, vol. 478, no. 8, pp. 1939–1944, 2020, doi: 10.1097/CORR.0000000000001295.
- [139] M. Viceconti, R. Muccini, M. Bernakiewicz, M. Baleani, and L. Cristofolini, “Large-sliding contact elements accurately predict levels of bone-implant micromotion relevant to osseointegration,” *Journal of Biomechanics*, vol. 33, no. 12, pp. 1611–1618, 2000, doi: 10.1016/S0021-9290(00)00140-8.